Observational Studies of Galactic Star-Forming Regions

A thesis submitted
in partial fulfillment for the degree of

Doctor of Philosophy

by

SWAGAT RANJAN DAS

DEPARTMENT OF EARTH & SPACE SCIENCES
INDIAN INSTITUTE OF SPACE SCIENCE AND TECHNOLOGY
THIRUVANANTHAPURAM - 695547, INDIA

JUNE 2018

Certificate

This is to certify that the project report entitled **"Observational Studies of Galactic Star-Forming Regions"** submitted by **Swagat Ranjan Das**, to the Indian Institute of Space Science and Technology, Thiruvananthapuram, in partial fulfilment for the award of the degree of **Doctor of Philosophy**, is a bonafide record of the project research work carried out by him under my supervision. The contents of this report, in full or in parts, have not been submitted to any other Institute or University for the award of any degree or diploma.

Dr. Anandmayee Tej
Professor
Department of Earth & Space Sciences

Counter signature of HOD with seal

Place: Thiruvananthapuram
June 2018

Declaration

I declare that this report titled **"Observational Studies of Galactic Star-Forming Regions"** submitted in partial fulfilment of the Degree of **"Doctor of Philosophy"** is a record of original work carried out by me under the supervision of **Dr. Anandmayee Tej**, and has not formed the basis for the award of any degree, diploma, associateship, fellowship, or other titles in this or any other Institution or University of higher learning. In keeping with the ethical practice in reporting scientific information, due acknowledgements have been made wherever the findings of others have been cited.

Swagat Ranjan Das
Research Scholar
Department of Earth & Space Sciences
Roll No. : SC12D016

Place: Thiruvananthapuram
June 2018

Acknowledgments

First and foremost, I would like to express my sincere gratitude to my advisor Dr. Anandmayee Tej for her guidance and continuous support throughout my PhD tenure. She was always there to support me especially during the most stressful times. I am thankful to her from the bottom of my heart for her patience, motivation, enthusiasm, and the immense knowledge she shared with me.

I would like to place on record my sincere thanks to Dr. Sarita Vig. She was not only a member of my Doctoral Committee but also was closely involved in my research work constantly giving her valuable inputs and comments to improve the data reduction, analysis and interpretation. I also like to express my sincere gratitude to my collaborator, Dr. Ishwara Chandra C. H. of NCRA, Pune. He is one of the nicest persons I have ever met. I learnt GMRT data reduction from him. Being an expert in the field of radio astronomy, his suggestions and advice made a lot of difference in my approach towards radio data reduction. I am greatly thankful to him for all his help and support. I also would like to express my gratitude to Dr. Tie Liu (East Asian Observatory, USA) and Dr. Hong-Li Liu (The Chinese University of Hong Kong, China) for the many fruitful discussions I had with them.

I appreciate the many interactions and discussion with the faculty members of the Department. I wish to thank the faculty of members of the A & A group, Dr. Anand Narayanan, Dr. Samir Mandal, Dr. Resmi Lekshmi, and Dr. Jagadheep D for their help, encouragement and motivation. I would also like to thank the other members of my doctoral committee – Prof. Chandrasekar A, Prof. Swarna K Ghosh, Prof. T. Chandrasekhar, Dr. S. Murugesh for monitoring my work and giving me their honest advice. Their constant support and guidance has definitely improved the quality of my research work. I am thankful to Dr. K. S. Dasgupta, former Director and Dr. Vinay Kumar Dadhwal present Director of IIST, for the academic support and the facilities provided to carry out the research work at IIST. I am also thankful to Dr. Raju K. George, Dean, Research and Development and Dr. Kuruvilla Joseph, Dean, Student Activities

for their encouragement and support. I also thank the Research Council of IIST for their support at various phases of the PhD program.

I thank the staff members of GMRT who helped me with the radio observations that have been extensively used in my research work. My thanks to my lab mates Veena, Namitha (PhD students), Varsha, Govind, Jim, Karthika, Gopika (MS students), Amrita, Dinil (Project students) for their fruitful informal discussions. I would like to thank Mr. Sai Krishnan, lab tutor for his constant help throughout my PhD time. Thanks to all staff members of the Department for their support. I thank the administration, library, and canteen staff members of IIST, for their support during this PhD period.

It is my pleasure to acknowledge the support of some special individuals – my friends. Because of the presence of such lovely people, time in IIST was very wonderful and memorable. I would like to acknowledge those for their moral support and motivation. Thanks to Abhishek, Sujit, Rakesh, and Najeeb for all the fun times we spend together while travelling around the city. These are the pleasant times which used to always supply the energy to overcome frustration. Thanks to Rajesh, Gopu, Manju, Dibyendu, and Randeep for sharing some good times in IIST. Also special thanks to Sachin, Aneesha, Veena, and Namitha for being part of many sweet memories.

I would like to acknowledge the people who mean the world to me, my parents. My special thanks to my mother for her love and care that she always has for me. She is my inspiration who always encourages me to move ahead in life. Thanks to my father who is one of nicest person, for his guidance to become a better human. I thank my brother, sister and sister-in-law for all the love and care. Special thanks to my niece whose presence and smile are enough to forget everything. I consider myself the luckiest to have such a supportive family, standing behind me with their love and support.

Swagat Ranjan Das

Thiruvananthapuram, India

Abstract

Massive stars, with their radiative, mechanical and chemical feedback, are key players influencing the local and global dynamical and chemical state of the interstellar medium through ionization and radiation pressure, stellar winds, outflows and supernovae. These stars are therefore fundamental and crucial for unravelling the astrophysics of the formation, sustenance, and dissipation of structures ranging from the largest, Galactic scales, to giant molecular clouds, disks, and planetary systems. The need for a complete and consistent picture of the processes involved in the formation of the high-mass stellar population is evident from the lack of consensus and the various theories proposed. This is compounded with the challenges in observing this regime.

Motivated by the above scenario, this thesis presents multiwavelength studies focussed towards a selected sample of Galactic massive star forming regions. With the aim to gain a better insight into the formation mechanism of massive stars and their feedback on the surrounding interstellar medium, we selected two infrared dust bubbles (S10, CS51) and two H II regions (G346.077−0.056 and G346.056−0.021). Towards north east of the bubble S10, an extended green object EGO G345.99−0.02 is located at an angular distance of $\sim 5'$, which is also studied along with S10. In addition, a statistical investigation of cold dust emission towards a large sample of seventeen IR dust bubbles has been achieved.

Low-frequency radio continuum maps are obtained using the Giant Metrewave Radio Telescope to probe the associated ionized gas. Our results provide the first low-frequency radio continuum maps of the targets under study and are a much required valuable addition to the database of high-mass stars. Radio continuum maps have helped us in exploring the associated ionized gas, the nature of the ionizing sources. In addition, exploiting the low-frequency domain where the contribution from non-thermal emission in significant, we have investigated the radiation mechanism from the generated radio spectral index maps. In case of the two H II regions studied, we attempt to shed more light on the cometary radio morphology by invoking the well known 'bow-shock' and 'champagne-flow' models.

The identification of the ionizing source and nature of the stellar population has been carried out using the available near- and mid-infrared data from various archives like the 2MASS, *Spitze*-GLIMPSE and the VVV surveys. Cold dust emission associated with these regions is investigated using far-infrared data from the *Herschel* Space Telescope archives. The generated column density probability distribution function give crucial clues to the feedback from the massive stars on the surrounding. For the bubble CS51, molecular line data from the MALT90 survey helped us in confirming the expansion of the bubble and to ascertain the evolutionary status of the cold dust clumps. These show signature of triggered star formation and the physical conditions are seen to be conducive with the 'collect and collapse' mechanism.

Studying a large sample of seventeen infrared dust bubbles yield promising results. With simplistic assumptions, the study of around hundred cold dust clumps, associated with these bubbles, lend support to the 'monolithic collapse' picture of formation. These results also impress upon the fact that bubbles are indeed ideal laboratories to explore triggered star formation.

Contents

List of Tables

List of Figures

Abbreviations

2MASS	2 Micron All Sky Survey
AGB	Asymptotic Giant Branch
AGN	Active Galactic Nuclei
AIPS	Astronomical Image Processing System
ATCA	Australian Telescope Compact Array
ATLASGAL	Atacama PathïňĄnder Experiment
BW	Band Width
CCP	Color Color Plot
CDMS	Cologne Database for Molecular Spectroscopy
CMP	Color Magniture Plot
CNM	Cold Neutral Medium
CC	Collect Collapse
EGO	Extended Green Object
EM	Emission Measure
FIR	Far Infrared
FWHM	Full Width Half Maximum
GBT	Green Bank Telescope
GHz	Giga Hertz
GLIMPSE	Galactic Legacy Infrared Mid-Plane Survey Extraordinaire
GMC	Giant Molecular Cloud
GMRT	Giant Meterwave Radio Telescope
hfs	Hyperfine Structure
HCH II	Hypercompact H II Region
HI-GAL	Herschel Infrared Galactic Plane Survey
HIFI	Heterodyne Instrument for the Far Infrared
HIPE	Herschel Interactive Processing Environment
HISA	H I Self Absorption
IF	Ionization Front
IMF	Intial Mass Function
ISM	Interstellar Medium
IR	Infrared
IRAS	Infra-Red Astronomical Satellite
IRAC	Infrared Array Camera
IRAF	Image Reduction and Analysis Facility
IRDC	Infrared Dark Cloud
IRSA	Infrared Science Archive

KDA	Kinematic Distance Ambiguity
LABOCA	Large APEX Bolometer Camera
LAMD	Leiden Atomic and Molecular Database
MALT90 survey	Millimeter Astronomy Legacy Team 90 GHz survey
MHz	Mega Hertz
MIPS	Multiband Imaging Photometer for Spitzer
MIPSGAL	Multiband Imaging Photometer Inner Galactic Plane Survey
MIR	Mid Infrared
MOPS	Mopra Spectrometer
MPG	Max Planck Gesellschaft
MYSO	Massive Young Stellar Object
NIR	Near Infrared
NVSS	NRAO VLA Sky Survey
PACS	Photodetector Array Camera and Spectrometer
PAH	Polycyclic Aromatic Hydrocarbon
PDF	Probability Distribution Function
PDR	Photon Dissociation Region
PSF	Point Spread Function
RDI	Radiation Driven Implosion
RMS survey	Red MSX Source Survey
RRL	Radio Recombination Line
SCUBA	Submillimetre Common-User Bolometer Array
SED	Spectral Energy Distribution
SEST	Swedish-ESO Submillimetre Telescope
SPIRE	Spectral and Photometric Imaging Receiver
SUMSS	Sydney University Molonglo Sky Survey
ThrUMMS	The Three-mm Ultimate Mopra Milky Way Survey
UCH II	Ultracompact H II Region
UV	Ultra Violet
VIRCAM	VISTA InfraRed CAMera
VVV	VISTA Variables in the Via Lactea
WNM	Warm Neutral Medium
YSO	Young Stellar Object
ZAMS	Zero Age Main Sequence

Chapter 1

Introduction

A clear dark sky reveals the sparkling celestial diamonds - the stars. Not only have these stars fascinated every civilization but have ignited numerous minds to unravel their mysteries. Stars are the fundamental units of luminous matter in the universe. They are predominantly made up of hydrogen with the presence of other heavier elements such as helium, carbon, oxygen, etc. Stars present a wide range in their fundamental parameters like mass, luminosity, temperature, and size. Based on their spectral properties, that follow a surface temperature sequence, they have been classified into the well known spectral classes of O, B, A, F, G, K, M. Table 1.1 lists the spectral types and the corresponding typical values of various fundamental parameters. Stars serve as the primary tracers to investigate the structure and evolution of galaxies and hence the universe. Therefore, it is of central importance in astrophysics to understand the mechanism of how stars form and what influence they have on the surrounding medium. The process of forming stars from interstellar gas and dust underpins most of astrophysics, yet many questions regarding the details still remain unanswered.

Of special focus are the massive members ($M \gtrsim 8_{\odot}$). High-mass stars play a crucial role in the dynamical, morphological, and chemical evolution of the galaxies considering that their feedback to the interstellar medium (ISM) is in the form of energy and heavy elements. This is rendered possible through powerful stellar winds and the outpouring of ultraviolet (UV) radia-

Table 1.1
Spectral types and the corresponding typical values of various fundamental parameters.

Star type	Color	App. surface temperature (K)	Average mass ($M_{\odot}$)	Average radius ($R_{\odot}$)	Average Luminosity ($L_{\odot}$)	Examples
O	Blue	> 25000	60	15	10^6	10 Lacertae
B	Blue	10000 – 25000	18	7	10^4	Rigel, Spica
A	Blue	7500 – 11000	3	3	10^2	Sirius, Vega
F	Blue to White	6000 – 7500	1.7	1.3	6	Canopus, Procyon
G	White to Yellow	5000 – 6000	1.1	1.1	1.2	Sun, Capella
K	Orange to Red	3500 – 5000	0.8	0.9	0.4	Arcturus, Aldebaran
M	Red	< 3500	0.3	0.4	0.04	Betelgeuse, Antares

tion that can ionize the surrounding gas and form H II regions, and at the end, through supernova explosions. In addition, for other galaxies, majority of the stars within the detection limit of the current telescope/instrumentation facilities are massive stars. Hence, to understand the distant galaxies, we use massive stars as tools. This further stresses the fact that massive stars are key to understanding many physical phenomena in our own Galaxy, and other galaxies. As will be clear in the sections that follow, the processes involved in the formation of stars of this mass regime is not that well understood, both theoretically and observationally, as compared to the low-mass star formation picture.

1.1 Overview of star formation

The basic concept of gravitational collapse of molecular clouds to form stars is a seemingly simple and widely accepted concept but it involves a whole field of astrophysics. The recent decades have seen a plethora of multiwavelength observations which are coupled with extensive theoretical and advanced computational work in this active research area. Though these have tremendously helped in understanding the physical processes involved, many questions still remain unanswered or debatable. This section gives a brief overview of the subject.

The ISM is the birthplace for stars because it is the repository of raw material needed for star formation. The ISM fills the region between stars and exists in both the gaseous and solid state phases. In our Galaxy, the ISM is mainly located in the spiral arms and consists of around $\sim$ 10 – 15% of the total mass (Ferrière, 2001). The gas in the ISM is broadly organized in various phases, the characteristics of these are summarized in Table 1.2. Stars formation occurs in giant

Table 1.2
Physical parameters of different phases of the ISM. The values are taken from Tielens (2005).

Component	Fractional Volume (%)	Temperature (K)	Scale Height (pc)	Number Density (cm^{-3})
Hot inter cloud	50%	10^6	3000	0.003
Warm Neutral Medium	30%	8000	200	0.5
Warm Ionized Medium	25%	8000	900	0.1
Cold Neutral Medium	1%	80	94	50
Molecular clouds	0.05	10	75	>200
H II region	–	10000	70	10^5

cloud complexes generally termed as the Giant Molecular Clouds (GMCs) that comprises the

bulk of the molecular component of the Galaxy. The GMCs are part of the cold neutral medium. GMCs, that are the birthplace to millions of stars (Blitz, 1993), are composed primarily of molecular hydrogen (H_2), which accounts for $\sim$ 70% of the total mass. The interstellar clouds can be classified broadly into three categories i.e. Dark clouds, Diffuse clouds and Translucent clouds (Ferrière, 2001). Dark clouds are made up of gas with very low temperatures (T$\sim$10 – 20 K) and are associated with very high extinction. Diffuse clouds are made up of atomic gas that is still cold (T$\sim$100 K) and have low extinction and associated with absorption feature at some particular wavebands. Translucent clouds are made of both molecular and atomic gases and show intermediate extinction. Molecular line observations have revealed the GMCs to be clumpy and inhomogeneous in nature (Myers & Benson, 1983; Bronfman et al., 1989). Further, Williams et al. (2000) classified this inhomogeneity into a convincing hierarchical structure with the nomenclature of clouds, clumps, and cores. "Clump" is ascribed to structures within the cloud, where clusters of stars are likely to form and "cores" describe dense regions of single (or binary) star formation. However, it should be kept in mind that the availability of higher resolution data have revealed further fragmentation within "cores". Table 1.3 shows the typical values of the physical properties of structures within molecular clouds. The values listed are compiled from various papers. These hierarchical sub-structures are formed by gravitational collapse followed by fragmentation of regions of high densities. This marks the first step in star formation which is detailed in the following discussion.

Table 1.3
Physical properties of structures within molecular clouds.

Cloud Type	Size (pc)	Mass ($M_\odot$)	Density (cm^{-3})	Temperature (K)
GMC	50 – 200	10^4 – 10^6	100 – 300	10 – 15
Cloud	3 – 20	10^3 – 10^4	10^3 – 10^4	15 – 30
Clump	0.5 – 3	10^3 – 10^4	10^4 – 10^6	15 – 40
Cold core	0.1 – 0.5	10^2 – 10^3	10^5 – 10^7	30 – 100
Hot core	$\leq$ 0.1	10^2	10^6 – 10^8	100 – 200

Star formation is a process which effects the galaxy at all scales. Gravity is the key player but different mechanisms come into play at different scales depending on the opposing forces. Starting from the largest scales of diffuse interstellar matter, galactic tidal forces become important and condensation proceeds when gravity overcomes this force. At the level of GMCs,

turbulence and magnetic fields are the dominating gravity opposing forces and dissipation of these leads to collapse. The sub-structure of molecular clouds, the clumps, and cores, serve as sites for formation of stars. At this small scale of individual cores, thermal pressure serves as the counteracting force opposing gravity and defines the minimum mass for core collapse leading to star formation. As the cores undergo gravitational collapse, the centrifugal force associated with the angular momentum becomes significant thus halting contraction. This may lead to the formation of binary or multiple star systems. As the central region of the core reaches stellar density, thermal pressure stops further collapse and the 'stellar embryo' or 'protostar' forms which grows by mass accretion from the envelope. This phase is accompanied by bipolar jets which announces the birth of the star.

1.2 Low mass star formation

Low-mass stars are much more abundant than high-mass stars (e.g. Salpeter 1955; Kroupa 2001). In addition, several low-mass star forming regions are located closeby. Both these factors have favoured the study of low-mass star formation in detail. The formation mechanism of low-mass stars is relatively well understood. Understanding this is the first step before we delve into the high-mass domain. The classical picture of low-mass star formation is well-chronicled in the pioneering papers by Shu (1977); Shu et al. (1987) and later by Lada & Shu (1990); Kennicutt & Evans (2012). Figure 1.1 gives an overview of the different stages involved in low-mass star formation.

In the beginning, the self gravity of GMCs is counterbalanced by the turbulent and magnetic pressures thus resisting collapse. Over time, due to ambipolar diffusion, neutral atoms get separated from the ions. This leads to dissipation of the magnetic support and allows the neutrals to gradually form a dense, slowly rotating, protostellar core. Time taken for this is longer compared to the free-fall time scale. However, the presence of turbulence can enhance the collapsing time scale (Fatuzzo & Adams, 2002; Zweibel, 2002; McKee & Ostriker, 2007). As the ambipolar diffusion continues, the magnetic pressure reduces eventually leading to collapse on free-fall timescales. In the initial stage, the gravitationally bound cloud of gas, with uniform density and temperature, is in hydrostatic equilibrium. Here, the cloud is supported by mostly thermal pressure. Thus, the collapse criteria is dictated by the virial theorem which states that

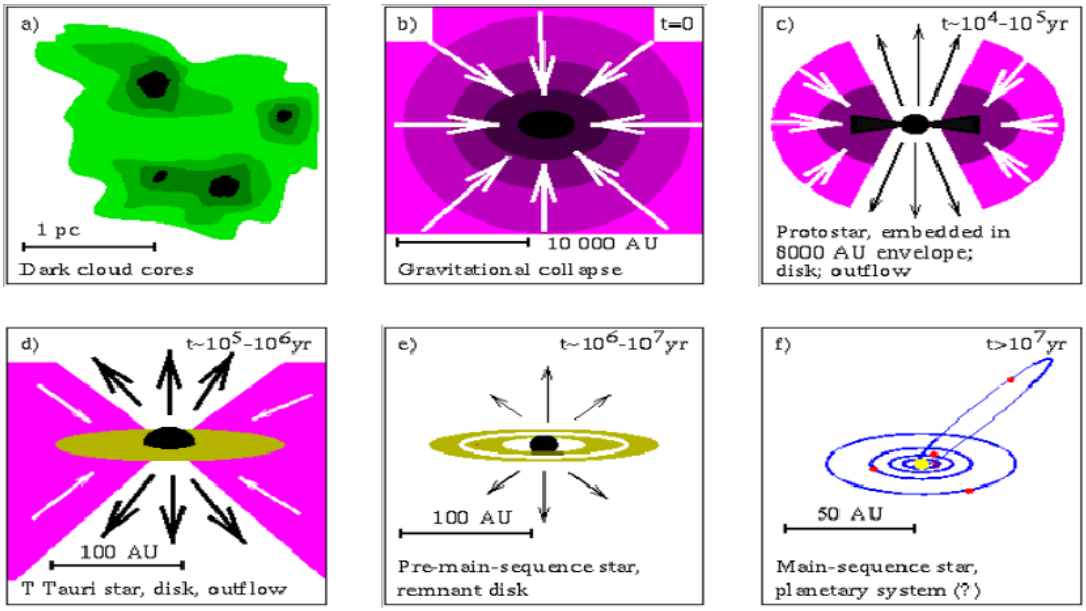

Figure 1.1: This figure taken from Hogerheijde (1998) (based on Shu et al. (1987)) displays the different stages involved in the formation of a low-mass star.

for a gravitationally bound system in equilibrium, the total kinetic energy is one half the gravitational potential energy. If the balance is perturbed, collapse ensues. Several triggers, like shock propagation from nearby supernova explosion, intense UV radiation from massive stars, collision of GMCs, could be responsible for this perturbation. The virial theorem then yields the minimum mass required to undergo gravitational collapse. This is known as the *Jeans'* mass which for an ideal gas can be expressed as follows

$$M_J = \left(\frac{5kT}{G\mu m_H}\right)^{3/2} \left(\frac{3}{4\pi\rho}\right)^{1/2} \tag{1.1}$$

where ρ and T are the local density and temperature, m_H is the mass of a hydrogen atom, μ is the mean molecular weight, G is the gravitational constant and k is Boltzmann constant.

The above equation shows the dependency on the density and temperature of the cloud, which implies that as the density increases, the minimum mass required to collapse decreases. In contrast, the increase in temperature means higher mass required to undergo collapse. Once the cloud achieves the *Jeans'* mass and due to the leaking of magnetic flux by the ambipolar diffusion, the cloud is in free-fall collapse. During the initial phase, the cloud is optically thin and the collapse is isothermal. In this stage, the gravitational energy lost due to free-fall

is radiated away efficiently without heating the cloud. As the temperature remains constant and density increases due to collapse, the *Jeans'* mass decreases. Density fluctuations in the cloud lead to clumps and cores where the *Jeans* criteria is satisfied locally. This gravitational fragmentation process puts in place a hierarchy of progressively smaller and denser clumps which possibly explains the clumpy structure observed within molecular clouds. However, GMCs have internal turbulent motions that are supersonic on all but the smallest scales, and fragmentation of the cloud and the clumpy structure can also be linked to the hierarchy of these motions. In case of the gravitational fragmentation, the cascading stops as the density increases and the cloud becomes more and more opaque to its own radiation. Eventually, a density state is reached where the collapse no longer remains isothermal and proceeds adiabatically. Under these conditions, the *Jeans'* mass increases with density thus setting a limit on the smallest cores. In the other case, the observed turbulent motions in molecular clouds become subsonic on the smallest scales, again suggesting a lower limit to the sizes of the compressed structures that are created by turbulence.

As the density increases towards the centre, the core undergoes an inside-out collapse and the collapse front expands out with speed of sound. Subsequent to this, an accretion phase follows in which the material from the envelope falls onto the protostar forming at the centre. As the material falls onto the central star, the residual angular momentum of the infalling material causes the envelope to spin down into a circumstellar disk as the protostar contracts. As the angular momentum is deposited into the surrounding medium, highly collimated outflows and jets are also observed. As the accreting material gets depleted (in $\sim 10^7$ years) in the protostar vicinity, the accretion stops. During this time the temperature and pressure of the central protostar increases and becomes sufficient to start nuclear fusion reactions, thus heralding the birth of a new young star on the main-sequence.

1.2.1 Evolution of low-mass star formation

Observationally, low-mass young stellar objects (YSOs) are seen to fit well into four distinct evolutionary classes. This is based on their spectral energy distributions (SEDs) (Lada & Wilking, 1984; Andre et al., 1993). Radiation powered by the central protostar is scattered, absorbed, and re-emitted by the dusty protostellar envelope before escaping the system. The nature of the resultant SED reveals the conditions in the envelope at each stage of evolution. The evolution

of the SED is due to gradual dissipation of gas and dust from the natal envelope. Lada (1987) give a quantitative classification scheme based on the spectral index (α) which is defined as

$$\alpha = \frac{dlog(\lambda F_\lambda)}{dlog(\lambda)} \tag{1.2}$$

For Class I sources $\alpha > 0$; Class II, or classical T Tauri stars $-2 < \alpha < 0$; Class III, weak emission T Tauri stars $\alpha < -2$. Figure 1.2 shows the evolutionary sequence and the corresponding SED.

A brief description of the different YSO classes is discussed below.

- **Class 0** - This class comprises deeply embedded, accreting protostars. Here, the mass of the core is much less compared to the mass of the envelope. Many Class 0 sources drive energetic bipolar outflows (Andre et al., 1993; Lada, 1999) that help to remove angular momentum, thus allowing accretion. These outflows imply that the accretion is not spherical and disk-like features are possibly formed. Class 0 objects display cold spectra which resemble single blackbodies with temperature between 20−30 K peaking in the far-infrared (FIR) or sub-millimetre (sub-mm) wavelengths thus making them visible at these wavelengths.

- **Class I** - As accretion continues the dust temperature rises and the peak of the SED moves to the FIR (∼100 μm). In this evolutionary phase, rotation causes the infalling material to form a circumstellar accretion disk around the central, protostellar object. The central object is still embedded in a molecular and dusty envelope. So, its emission suffers high extinction. The SEDs of these YSOs show two distinct components – one of temperature 50 − 100 K corresponding to the accreting envelope and the second with temperatures between 200 – 400 K originating from the disk. Observationally, disks, outflows, and jets can be seen in this phase. During this stage, the protostar becomes visible at FIR and mid-infrared (MIR) wavelengths; it also shows a strong near-infrared (NIR) excess, mainly caused by the emission of the disk. The 10 μm silicate absorption feature, indicating an optically thick envelope of dust, is generally detected in this class of YSOs.

- **Class II** - After around 10^6 yrs most of the surrounding material are swept away by

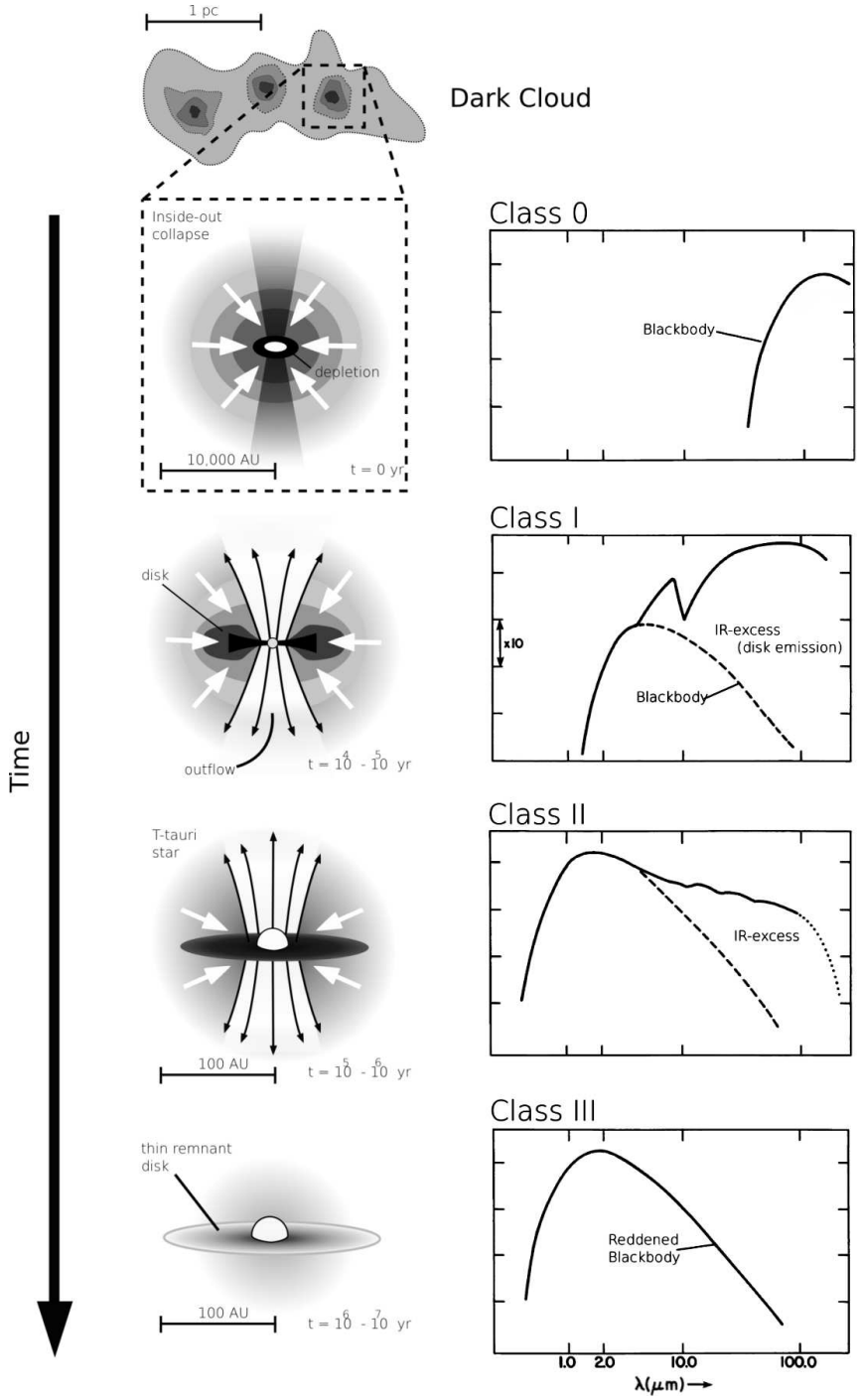

Figure 1.2: Schematic view of the classification scheme for low-mass YSOs based on observed SEDs. This image is taken from Purcell (2006, PhD Thesis) which was adapted from Lada & Wilking (1984) and van Dishoeck & Blake (1998).

winds and molecular outflows which clear out the accreting envelope, thus exposing the circumstellar disk (the proto-planetary disk which are sites of future planet formation). In this stage, the central object can be seen also in the optical wavebands. Mass accretion onto the protostar continues. This evolutionary stage is also identified as the Classical T-Tauri phase. Class II objects still show signs of accretion and display NIR excess.

- **Class III** - The material in the disk is slowly consumed (being accreted onto the central object or expelled by outflows) thus reducing mass accretion. The central object does not show any NIR excess. Some circumstellar material may be present in the form of a thin disk, however, the SED displays a single reddened blackbody with little or no infrared (IR) excess emission. This is consistent with a reddened stellar photosphere of a star on the zero-age-main-sequence (ZAMS).

Excellent reviews on low-mass star formation can be found in Lada (1999); Shu et al. (1999); Andre et al. (2000). Do massive stars follow the same formation and evolution stages? We attempt to answer this in the following section.

1.3 High-mass star formation

Having given a brief overview of the relatively well understood processes leading to low-mass star formation, we shift to the high-mass regime. A fundamental difference in the formation mechanisms lies in the timescales involved. The timescale for the gravitational collapse is given as the free-fall time (which relates to the period of accretion for the envelope) (Shu et al., 1987).

$$t_{\rm ff} = \left(\frac{3\pi}{32G\rho}\right)^{0.5} = 3.4 \times 10^7 n^{-0.5} \text{years} \tag{1.3}$$

where G is the gravitational constant, ρ is the average mass density and n is the number density. For a typical molecular cloud with $n \sim 10^4$ cm^{-3}, the free-fall time scale is, $t_{\rm ff} \sim 4 \times 10^5$ yr. As the cloud contracts, the gravitational potential energy is converted to thermal energy and the timescale on which this happens is known as the Kelvin-Helmholtz (K-H) timescale and is given by

$$t_{\rm KH} = \frac{GM^2}{RL} \tag{1.4}$$

where M, R, and L are the protostellar mass, radius, and luminosity, respectively. The K-H timescale is the time a protostar maintains a given luminosity without hydrogen burning in the core. The numerical calculations from Iben (1965) estimates the K-H timescale to be 5×10^7 yr and 6×10^4 yr for a $1M_\odot$ and $15M_\odot$ star, respectively. Thus, for low-mass stars, the K-H timescale is longer compared to the free-fall timescale ($t_{\rm KH} >> t_{\rm ff}$), in which case the accretion is over before the hydrogen burning starts. On the other hand, for high-mass stars, the K-H timescale is considerably smaller compared to the free-fall timescale ($t_{\rm KH} << t_{\rm ff}$). This implies that accretion continues while hydrogen burning starts in the core and the star reaches the main sequence (Kahn, 1974).

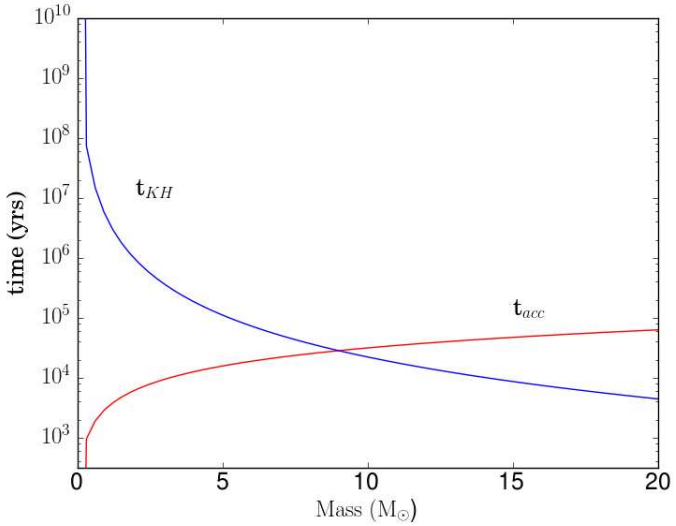

Figure 1.3: The K-H timescale and the accretion timescale for stars of masses 0 – 20 $M_\odot$ are shown in this figure. For the low-mass regime, the K-H timescale is longer than the accretion timescale. Beyond $\gtrsim 8M_\odot$ the accretion timescale is longer.

Figure 1.3 shows the K-H and accretion timescale ($t_{\rm acc} = \dot{M}/M$) for a range of masses considering a typical accretion rate of $10^{-3.5}$ $M_\odot yr^{-1}$. As is clearly seen, for stars with masses $M \gtrsim 8$ $M_\odot$, $t_{\rm KH} << t_{\rm ff}$, thus defining the high-mass domain, where the star begins nuclear fusion while it is still accreting more gas (Palla & Stahler, 1993; Keto & Wood, 2006). This poses the 'radiation pressure' problem where the radiation field, due to the onset of hydrogen fusion in the newly-formed massive star, pushes against the infalling material. This could lead to halting of further accretion, dissipation of the infalling envelope, and hence, potentially setting a limit for the final mass of the star. Calculations, based on the low-mass regime, of spherical accretion, do

suggest that the radiation pressure acting on dust grains is sufficient to halt the further accretion onto the forming massive protostar (Kahn, 1974; Wolfire & Cassinelli, 1987; Stahler, 2000). Of further importance and consequence, is the large size scales involved in high-mass protostar formation. Density fluctuations within high-mass star-forming cores and clumps would lead to the cascading fragmentation scenario. Thus additional support is required in the high-mass domain to counter this.

1.3.1 Competing theories of high-mass star formation

Several theories have been proposed to address the above crisis in forming high-mass stars, like disk accretion to overcome the radiation pressure problem, or magnetic fields to resist fragmentation. Broadly, three main theories are being debated since the last decade or so. In the following discussion, we give a brief overview of these. The primary difference being, how the gas which leads to the formation of the massive star is assembled.

- **Monolithic collapse and core accretion:** In this scenario, the high-mass star formation is considered to be a 'scaled-up' version of the mechanisms in play in the low-mass regime. The initial conditions involve self-gravitating, centrally concentrated cores that form from a fragmenting clump. The high-mass star-forming cores are large enough where internal turbulence could dominate thermal motion (Myers & Fuller, 1992; Caselli & Myers, 1995). This was extended further in the 'Turbulent core' model by McKee & Tan (2003). In this model, the additional support during the collapse is mostly non-thermal, in the form of turbulence and/or magnetic fields. This model also approximates the initial core to be a singular polytropic sphere since it is in internal virial equilibrium. Thus, the material that forms the star is accreted from the single massive core, which forms the protostar. The radiation pressure problem is countered by high accretion rates ($\sim 10^{-4} - 10^{-3} M_{\odot} yr^{-1}$) and reduced dust opacities (Osorio et al., 1999; Edgar & Clarke, 2003). Further, in their simulation, (Krumholz et al., 2009) show that radiation does not halt accretion and it continues through the rotating disk onto the massive protostar. In addition, cavities created by jets and outflows are also shown to be channels for radiation escape without hindering accretion. Detection of highly collimated jets and outflows (e. g., Marti et al. 1993; Beuther et al. 2005) and rotating structures (e. g., Patel et al.

2005; Beltrán et al. 2006b) lend support to this model. In the current times, there is also growing evidence that at least some massive protostars (B-type) are indeed surrounded by accretion disks (Kraus et al., 2010; Cesaroni et al., 2014). Simulations by Dobbs et al. (2005) show the prevalent nature of the fragmentation in turbulent cores, which will dominate over the single massive core and lead to the formation of substructures. So to prevent the fragmentation, Tan et al. (2013) suggest additional magnetic fields of ~ 5 mG.

- **Competitive Accretion:** This model gives an alternate hypothesis for the formation of high-mass stars and favours fragmentation of the cloud resulting in the formation of several low-mass protostars. The foundation of this model is based on the fact that massive stars are mostly observed in clusters (Bonnell et al., 1998; Stahler et al., 2000). In isolated single star formation, accretion is from the parental clump. The situation changes for formation in a cluster. The model assumes a large reservoir of gas from which the cluster forms and protostars 'compete' to accrete gas. The size of the accretion domain, the mass of the protostellar embryo, the spatial distribution of nearby protostars are crucial factors governing this hypothesis. The fragments grow in size in a highly non-uniform manner depending on their location within the cluster (Bonnell et al., 1998). As per this model, the most massive member of clusters should be located at the center of the cluster, which is the centre of the gravitational potential well of the cluster. This location would have maximum gas reservoir for individual stars.

- **Coalescence or Merger:** In this hypothesis, the initial formation of cores and protostars follow the low-mass theory but in a dense and clustered environment (Bonnell et al., 1998). If the prevailing stellar density in the cluster is high ($\sim 10^{6-8}\,\mathrm{pc}^{-3}$), then the merger of two or more protostars leads to the formation of a massive star. However, recent studies in stellar rotation seem to rule out this merger model (Wolff et al., 2006).

There has been numerous studies addressed towards unravelling the elusive recipe for setting up the initial conditions for local and global episodes of massive star formation. Of major concern is the gas mass accretion rate, which needs to be huge, 10^{-4} – $10^{-3}\mathrm{M}_{\odot}\mathrm{yr}^{-1}$ (e.g., Wolfire & Cassinelli 1987; Tan & McKee 2003; Krumholz et al. 2009; Hosokawa & Omukai 2009; Kuiper et al. 2011) and within a short timescale to counter feedback effects. In recent times,

there is increasing observational evidence for cloud-cloud collision as a triggering mechanism leading to high-mass star formation (e.g. Torii et al. 2015, 2017; Fukui et al. 2016 and references therein). These authors propose the formation scenario of O-type stars triggered by supersonic compression in cloud-cloud collision. A pioneering study of the numerical calculations of cloud-cloud collision was done by Habe & Ohta (1992), followed by other studies like the ones by Anathpindika (2010); Inoue & Fukui (2013); Takahira et al. (2014). Further, the ubiquity of filamentary structures in molecular clouds (Carey et al., 1998; Churchwell et al., 2009; André et al., 2010; Molinari et al., 2010a) have invoked discussion regarding their connection with high-mass star formation (e.g. Lu et al. 2018; Yuan et al. 2018; Peretto et al. 2013 and references therein). These studies have investigated formation of dense cores via fragmentation of filaments, the growth of cores and formation of protostars resulting from accretion flows along the filaments. In addition, massive filaments are seen to possess strong turbulence and powerful outflows. These findings strongly suggest that these massive filamentary clouds, dominated by turbulent motions, are closely related to the processes leading to high-mass star formation.

In spite of various theories proposed for high-mass star formation, the decision is still not sealed on the preferred mechanism. Lack of good and adequate observational guidance has kept the theoretical models debatable. The following subsection briefly addresses the observational challenges.

1.3.2 Difficulties in studying high-mass stars

To validate the proposed models, observations of a large sample of high-mass star forming regions are required. Each reveals a different story which needs to be strung together to present the global picture. The properties of the associated winds, disks, outflows, and other features as a function of age, metallicity, and environment are key to constraining the models, and to ultimately evolve an accurate picture of massive star formation. Observational investigation of the processes involving the formation of high-mass stars are severely limited, especially in the pre-stellar (prior to the onset of stellar activity) and protostellar (after the onset of stellar activity and during the assembly process of the star) stages. The possible reasons being

- The timescales involved are short, thus making it difficult to detect and study the various

stages of evolution.

- The number distribution of high-mass stars is controlled by the stellar initial mass function (IMF) (Salpeter, 1955; Kroupa, 2001; Chabrier, 2003) and reveals the rarity of massive stars.

- Rarity implies that statistically they are found at larger distances from the Sun (beyond ~1 kpc). This requires high-angular resolution observations.

- Massive protostars are deeply embedded in their birth clouds, preventing the new born stars to be directly observed at optical or near-infrared wavelengths due to high extinction.

- High-mass stars are predominantly found in clustered environments.

- Massive stars greatly influence the local/primordial environment.

Tremendous progress has been made in the field in recent years. Improvements in sensitivity and angular resolution across the electromagnetic spectrum are making it possible to observe deeper into the massive star-forming regions. Excellent reviews by Tan et al. (2014) and Motte et al. (2017) discuss the current theoretical and observational scenario of high-mass star formation.

1.3.3 Evolutionary sequence of high-mass stars

Based on observation, an evolutionary sequence of high-mass star has been proposed (Walsh et al., 1999; Minier et al., 2003) and shown in Figure 1.4. The various stages are explained below.

1. High-mass stars are formed in the dense cores of molecular clouds.

2. With time, these dense cores of gas and dust undergo gravitational collapse and grow in mass by accretion or mergers.

3. In this stage, the heat and outflows from the central object evaporate the ice from dust grains. This leads to the formation of complex hydrocarbons in the hot molecular core. This phase is also conducive for formation of CH_3OH masers.

4. The outpouring of UV radiation from the young embedded star(s) ionize the surrounding hydrogen, creating a hypercompact H II region. This expands into an ultra-compact H II (UCH II region and further. Complex molecules are destroyed in this stage.

5. The ionized region eventually expands to form the classical H II region. The gas and dust are driven away by ionized wind exposing the young cluster.

1.4 Feedback of high-mass stars on the ambient ISM

Given their radiative, mechanical and chemical feedback, high-mass stars profoundly influence the surrounding ISM. Observational manifestations of the interplay between high-mass stars and the surrounding ISM are important probes for studying the various evolutionary phases involved in their formation. The very early stages are marked by the presence of energetic outflows and jets. Once the 'switching-on' takes place, the outpouring of UV photons ionize the surrounding neutral medium forming H II regions (Wood & Churchwell, 1989; Churchwell, 2002). The H II region around a newly formed massive star expands into the ambient ISM driven by various feedback mechanisms like thermal overpressure, powerful stellar winds, radiation pressure or a combination of all (Churchwell et al., 2006; Deharveng et al., 2010; Simpson et al., 2012). The result is a 'bubble' that shows up as a dense shell of swept up gas and dust between the ionization and the shock fronts encompassing a relatively low-density, evacuated cavity around the central star (Weaver et al., 1977). This section deals with understanding briefly various aspects of H II regions and dust bubbles.

1.4.1 HII region

Massive O and B star formation is accompanied by enormous Lyman continuum emission. The outpouring of UV photons ionize the ISM forming H II regions and thus revealing the location of ongoing high-mass star formation through radio free-free emission. In the evolutionary sequence, it starts with deeply embedded, hypercompact H II regions which eventually expands forming the ultra-compact (UC H II), compact and extended or classical H II regions. The earliest evolutionary phase is closely linked to the formation process where the newly born massive star is still in the accretion phase. The classical H II regions, on the other hand, are mostly associated with more evolved objects. Apart from being bright in the radio, the high-luminosity

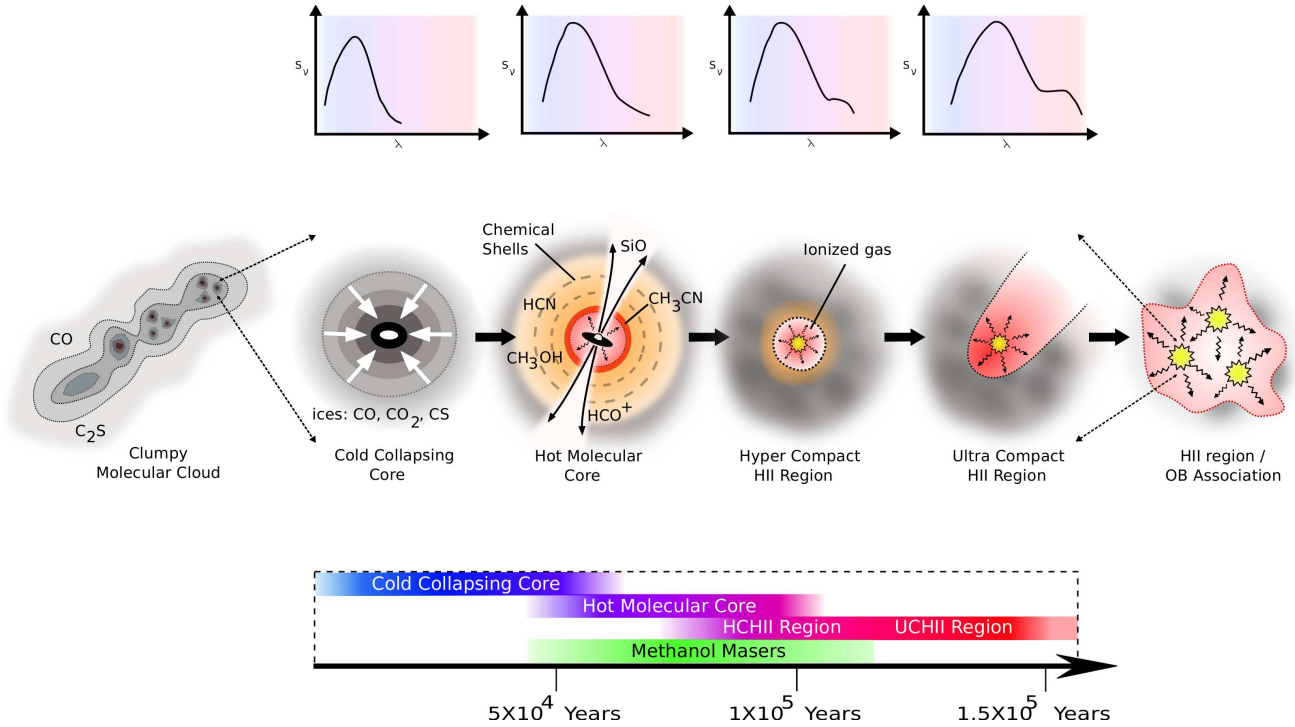

Figure 1.4: Figure shows the schematic representation of the evolutionary stages involved in the formation of high-mass stars. This image has been taken from the website of Dr. Cormac Purcell (http://www.physics.usyd.edu.au/ cpurcell/public/index.php).

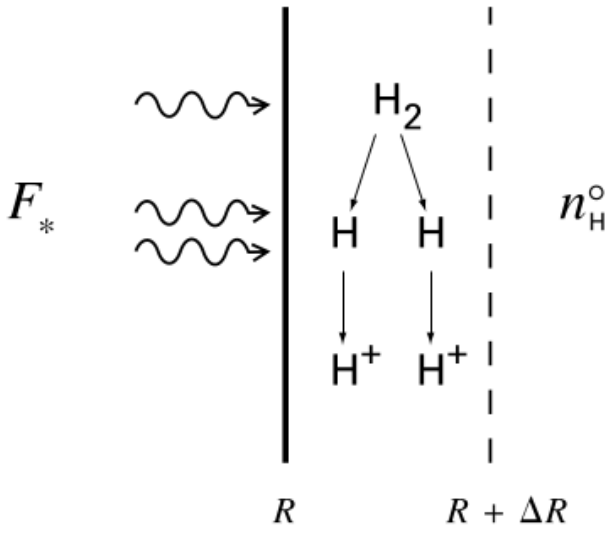

Figure 1.5: Spreading of the ionization front into the surrounding neutral medium. This figure is taken from Stahler & Palla (2005).

of the massive stars also makes the H II regions bright in the IR. The UV and optical radiation from the star is absorbed by the dust and is re-emitted in the IR. The radio and the thermal IR being least affected by extinction, studies in these wavelength regimes allow us to probe deep into the star-forming clouds to unravel the processes associated with high-mass star formation and the cooler dust environment. Complimentary NIR studies further provide the census of the associated young stellar population. Excellent reviews on the nature and physical properties of H II regions can be found in Wood & Churchwell (1989); Garay & Lizano (1999); Churchwell (2002); Hoare et al. (2007).

For the formation of an H II region within a molecular cloud, dissociation of molecular hydrogen (H_2 molecules) followed by ionization of neutral atomic hydrogen (HI) is required. For the first step, photons with energies > 11.2 eV are required while for ionization, energies > 13.6 eV is needed. In the earliest stage when the massive star forms, there exists no H II region around it. This is followed by a short formation period and eventually a slow expansion. The initial evolution is depicted in Figure 1.5 taken from Stahler & Palla (2005). In the expanding H II region, ionization is accompanied by recombination. Initially, when the ionization front radius, R, is small, the massive star's output of ionizing flux overwhelms the rate of recombination and the extra photons reach the ionization front and continue to ionize the neutral medium.

In this phase, expansion of the ionization front is very rapid (the speed of the ionization front exceeds the isothermal sound speed within this region). The expansion timescales become comparable to the recombination timescale. As a result, the gas does not get time to react to its increase in pressure and the situation is similar to that of a static cloud. A state of equilibrium, where ionization balances recombination, is achieved almost instantly. The ionized gas fills isotropically the surrounding volume, forming what is called a *Strömgren* sphere. The radius of this sphere is expressed as (Dyson & Williams, 1997; Stahler & Palla, 2005).

$$R_S = \left(\frac{3\, N_\star}{4\pi\, (n_H^0)^2\, \alpha'_{rec}} \right)^{1/3} \tag{1.5}$$

where $N_\star$ is the Lyman continuum photon rate from the central star, (n_H^0), is the neutral hydrogen number density, α'_{rec} is the recombination coefficient. Photons having energy < 13.6 eV escape without ionizing the gas. However, an appreciable fraction would have enough energy to dissociate the surrounding molecular region forming the photons dissociation region (PDR). Both the H II region and the PDR are limited by the photon flux satisfying the energy criteria (Whittet, 1992; Stahler & Palla, 2005). Considering a massive star of spectral type O6V, ($N_\star = 10^{49}$photons s^{-1}) located within a neutral medium of density $10^4 cm^{-3}$, the first expansion phase lasts for ~ 50 yrs and at the end of this phase, the radius of the *Strömgren* sphere is ~ 0.15 pc (Deharveng et al., 2010).

The initial assumptions under which the H II region expands is that the mass density is same within and outside the H II region. This assumption is justified when the front has supersonic velocity. Beyond the formation phase, a long expansion phase ensues due to the pressure difference. The pressure in the warm ionized gas ($T_e \sim 10^4$ K) is much higher than that in the cold neutral medium ($T_e \sim 10 - 100$ K). So when R approaches R_S, the front speed decreases and the pressure difference is able to drive the second phase of expansion. Figure 1.6, taken from Stahler & Palla (2005), pictorially describes the second phase of expansion. During the second phase, the pressure disturbance within the H II region is able to cross the ionization front creating an expanding shock on the neutral side. This leads to the surrounding neutral material being compressed into a thin shell bounding the H II region. Due to the continuous influx of UV photons, the mass of the ionized gas continues to increase, whereas, the density decreases due

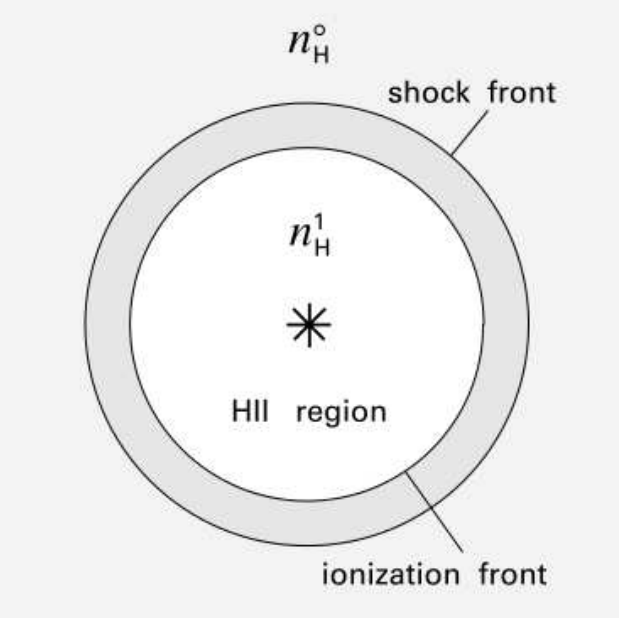

Figure 1.6: Second expansion phase of a spherical H II region and the formation of thin shell around it. This figure is taken from Stahler & Palla (2005).

to expansion. The second phase of expansion proceeds till pressure equilibrium is achieved.

The dynamical expansion of H II regions depends on various factors like the spectral type of the ionizing star, multiple ionization stars, age, density and size of the neutral cloud. As the H II region evolves it goes from the hypercompact (< 0.01 pc size; Sewilo et al. 2008) stage to the UCH II , (< 0.1 pc size; Churchwell 2002, Thompson et al. 2006). This is followed by the compact and then a full or classical H II region. Kurtz (2005) opine that single stars are responsible for hypercompact H II regions and UCH II regions are the result of multiple stars. Physical parameters of H II regions span orders of magnitude in scale and are listed in Table 1.4. The final structure of the H II region may be described as one of the following

- Density bounded: boundary determined by the limit of the cloud (no neutral gas left to be ionized).
- Ionization bounded: extent determined by the balance between ionization and recombination.

Interestingly, the H II regions display various morphologies. Wood & Churchwell (1989) initiated the classification of UCH II regions based on radio maps. The classification is shown in

Table 1.4
Physical properties of H II regions taken from Kurtz (2005).

Type of region	Diameter (pc)	Ionized mass ($M_\odot$)	Density (cm^{-3})	Emission measure pc cm^{-6}
Hypercompact	~ 0.03	$\sim 10^{-3}$	$\gtrsim 10^6$	$\gtrsim 10^{10}$
Ultracompact	$\lesssim 0.05$	$\sim 10^{-2}$	$\gtrsim 10^4$	$\gtrsim 10^7$
Compact	$\lesssim 0.5$	~ 1	$\gtrsim 5 \times 10^3$	$\gtrsim 10^7$
Classical	~ 10	$\sim 10^5$	$\sim 10^2$	$\sim 10^2$
Giant	~ 100	$10^3 - 10^6$	~ 30	$\sim 10^6$
Supergiant	> 100	$10^6 - 10^8$	~ 10	$\sim 10^5$

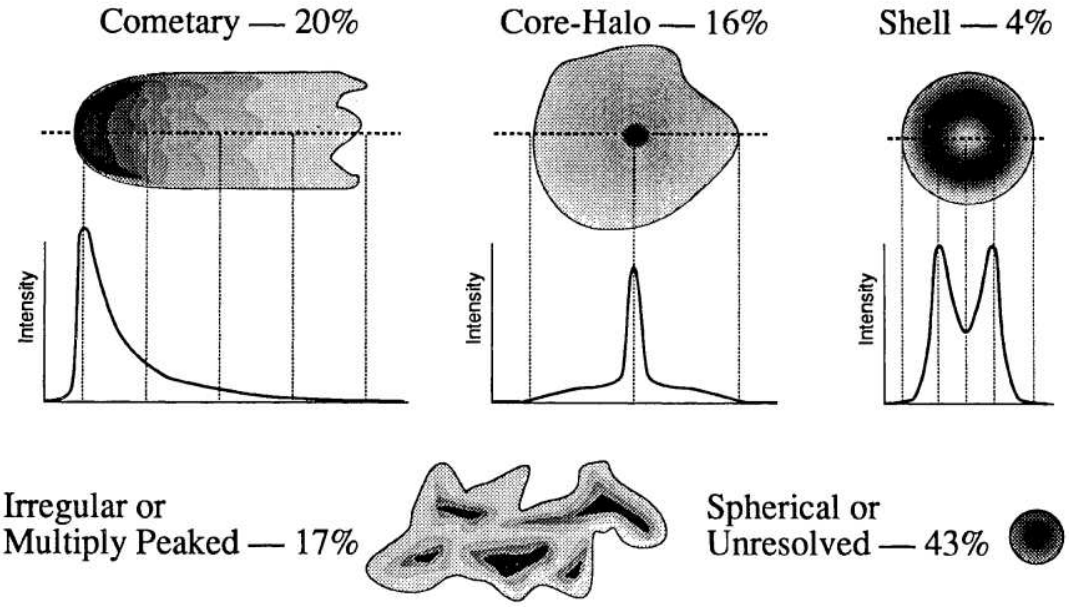

Figure 1.7: Figure, taken from Wood & Churchwell (1989), displaying the distinct morphologies of UCH II regions.

Figure 1.7 which is taken from their paper. In their study, they analysed 75 UCH II regions and classified them into spherical or unresolved (43%), cometary (20%), core-halo (16%), shell (4%), and irregular (17%). These have been summarized in Table1.5. The table also includes the morphological classification of UC H II regions made by Kurtz et al. (1994) and De Pree et al. (2005). De Pree et al. (2005) introduced the bipolar morphology. Bodenheimer et al. (1979) show numerical simulation of the formation and evolution of bipolar H II regions, a schematic and further discussion of which is presented in Deharveng et al. (2015). Though these classifications are based on UCH II regions, they can be applied to compact H II regions as well (Garay et al., 1993).

Table 1.5
Characteristics and relative abundance of H II regions taken from Wood & Churchwell (1989) (WC89), Kurtz et al. (1994) (KU94), and De Pree et al. (2005) (DE05).

Type	Characteristics	WC89	KU94	DE05
Spherical	symmetric, centrally peaked	24%	36%	21%
Cometary	bright edge and extended tail	20%	16%	14%
Core-halo	compact peak with fainter halo	16%	9%	–
Shell-like	(possibly broken up) ring of emission	4%	1%	28%
Irregular	several peaks with common halo	17%	19%	11%
Bipolar	elongated	–	–	8%
Unresolved	emission peak of beam size	19%	19%	18%

1.4.2 Infrared bubbles

The *Spitzer*-GLIMPSE survey unfolded an interesting and 'bubbling Galactic disk' (Churchwell et al., 2006, 2007). These authors cataloged ∼ 600 dust bubbles in the Galactic plane. Subsequent to this, The Milky Way Project, which is a citizen science initiative, identified ∼ 5000 IR bubbles (Simpson et al., 2012). As is evident, these interesting objects are ubiquitous in the Galaxy. Detected in the MIR, these reveal mostly as full or partial rings or shell structures though other morphologies are also seen. The bright MIR emission is attributed to polycyclic aromatic hydrocarbon (PAH) molecules, which are excited by the soft UV photons in the PDRs. PAH emission feature includes several modes of vibrational C-H and C-C stretching which emit strongly in the IR. Several of these PAH emission features at 3.3, 6.2, 7.7, and 8.6 μm (Povich et al., 2007) fall within the IRAC bands (3.6, 5.8, and 8 μm). This is consistent with the bright-rimmed morphology observed in the IRAC images. The interior of the bubbles are devoid of PAH emission, because of the destruction of PAH molecules by the hard UV photons. Going towards the longer wavelength, the 24 μm emission mostly fills the bubble interior. The 24 μm emission which spatially correlates well with the ionized component can be considered to be due to Lyα heating of normal size dust grains that could maintain the temperatures close to 100 K in the ionized region (Hoare et al., 1991). Several authors also associate this emission in H II regions with either Very Small Grains or Big Grain replenishment (Everett & Churchwell, 2010a; Paladini et al., 2012). Apart from the PAH emitting features, the bubbles also emit at the 4.5 μm band which is attributed to continuum emission. This general picture of a bright 5.8 or 8 μm emission at the border with 24 μm emission in the interior has been seen in a large of

number bubbles studied by various authors (Churchwell et al., 2006, 2007; Watson et al., 2008; Deharveng et al., 2010; Anderson et al., 2012b; Kendrew et al., 2012; Ochsendorf et al., 2014b; Liu et al., 2016; Das et al., 2017).

1.4.3 Formation scenarios

Before we proceed to understand the likely formation mechanisms, we briefly overview the various morphologies observed based on the 5.8 or 8 μm emission (Churchwell et al., 2006, 2007). Figure 1.8 displays a sample of bubbles chosen from Churchwell et al. (2006) having different morphologies. Various factors that dynamically affect the shape and sizes of the bubbles are the density variation of ambient ISM around the central ionizing star(s), the luminosity of the central star(s), age, and motion of central star within the ISM.

As the H II region expands, neutral material accumulates between the ionization front and the shock front. Thus the ionized region is enveloped by a shell of dense, neutral material forming what we refer to as a bubble. Figure 1.9, which is a detailed version of Figure 1.6, sums it up. The assumption of the evolution of H II regions in a homogeneous medium is unrealistic. We expect the surrounding ISM to be turbulent and thus inhomogeneous. Several authors have carried out simulations on the expansion of H II regions in turbulent medium (Icke, 1979; Franco et al., 1990; Elmegreen et al., 1995; Mellema et al., 2006). Elmegreen et al. (1995) discuss that the clumps, which form due to turbulence, are compressed into the massive core in the surrounding layer. These protrude out into the ionized region forming bright rims. Franco et al. (1990) have shown that in regions following a power-law density stratification, there is a critical value of the exponent above which the ionization front cannot be trapped and enters a 'champagne-flow' phase and no neutral material is further accumulated. A bubble forms if the exponent is below the critical value. In a relatively recent work, Bisbas et al. (2009) investigated the case of off-centered evolution in a homogeneous medium. This results in an opening where the ionization front reaches the cloud edge. Thus, the presence of a turbulent medium or non-spherical evolution reduces the collection of neutral material to form the shell.

Theoretical work regarding the formation of bubbles, with the support of stellar winds from high-mass stars, was pioneered by Castor et al. (1975); Weaver et al. (1977); McCray (1983). In the early phases, the high-mass stars are accompanied by powerful stellar wind. As the wind

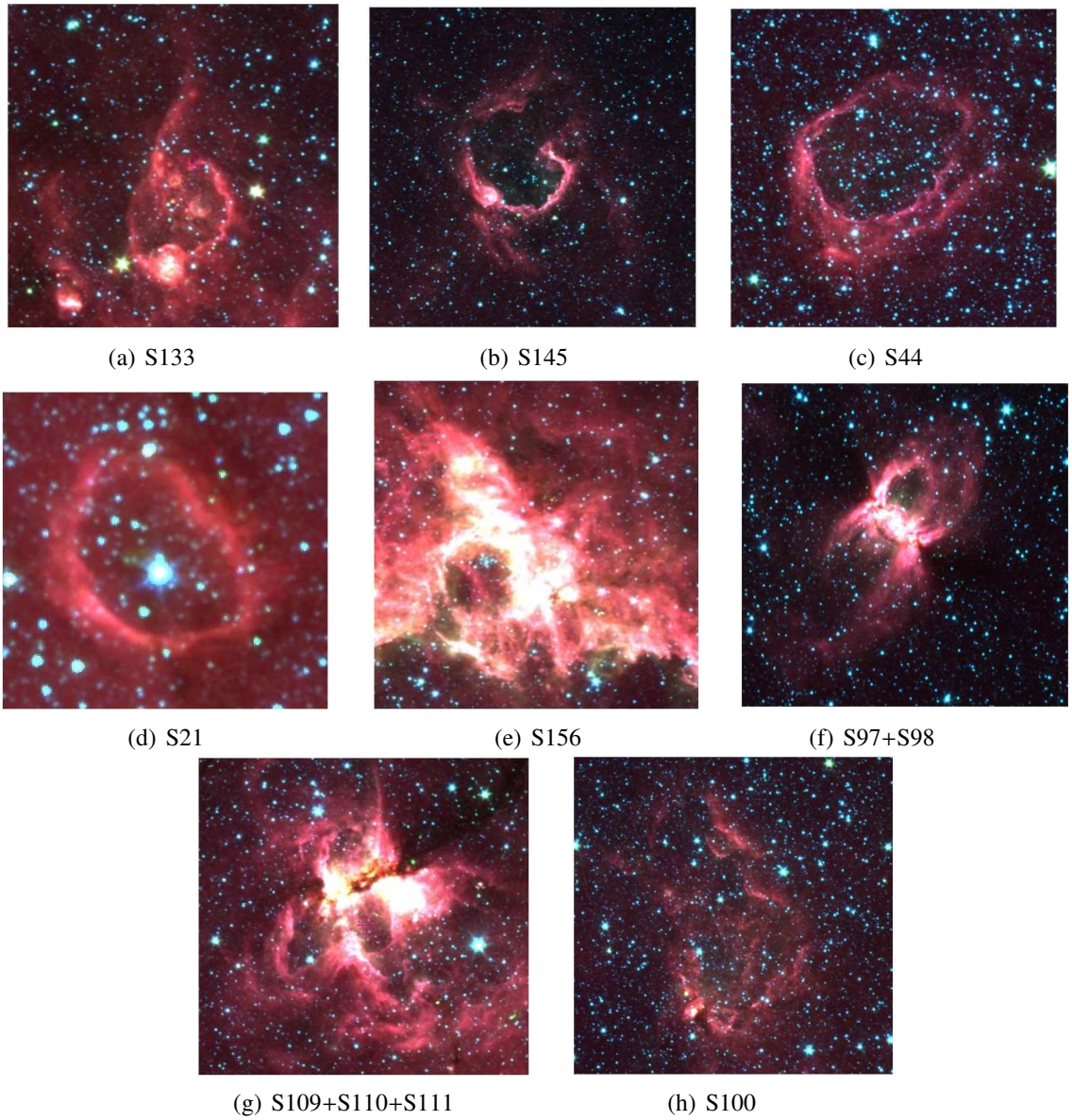

(a) S133 (b) S145 (c) S44

(d) S21 (e) S156 (f) S97+S98

(g) S109+S110+S111 (h) S100

Figure 1.8: Examples of various observed morphologies seen in IR dust bubbles (Churchwell et al., 2006). The classification are (a) S133 – multiple bubble, (b) S145 – broken bubble, (c) S44 – complete bubble, (d) S21 – complete bubble with a central star, (e) S156 – with a central star cluster, (f) S97+S98 – bipolar bubble, (g) S109+S110+S111 – tripolar bubble, (h)S100 – flocculent bubble.

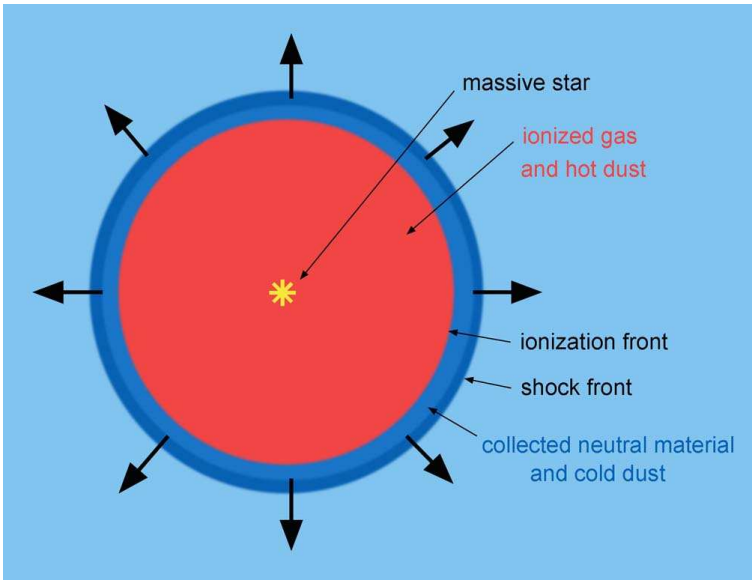

Figure 1.9: Model of a spherical H II region expanding into a homogeneous medium and the accumulation of neutral material at the border during the expansion phase. This figure is taken from Deharveng et al. (2010).

interacts with the ambient ISM, a bubble system results which during its dynamical evolution has the basic structure as shown in Figure 1.10 taken from Weaver et al. (1977). As discussed by these authors, the initial expansion of the bubble system is rapid and hence the radiative loses in the gas does not affect the entire system and the dynamics of the regions are described by an adiabatic flow. Subsequently, the radiative loses cause the swept-up and expanding material to collapse into a thin shell but the region of shocked stellar wind conserves energy. However, in the final evolutionary phase, the dynamics of this region is also affected by radiative loses. To sum up the picture, powerful stellar winds around massive stars drive shocks into the ambient ISM, pushing away the neutral material. This results in a cavity filled with hot ($T \sim 10^7$ K), tenuous ($n_H \sim 0.01$ cm^{-3}), collisionally ionized gas surrounded by a dense ($n_H \sim 10^5$ cm^{-3}) shell. A significant amount of work (numerical and theoretical) has been carried out to investigate the effect of stellar wind and bubble formation (Capriotti & Kozminski, 2001; Freyer et al., 2003; Raga et al., 2012; Dale et al., 2013b). Observational support for this wind blown picture is seen in the study by Watson et al. (2008, 2009), where a few bubbles in their sample show the presence of possible wind-evacuated cavities towards the centre of the ionized emission filling the bubble interior.

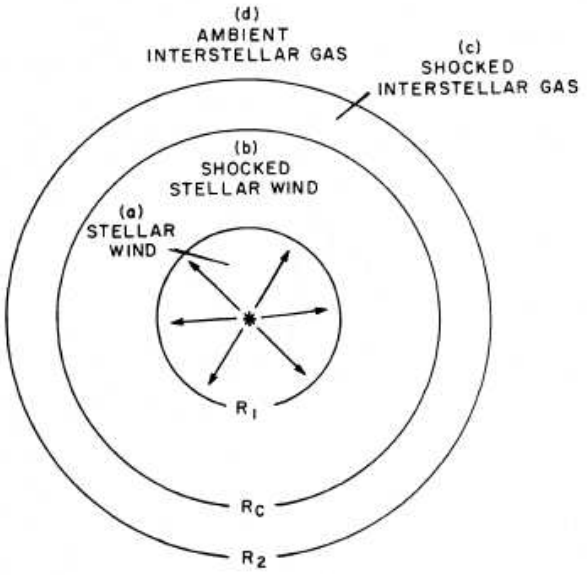

Figure 1.10: Different regions of the wind-blown bubble are shown. This figure has been adapted from Weaver et al. (1977).

The contribution of stellar winds in the formation of most bubbles though claimed (Churchwell et al., 2006, 2007) is debatable. X-ray detection is expected from the hot gas filling the bubble interior. Except for extreme cases of Wolf-Rayet stars (Toalá et al., 2015) and extreme ionizing power nebulae like M17 and Rosette (Townsley et al., 2003), X-ray emission from bubbles have not been detected. Further, winds from low-luminosity O stars are likely to be less powerful (Martins et al., 2005b; Marcolino et al., 2009) thus questioning their role in forming bubbles around these stars. Presence of dust in the bubble interior (Deharveng et al., 2010; Martins et al., 2010; Anderson et al., 2012b) is added evidence that wind is not solely in action. To circumvent the caveats in models supporting the wind blown picture, Ochsendorf et al. (2014b) have performed hydrodynamical simulations and propose the bubble formation to be due to thermal overpressure of the ionized gas. These authors also discuss the formation of dust and bow waves highlighting the importance of radiation pressure for the bubble dynamics. Their models adequately explain the detection of arc-like IR features close to the ionizing star (Ochsendorf et al., 2014a). Further details on this scenario is presented in Chapter 3.

The discussion in the preceding paragraph suggests that bubble formation is likely to be a combination of an expanding H II region, thermal overpressure and action of powerful stellar winds

with the contribution of each being dependent on various stellar parameters and the nature of the ambient ISM.

1.4.4 Triggered star formation

As is clear by now, high-mass stars play a significant role in regulating the star formation in molecular clouds. Scenarios of triggered star formation has been explored in few theoretical models and investigated observationally also. Lee & Chen (2007) give a lucid overview on massive stars and triggered star formation. High-mass stars are seen to trigger the birth of the next generation of stars through their energetic stellar winds, UV radiation, expanding H II regions, and supernova explosions. Elmegreen & Lada (1977) and Lada (1987) suggest that first low-mass stars form from fragments in the molecular cloud and are distributed throughout the cloud. With the onset of high-mass star formations, the expanding ionization front triggers sequential star formation in the neighbouring fragments or clouds by prompting their collapse. Interestingly, a counter picture is viable which suggests that massive stars can inhibit further star formation by evaporating the molecular clouds through their radiation and energetic winds (Herbig, 1962). Thus, these massive stars could have both a destructive or a promotional influence on the star formation activity in molecular clouds. Triggering feedback leading to star formation could take place on various scales (Elmegreen, 1998). The formation of the Upper Scorpius and Lower Centaurus Crux associations is an apt example of large scale triggering activity (de Geus et al., 1989). Such large scale feedback can also be related to supernova explosions (Preibisch & Zinnecker, 2007). On smaller scales, triggered star formation can happen on the borders of expanding H II regions. Figure 1.11 shows a good schematic, taken from Deharveng et al. (2010), depicting the various processes of triggered star formation in play at the border of H II regions. Here, the formation of both low and high-mass stars is possible depending upon the scale of the gravitational instabilities. Mainly two kinds of triggering processes have been proposed in literature - the “Collect & Collapse (C&C)” and the “Radiation Driven Implosion (RDI)” mechanisms. There are observational evidence of both mechanisms at play in the bubble rim.

- **Collect & Collapse model**

  The origin of dust bubbles and the C&C model are interlinked where the shell between the

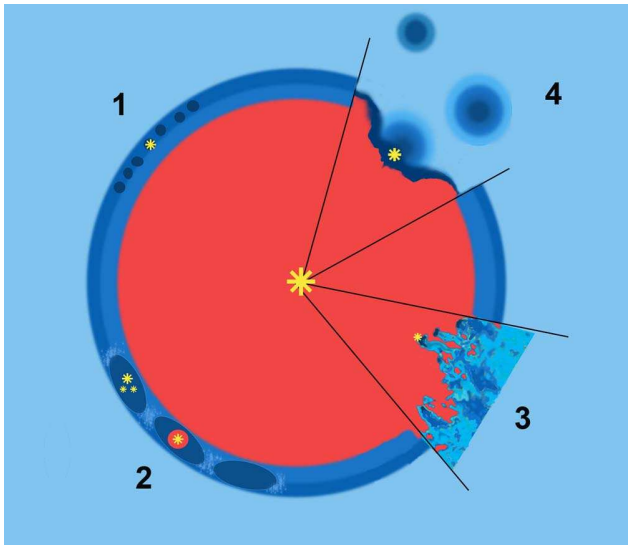

Figure 1.11: Different processes of triggered star formation which may occur at the border of expanding H II region, 1 - small-scale gravitational instabilities; 2 - large-scale gravitational instabilities leading to the formation of high-mass fragments; 3 - ionizing radiation acting on a turbulent medium; 4 - radiation-driven compression of pre-existing dense clumps. This figure is taken from Deharveng et al. (2010).

ionization and the shock fronts becomes massive as it evolves which makes it gravitationally unstable. Thus, collapse ensues and the process self-propagates leading to sequential star formation (Elmegreen & Lada, 1977; Whitworth et al., 1994a; Whitworth & Francis, 2002). Several simulations propose that the ionizing feedback from expanding H II regions should be an efficient trigger for star formation in molecular clouds if the mass of the ambient molecular material is massive enough (Hosokawa & Inutsuka, 2005, 2006; Dale et al., 2007, 2012, 2013a). This has been investigated observationally by many authors (Zavagno et al., 2006, 2007, 2010; Dewangan et al., 2012; Liu et al., 2015, 2016). In Figure 1.11 processes 1 and 2 show the C&C mechanism.

- **Radiation Driven Implosion (RDI) model**

  In the RDI model (Bertoldi, 1989; Lefloch & Lazareff, 1994; Bisbas et al., 2009; Miao et al., 2009), star formation begins with the photoionization of the nearest molecular cloud by high-mass stars. Here, the expanding H II region drives a shock into the surrounding molecular cloud. This initiates star formation in the molecular cloud by collapsing the pre-existing, subcritical clumps within the cloud. Pictorially this is shown in Figure 1.11

through processes 3 and 4. Bisbas et al. (2011) has investigated the RDI model through simulations. Their analysis show that the time taken for star formation depends on the initial mass of the clump and strength of the ionizing radiation. They have proposed that for the low ionizing fluxes, the evolution of the cloud is slow. They also suggest that star formation mainly takes place in the inner side of the cloud, some distance behind the ionization front. This corroborates with the findings of Sugitani et al. (1999, 2000), in which they have probed star formation in bright-rimmed clouds. Bisbas et al. (2011) further discuss that inspite of the weak compression of the cloud, star formation efficiency is quite high and high-mass star formation is likely as the clumps grow in mass by continuously accreting matter from their surrounding.

1.5 Outline of the thesis

As we delve into the depths to understand star formation, a challenging scenario unfolds for massive stars. The 'fuzzy' state of affairs in the field of high-mass star formation, wherein detailed observational studies of complexes are a valuable input to the field, is the main motivation behind this thesis work. The aim of this thesis is to obtain a comprehensive understanding of the formation of high-mass stars and their feedback on the surrounding ambient ISM. There is no better way than being able to probe the regions of interest at different wavelengths. This allows detailed investigations of the associated ionized region, dust environment, and stellar population. By analyzing the association of Red MSX massive young stellar objects (MYSOs) with the dust bubbles, it is seen that $\sim$ 65% of MYSOs and UCHII regions appear to be associated with bubbles and a significant $\sim$ 20% of MYSOs may have formed as a result of feedback from expanding H II regions (Kendrew et al., 2012). Thus, these IR bubbles are ideal laboratories for investing high-mass star formation, triggered star formation and stellar feedback in the Galaxy. In this research work, two southern bubbles, S10 and CS51 from the catalog of Churchwell et al. (2006, 2007) have been studied in detail from radio through infrared wavelengths. In addition, two Galactic H II regions G346.056−0.021 and G346.077−0.056 have been investigated. A statistical study of cold dust emission associated with a sample of seventeen IR bubbles has also been conducted.

In order to achieve the goals set to scrutinize and understand various components and aspects

associated with these high-mass star forming regions, low-frequency (610 and 1280 MHz) radio observations were carried out with the GMRT, India. These observations offer for the first time an unique frequency range for investigating the ionized emission associated with the complexes under study. These observations not only help in comprehending the morphology of the associated ionized gas and the nature of the exciting source but also aid in deciphering the radiation mechanism involved. Further, the envisaged multiwavelength study is rendered possible with high quality data from various archives. In presenting the work, we have organized the thesis in the following way

- **Chapter 1:** This (the present chapter) gives a broad introduction to the subject of star formation with focus towards the high-mass regime. Brief overviews of H II regions and IR dust bubbles are also presented.

- **Chapter 2:** This chapter describes the details of observation using the Giant Meterwave Radio Telescope (GMRT) and the associated data reduction procedures. The goals of this thesis was realized partly because of the excellent multiwavelength datasets available from various archives. These are briefly introduced in this chapter. Various formulations to study the associated stellar population and understand the nature of cold dust emission have been adopted in our investigations of the selected targets. These formulations are discussed in detail in this chapter.

- **Chapter 3:** Chapter 3 concentrates on the study towards southern IR bubble S10. EGO G345.99-0.02 is located close to S10 and possibly associated with the same star forming complex. We have also investigated the region associated with EGO G345.99-0.02.

- **Chapter 4:** This chapter reveals the star formation scenario associated with another southern IR dust bubble CS51.

- **Chapter 5:** Chapter 5 focuses on two southern Galactic H II regions G346.056−0.021 and G346.077−0.056.

- **Chapter 6:** Chapter 6 presents a statistical study of cold dust emission towards a sample of seventeen IR dust bubbles.

- **Chapter 7:** This chapter summarizes the results from this thesis and briefly discusses the future plans.

Chapter 2

Observation, Data Reduction, Archival Data and Analysis procedures

The main aim of this thesis is to carry out detailed multiwavelength studies of several high-mass star-forming regions within the Galaxy. This has been accomplished by using data in the radio, NIR, MIR, FIR, and sub-mm bands. In this chapter, we discuss radio observations carried out and the related data reduction procedures. Various data sets from several archives have also been used to probe the different phases and components associated with the star-forming complexes under study. We give a brief overview of the data sets used. In addition to this, we discuss the formulations adopted in studying the stellar population and cold dust emission associated with the regions.

2.1 Radio continuum observation and data reduction

2.1.1 Observations

In order to study the ionized gas component associated with our star-forming regions of interest, we carried out low-frequency radio continuum mapping with the Giant Metrewave Radio Telescope (GMRT), Pune India. GMRT has a hybrid configuration of 30 antennas arranged in a 'Y' shaped layout. Each antenna is a parabolic reflecting dish of 45 m diameter. The central square has 12 randomly placed antennas within a compact area of 1×1 km^2 with shortest baselines of $\sim$ 100 m. This is sensitive to large-scale diffuse emission. The remaining 18 antennas are placed six each in the three arms. The largest baseline possible with GMRT is $\sim$ 25 km which accounts for the high angular resolution. Details regarding the GMRT configuration can be found in Swarup et al. (1991). Figure 2.1 shows the location and 'Y' shaped array configuration of GMRT and a close-up view of one of the antennas. In comparison to other existing multi-element, earth rotation, aperture synthesis telescopes, that are operating at meter wavelengths, GMRT provides the largest collecting area. The central square baselines of GMRT are similar

in length to the VLA-D array and the baselines obtained from the arm antennas are similar to VLA-A and VLA-B configuration. So a single observation of GMRT samples the (u, v) plane adequately with reasonable sensitivities.

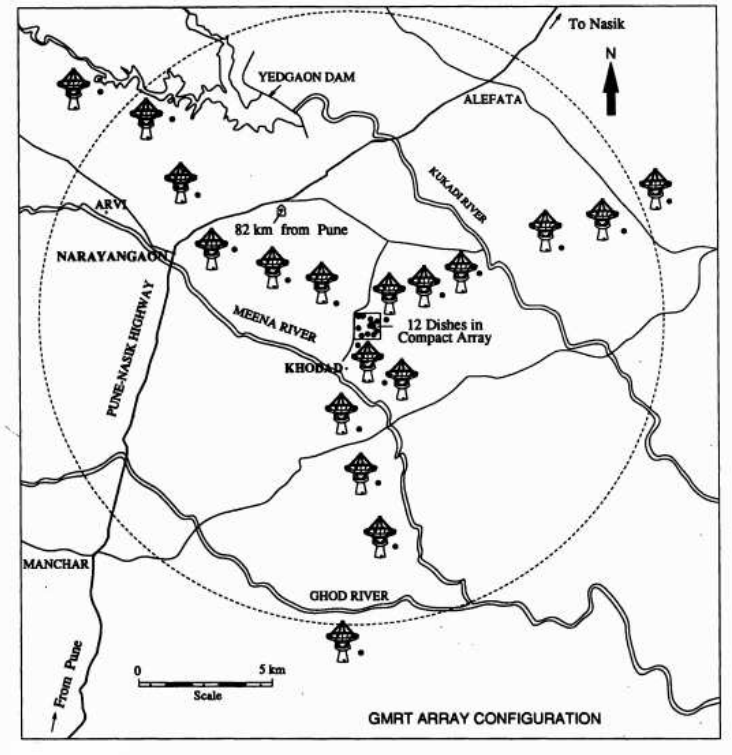

(a)

(b)

Figure 2.1: (a) Location and configuration of the GMRT antennas. (b) Close-up view of a single parabolic antenna with several others in the back ground. (Images are taken from http://gmrt.ncra.tifr.res.in.)

Observations were carried out for IR bubbles S10, CS51 and two HII regions G346.077-0.056, G346.056-0.021. The H II regions are located north-east of the bubble S10 and were observed as part of the same field with S10 being at the phase centre. The amplitude of the visibility function is proportional to the flux density of the source. To get the flux density of the source, the normalized visibility is converted to flux density. This is done using the measured visibility of a source of known but non-variable flux density, which is referred to as flux density calibrator. Also, the complex antenna based gain vary over time, mainly due to the changes in the upper ionosphere. In order to correct these variations, we need periodic observation of a source of known structure, usually an unresolved source. This source is referred to as the phase calibrator. The flux density of the phase calibrator is also calibrated using the flux density of the flux calibrator. So each observation requires atleast one observation of the flux calibrator and periodic observation of the phase calibrator. In our observations, we have used the VLA calibrators, 3C286 and 3C48, as flux calibrators and 1626-298 and 1714-252 as phase calibrators. Table 2.1 lists the targets of interest and the observation details. We observe the flux calibrators for $\sim$ 15 mins in the beginning and end of the observation sequence. The phase calibrator is observed periodically along with the target source. In each period we observe the target for $\sim$ 40 mins and the phase calibrator for $\sim$ 5 mins. Figure 2.2 shows the flow chart of the sequence of observation.

Table 2.1
Details of GMRT observations.

Date	Target	Frequency (MHz)	Time	BW (MHz)	$N_{\rm chan}$	Flux Cal.	Phase Cal.
17 July 2011	S10	610	$\sim$ 4 hr	32	256	3C286, 3C48	1626-298
20 July 2011	S10	1280	$\sim$ 4 hr	32	256	3C286, 3C48	1626-298
8 August 2014	CS51	610	$\sim$ 5 hr	32	256	3C286, 3C48	1714-252
14 August 2014	CS51	1300	$\sim$ 5 hr	32	256	3C286, 3C48	1714-252

2.1.2 Data reduction

Data reduction was carried out using the Astronomical Image Processing System (`AIPS`). Flow charts shown in Figure 2.3 (a) and (b) gives the detailed reduction procedure involved. Brief explanations of the tasks involved are given below.

1. Originally GMRT data is in the `LTA` format, which is subsequently converted to the FITS

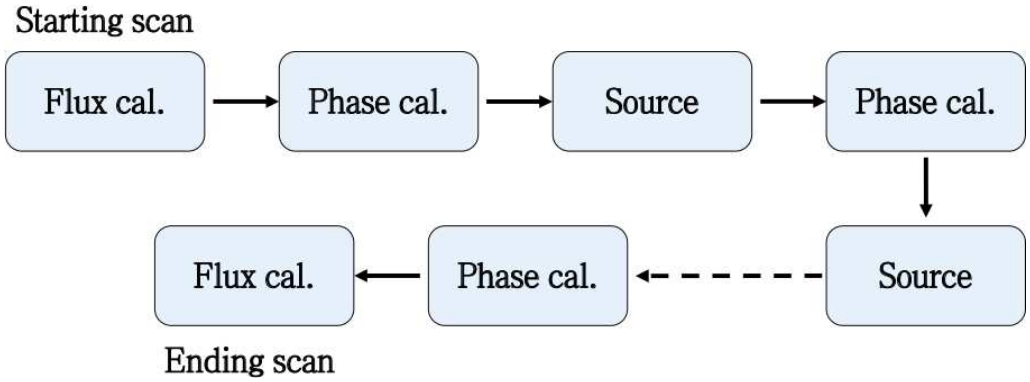

Figure 2.2: Flow chart of the sequence followed for the GMRT observations.

format using the tasks `listscan` and `gvfits`. This is done outside the `AIPS` environment. The FITS file is then imported into the `AIPS` environment through the task `FITLD`. This creates a multi-source visibility data base in `AIPS`.

2. The task `INDXR` indexes the *uv* data files. This creates the `CL1` and `NX` tables. The task is run with setting CPARM(3)=1, which computes gain in every one minute interval and writes into the `CL1` table which is then used for calibration and editing. This table is used as a template to determine the time resolution for the subsequent `CL` and antenna gain tables (`SN` tables).

3. Task `QUACK` is used to flag selected portion of each scan. The initial time range of each scan may contain corrupted data due to slewing of the telescope while data acquisition is initiated. Careful checking of the data is necessary to identify such bad points before running this task to flag data points.

4. Task `SETJY` is used to set the flux density of the flux calibrators within the multi-source data file. The flux density values of the standard VLA flux calibrators, that are used in our observation exist within the task. Before proceeding for further calibration, the flux density of these calibrators must be set accurately. The visibility amplitude of an unresolved source (in this case the flux calibrator) remains constant as a function of baseline length. Data points deviating from this are edited out.

5. The *uv* data is viewed using standard tasks like `TVFLG`, `UVPLT`, `VPLOT` to identify bad data such as dead antennas, bad baselines, spikes, RFI, etc. The details of these bad data can

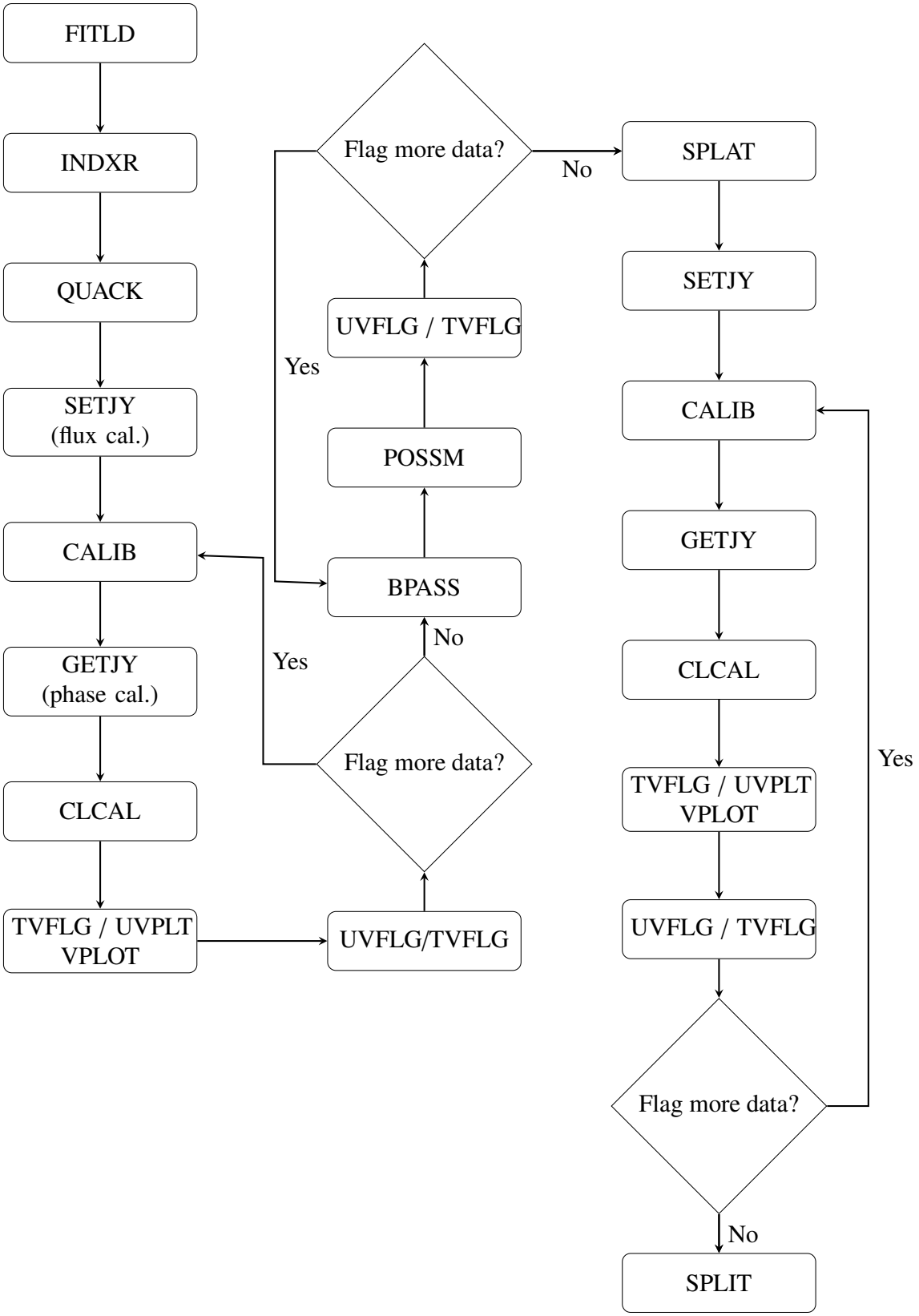

Figure 2.3: (a) Flow chart detailing the sequence of tasks for data editing and calibration.

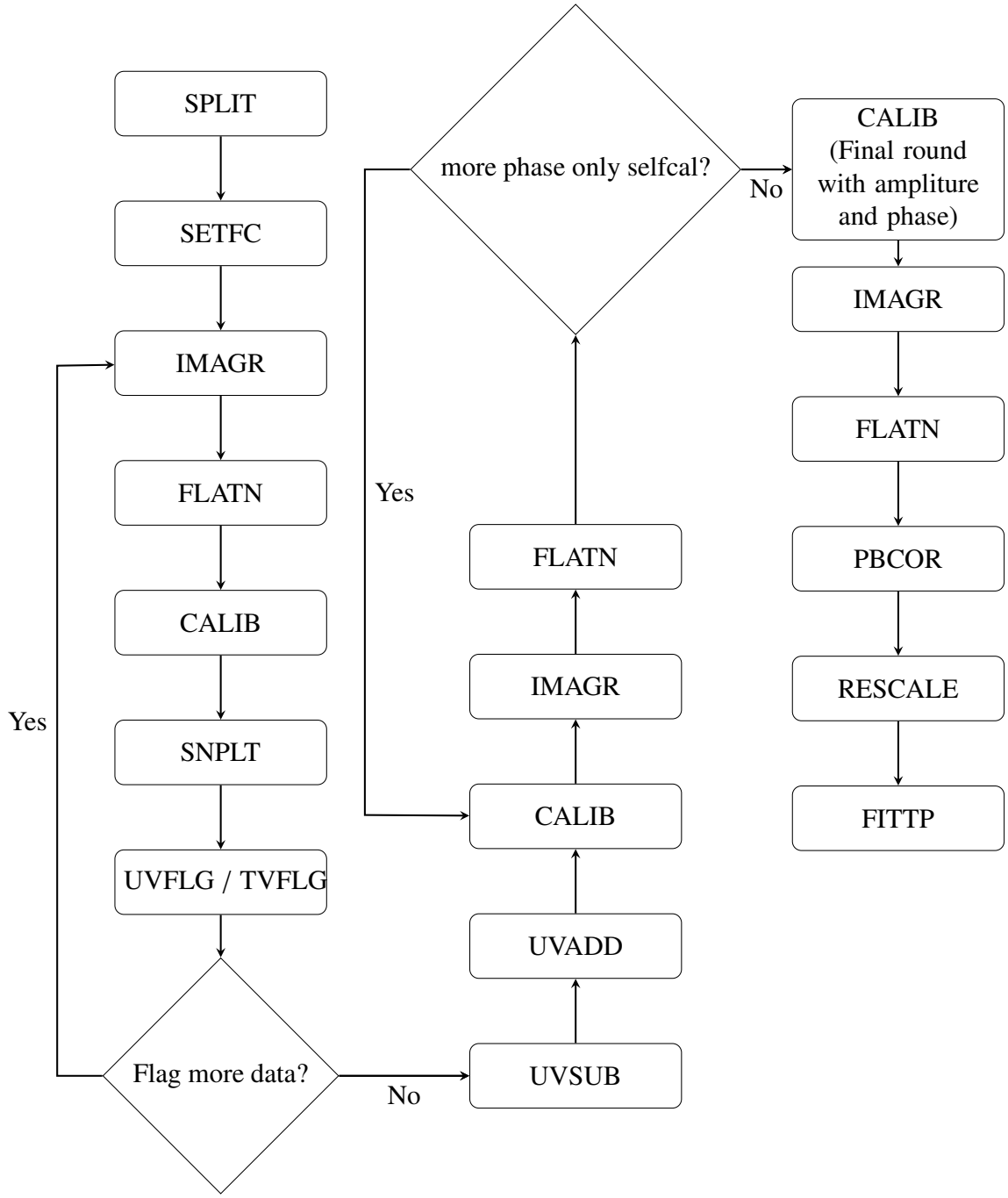

Figure 2.3: (b) Flow chart detailing the sequence of tasks for imaging and self-calibration.

be recorded within a flagfile. Task UVFLG is used to flag these bad data, based on the input flagfile. In some cases, the task TVFLG is also used for interactive flagging.

6. Task CALIB is used to calibrate the data. This task is very sensitive to the presence of bad or dead antennas. A careful examination and flagging of bad data is essential before proceeding for calibration. The task CALIB computes the antenna based gains for the primary calibrators. This creates the SN1 table, which records the complex gain solutions.

7. Task GETJY is used to estimate the flux densities of the phase calibrators. The flux density value obtained from the task should be close to the value listed in the VLA manual.

8. Task CLCAL is used to generate the CL2 table containing the solutions from SN1 table. The CL2 table contains flux calibration of all the sources and is the basic calibration table.

9. Further editing of the data is done by examining the data with tasks UVPLT and VPLOT, setting the parameter DOCALIB = 1, which allows to display the calibrated data. If further flagging is needed then the tables SN1 and CL2, can be deleted, before running the tasks CALIB and CLCAL. Data editing and calibration are done iteratively till nearly all bad data are flagged.

10. Initial data editing is carried out over a single clean channel free from RFI contamination. This is done with the assumption that the calibrators are strong enough for the above editing and calibration steps. However, to generate an image, we require to use all the channels. Thus a bandpass calibration is applied to account for channel dependent gain variations.

11. The antenna based complex gain solutions vary across the pass band. This is due to the variation in antenna based band shapes and the residual fixed delay errors. So before we proceed to average the channels for individual frequencies, the complex gains need to be corrected. Phase calibrators are strong sources to provide enough signal-to-noise ratio for the computation of channel dependent, antenna based complex gains and are used for the antenna band shape corrections. After computing an average gain for each phase calibrator scan per channel, the linearly interpolated data are applied to the target source

to correct the channel dependent complex gains. Task BPASS is used for this purpose, which creates the BP table by time averaging the data within the phase calibrator scans.

12. The BP table and band pass corrected band shapes can be visualized and examined using task POSSM. Occasionally few antennas may show large scale oscillations across the band. These need to be flagged from the data base.

13. After completing flagging and calibration properly, the channels need to be averaged. Task SPLAT is used to average all channels over frequency. The main aim of this task is to reduce the data volume. In addition, averaging of channels helps to increase the signal-to-noise ratio. This enables other processing steps to be carried out faster. A point to be kept in mind is that, averaging leads to bandwidth smearing which affects sources in the outer part of the primary beam. So channel averaging has to be done in an optimum way to keep the bandwidth smearing effect to the minimum.

14. After successfully running SPLAT, a *uv* data file is created which is similar to the original one but with less number of channels. Editing of this file is done as before. Subsequent to this, the individual source of interest is extracted out for further analysis. This is done using task SPLIT which extracts the target from the multi-source *uv* data file.

15. Task SETFC is used to create facets. The idea of creating facets is to account for the *w*-term effects (non-coplanarity). This is called wide-field imaging technique which is essential for generating the 2D sky brightness distribution from a 3D image volume. For a source of size θ, the number of facets required for imaging is equal to ratio between the solid angle of the mapped region (θ_f^2) and solid angle of the synthesized beam (θ^2), and is given as $N = 2\theta_f^2 B_{max}/\lambda$, where B_{max} is the longest projected baseline and λ is the wavelength.

16. The final calibrated data now can be used to generate the actual brightness distribution of the target field. Task IMAGR is used for the same. This task does the Fourier transform of the visibilities and generates, what is called a 'dirty beam'. Convolution of the 'dirty beam' with the true source brightness gives the 'dirty map'. Deconvolving the 'dirty map' gives the 'true map'. The CLEAN algorithm within the IMAGR task is used for deconvolu-

tion. The algorithm uses a non-linear iterative method for deconvolving the instrumental point source response from the observed data (Clark, 1980). The `IMAGR` task generates several images depending upon the number of facets. A single image of the sky is then retrieved using the task `FLATN`.

17. After creating this image the next step is to remove the errors present due to the temporal fluctuations of earth's atmosphere. Such fluctuations affect the response of an individual antenna in the array. The main idea behind self-calibration is to correct these fluctuations by using the Phase closure and Amplitude closure methods. This is accomplished by the task `CALIB`. Several rounds of self-calibrations are then performed to reduce amplitude and phase errors.

18. Further improvement in the image can be made by removing low level noise present in the *uv* data file. The task `UVSUB` helps to subtract a model (set of CLEAN components) from the *uv* data file. The residual *uv* data file is inspected and any detected noise is removed. After proper editing, the model is added back to the *uv* data file using the task `UVADD`. Subsequent to this `IMAGR` is run to obtain the image.

19. Self-calibrated images of all the facets are then combined, using the task `FLATN`, to reconstruct the sky. Following this primary beam correction is done using the task `PBCOR`.

20. While observing close to the Galactic plane, the Galactic diffuse emission becomes significant and contributes toward increasing the system temperature which becomes relevant at low frequencies. At the frequencies of our radio observations (especially at 610 MHz), a rescaling of the final image is essential. To determine the scaling factor, we follow the general method of estimating the sky temperature, T_{sky}, using the measurements obtained from the all-sky 408 MHz survey of Haslam et al. (1982). This method assumes the Galactic diffuse emission to follow a power-law spectrum and T_{sky} at frequency ν for the target position is determined using the following equation

$$T_{sky} = T_{sky}^{408} \left(\frac{\nu}{408 \text{ MHz}} \right)^{\gamma} \tag{2.1}$$

where, γ is the spectral index of the Galactic diffuse emission and is taken as -2.55 (Roger

et al., 1999). Scaling factor in each band is obtained as below

$$\text{scaling factor} = \frac{(T_{sky} + T_{sys})}{T_{sys}} \tag{2.2}$$

where T_{sys} is the system temperature of GMRT at a particular frequency. The derived scaling factor applied to the final image using the task `RESCALE` in `AIPS`.

2.2 Data from archives

While studying the selected star-forming complexes, it is crucial to carry out a thorough investigation in all wavelengths, to unravel the details of the associated ionized emission, warm and cold dust emission, cold dust clumps, stellar population, and molecular gas. In this thesis work, apart from our proposal based radio interferometric observations discussed in the previous section, we have also exploited the high-quality data available from various surveys. The details of each are briefly discussed below.

2.2.1 Far infrared data from *Herschel* Space Observatory

To probe the cold dust components associated with our regions of interest, we have used FIR data from the archives of *Herschel* Space Observatory which was launched in May 2009. This houses the 3.5 m diameter *Herschel* Space Telescope (Doyle et al., 2009; Pilbratt et al., 2010). The on-board instruments include the Photodetector Array Camera and Spectrometer (PACS ; Poglitsch et al. 2010), the Spectral and Photometric Imaging Receiver (SPIRE ; Griffin et al. 2010) and the Heterodyne Instrument for the Far Infrared (HIFI ; de Graauw et al. 2010). These instruments are capable of observing in the FIR and submillimetre wavelength range of 55 – 671 μm. For our study, we have retrieved images from the *Herschel* infrared Galactic plane survey (HI-GAL; Molinari et al. 2010b). This is a key program of *Herschel* space telescope, which has used 343 hrs of observing time and carried out a 5-band photometric imaging survey at 70, 160, 250, 350, and 500 μm of the Galactic plane in the longitude range of $-60^\circ \leq l \leq 60^\circ$ and latitude range of $-1^\circ \leq b \leq 1^\circ$. The HI-GAL survey filled the crucial gap between 70 – 500 μm, where most of the cold dust in the Galaxy emit and reach the peak of their SED. Prior to this, the Galactic plane surveys covered the MIR at $\lambda \leq 70$ μm (Price et al., 2001; Benjamin et al., 2003; Omont et al., 2003; Carey et al., 2009) and in the sub-mm at $\lambda \geq 800$ μm

(Schuller et al., 2009; Rosolowsky et al., 2010). Owing to the large wavelength coverage, high sensitivity, high spatial resolution, and the survey speed, the HI-GAL survey becomes the first project dedicated towards the study of early phases of GMCs and high-mass star formation in the Galaxy.

The Hi-GAL observations were carried out in 'parallel mode' covering 70, 160 μm (PACS) as well as 250, 350 and 500 μm (SPIRE). We use PACS level 2.5 and SPIRE level 3 data products for our analysis. The level numbers assigned to the *Herschel* maps refer to the quality of these final maps obtained at different stages of processing. It starts from level 0 (raw-data) to level 3 (high-quality data). More details regarding the levels can be found at https : //www.cosmos.esa.int/web/herschel/data − products − overview. The retrieved images have resolutions of 5, 11.4, 17.9, 25, and 37″ and pixels sizes of 3.2, 3.2, 6, 10, and 14″ at 70, 160, 250, 350 and 500 μm, respectively.

2.2.2 Submillimetre data from ATLASGAL survey

The sub-mm wavelength regime is very important in studying star-forming environments, as it traces the earliest phases of star formation by sampling the densest regions of the clouds. Schuller et al. (2009) used the 870 μm band to perform a systematic survey of the Galactic plane, to generate a large-scale database of massive pre- and proto-stellar clumps in the Galaxy. The Atacama Pathfinder Experiment (APEX ; Güsten et al. 2006b,a) is ideally located to study the inner Galaxy. This is a 12 m diameter telescope situated at the height of 5100 m in Chajnantor. The Large APEX Bolometer Camera (LABOCA ; Siringo et al. 2007, 2009) was used by Schuller et al. (2009) for the APEX Telescope Large Area Survey of the Galaxy (ATLASGAL). LABOCA is a 295 element bolometer array observing at 870 μm, with a beam size of $\sim$ 19.2″. This survey aims to cover the inner Galactic plane mapping of $\sim$ 100 deg^2. The ATLASGAL survey supersedes all the previous ground based surveys providing a complete and sensitive view of the inner Galaxy at sub-mm wavelengths.

The primary goal of the ATLASGAL survey is to provide a large and systematic sample of cold molecular clumps which are the potential sites of high-mass star formation. ATLASGAL data has been largely used to investigate the Galactic distribution of cold dense gas (Beuther et al., 2012; Csengeri et al., 2014, 2016). Using this ATLASGAL survey data, $\sim$ 10000 dense

clumps have been extracted and compiled into ATLASGAL Compact Source Catalogue (CSC; Contreras et al. 2013; Urquhart et al. 2014c). The retrieved images have resolution of 18.2″ and pixel size of 6″. In this thesis work, we have used data from the ATLASGAL survey along with data from the Hi-Gal survey to understand the nature of cold dust emission in the complexes under study.

2.2.3 Mid infrared data *Spitzer* Space Telescope

The MIR offers not only the view of warm dust environment but also helps in identifying and studying the nature of the embedded stellar population. Implementing such studies in this thesis has been largely possible because of the MIR data available from the *Spitzer* Space Telescope archives. The *Spitzer* Space Telescope (Werner et al., 2004) is a cryogenically cooled IR observatory, with a 0.8 m diameter primary mirror. It was launched in August 2003. The on-board instruments are the Infrared Array Camera (IRAC ; Fazio et al. 2004), the Multiband Imaging Photometer for *Spitzer* (MIPS ; Rieke et al. 2004), and Infrared Spectrograph (IRS ; Houck et al. 2004). These provide imaging and spectroscopy in the MIR and FIR bands ranging from 3.6 to 160 μm. The IRAC consists of a four-channel camera that obtains simultaneous broadband images at 3.6, 4.5, 5.8 an 8 μm. All the four cameras are of 256×256 pixels in size, where the two shorter wavelength channels are InSb and the longer wavelength channels are SiAs IBC detectors. The MIPS consist of three distinct array detectors of 128×128, 32×32, and 20×20 pixels in size for operating at three FIR wavebands 24, 70 and 160 μm, respectively.

Using the IRAC and MIPS instruments, two excellent surveys of the Galactic plane has been carried out - Galactic Legacy Infrared Mid-Plane Survey Extraordinaire (GLIMPSE ; Benjamin et al. 2003) and MIPS Galactic Plane Survey (MIPSGAL ; Rieke et al. 2004). GLIMPSE consists of three surveys, namely, GLIMPSE I, GLIMPSE II and GLIMPSE 3D. GLIMPSE I maps the infrared emission in the (l, b range of $|l| = 10^\circ - 65^\circ$ and $|b| \leq 1^\circ$. This survey used $\sim$ 400 h of observing time that consisted of over 80,000 pointings, each resulting in four simultaneous images in the IRAC wavebands. Keeping the resolution and sensitivity as that of GLIMPSE I, the GLIMPSE II survey covers the inner 20° of the Galactic plane. For $2^\circ \leq l \leq 5^\circ$, the range for b is $-1.5^\circ \leq b \leq 1.5^\circ$ and for $0^\circ \leq l \leq 2^\circ$, the range is $-2^\circ \leq b \leq 2^\circ$. This increase in the range of latitudes covered was to obtain more coverage of the Galactic bulge. Further, the GLIMPSE 3D survey coverage extends to ±3° of GLIMPSE I & II survey, in nine selected

regions. This survey also covers ±4° within $b = 2°$ of the Galactic Plane. The MIPSGAL survey coverage is same as GLIMPSE and both survey results play important roles towards the understanding the warm dust dust emission and associated stellar population.

Images and catalogs of GLIMPSE and MIPSGAL survey are obtained from the Infrared Science Archive (IRSA)[1]. Photometric data in the IRAC bands are used from the highly reliable catalog of GLIMPSE II Spring'07 and Spring'08 catalog and photometric data at 24 μm are obtained from the 24 μm point source catalog (Gutermuth & Heyer, 2015). The resolution and pixel size of the IRAC bands are $\sim 2''$ and $0.6''$, respectively. We have used the 24 μm data alone from the MIPSGAL which has resolution of $6''$ and pixel size of $1.25''$.

2.2.4 Near infrared data from 2MASS

The Two Micron All Sky Survey (2MASS[2]; Skrutskie et al. 2006) is an all sky survey in three near-infrared (NIR) bands J, H and K_s, having wavelengths 1.25, 1.65 and 2.16 μm, respectively. The survey has been carried out using two highly automated 1.3 m telescopes, one at Mt. Hopkins, AZ, and one at CTIO, Chile. Both the telescopes are equipped with a three-channel camera, each channel consisting of a 256×256 array of HgCdTe detectors, capable to observe the sky simultaneously at the three bands. The 2MASS survey images have a resolution of $\sim 5''$. Photometric data in the three NIR bands are taken from the 2MASS Point source catalog (2MASSPSC). Only good quality photometric sources have been retained in our analysis. The selection of sources are based on the "read-flag". This flag indicates the photometric uncertainties. In our analysis, we have used only those sources with "read-flag" value of 2. The retrieved magnitudes are used to study the nature of the associated stellar population and identification of the ionizing stars.

2.2.5 Near infrared data from the VVV survey

Additional NIR, photometric data is also used in the study of the two H II regions G346.056−0.021 and G346.077−0.056. To go deeper and probe the deeply embedded sources in these region we

[1]In addition, a web browser that permits a user to scan and zoom-in on any object in the entire survey false color images of GLIMPSE bands alone and a combined GLIMPSE plus MIPSGAL 24 μm image is located at http://www.alienearths.org/glimpse/. This browser was developed by Dr. James Harold of Space Science Institute.

[2]This publication makes use of data products from the Two Micron All Sky Survey, which is a joint project of the University of Massachusetts and the Infrared Processing and Analysis Center/California Institute of Technology, funded by the NASA and the NSF.

have used data from the VISTA Variables in the Vía Láctea (VVV ; Minniti et al. 2010; Saito et al. 2010) survey. This survey studies the Milky way bulge and adjacent sections of the disk using the 4 m Visible and Infrared Survey Telescope for Astronomy (VISTA). The telescope is equipped with the wide-field, NIR camera VIRCAM (VISTA InfraRed CAMera; Dalton et al. 2006), which is a mosaic of 16 2048×2048 detectors, each sensitive over a spectral region of 0.8 – 2.5 μm, with a pixel scale of 0.34″ pixel^{-1} and having an effective field of view (FOV) of 1.1×1.5 deg^2. This survey has an observing time of $\sim$ 1929 h covering an area of $\sim 510^2$ monitoring $\sim 10^9$ sources. The VVV survey has higher resolution of $\sim 0.8''$ at wide range of effective wavelength (Z, Y, J, H, K_s filters) compared to previous NIR surveys and is thus capable of probing much deeper into the high extinction regions and study the star formation activity near the Galactic bulge and its surrounding region. For source selection in VVV survey, we have followed the criteria outlined in Froebrich (2013). This is based on `pstar` ≥ 0.999656, `merged class` = (-2 or -1), and `priOrSec` = 0 or framesetID. This ensures that only stellar like objects with good photometric quality are selected. Given the saturation limits, for sources brighter than 11 mag we use the 2MASSPSC.

2.2.6 843 MHz radio data from SUMSS survey

In investigating one of our sources (IR dust bubble S10), we have utilized the low-resolution radio continuum map at 843 MHz from the Sydney University Molonglo Sky Survey (SUMSS; Mauch et al. 2003). This is a radio imaging survey of the sky, south of declination, $\delta = -30°$. This survey has been carried out using Molonglo Observatory Synthesis Telescope (MOST) operating at 843 MHz and provides images with a resolution of $45'' \times 45''$ and sensitivity of 20 mJy/beam. The SUMSS survey is similar in sensitivity and resolution to the northern NRAO VLA Sky Survey (NVSS). The low-resolution map helps is investigating the large-scale radio emission in the bubble interior.

2.2.7 Molecular line data from the MALT90 survey

Study of cold dust clumps in the periphery of IR dust bubbles have the potential to address the processes leading to the origin of bubbles, the physical and chemical conditions in these clumps also throw light on their evolutionary phases. The MALT90 (Millimeter Astronomy Legacy Team 90 GHz) survey was aimed in part at characterizing the physical and chemical

conditions of dense molecular clumps in the vicinity of star-forming regions. The target list for the MALT90 survey was taken from the ATLASGAL (Schuller et al., 2009) 870 μm continuum survey which detects both cold and warm clumps. The survey was carried out using the ATNF Mopra 22 m telescope equipped with Mopra Spectrometer (MOPS) and performs simultaneous mapping of 16 molecular lines near 90 GHz with a spectral resolution of 0.11 km s^{-1}. The details regarding the survey can be found in Foster et al. (2011) and Jackson et al. (2013). Table 2.2 adopted from Jackson et al. (2013) lists all the transitions observed in the survey. The table also highlights the specific environments which are traced by these molecules. The data used in our study has been retrieved from the MALT90 site (http://malt90.bu.edu).

Table 2.2
Spectral Lines probed in the MALT90 Survey (Jackson et al., 2013).

Transition	Frequency (MHz)	Tracer
N_2H^+ (1 − 0)	93173.772	Density, chemically robust
^{13}CS (2 − 1)	92494.303	Optical depth, Column density, V_{LSR}
H41 α	92034.475	Ionized gas
CH_3CN 5(0) − 4(0)	91987.086	Hot core
HC_3N (10 − 9)	90978.989	Hot core
$^{13}C^{34}S$ (2 − 1)	90926.036	Optical depth, Column density, V_{LSR}
HNC (1 − 0)	90663.572	Density; Cold chemistry
$HC^{13}CCN$ (10 − 9)	90593.059	Hot core
HCO^+ (1 − 0)	89188.526	Density; Kinematics
HCN (1 − 0)	88631.847	Density
HNCO 4(1,3) − 3(1,2)	88239.027	Hot core
HNCO 4(0,4) − 3(0,3)	87925.238	Hot core
C_2H (1 − 0) 3/2–1/2	87316.925	Photodissociation region
$HN^{13}C$ (1 − 0)	87090.859	Optical depth, Column density, V_{LSR}
SiO (1 − 0)	86847.010	Shock/outflow
$H^{13}CO^+$ (1 − 0)	86754.330	Optical depth, Column density, V_{LSR}

2.2.8 Molecular line data from the ThrUMMS survey

Additional molecular line observation from the ThrUMMS (The Three-mm Ultimate Mopra Milky Way Survey; Barnes et al. 2015) has also been investigated. ThrUMMS, simultaneously maps the Galactic plane in the *l, b* range of $300^\circ \leq l \leq 360^\circ$ and $-1^\circ \leq b \leq 1^\circ$ (fourth quadrant) in four molecular transitions of ^{12}CO(1 − 0), ^{13}CO(1 − 0), $C^{18}O$(1 − 0), and CN(1 − 0). This survey uses the Mopra telescope of diameter 22 m and the techniques of fast-mapping, beam

sampling mode ($\sim$ 1′) to produce wide-field and high-resolution data. Table 2.3 adopted from Barnes et al. (2015) lists the transitions along with their importance. Data from this survey have been obtained from http://www.astro.ufl.edu/peterb/research/thrumms/. This survey data along with data from the MALT90 survey have been used to study the nature of the molecular clumps.

Table 2.3
Spectral Lines probed in the ThrUMMS Survey (Barnes et al., 2015).

Transition	Frequency (GHz)	Tracer
^{12}CO (1 − 0)	115.271	Largest scales, GMC envelopes, temperatures, outflows
^{13}CO (1 − 0)	110.201	PDRs, fractionation, optical depth, velocity dispersion
C^{18}O (1 − 0)	109.782	Column density, depletion, dense gas finder
CN (1 − 0)	113.5	Dense clumps, Zeeman candidates

2.3 Analysis Procedures

In the thesis, we have adopted various techniques and formalisms to understand the complexes under study by using various datasets. In this section, we detail the formulations which are common to all the regions investigated. Further analysis procedures will be introduced in individual chapters which are specific to the source under study.

2.3.1 Identification of YSOs from NIR and MIR photometric data

In the previous chapter, we have discussed the various evolutionary phases associated with low- and high-mass stars. NIR and MIR photometry and the derived colours provide means to differentiate between the various classes of YSOs. This is made possible because of the distinct shapes of the SEDs in the evolutionary diagram. Several authors have used colours based on the IRAC bands, the NIR JHK bands to reveal the nature of the stellar population in numerous star-forming regions. However, it should be kept in mind that YSOs identified using photometric colour criteria can have significant contamination from mass-losing AGB stars or supergiants (Nandakumar et al., 2018). This makes follow-up spectroscopic studies important and crucial. In the discussion below, we explain the various schemes adopted in our study.

1. Allen et al. (2004) have used the IRAC band colours to distinguish between YSOs of different evolutionary classes. They compare the IR colours predicted by theoretical models

of YSOs dominated by emission from protostellar envelopes (Class I objects) and those dominated by emission from protoplanetary disks (Class II objects) with the observed IRAC colors of four young embedded clusters (S140, S171, NGC 7129, and Cep C). YSOs of different classes are found to occupy specific regions on the [3.6] − [4.5] vs [5.8] − [8.0] colour-colour plot (CCP) based on their colors. Figure 2.4, shows the CCP, where the boxes adopted from Vig et al. (2007) demarcate the regions occupied by the Class I and Class II sources.

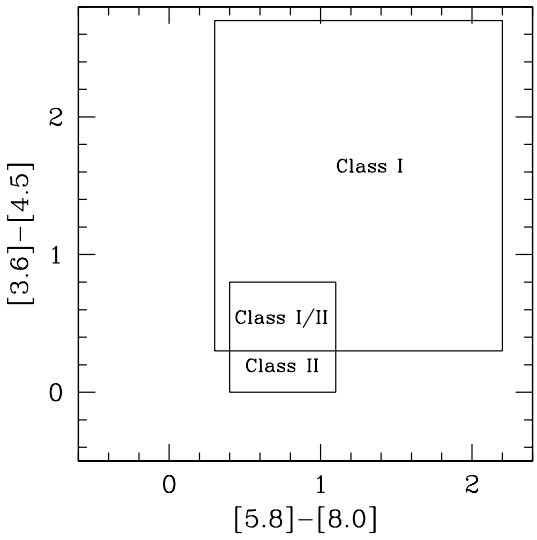

Figure 2.4: IRAC CCP following the criteria discussed in Allen et al. (2004). The boxes on the plot, adapted from Vig et al. (2007) show the region occupied by YSOs of different evolutionary classes.

2. Simon et al. (2007) have done a detailed study of the young stellar population of N66, a large and bright H II region in the SMC. They used the flux densities in the IRAC and MIPS band for SED fitting and identification of YSOs. Based on the SED fitting results, they classify the sources into YSOs, background galaxies, AGB stars, and PAH sources. After removing contamination from sources such as background galaxies, AGB stars, PAH sources, they propose a set of criteria for the identification of YSOs based on the IRAC colours. The defined colour cuts are given below:

$$[3.6] - [4.5] > 0.6 \times ([4.5] - [8.0]) - 1.0$$

$[4.5] - [8.0] < 2.8$

$[3.6] - [4.5] < 0.6 \times ([4.5] - [8.0]) + 0.3$

$[3.6] - [4.5] > -([4.5] - [8.0]) + 0.85$

Figure 2.5 shows the [3.6] − [4.5] vs [5.8] − [8.0] CCP, where the closed box highlights the region for YSOs based on the colour cuts defined by Simon et al. (2007).

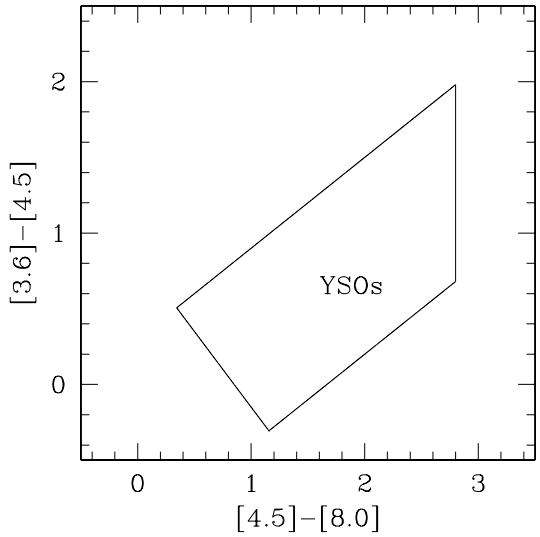

Figure 2.5: Criteria adopted from Simon et al. (2007). YSOs identified with this scheme fall within the enclosed region shown on the plot.

3. Gutermuth et al. (2008) have also devised a colour-based scheme to identify and classify the YSOs using IRAC band photometry. Their study is based on the embedded cluster, NGC 1333. They proceed through various steps of removal of contaminants such as galaxies dominated with PAH emission, AGN sources, sources dominated by shock emission. As discussed in their paper, the following colour criteria are used to isolate these contaminants.

   According to Stern et al. (2005), galaxies dominated by the PAH emission occupy an unique area in most of the IRAC CCPs. The PAH dominated galaxies are found to obey the following color criteria found from the [4.5] − [5.8] vs [5.8] − [8.0] CCP

$$[4.5] - [5.8] < \frac{1.05}{1.2} \times ([5.8] - [8.0] - 1)$$

$$[4.5] - [5.8] < 1.05$$

$$[5.8] - [8.0] > 1.0$$

In addition to above, the PAH dominated galaxies also obey the following color criteria found from the [3.6] − [5.8] vs [4.5] − [8.0] CCP

$$[3.6] - [5.8] < \frac{1.5}{2} \times ([4.5] - [8.0] - 1)$$

$$[3.6] - [5.8] < 1.5$$

$$[4.5] - [8.0] > 1.0$$

Further, broad-line AGNs have their MIR colors, which are mostly consistent with YSOs (Stern et al., 2005). So it is essential to remove these sources before identifying the YSOs. The following color cuts based on the location in the [4.5] vs [4.5] − [8.0] color magnitude plot (CMP) are used to exclude AGNs.

$$[4.5] - [8.0] > 0.5$$

$$[4.5] > 13.5 + ([4.5] - [8.0] - 2.3)/0.4$$

$$[4.5] > 13.5$$

In addition, the AGN sources also follow one of the following conditions.

$$[4.5] > 14 + ([4.5] - [8.0] - 0.5)$$

$$[4.5] > 14.5 - ([4.5] - [8.0] - 1.2)/0.3$$

$$[4.5] > 14.5$$

After removing contaminants such as PAH dominated galaxies and AGNs, the next step is to remove sources dominated by shock emission. These sources follow the following conditions.

$$[3.6] - [4.5] > \frac{1.2}{0.55} \times ([[4.5] - [5.8]] - 0.3) + 0.8$$

$$[4.5] - [5.8] \leqslant 0.85$$

$[3.6] - [4.5] > 1.05$

After the successful removal of non-YSO contaminants, the YSOs are classified according to the following criteria

(i) Sources are likely protostars (Class I) if they have an extremely red discriminant colour ($[4.5] - [5.8] > 1$). Sources having moderate red discriminant colour ($0.7 < [4.5] - [5.8] \leqslant 1$) and $[3.6] - [4.5] > 0.7$ are also considered as likely protostars.

(ii) Class II sources should satisfy

$$[4.5] - [8.0] > 0.5$$

$$[3.6] - [5.8] > 0.35$$

$$[3.6] - [5.8] \leqslant \frac{0.14}{0.04} \times ([[4.5] - [8.0]] - 0.5) + 0.5.$$

Figure 2.6 (a) and (b), shows the IRAC CCP to isolate likely protostars and Class II objects based on the colour indicator proposed by Gutermuth et al. (2008) and discussed above.

4. The inclusion of 24 μm data along with IRAC data to identify YSOs have been discussed in Guieu et al. (2010) and Rebull et al. (2011). These authors propose the $[3.6] - [24]$ vs $[3.6]$ colour magnitude plot (CMP) to segregate YSOs. Guieu et al. (2010) used the MIR observations towards IC 2118 to suggest colour criteria for identifying YSOs. Similarly, Rebull et al. (2011), based on their multi-wavelength observation of the CG4+Sa101 region, arrive at a set of colour criteria. They focus on finding sources having an infrared excess, characteristic of YSOs surrounded by a dusty disk. The use of 24 μm photometry allows us to detect YSOs which may not be detected though IRAC colors only. The $[3.6] - [24]$ vs $[3.6]$ CMP is shown in Figure 2.7. Dashed lines demarcate regions for YSOs of different evolutionary classes.

5. Another approach is to classify YSOs of different evolutionary classes based on their IRAC spectral index. The spectral index ($\alpha = d \log(\lambda F_\lambda)/d \log(\lambda)$) was proposed as an efficient tool for YSO classification by Lada (1987). They introduced three classes - Class I (star with infalling envelope), Class II (star sporting a disk), and Class III (post–T Tauri

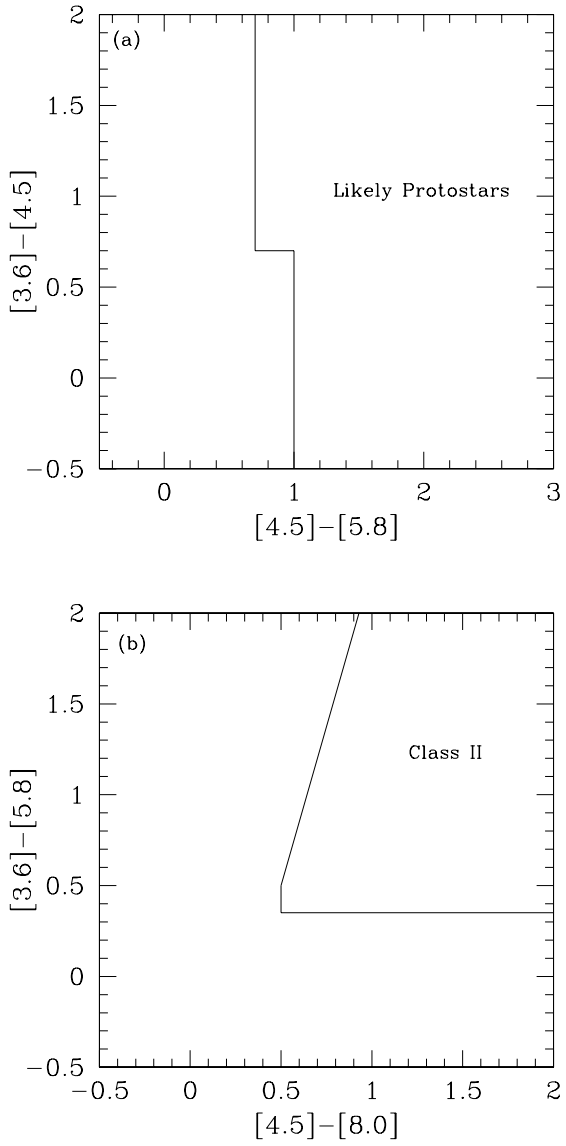

Figure 2.6: Criteria following Gutermuth et al. (2008). (a) region occupied by likely protostars (Class I) and (b) location of Class II sources.

stars). Later, Greene et al. (1994) and Andre et al. (2000) included further categories like Class 0 and flat spectrum sources. Chavarría et al. (2008) used the spectral index indicators from these studies in understanding the nature of the stellar population associated with the S254-S258 complex. The spectral index is estimated for each source by a linear regression fit following which the YSOs are classified into Class I ($\alpha > 0$) and Class II ($-2 \leqslant \alpha \leqslant 0$) Chavarría et al. (2008). Figure 2.8 shows spectral index ranges for different

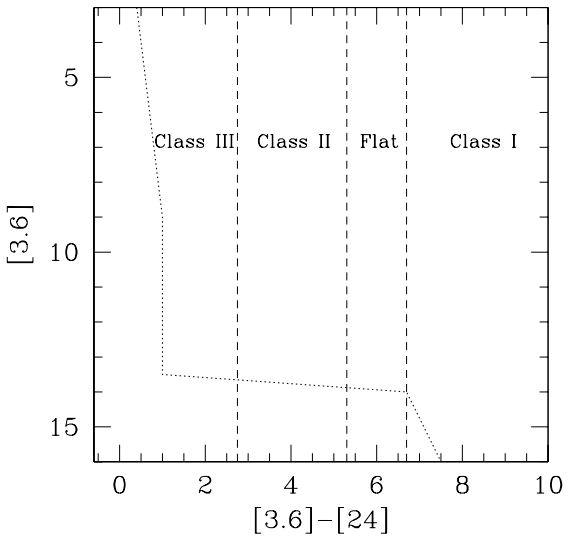

Figure 2.7: [3.6] − [24] vs [3.6] CMP on which the vertical dashed lines adopted from Guieu et al. (2010) and Rebull et al. (2011) demarcate the regions for different classes of YSOs. The dotted curve marks the boundary of contaminated sources such as galaxies and disk-less stars.

classes of YSOs.

6. JHK_s CCPs have been efficiently used by various authors (Sugitani et al., 2002; Ojha et al., 2004b,a; Tej et al., 2006; Ji et al., 2012; Mallick et al., 2015) to identify YSOs. In this criteria, the JHK_s CCP has been used to identify and classify the YSOs into different evolutionary classes. The CCP based on this criteria is shown in Figure 2.9. The loci of main sequence (thin line) and giants (thick line) are taken from Bessell & Brett (1988). The classical T Tauri locus shown as a long-dashed line is taken from Meyer et al. (1997). The parallel dotted lines are the reddening vectors, on which the cross marks are the visual extinction placed at intervals of 5 mag. The short-dashed line represents the locus of Herbig AeBe sources which is from Lada & Adams (1992). We have assumed the interstellar reddening law from Rieke & Lebofsky (1985). In this plot, all the colours and curves are converted into Bessell & Brett (1988) system. For better classification, this plot is divided into three regions. The sources in 'F' region are field stars or Class III or Class II stars with small NIR excess. Sources in 'T' region are mainly classical T-Tauri or Class II stars. Sources in the 'P' region are mostly Class I YSOs. To classify YSOs,

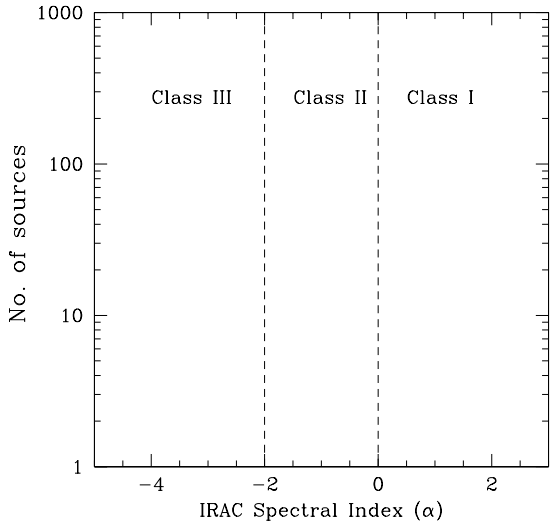

Figure 2.8: Plot of spectral index bands used to classify Class I, Class II and Class III sources as discussed in Chavarría et al. (2008).

we have considered sources falling above T-Tauri locus, since there could be overlap of Class I and Class II sources with Herbig AeBe sources.

2.3.2 Column density and temperature maps

We study the nature of the cold dust emission associated with the star-forming regions using the 70 – 500 μm *Herschel* data. The thermal dust emission peaks in the FIR and the Rayleigh–Jeans regime of the cold dust SED is covered in the *Herschel* wavelength range. Line-of-sight average molecular hydrogen column density and dust temperature maps are generated by pixel-wise modified blackbody fits. A careful literature survey shows that several studies (Peretto et al., 2010; Anderson et al., 2010; Battersby et al., 2011; Liu et al., 2016) have excluded the 70 μm emission while using the *Herschel* data to study properties of dust emission. These studies reason that the emission at 70 μm may not be optically thin and that there may be a significant contribution from the warm dust components (e.g., very small dust grains, protostars). According to Compiègne et al. (2010), the contribution from the stochastically heated very small grains (radius < 0.005 μm) to the PACS 70 μm channel can be as large as $\sim$ 50%. Hence, the emission cannot be modeled with a single temperature gray body. Few authors include the 70 μm data although there is seen to be a significant contribution from warm dust component which has

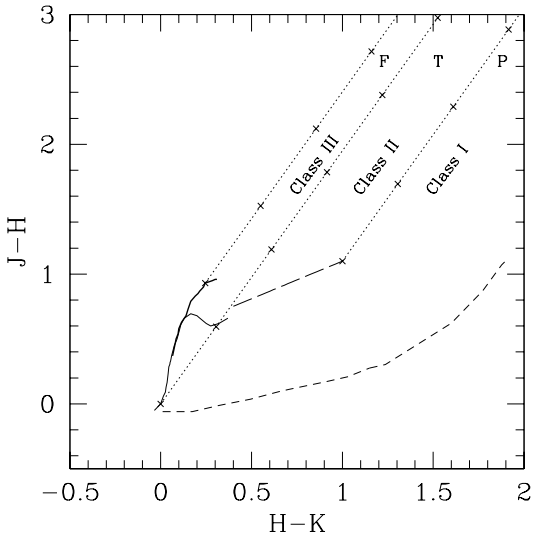

Figure 2.9: The J−H vs H−K CCP , in which the three separate regions are labeled as 'F', 'T', and 'P' (refer text).

not been taken into consideration. Anderson et al. (2012b) has elaborated on the effect of this on the derived temperatures and dust emissivity index. These authors have studied the properties of dust emission using *Herschel* data towards a sample of H II regions associated with infrared dust bubbles. They conclude that inclusion of 70 μm emission is crucial in the absence of 100 μm data which is the case with many regions of the Hi-Gal survey. They also infer from the analysis carried out that the effect of not considering the warm component has only a small impact on the derived values of the parameters. We have looked into both the scenarios and examined maps with and without the 70 μm emission. However, after a careful scrutiny of the χ^2 maps, it is seen that fitting is better (lower χ^2 values) when we exclude the 70 μm data point. Further, since we are probing the cold dust emission, we did pay attention to the morphology of generated column density maps and compared the same with the longer wavelength *Herschel* maps. This prompted us to present maps excluding 70 μm data and use the same for further analysis.

Prior to the SED modelling, the following preliminary steps are carried out using the *Herschel* data compatible software HIPE[3]

[3]The software package for Herschel Interactive Processing Environment (HIPE) is the application that allows users to work with the Herschel data, including finding the data products, interactive analysis, plotting of data, and data manipulation.

1. Using the task 'Convert Image Unit', the image units of the SPIRE images (MJy Sr^{-1}) are converted to a common surface brightness unit of Jy $pixel^{-1}$ of the PACS images.

2. The plug-in 'Photometric Convolution' is then used to project all the images onto a common grid with the same pixel size and resolution of 14″ and 35.7″, respectively, which are the parameters of the 500 μm image (lowest among the four bands). The convolution kernels are taken from Aniano et al. (2011). These convolution kernels allows to generate images with a common PSF, by preserving the colors of astronomical sources.

We model the FIR emission with a modified blackbody that takes into consideration the optical depth, and the dust emissivity. As mentioned earlier, this is done pixel-wise, adopting the following functional form (Battersby et al., 2011; Faimali et al., 2012; Launhardt et al., 2013; Mallick et al., 2015).

$$S_\nu(\nu) - I_{bkg}(\nu) = B_\nu(\nu, T_d)\ \Omega\ (1 - e^{-\tau_\nu}) \tag{2.3}$$

and

$$\tau_\nu = \mu_{H_2}\ m_H\ \kappa_\nu\ N(H_2) \tag{2.4}$$

where, $S_\nu(\nu)$ is the observed flux density, $I_{bkg}(\nu)$ is the background flux, $B_\nu(\nu, T_d)$ is the Planck's function, T_d is the dust temperature, Ω is the solid angle (in steradians) from where the flux is obtained (solid angle subtended by a 14″ × 14″ pixel), μ_{H_2} is the mean molecular weight, m_H is the mass of hydrogen atom, κ_ν is the dust opacity and $N(H_2)$ is the column density. We have assumed a value of 2.8 for μ_{H_2} (Kauffmann et al., 2008). The dust opacity κ_ν is defined to be $\kappa_\nu = 0.1\ (\nu/1000\ \mathrm{GHz})^\beta\ \mathrm{cm}^2/\mathrm{g}$, where, β is the dust emissivity spectral index (Hildebrand, 1983; Beckwith et al., 1990; André et al., 2010).

We estimate the background flux, I_{bkg}, in each band from a relatively smooth and dark region devoid of bright, diffuse emission and filamentary structures. The background value was estimated by fitting a Gaussian function to the distribution of individual pixels in the specified region. The fitting was carried out iteratively by rejecting the pixels having values outside $\pm 2\sigma$ till the fit converged (Battersby et al., 2011; Launhardt et al., 2013). We have used the same region for the determination of background offset in all the bands.

Subsequent to the background subtraction, the SED fitting was carried out using non-linear least

square Levenberg-Marquardt algorithm, in which T_d and $N(H_2)$ are kept as free parameters. Given the limited number of data points, we prefer to fix the value of β to 2 (Hildebrand, 1983; Beckwith et al., 1990; André et al., 2010) which is also a typical value used in studies related to IR dust bubbles (Anderson et al., 2012b; Liu et al., 2016; Ortega et al., 2016). We have used a conservative 15% uncertainty on the background subtracted flux densities (Launhardt et al., 2013). The generated column density and dust temperature maps reveal crucial aspects of star formation activities in the regions under study.

Chapter 3

High-mass star formation towards southern infrared bubble S10

3.1 Introduction

In this chapter, we present an observational study of a high-mass star-forming region which includes the southern Galactic bubble S10 and an Extended Green Object (EGO) G345.99−0.02 (hereafter EGO345), which is located ∼ 5′ toward the north-east of S10. Both these regions are shown to harbour massive protostellar candidates (Fontani et al., 2005; Beltrán et al., 2006a).

Figure 3.1 shows the *Spitzer*-IRAC colour composite images of the two regions under study. The MIR emission towards the bubble S10 clearly displays a broken morphology as mentioned in Churchwell et al. (2006). Broken morphologies of bubbles are believed to be due to non-uniform density of the ambient ISM and/or anisotropic stellar winds and radiation fields. Based on the 24 μm MIPSGAL image, these authors suggest identification of possible central driving star(s). S10 is also identified as a bubble in the Milky Way Project (Simpson et al., 2012). A bright IRAS source (IRAS 17036−4033), with a bolometric luminosity of 2.5×10^4 $L_\odot$ (Beltrán et al., 2006a), is located towards the eastern arm of S10. The estimated centre position of S10 as given by these authors lies within the error ellipse of the IRAS point source position. An arc-type structure with an opening in the north-east direction is seen towards the west of the likely centre of the bubble. The second region, which includes EGO345, shows an extended emission to the north-east and a bright compact emission to the south-west of the EGO. The EGOs, which display enhanced 4.5 μm emission (given common colour coding of green in the *Spitzer*-GLIMPSE colour composite images and hence the name), are likely candidates tracing outflows from massive young stellar objects (Cyganowski et al., 2008; Chambers et al., 2009; De Buizer & Vacca, 2010; Lee et al., 2012, 2013; Caratti o Garatti et al., 2015). This region is associated with IRAS 17039−4030 (Cyganowski et al., 2008). It has no association with any Infrared Dark Clouds (IRDCs) or OH masers but is associated with Class I and Class II

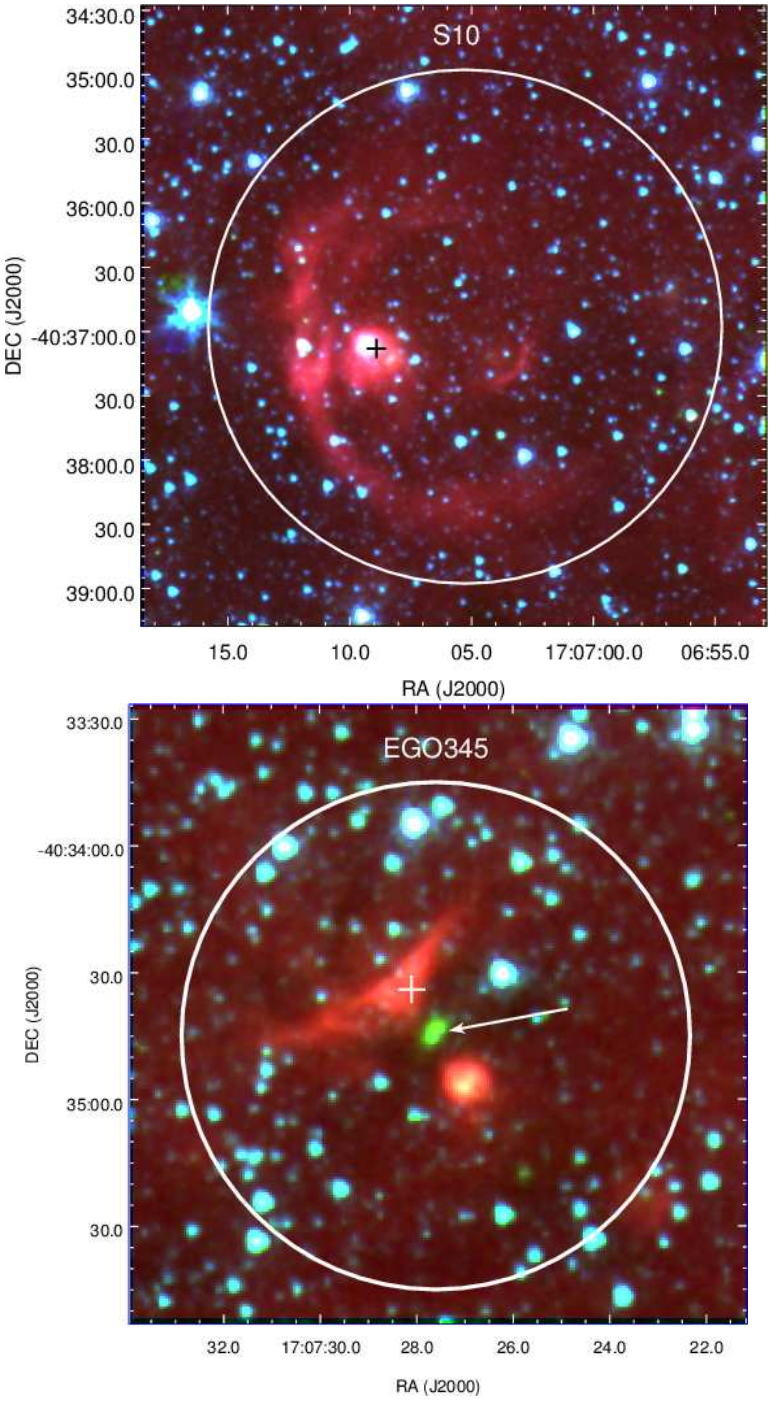

Figure 3.1: Colour composite image of bubble S10 (top panel) and EGO345 (bottom panel) with 8.0 μm (red), 4.5 μm (green) and 3.6 μm (blue) colour coding. The '+' marks show the positions of associated IRAS point sources and the arrow points to the position of EGO345. Circles show the regions of study towards S10 and EGO345.

methanol masers, which are signposts of high-mass star-forming regions (Caswell et al., 2010; Chen et al., 2011).

Figure 3.2 shows the relative location of S10 and EGO345. In this figure, we trace the elliptical and almost spherical morphologies of S10, as suggested by Churchwell et al. (2006) and Simpson et al. (2012), respectively. We support the larger spherical morphology of Simpson et al. (2012) given the extended southern part of the bubble. However, the thickness of 0.98′ estimated by them is on the higher side compared to 0.3′ quoted by Churchwell et al. (2006). We have adopted the latter value.

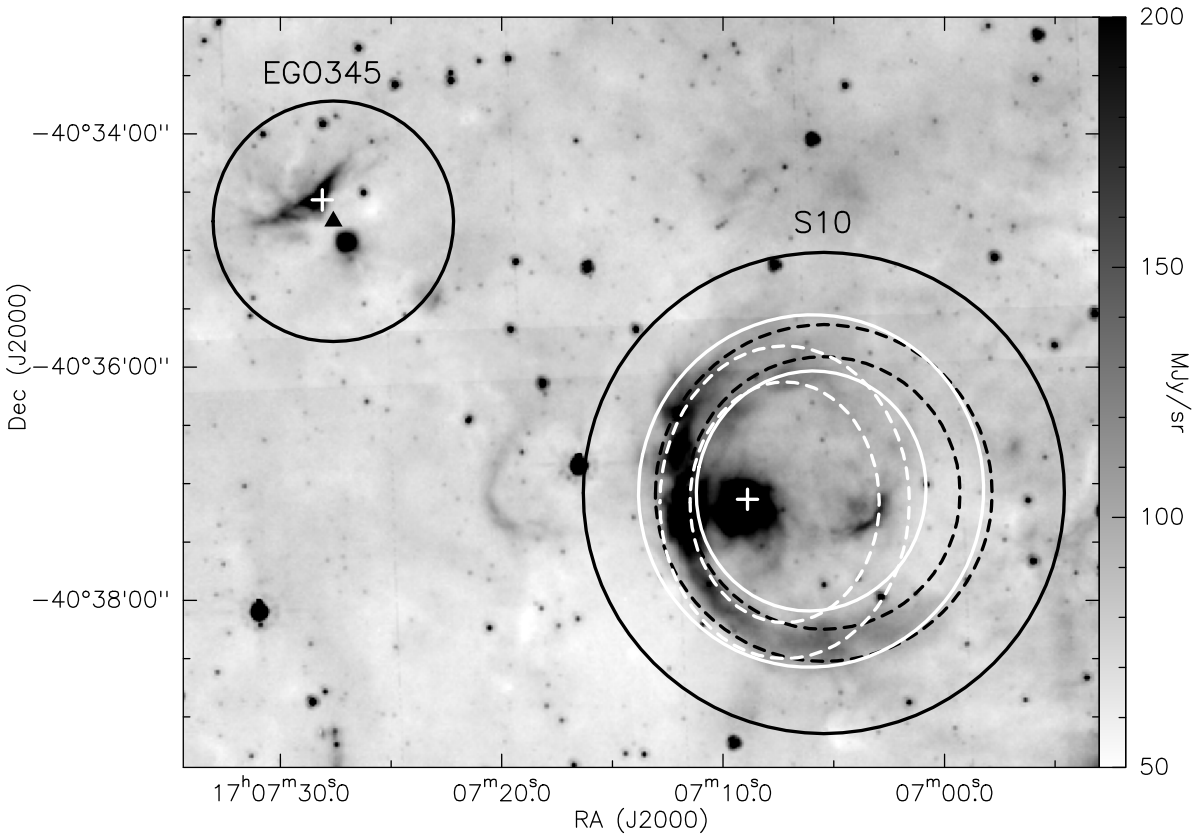

Figure 3.2: IRAC 8.0 μm image of the regions (shown as black circles) probed in this chapter. The '+' marks show the positions of the associated IRAS point sources, IRAS 17036−4033 (S10) and IRAS 17039−4030 (EGO345). The filled black triangle shows the location of the EGO. We show the various morphologies proposed for the bubble - white dashed (Churchwell et al., 2006); white solid (Simpson et al., 2012) and black dashed (our estimate).

Both these regions have been studied in the rotational transition lines of CS and $C^{17}O$ molecules, and 1.2 mm continuum emission as part of the survey for the search of massive protostellar

candidates using SEST telescope (Fontani et al., 2005; Beltrán et al., 2006a). As discussed in Beltrán et al. (2006a), the 1.2 mm dust continuum emission map shows the presence of six massive clumps with derived masses between 85 and 423 $M_{\odot}$. Four of these clumps are located in the eastern periphery of S10 and associated with IRAS 17036−4033. The other two clumps are towards the north-east and associated with EGO345. Beltrán et al. (2006a) assume these six clumps to belong to the same star-forming region. This is supported by the distance estimates to IRAS 17036−4033 and EGO345. Using the CS line velocity, Fontani et al. (2005) estimate the near and far kinematic distances for IRAS 17036−4033 to be 5.7 and 10.8 kpc, respectively. Following Beltrán et al. (2006a), we too adopt the near distance in our study. The distance to the region EGO345 is also estimated to be 5.6 kpc (Chen et al., 2011). Further, the location of the four clumps in the periphery of S10 strongly suggests a fragmented shell interacting and shaped by the expansion of the bubble. Similar dust clumps have been observed at the borders of several IR bubbles (Zavagno et al., 2010; Ji et al., 2012; Liu et al., 2016).

We have studied these two regions in detail in radio and IR. Results and discussion from the study is presented in Section 3.2 and in Section 3.3, we summarize our results.

3.2 Results and Discussion

3.2.1 Ionized Emission

To probe the ionized emission associated with our regions of interest, low frequency radio observations were carried out with the GMRT on 17 and 20 July 2011. Data reduction has been performed using AIPS. Chapter 2 describes the details regarding observation using GMRT and the data reduction procedure. The details of the observations are given in Table 3.1. We generate the continuum maps at 610 and 1280 MHz by setting the 'robustness' parameter to +1 (on a scale where +4 represents nearly natural weighting and −4 is close to uniform weighting of the baselines) while running the task `IMAGR`. We further use the task `UVTAPER` to weigh down the long baselines. The above procedures enable us to probe larger spatial scales of the extended diffuse emission in the regions. To correct the effect of Galactic diffuse emission, the final radio maps have to be properly rescaled. In Chapter 2, we have discussed the procedure of determining the scaling factor. Following this, the scaling factor at 1280 MHz is estimated to be 1.2. For 610 MHz, we obtain the scaling factor from the observed self-power of the

antennas following the procedure outlined in Marcote et al. (2015). Self-power of each antenna is measured at the position of the flux calibrator (3C286) and the target at similar elevations. After retaining only the antennas with stable self-power, the ratio of individual data points of S10 and 3C286 is calculated for each antenna and polarization. Median of the ratios removes the outliers and gives a scaling factor of 1.7 ± 0.02.

Table 3.1
Details of the radio interferometric continuum observations.

Details	610 MHz	1280 MHz
Date of Obs.	17 July 2011	20 July 2011
Flux Calibrators	3C286,3C48	3C286,3C48
Phase Calibrators	1626−298	1626−298
Synth. beam	14.4″×8.5″	8.8″×4.4″
Position angle. (deg)	10.61	15.02
rms noise (mJy/beam)	0.7	0.2
Int. Flux (mJy)	203 (S10)	44 (S10)
(integrated upto 3σ level)	43 (EGO345)	132 (EGO345)

Figure 3.3 shows the radio continuum maps overlaid on the 8 μm IRAC image. Table 3.1 gives the details of the observation and the maps. The region associated with S10 shows the presence of faint diffuse emission mostly distributed in the second quadrant in the interior of the bubble. The 610 MHz emission displays a relatively steep density gradient with enhanced emission towards the likely centre of the bubble and a more extended emission towards the north-east. However, the higher frequency map at 1280 MHz is seen to be less extended in the south-east and north-west direction, but follows the general morphology seen at 610 MHz. The radio contours near the centre are enveloped in the south-west direction by an arc-type 8 μm structure. Apart from this, in the 1280 MHz map, we see ionized emission beyond the west periphery of the bubble. This emission is not detected in the 610 MHz map down to the 3σ level. This could be due to a combination of the nature of the ISM there as well as the lower sensitivity achieved at 610 MHz. It is difficult to comment on the association of this detached emission with that of the bubble.

For the region associated with EGO345, the 610 MHz map shows a smooth and nearly spherical morphology with the 8 μm triangular shaped emission located towards its lower half. The 1280 MHz map shows a relatively clumpier morphology, which is more extended in the north-

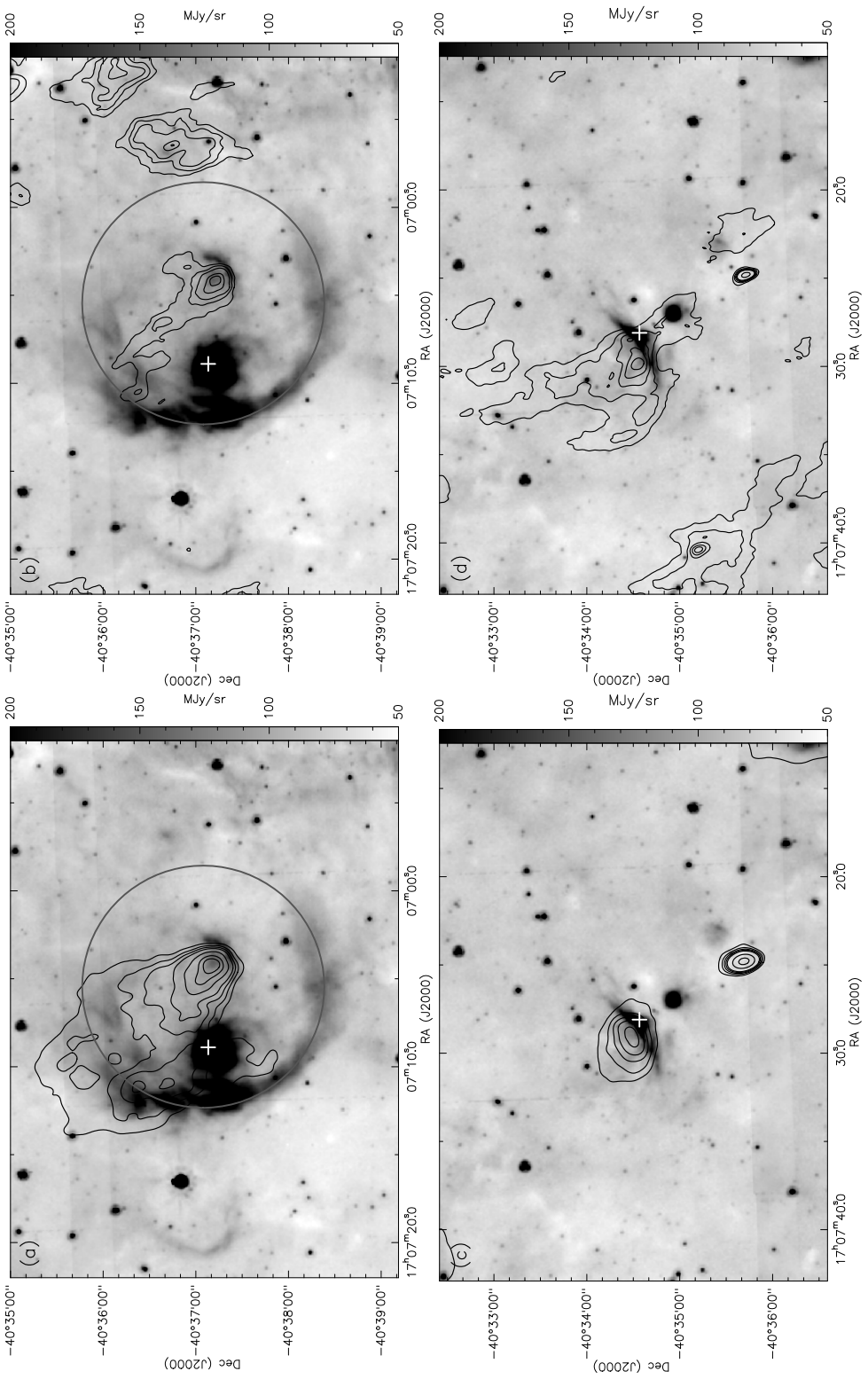

Figure 3.3: Radio continuum emission probed in both the regions over plotted on the IRAC 8.0 μm images. (a) 610 MHz map of the region associated with S10. The contour levels are 3, 3.5, 4.0, 4.5, 5.5, 6.5, 7 times σ (0.7 mJy/beam). (b) 1280 MHz of the region associated with S10. The contour levels are 3, 4, 5, 7, 8 times σ (0.2 mJy/beam). (c) Same as (a) but for the region associated with EGO345. The contour levels are 3, 4, 5, 6, 7 times σ. (d) Same as (b) but for the region associated with EGO345. The contour levels are 3, 4, 5, 7, 9, 13 times σ. The circles in (a) and (b) shows the extent of the bubble S10. The '+' marks indicate the position of the IRAS point sources associated with both the regions.

east and south-west direction as compared to the 610 MHz emission. The position of peak flux density lies $\sim 24''$ north-east of the position of the EGO.

For optically thin and free-free emission, the excitation parameter, u, and the total flux of ionizing Lyman continuum photons, N_{lyc}, at a given frequency, ν, can be estimated using the following formulation from Schraml & Mezger (1969) and Panagia (1973),

$$\left[\frac{u}{\mathrm{pc\ cm^2}}\right] = 4.5526 \left[a\,(\nu, T_e)^{-1} \left[\frac{\nu}{\mathrm{GHz}}\right]^{0.1} \left[\frac{T_e}{\mathrm{K}}\right]^{0.35} \left[\frac{S}{\mathrm{Jy}}\right] \left[\frac{D}{\mathrm{kpc}}\right]^2\right]^{\frac{1}{3}} \tag{3.1}$$

$$u = 2.01 \times 10^{-19} \left[\frac{N_{lyc}}{\beta_{\mathrm{RR}}}\right]^{\frac{1}{3}} \mathrm{pc\,cm^{-2}} \tag{3.2}$$

where, $a\,(\nu, T_e)$ is the correction factor taken as 0.99 (Mezger & Henderson, 1967), T_e is the electron temperature, S the integrated flux density, and D the distance to the source. β_{RR} is the recombination rate to the excited levels of hydrogen, which is assumed to be 3.43×10^{-13} for an electron temperature of 7000 K (Panagia, 1973). We determine T_e using the Galactic temperature gradient relation given in Deharveng et al. (2000). The Galactocentric distance to our regions is determined to be 2.8 kpc using the expression given in Xue et al. (2008). This Galactocentric distance corresponds to T_e of 5300 K. To account for the corresponding value of β_{RR} for this temperature, we have applied a scaling factor of 1.0976 to Equation 3.2 as discussed in Panagia (1973).

As discussed in Churchwell et al. (2006), the probability of chance alignments of bubbles with H II regions is very small ($< 1\%$), hence the detected ionized emission can be assumed to be due to the massive star(s) driving the bubble S10. To determine the excitation parameter, total flux of ionizing Lyman continuum photons and the spectral type of the ionizing source responsible for the bubble S10, we assume the emission to be free-free and optically thin at 1280 MHz. We integrate the flux densities upto 3σ level and plug in the values in Equations 3.1 and 3.2. For an integrated flux density of 44 mJy and an electron temperature, T_e, of 5300 K, we derive values of 13.3 pc cm^{-2} for the excitation parameter (u) and 47.0 for the logarithm of the ionizing Lyman continuum photon flux ($\log N_{lyc}$). Assuming a single exciting source responsible for the ionized emission, we estimate the ZAMS spectral type to lie between B0.5 – B0 (see Table II of

Panagia 1973). This estimate is with the assumption of optically thin emission and hence serves as a lower limit because the emission could be optically thick at 1280 MHz. Various studies in the literature have shown that dust absorption of Lyman continuum photons can be very high (Inoue et al., 2001; Arthur et al., 2004; Paron et al., 2011). With limited knowledge of the dust properties, we have not accounted for the dust absorption here. We determine the spectral index, α defined by $S \propto \nu^{\alpha}$, using the peak flux densities from the two maps after convolving the 1280 MHz map to the resolution of the 610 MHz map ($14.4'' \times 8.5''$). The estimated spectral index of -0.1 is consistent with what is expected from optically thin free-free emission. Close to the radio peak ($\alpha_{2000} = 17^{h}07^{m}04.20^{s}$, $\delta_{2000} = -40^{\circ}37'11.00''$), there is a red NIR source (hereafter IRS1) ($\alpha_{2000} = 17^{h}07^{m}03.60^{s}$, $\delta_{2000} = -40^{\circ}37'10.70''$) with colours J − H = 2.44 and H − K = 1.67. The nature of this source will be discussed later to ascertain whether it is the NIR counterpart of the ionizing star.

Using the integrated flux density of 132 mJy at 1280 MHz and following the above formulation, we also estimate the physical parameters for the region associated with EGO345. The excitation parameter, total flux of ionizing Lyman continuum photon, and spectral type range is determined to be 18.9 pc cm^{-2}, 47.45, and B0 – O9.5, respectively. It should be noted here that the peaks at 610 and 1280 MHz are offset from each other by $\sim 10''$. A possible reason for this offset could be the nature of the ISM in this region. If there is an inhomogeneous density distribution, then it could lead to varying optical thickness. EGOs are known to harbour outflows and jets, hence one would also expect thermal emission from jets giving rise to positive spectral indices. Shock-induced non-thermal emission could also co-exist in such environments.

Apart from S10 and EGO345, the radio maps (Figure 3.3) show the presence of a relatively strong radio emitting region $\sim 1'$ to the south-west of the position of EGO345 with integrated flux densities of 21 and 7.5 mJy and peak flux densities of 16.9 and 6.5 mJy/beam at 610 and 1280 MHz, respectively. From the peak flux density values, we infer the associated emission to be non-thermal with a steep negative spectral index of -1.3. It is unclear whether this emission is associated with EGO345. No counterpart is reported in NED or Simbad. The SUMSS map shows a faint blob coincident with the location of this source.

3.2.2 Population of Young Stellar Objects

In order to understand the stellar population and probe the star-forming activity in the two regions, we identify and classify the associated young stellar objects (YSOs). Infrared colors have been proven to be a powerful tool for the identification of YSOs (Allen et al., 2004; Simon et al., 2007; Gutermuth et al., 2008). We have used the GLIMPSE 'highly reliable' catalog to retrieve the IRAC band magnitudes within 120″ of the expected centre of the bubble (α_{2000} = $17^h07^m05.45^s$, δ_{2000} = $-40°37'04.80''$) and within 60″ centered on the position of EGO345 (α_{2000} = $17^h07^m27.60^s$, δ_{2000} = $-40°34'45.00''$). We retrieved 65 and 23 sources with good quality data in all IRAC bands for the regions associated with S10 and EGO345, respectively. The red source IRS1 has photometric magnitudes available in the first three IRAC bands only. Using IRAF task *qphot*, we estimate its magnitude at 8 μm.

Details regarding the procedures followed for the identification of YSOs have been discussed in Section 2.3.1 of Chapter 2. In this study we use the criteria outlined in Allen et al. (2004), Simon et al. (2007), and Gutermuth et al. (2008). Figure 3.4 displays the IRAC CCPs for the adopted criteria. Adopting the various criteria, we have identified 14 YSOs including IRS1 in the region associated with S10 and 5 YSOs in the region associated with EGO345. Table 3.2 lists the identified YSOs in S10 and EGO345. In Figure 3.5, we show the spatial distribution of the identified YSOs overplotted on the 8 μm image. In the figure, we mark the location of two additional sources, which are listed as extreme red sources in Robitaille et al. (2008). The distribution of the identified YSOs are mostly towards the western part of the bubble and the north-eastern part of EGO345. It should be kept in mind that the identified YSOs are a sub-sample given the fact that we are concentrating only on those detected in all four IRAC bands.

3.2.3 Nature of IRS1

As discussed in the previous section, IRS1 is a likely Class I (Allen et al., 2004) or Class II (Gutermuth et al., 2008) YSO. It is located ~ 7″ westward from the peak position of the ionized emission probed in the radio frequencies. To derive the physical parameters of IRS1, we have carried out SED modelling using the online SED fitting tool of Robitaille et al. (2007). The basic models are computed using Monte Carlo based radiative transfer algorithm, which uses

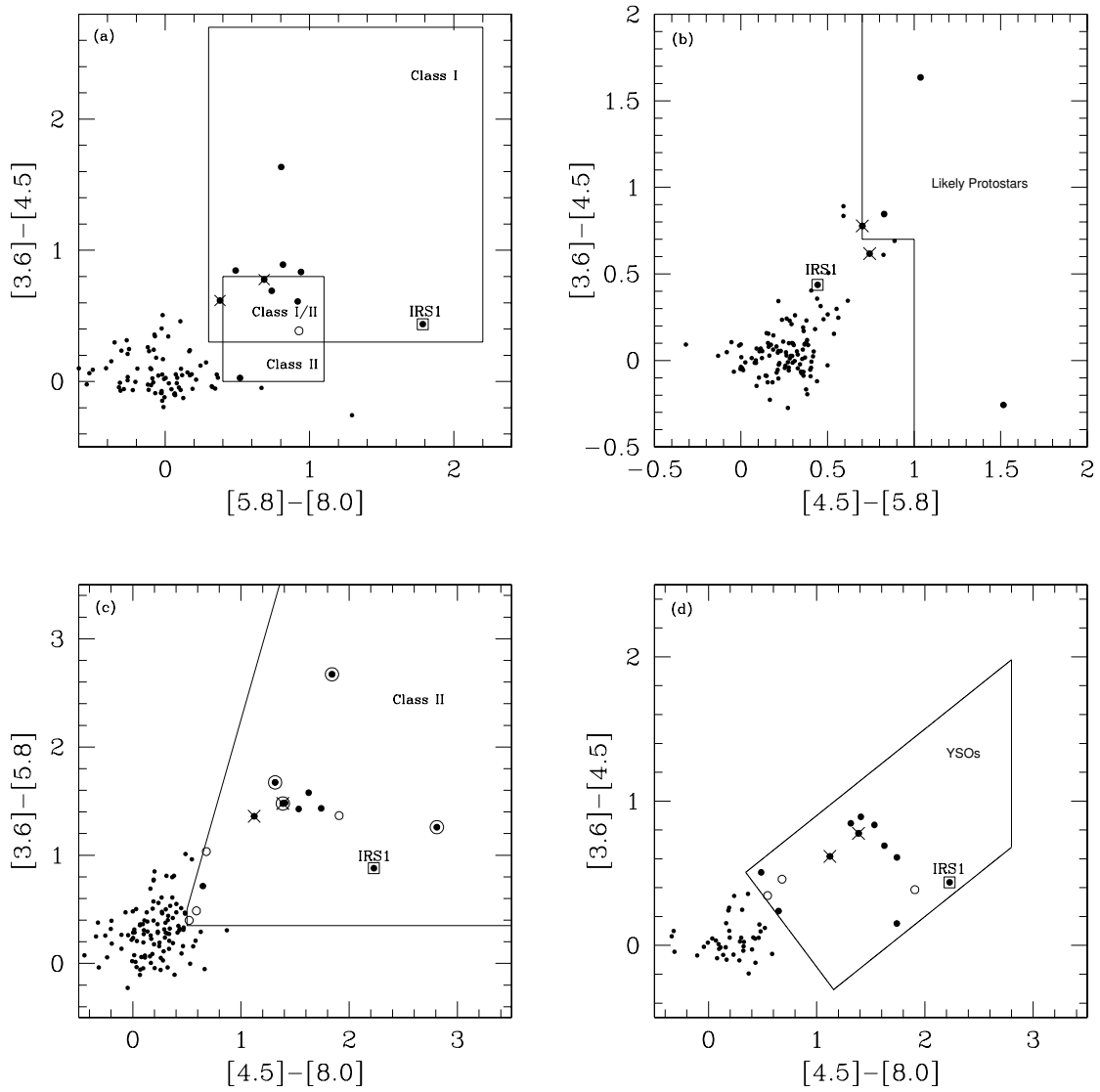

Figure 3.4: IRAC CCPs describing the various criteria discussed in the text. YSOs identified in the regions associated with S10 and EGO345 are shown as filled and open circles, respectively. Crosses denote the two extreme red sources identified in Robitaille et al. (2008). The location of IRS1 is also highlighted with an overplotted open square. (a) YSO identification as per criteria discussed in Allen et al. (2004). The boxes to demarcate the location of Class I (larger box) and Class II (smaller box) are adopted from Vig et al. (2007). Sources falling in the overlapping area are designated as Class I/II. (b) Criteria following Gutermuth et al. (2008). The region occupied by likely protostars (Class I) is shown. (c) Criteria for Class II sources following the method of Gutermuth et al. (2008). The four protostars (Class I) sources identified in (b) are also marked with overplotted open circles. (d) Criteria adopted from Simon et al. (2007).

Table 3.2
List of YSOs detected in S10 and EGO345 based on the three classification schemes.

Source	RA (J2000) (hh:mm:ss.ss)	DEC (J2000) (dd:mm:ss.ss)	Allen et al. (2004)	Gutermuth et al. (2008)	Simon et al. (2007)
YSOs in S10					
1	17:06:55.51	−40:36:46.33	Class I/II	Class II	YSO
2†	17:06:56.03	−40:37:39.68	Class I/II	Class I	YSO
3	17:06:57.34	−40:37:28.67	Class I	Class I	—
4	17:06:58.25	−40:36:44.42	Class II	—	—
5	17:06:58.26	−40:36:15.30	—	Class I	—
6	17:06:58.57	−40:37:58.73	Class I	Class I	YSO
7	17:07:03.43	−40:36:32.22	—	Class II	YSO
8*	17:07:03.60	−40:37:10.70	Class I	Class II	YSO
9†	17:07:03.84	−40:37:48.76	Class I	Class II	YSO
10	17:07:05.56	−40:36:37.40	—	—	YSO
11	17:07:06.63	−40:36:26.24	Class I/II	Class II	YSO
12	17:07:10.66	−40:38:44.02	—	—	YSO
13	17:07:11.98	−40:37:06.42	Class I	Class II	YSO
14	17:07:14.77	−40:36:15.84	Class I	Class II	YSO
YSOs in EGO345					
1	17:07:25.85	−40:34:03.97	—	—	YSO
2	17:07:29.23	−40:33:54.29	—	Class II	YSO
3	17:07:31.10	−40:34:47.86	Class I/II	Class II	YSO
4	17:07:31.66	−40:35:12.88	—	Class II	—
5	17:07:32.74	−40:34:19.45	—	Class II	—

*The NIR source IRS1; †extreme red sources from Robitaille et al. (2008)

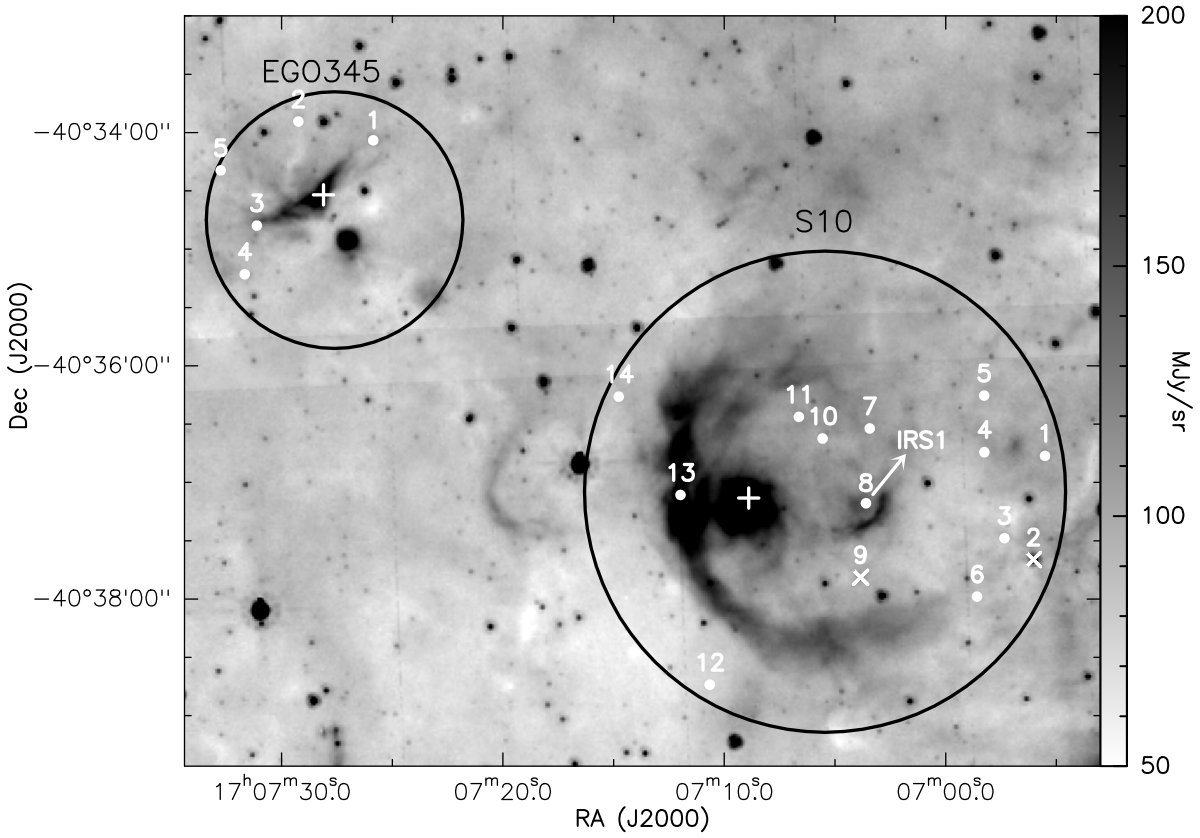

Figure 3.5: YSOs (white filled circles) identified by the various methods discussed in the text are marked over the 8.0 μm image. The '+' marks show position of IRAS 17036−4033 and IRAS 17039−4030 in the regions associated with S10 and EGO 345, respectively. The cross marks are the extreme red sources identified by Robitaille et al. (2008). The position of IRS1 is highlighted.

various combinations of central star, disk, infalling envelope, and cavities carved out by bipolar outflows. A reasonably large parameter space is explored in these models. Assuming that IRS1 is associated with the bubble S10, we have used a distance range of 5.5 – 5.9 kpc in the model fitting tool. As discussed in Section 3.2.1, IRS1 is a reddened source and its location in the JHK CCP (not presented here) gives an estimate of $A_v \sim 15$ mags. Hence, for the model fitting, we use a range of A_v = 1 – 20 mags. Apart from the MIR fluxes, we use the NIR JHK fluxes from 2MASS[1]. IRS1 is enclosed within a FIR clump (discussed later). Taking the retrieved clump aperture with an effective diameter of $\sim 12''$, we extract the flux densities at 24, 70, 160,

[1]This publication makes use of data products from the Two Micron All Sky Survey, which is a joint project of the University of Massachusetts and the Infrared Processing and Analysis Center/California Institute of Technology, funded by the NASA and the NSF.

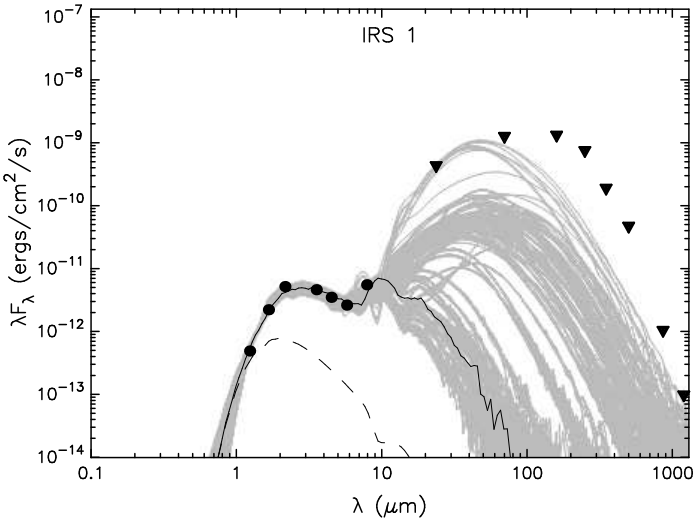

Figure 3.6: Best-fit SED models of IRS1 using the online tool of Robitaille et al. (2007). NIR and MIR fluxes are shown as solid circles. Flux densities for MIPSGAL 24 μm, PACS 70, 160 μm, SPIRE 250, 350, 500 μm, ATLASGAL 870 μm and 1200 μm are given as upper limits (filled triangles). The best fit model is shown as solid black line. The plots shown in grey are the models satisfying the criteria $\chi^2 - \chi^2_{\rm best}$ (per data point) < 3. The photosphere of central source is shown as the dashed curve (with interstellar extinction but with absence of circumstellar dust).

250, 350, 500, 870, and 1200 μm and use them as upper limits for the SED fits. The 870 μm and 1200 μm data are from ATLASGAL[2] survey and Beltrán et al. (2006a), respectively. The model SED is generated using seven data points and eight upper limits. We have assumed a conservative 10% error on the used flux densities. In Figure 3.6, we show the model fits for IRS1 satisfying the criteria $\chi^2 - \chi^2_{\rm best}$ (per data point) < 3. The weighted average (weight is taken as $1/\chi^2$) of the physical parameters retrieved from the above best fitting models are listed in Table 3.3 with the values obtained for the best fit given in parenthesis. The best fit model gives the mass estimate of the source as 6.2 $M_\odot$, which suggests IRS1 to be an intermediate-mass star. IRS1 is therefore unlikely to be the NIR counterpart of the exciting B0.5 – B0 star responsible for the ionized emission. It is possible that the massive ionizing star is deeply embedded and does not reveal itself in the NIR. However, it should be noted that these values of the parameters are to be taken with caution since we are dealing with a large parameter space with very few data points to constrain the models.

[2]This project is a collaboration between the Max Planck Gesellschaft (MPG: Max Planck Institute fÃijr Radioastronomie, MPIfR Bonn, and Max Planck Institute for Astronomie, MPIA Heidelberg), the European Southern Observatory (ESO) and the Universidad de Chile

Table 3.3
Weighted mean of the physical parameters for IRS1 retrieved from the SED modelling. Values in the parenthesis are from the best fit model. Second row lists the range for each parameter fitted by all the models satisfying $\chi^2 - \chi^2_{\rm best}$ (per data point) < 3.

log t_* (yr)	Mass ($M_\odot$)	log M_{disk} ($M_\odot$)	log $\dot{M}_{disk}$ ($M_\odot\ yr^{-1}$)	log M_{env} ($M_\odot$)	log T_* (K)	log L_{total} ($L_\odot$)	A_V (mag)
5.70 (6.19)	4.75 (6.24)	−4.02 (−6.70)	−9.50 (−12.04)	−2.46 (−5.60)	3.96 (4.28)	2.42 (3.31)	14.29 (14.33)
3.03 – 7.00	1.04 – 10.23	−7.13 – −0.17	−13.51 – −4.36	−7.67 – 2.65	3.60 – 4.32	1.43 – 3.37	2.92 – 20.00

3.2.4 Emission from dust component

Figure 3.7 shows the dust emission toward the regions associated with bubble S10 and EGO345 sampled at IRAC, MIPSGAL, Hi-Gal and ATLASGAL images. These images reveal different dust emission features of the bubble and the EGO. As discussed in Watson et al. (2008), emission in IRAC bands are dominated by thermal dust emission along with diffuse PAH emission. The 3.6 and 4.5 μm bands detect mostly the bright sources since these bands are dominated by emission from stellar photospheres. Apart from this, the 3.6 μm band also has the contribution from weak, diffuse PAH emission feature at 3.3 μm, whereas the 4.5 μm band is free from PAH emission. At these bands, the faint arc of S10 is seen. As we move to the longer wavelengths, the brightness of the arc and the associated diffuse emission increases. At 5.8 and 8.0 μm, the bubble rim becomes clearly visible and extended emission is seen towards the EGO. The 24 μm emission is much more localized. Emission at longer wavelengths starts to be dominated by cold dust and shows extended features, as is seen the in the *Herschel* and ATLASGAL wavebands. A comparative view of the dust emission associated with S10 and EGO345 is presented in Figure 3.8, as a colour composite image with 250 μm (red), 70 μm (green), and 24 μm (blue). Warm dust is seen in localized areas near the bubble and the EGO, whereas, the cold dust emission is seen to be distributed in a diagonal stretch along the north-east and south-west direction.

Temperature and column density maps

In order to understand the properties of cold dust emission in the regions associated with S10 and EGO345, we generate column density and dust temperature maps following the procedure

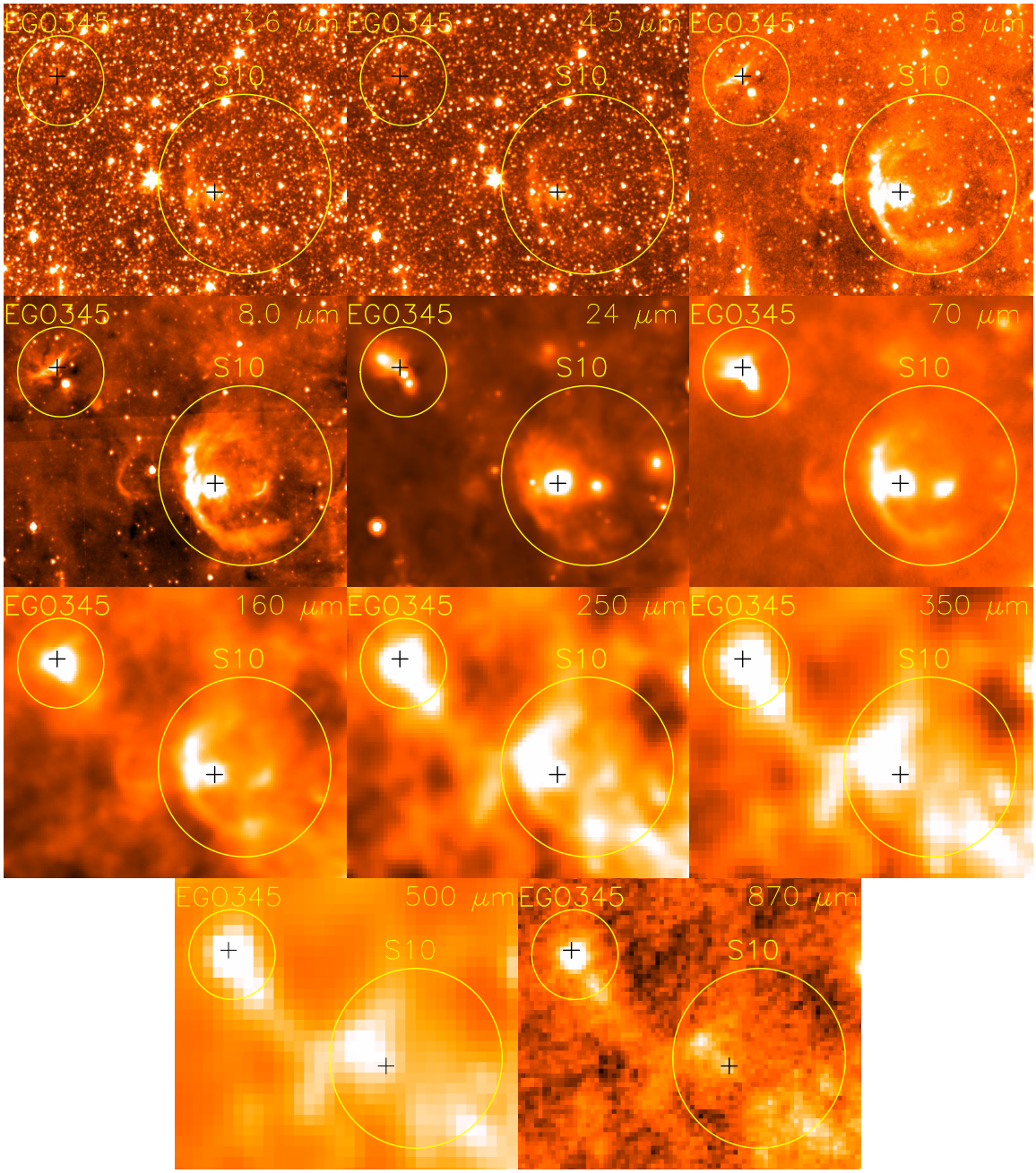

Figure 3.7: Dust emission associated with bubble S10 and EGO345 are displayed. Emissions at wavelengths of IRAC bands (3.6, 4.5, 5.8 and 8.0 μm), MIPSGAL (24 μm), PACS (70, 160 μm), SPIRE (250, 350, 500 μm), and ATLASGAL (870 μm) are shown. The '+' mark shows the position of associated IRAS point sources.

detailed in Chapter 2. The background flux density, I_{bkg}, is estimated from a relatively 'smooth' (free of clumpy emission) and 'dark' (free of bright dust emission) region. This is done by

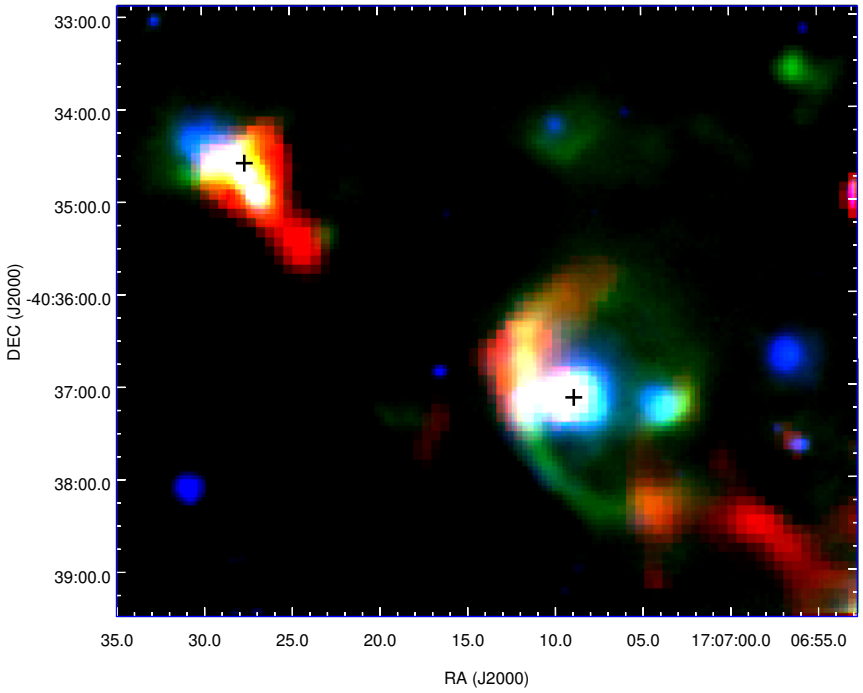

Figure 3.8: Three-color composite image of the regions associated with S10 and EGO345 with 24 μm *Spitzer*- MIPSGAL (blue), 70 μm *Herschel*-PACS (green), 250 μm *Herschel*-SPIRE (red).

visual inspection. We select a region $\sim$ 1° away from S10 and EGO345. The background fluxes in the four bands are estimated by fitting a Gaussian to the distribution of individual pixel values in the selected region (Battersby et al., 2011; Launhardt et al., 2013; Mallick et al., 2015). The fitting is done iteratively by rejecting the pixel values outside $\pm 2\sigma$, until the fit converges to a value. Figure 3.9 shows the iterative Gaussian fitting for the background images. The resultant background flux levels at 160, 250, 350, and 500 μm are -3.22, 1.45, 0.72, 0.26 Jy pixel^{-1}, respectively. The negative flux value at 160 μm is due to the arbitrary scaling of the PACS images. The SED modeling is then carried out using non-linear least square Levenberg-Marquardt algorithm pixel wise. We use a conservative 15% uncertainty on the background subtracted flux densities (Launhardt et al., 2013). Dust temperature and column density are taken as free parameters in the code. As discussed in Chapter 2, we fix the dust emissivity to 2. From the best-fit values, the temperature and column density maps are generated and shown in Figure 3.11. This figure also shows the chi-square (χ^2) map, which displays the goodness of fit. To visualize the same, in Figure 3.10, we show the SED modelling for two individual pixels,

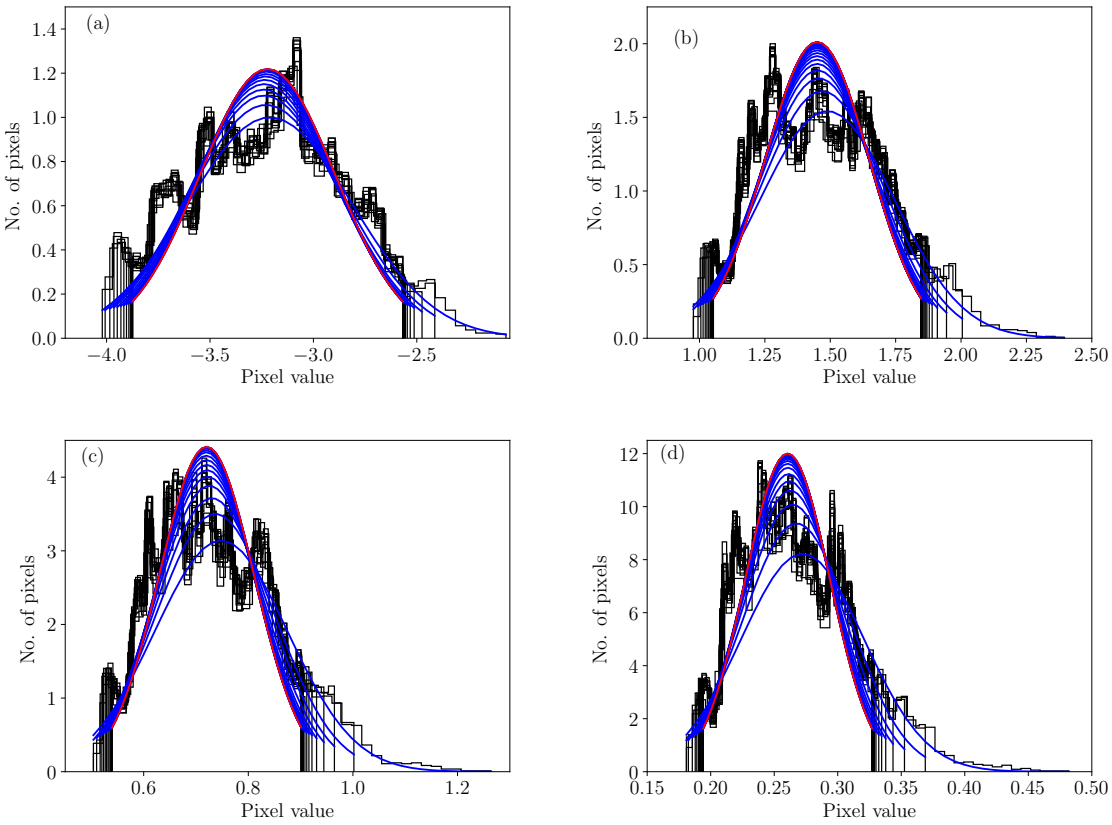

Figure 3.9: Iterative Gaussian fitting of the distribution of individual pixel values for (a) 160 μm, (b) 250 μm, (c) 350 μm, and (d) 500 μm. The final fitting is shown in red.

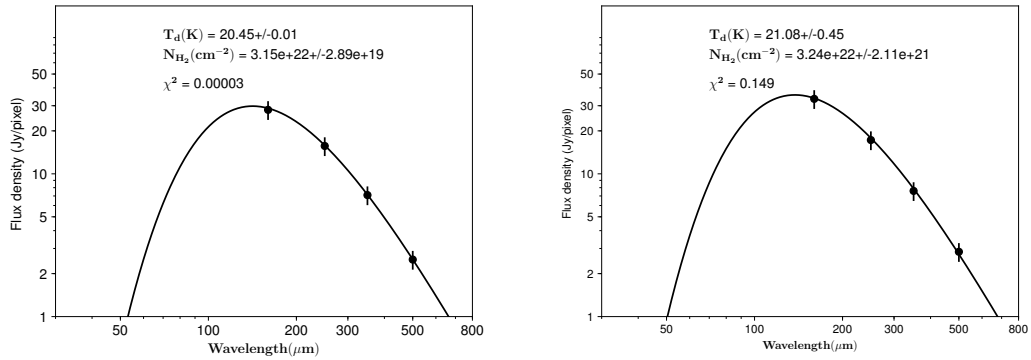

Figure 3.10: Modified black body fitting for two individual pixels having the best and the worst χ^2 values.

possessing the best (3×10^{-5}) and worst (0.15) χ^2 values.

The temperature map shows two peaks ($\sim$ 23 K) close to the IRAS point sources in the two

regions. From the overlay of radio contours, it is evident that the ionized regions are traced by warmer dust component compared to the other regions of the map. The peak temperature positions are $\sim$ 1′ and 24″ toward north-east of the radio peaks in region S10 and EGO345, respectively. The column density map for the region associated with S10 shows a high density elongated clump toward the south-west of the bubble mostly outside the periphery. A high density region is also seen stretching in the south-east and north-west direction on the opposite periphery. The column density map also shows a dense clump associated with the EGO345 region. Another dense clump is seen towards the south-west of EGO345 and north of the position of the bright radio emitting region mentioned in Section 3.2.1. Apart from this, an extended filamentary structure is seen connecting the two regions.

Properties of dust clumps

The resolution of the column density map is low (35.7″) and hence does not allow us to detect sub-structures in the map. In order to identify dust clumps or condensations associated with the region around S10 and EGO345, we use the 250 μm image, which has a optimum resolution of 18″. The threshold for detecting the clump peaks was set to 1.9 Jy pixel^{-1} (= 20σ; σ = 0.09 Jy pixel^{-1} being the uncertainty determined from a region $\sim$ 10′ away) to avoid spurious clump detection. To detect the cold dust clumps, we have used the 2D *clumpfind* algorithm (Williams et al., 1994). This algorithm has been widely used for the decomposition of cold dust clumps in both 2D and 3D data set. The 2D *clumpfind* algorithm works on the principle of identifying the peak position of emission within the image and then it contours the data from peak to the threshold level. The contour levels are basically user defined, which helps in separating out the peaks. In our case the positions of peak intensities in the map are determined by identifying the pixels having the highest value in 3×3 pixel matrices, with flux values above the estimated threshold. Subsequent to the peak identification, contours are generated to isolate the clumps around these peaks. Using these generated contour levels in the 2D variation of the *clumpfind* algorithm, we detect a total of eight clumps (six in region S10 and two in region EGO345). Figure 3.12 shows the clumps detected using the 250 μm image overlaid on 24 μm *Spitzer*-MIPS and the five *Herschel* bands. In Figure 3.12(a), we also show the six 1.2 mm clumps of Beltrán et al. (2006a). As seen from the figure, there is an overall overlap of the clumps detected in this work and those from Beltrán et al. (2006a). The different numbers,

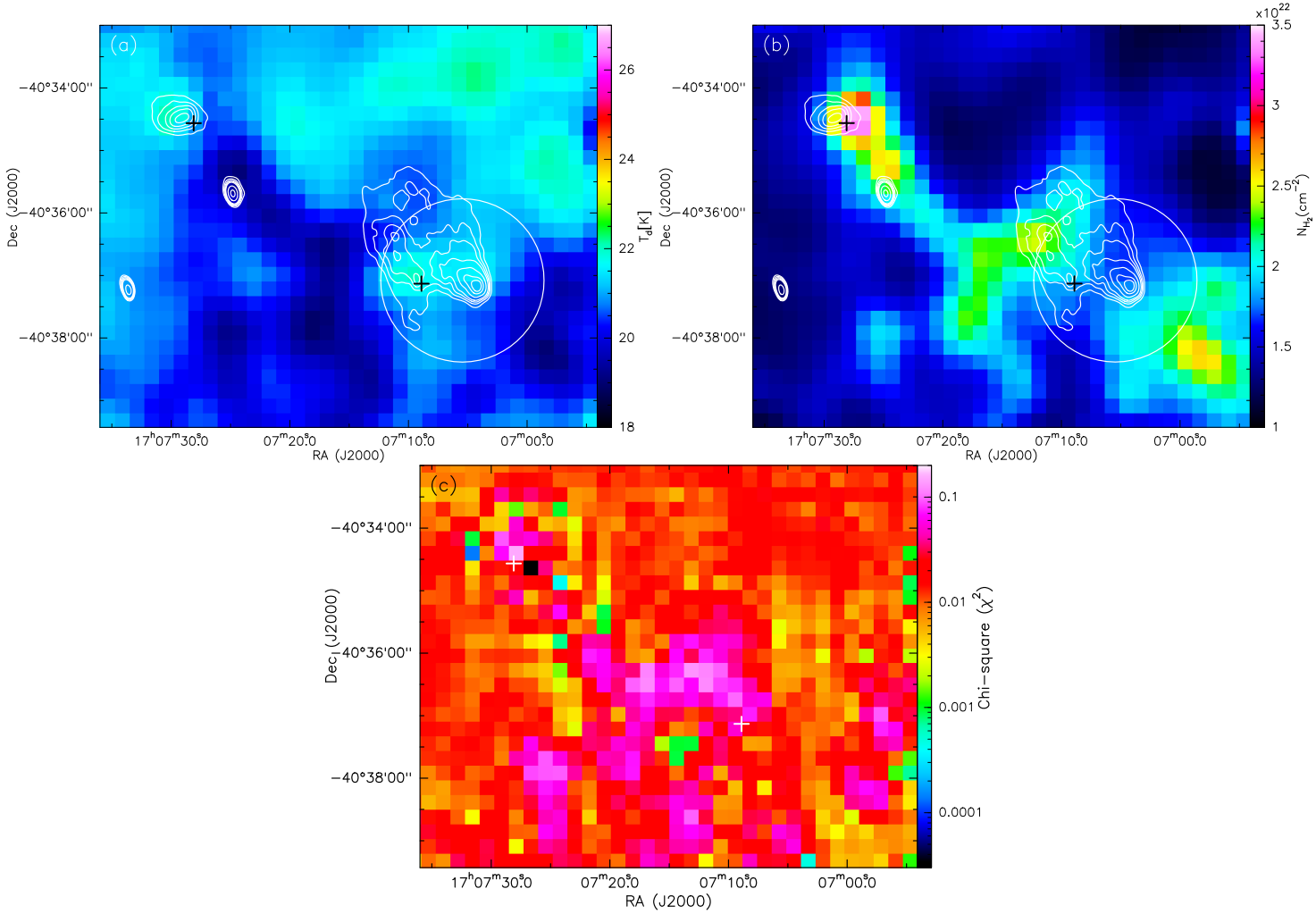

Figure 3.11: (a) Dust temperature, (b) column density, and (c) chi-square (χ^2) map of regions associated with S10 and EGO345. The radio emission at 610 MHz is also shown as contours with the same levels as in Fig. 3.3. The white circle shows the extent of the bubble S10. The '+' symbols mark the position of IRAS point sources associated with the regions.

shapes, and sizes of the clumps could be attributed to the different wavelength of the maps and the threshold and contour spacing adopted. The above reason would mostly justify the non detection of Clumps 4, 5, and 6 by Beltrán et al. (2006a).

We determine the masses of the clumps from the column density as well as the 250 μm maps. The expressions used are outlined below.

1. *From column density map*: The masses of the clumps are estimated by determining the mass in each pixel and then summing over all the pixels inside the clump by using the following equation,

$$M_{\rm clump} = \mu_{\rm H_2} m_{\rm H} A_{\rm pixel} \Sigma N({\rm H_2}) \tag{3.3}$$

   where m_H is the mass of hydrogen nucleus, A_{pixel} is the pixel area in cm^2, μ_{H_2} is the mean molecular weight, and $\Sigma N(H_2)$ is the integrated column density within the clump apertures. The clumps apertures are retrieved from the *clumpfind* algorithm.

2. *From 250 μm image*: Here, the masses of the clumps are estimated from the 250 μm integrated flux values obtained using the *clumpfind* algorithm and the following expression from Kauffmann et al. (2008)

$$M = 0.12\ M_{\odot} \left(e^{1.439(\lambda/{\rm mm})^{-1}(T_d/10{\rm K})^{-1}} - 1\right) \left(\frac{\kappa_\nu}{0.01{\rm cm^2 g^{-1}}}\right)^{-1} \left(\frac{S_\nu}{\rm Jy}\right) \times \left(\frac{\rm D}{100{\rm pc}}\right)^2 \left(\frac{\lambda}{\rm mm}\right)^3 \tag{3.4}$$

   where T_d is the dust temperature, κ_ν is the dust opacity, which is taken as $0.1 \left(\frac{\nu}{1000GHz}\right)^{\beta}$, D is the distance, and S_ν is the integrated flux. For T_d, we use the mean dust temperatures of the clumps estimated from the temperature maps.

The derived masses and other physical properties of the clumps are listed in Table 3.4. As seen from the table, the masses derived from the column densities are lower (by an average factor of $\sim$ 0.9) compared to those derived from the 250 μm image alone. The masses derived from

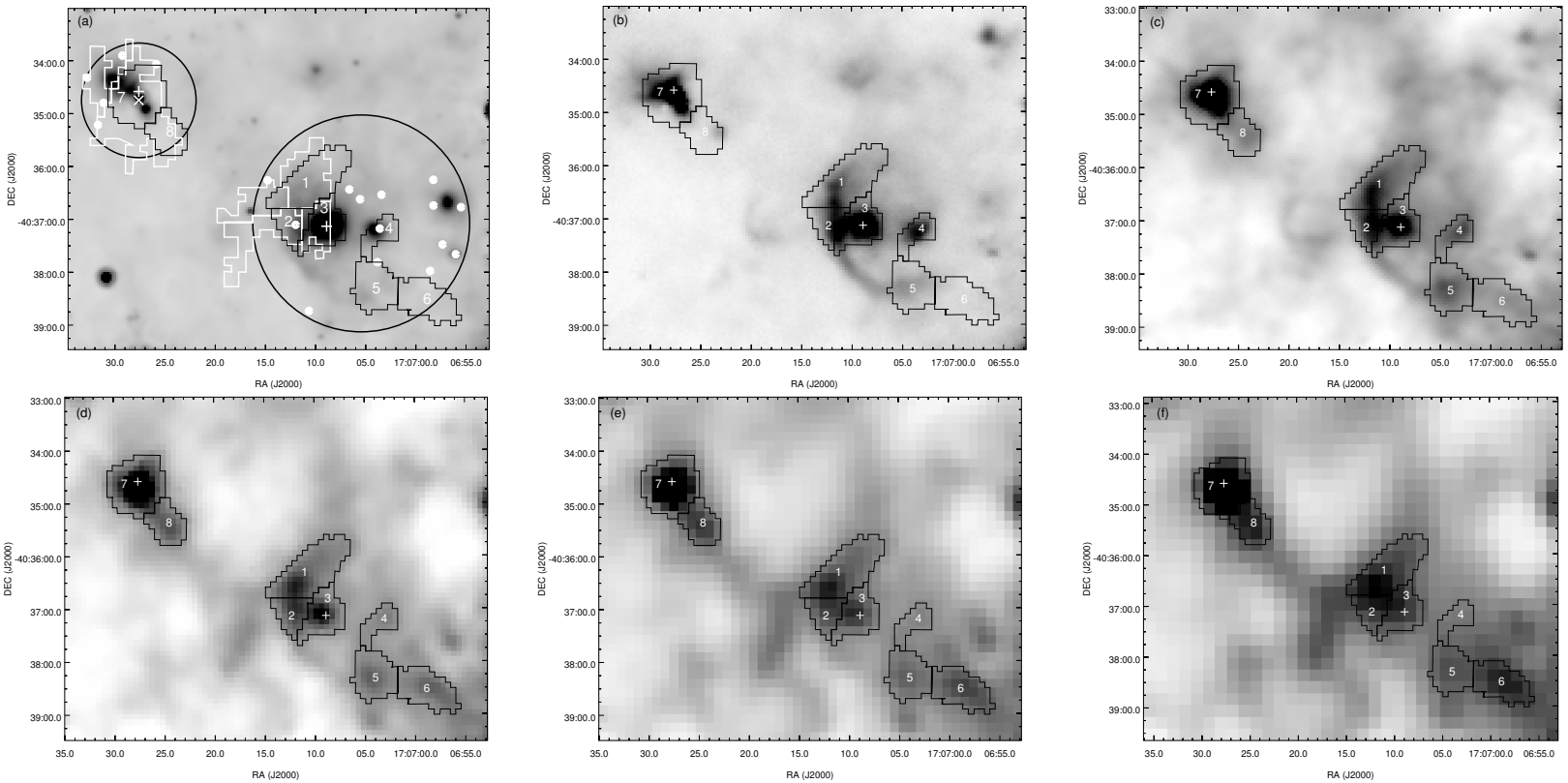

Figure 3.12: Eight clumps (apertures shown as black contours) detected from 250 μm image are shown on (a) 24 μm (b) PACS 70 μm (c) PACS 160 μm (d) SPIRE 250 μm (e) SPIRE 350 μm (f) SPIRE 500 μm images. The retrieved clump apertures from the 1.2 mm map (Beltrán et al., 2006a) are shown as white contours in (a) where the two regions are also marked as black circles. The '+' symbols mark the position of IRAS point sources associated with the regions. The positions of the identified YSOs (see Section 3.2.2) are shown on the 24 μm image.

Table 3.4

Physical parameters of the clumps. F_{250} is total flux density in 250 μm. The listed positions correspond to the peaks of the clumps as derived from the 250 μm image using the *clumpfind* algorithm. The linear diameter listed here are the deconvolved (without parenthesis) and the effective diameter (within parenthesis). T_d and $N(H_2)$ are the mean dust temperature and column density respectively. M_{250} is mass calculated using fluxes from 250 μm and M_{CD} is the mass calculated using the column density map.

Clump No.	RA (2000) (hh:mm:ss.ss)	DEC (2000) (dd:mm:ss.ss)	F_{250} (Jy)	Linear Diameter (pc)	Mean T_d (K)	Mean $N(H_2)$ ($\times 10^{22} cm^{-2}$)	M_{250} ($M_\odot$)	$\sum N(H_2)$ ($\times 10^{23} cm^{-2}$)	M_{CD} ($M_\odot$)
				S10					
1	17:07:12.02	−40:36:33.00	222	1.1 (1.9)	20.6	2.0	1436	4.2	1390
2	17:07:12.02	−40:36:57.00	85	0.2 (1.1)	20.8	1.7	533	1.1	354
3	17:07:09.40	−40:37:09.09	131	0.6 (1.4)	21.5	1.7	750	2.1	685
4	17:07:03.08	−40:37:15.40	63	0.3 (1.0)	21.0	1.6	390	1.0	337
5	17:07:04.70	−40:38:27.90	134	0.6 (1.5)	20.5	1.8	875	2.5	845
6	17:06:58.90	−40:38:27.60	143	0.7 (1.6)	19.6	2.1	1074	2.6	852
				EGO345					
7	17:07:27.77	−40:34:44.05	283	0.7 (1.9)	21.0	2.3	1754	4.7	1564
8	17:07:24.63	−40:35:26.24	99	0.3 (1.3)	19.4	2.2	770	2.0	655

the column density map would be a better estimate given that it uses data from four bands. The table also lists the linear diameters of the clumps. We have estimated the deconvolved sizes following the method outlined in Beltrán et al. (2006a). We also list the diameters derived based on the physical size of the clump (Kauffmann & Pillai, 2010) in parenthesis. The later does not have the beam effect removed, and we refer to it as the effective diameter.

In order to understand the nature of the sources towards these clumps, we use the online SED model fitting tool of Robitaille et al. (2007) to fit the clump fluxes with the inbuilt YSO models. This is along the lines discussed in Zavagno et al. (2010). Here, we assume that each clump would produce a single high-mass star. Apart from the MIPS and *Herschel* data, we have used 870 μm ATLASGAL and 1.2 mm (Beltrán et al., 2006a) fluxes. We use the clump apertures retrieved from the *clumpfind* algorithm to obtain flux densities in all wavelengths. The same apertures were used on nearby 'smooth' and 'dark' regions to estimate the background emission, which is subtracted out from the clump fluxes. As done earlier, we take a conservative uncertainty of 15% on the background subtracted flux densities. Figure 3.13 shows the results of the fits towards the clumps. In Table 3.5, we list the range of values of various parameters of the first ten best fitting SED models with the best-fit values in parenthesis. The envelope masses retrieved from fitting the SED models are seen to be $\sim$ 1.5 – 3 times larger than the derived masses of the clumps, except for Clump 4 where both the masses are similar. All clumps are seen to harbour high luminosity, high envelope accretion rate, and massive YSOs. As mentioned in Section 3.2.3, the retrieved values of the parameters are to be used as indicative only as these models involve a large range in parameters with limited data points. Hence, instead of fitting to a unique combination, the models return a range in the parameter space.

Kauffmann & Pillai (2010) suggest an empirical mass-radius relation to define a threshold for clouds to form massive stars. They derive this relation by comparing the mass-radius relation of clouds with and without massive star formation. The clouds devoid of massive star formation are shown to generally obey the relation, $m(r) \leqslant 870 \mathrm{M}_{\odot}(\mathrm{r/pc})^{1.33}$. In Figure 3.14(a), we plot the estimated mass (from column density map) as a function of the effective radius of the clumps. It should be noted here that the threshold estimated by Kauffmann & Pillai (2010) is based on effective radii derived using the physical area of the clumps. Hence, if we look at the filled circles in the figure, most of the clumps detected in the regions associated with S10 and EGO345

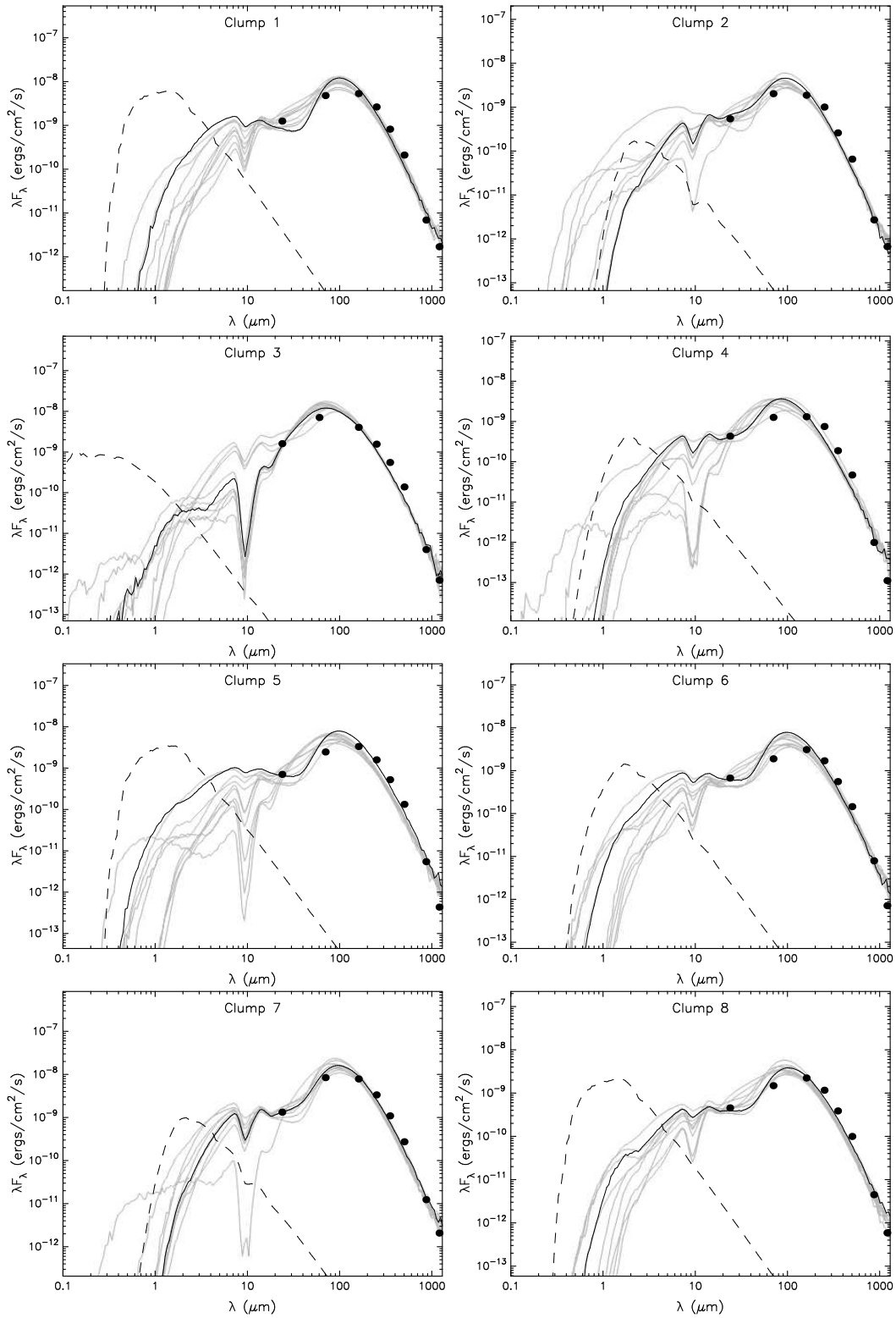

Figure 3.13: Results of the online SED modelling of Robitaille et al. (2007) for the eight clumps. The grey lines are the ten best fitting models and the black line is the best-fit model.

are above the threshold. Two clumps are seen just below, but very close to, the dividing line. This implies that all the clumps are potential high-mass star-forming regions. We have also plotted the deconvolved radius of the clumps as open circles. The dashed line denotes the slope from Urquhart et al. (2013b) and the region lying above that marks the location of high-mass star-forming clumps. The relation given in Urquhart et al. (2013b) is based on deconvolved sizes. Both these empirical mass-radius relations strongly suggest that the clumps detected in these regions are capable of forming high-mass stars.

Table 3.5
Physical properties derived from the ten best fitting SED models of Robitaille et al. (2007) for the eight detected clumps. The values in parenthesis are for the best fit models.

Clump No.	M_* ($M_\odot$)	$\dot{M}_{\rm env}$ (10^{-3} $M_\odot$ yr^{-1})	$M_{\rm env}$ ($M_\odot$)	Luminosity (10^3 $L_\odot$)
		S10		
1	12 – 22 (19.7)	5 – 9 (9.2)	2000 – 5000 (2200)	6 – 15 (12.3)
2	9 – 14 (10.8)	2 – 7 (5.0)	400 – 2000 (613)	2 – 6 (4.5)
3	11 – 22 (11.7)	2 – 9 (2.3)	1000 – 2000 (1450)	10 – 31 (15.1)
4	8 – 12 (11.8)	1 – 5 (3.3)	100 – 700 (333)	2 – 9 (4.1)
5	11 – 18 (17.8)	3 – 7 (6.9)	600 – 2500 (1990)	4 – 10 (8.9)
6	12 – 18 (17.8)	4 – 7 (6.9)	2000 – 5000 (1990)	4 – 9 (8.9)
		EGO345		
7	15 – 25 (24.8)	5 – 10 (9.3)	2000 – 5000 (4410)	11 – 26 (18.3)
8	10 – 14 (11.5)	2 – 6 (5.1)	600 – 3000 (1820)	2 – 6 (4.4)

Clumps 3, 4, and 7 show the presence of 24 μm emission peaks of which Clumps 4 and 7 also include radio peaks. Clump 7 includes the EGO and Class I and II methanol masers. An intermediate mass YSO, IRS1, is shown to be located in Clump 4. Given these signatures of star formation, these three clumps can be considered to be active high-mass star-forming clumps. Of these, Clump 3 seems to be in the earliest evolutionary phase prior to the formation of UCH II region. The peak of the bright radio emitting region lies in Clump 8. Apart from this, rest of the clumps do not reveal any signposts of active star formation. Following the discussion in Molinari et al. (2008) and Giannetti et al. (2013), these could be regarded as either being starless or with a deeply embedded ZAMS star. All clumps in our sample have luminosities $L > 10^3 L_\odot$ and hence are likely to host ZAMS stars (Giannetti et al., 2013).

To further understand the evolutionary phase of these clumps, we follow the discussion in Molinari et al. (2008), which is based on the SED of massive YSOs. They discuss the evolutionary

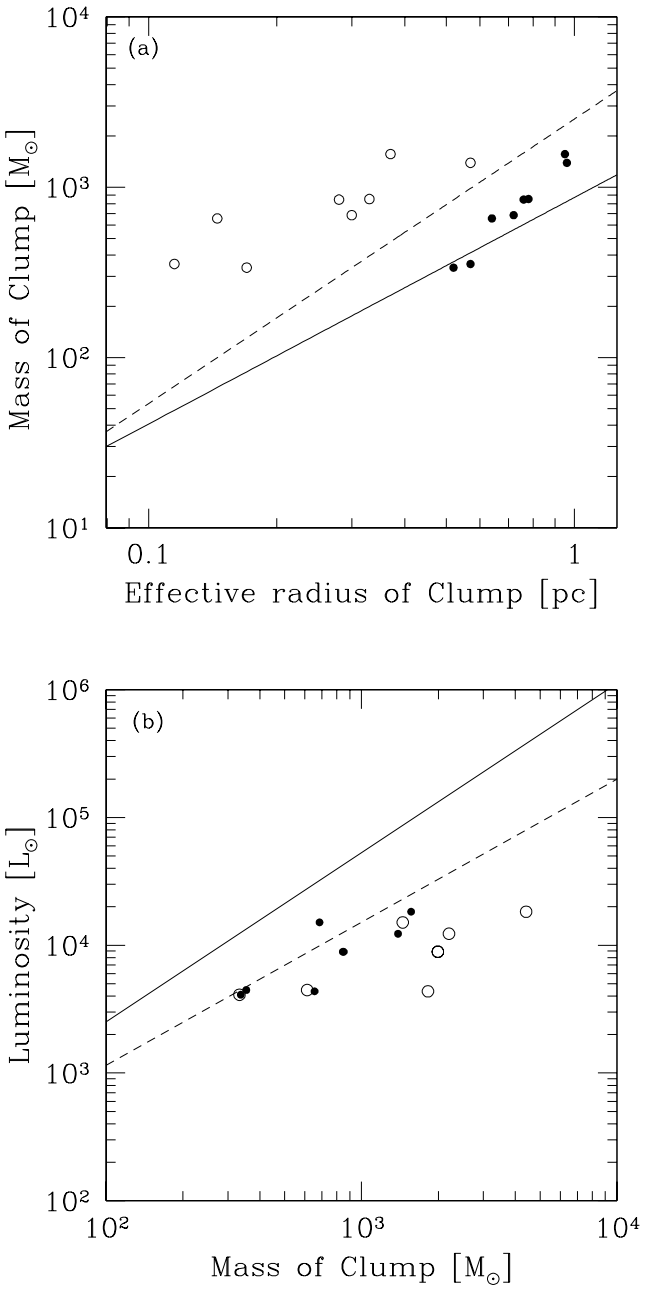

Figure 3.14: (a) Clump masses as a function of the effective radius. Filled circles denote the effective radii derived based on the physical sizes of the clumps and open circles are the deconvolved sizes (see text for details).The straight solid line shows the threshold for high-mass star formation based on the relation from Kauffmann & Pillai (2010). Also plotted as the dashed line is the slope from Urquhart et al. (2013b). (b) Clump luminosity as a function of mass. The solid and dashed lines are adopted from Fig. 9 of Molinari et al. (2008). These lines distinguish the accelerating accretion phase and the onset of envelope clearing phase. Filled circles represent the luminosity of the clumps as a function of the derived clump masses and the open circles represent the luminosity as a function of envelope masses derived from the SED modelling.

sequence of massive YSOs on a $L_{bol} - M_{env}$ plot (see their Fig. 9). Their plot also includes the regime of low-mass YSOs from Saraceno et al. (1996) and shows the behaviour of the bolometric luminosity, L_{bol} and the envelope mass, M_{env} as the YSO moves from the accelerating accretion phase to the end of it reaching the ZAMS (or close to it) and then proceeding to the envelope clean-up phase. In Figure 3.14(b), we plot the clump masses (and the corresponding envelope masses determined from the SED models) as a function of the derived luminosities. The loci demarcating the accelerating accretion and onset of envelope clearing phases, adopted from Fig. 9 of Molinari et al. (2008), are also plotted in this figure. Our plot shows the high-mass end of their figure. Two of the active clumps (4 and 7), which show radio peaks, are possibly in the early envelope clearing phase. This is consistent with the fact the ZAMS phase is marked by detectable ionized emission. Apart from clump 2, which is also close to the demarcating loci, rest of the clumps lie in the region associated with accelerating accretion phase of evolution. As discussed by these authors, the end of the ascending phase is accompanied by very high accretion rates, which is consistent with the values obtained from the SED modelling of the clumps.

Figure 3.15(a) plots the envelope mass as a function of the final mass of the star, M_* based on the best-fit SED model values. The derived envelope mass can be considered here as the initial mass of the envelope given the almost vertical evolutionary track in the $L_{bol} - M_{env}$ plot of Molinari et al. (2008), where the mass of the envelope remain the same from the initial to the end of accelerating accretion phase. As seen from the figure, the final mass of the star follows a decreasing trend with decrease in mass of the envelope. The figure also shows log-log fit from Molinari et al. (2008). The general trend and slope seen in our clumps are consistent with the fit adopted from the above paper, but shifted to the left. Based on SED model fitted values, our results also indicate a disagreement with the prediction of competitive accretion model of Bonnell et al. (2004), where the final mass of a star is shown to be unrelated to the initial mass of the clump. From the estimated mass of the stars and the envelopes, we calculate the star formation efficiency, $\epsilon = \left[\frac{M_*}{M_{\rm env}} \times 100\right]$ for the eight clumps. Figure 3.15(b) shows this as a function of the envelope mass. As is clearly evident from the plot, the efficiency decreases from 3.5 % to 0.6% with increasing envelope mass, which in this case is assumed to be the initial envelope mass. These are a factor of 2 on the lower side compared to the results obtained in

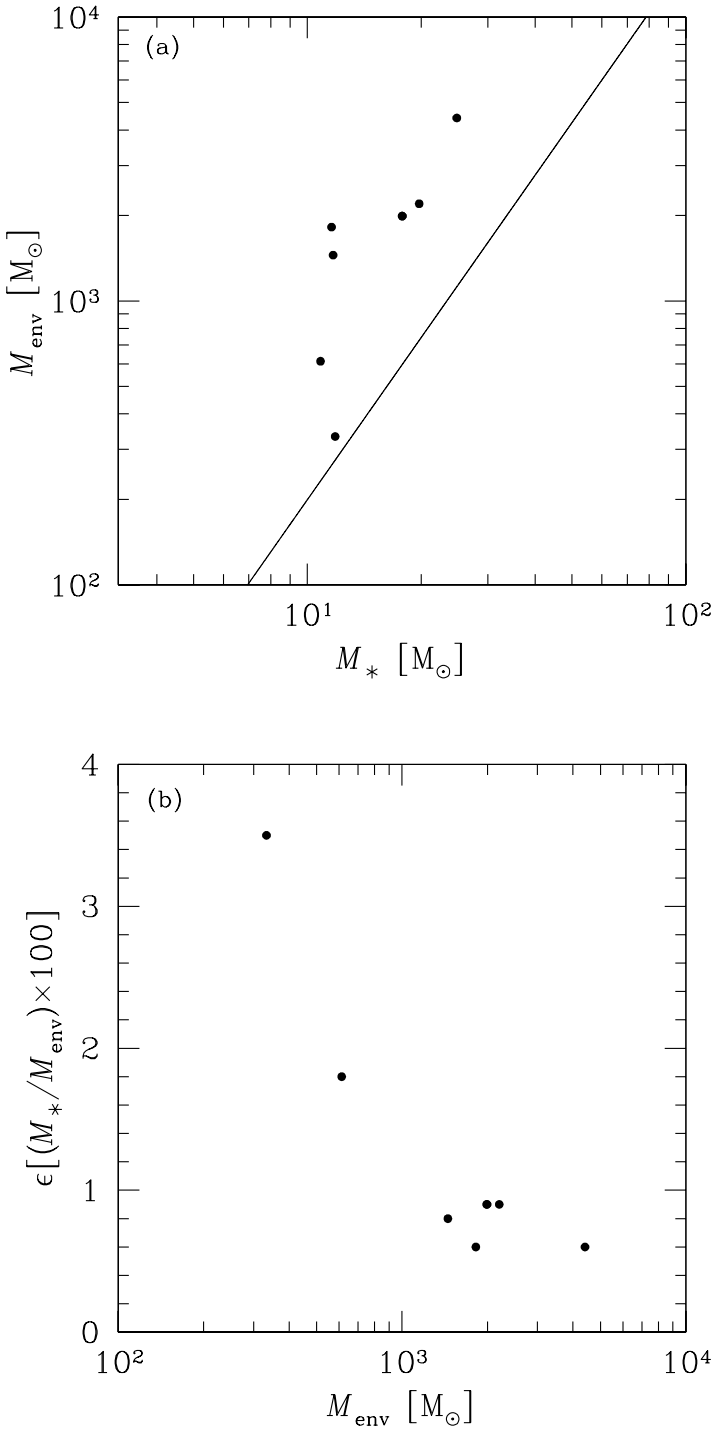

Figure 3.15: (a) The final mass of the massive star, M_* as a function of the envelope mass (assumed to be the initial mass of the envelope here). The straight line is the fit adopted from Molinari et al. (2008). (b) The star forming efficiency of the clumps as a function of the envelope mass.

Molinari et al. (2008) and the average star-forming efficiency across the Galaxy as discussed in Williams & McKee (1997). As discussed in Molinari et al. (2008), the estimated values of the star-forming efficiency should be taken as a lower limit considering the fact that massive YSOs form in clusters alongwith low- and intermediate-mass stars. The larger the clump mass, the more populous would be the cluster and hence relatively less mass goes to the most massive member. Hence, using the mass of the most massive member understates the star-forming efficiencies.

3.2.5 Possible bow-wave in S10?

Detailed study on the formation and nature of bubbles have been in focus since the first published catalogs of Churchwell et al. (2006, 2007) based on the *Spitzer* - GLIMPSE and MIPSGAL survey images. The observed bright-rimmed morphology in the MIR is a combination of UV radiation, excited polycyclic aromatic hydrocarbons (PAHs), emission in the IRAC bands, and the thermal emission from hot dust surrounding the newly formed star. Given the prominent MIR morphology, these are more commonly known as IR bubbles. The general bubble structure is a photodissociation region (PDR) visible at 5.8 and 8 μm and an evacuated cavity within this (Churchwell et al., 2006, 2007; Watson et al., 2008, 2009; Anderson et al., 2010; Deharveng et al., 2010; Zavagno et al., 2010; Kendrew et al., 2012). More recently, another catalog of IR bubbles was published by Simpson et al. (2012) - The Milky Way Project.

As mentioned in the Introduction, several feedback mechanisms are believed to be responsible for the formation of the bubbles. Even though the relevance of each depends on the nature of the ionizing star, the traditional picture of wind-blown bubbles (Weaver et al., 1977) lacks observational support as outlined in Ochsendorf et al. (2014a). The non-detection of X-ray emission inside bubbles and presence of dust in the H II regions are observations which challenge the wind-blown bubble model. The view that evaporation of dense cloudlets replenishes the interior of bubbles with a new generation of dust grains could explain the presence of dust seen in the H II regions associated with the bubbles (Everett & Churchwell, 2010a). However, this mechanism fails to account for the growing evidence of arc-type structures seen at 24 μm in the interior of bubbles and the observation of incomplete shells in H II bubbles (Watson et al., 2008; Kang et al., 2009; Deharveng et al., 2010).

Ochsendorf et al. (2014a,b) have explored the formation of infrared bubbles for weak wind stars (log ($L/L_{\odot}$) $\lesssim$ 5), which invokes thermal pressure of the ionized gas instead of stellar wind. The two-dimensional hydrodynamical simulations of this model by Ochsendorf et al. (2014b) focuses on the formation of arc-type structures seen to exist close to the ionizing star in the bubble interior. Referring to Fig. 2 of Ochsendorf et al. (2014b), the newly born massive star starts of with ionizing the surrounding and forming an expanding sphere of ionized gas. The thermal pressure in the interior causes the bubble to expand, sweeping up neutral gas in a dense encompassing shell. Formation of a shock front may occur provided the expansion is supersonic. In case of a density gradient or a break in the bubble shell, the ionized gas is shown to flow towards the low-density regions and leaks out to the surrounding ISM. This releases the pressure of the overpressurized bubble. Along with the ionized gas, the dust is also dragged along but is halted in the flow direction by the radiation pressure forming a dust or bow wave, which shows up as arcs in the mid-infrared wavelengths. This model simulation finds observational validation in the arcs seen at 24 μm around σ Ori AB (Ochsendorf et al., 2014a), which is possibly the first detection of the predicted radiation driven dust wave around a weak wind star. Similar arcs detected in the interiors of bubbles RCW 120 and RCW 82 are also well explained by this model (Ochsendorf et al., 2014b).

The scenario associated with bubble S10 is rather interesting. In Figure 3.16, we show the three colour composite image of S10 using 8 μm (*Spitzer* - IRAC), 24 μm (*Spitzer* - MIPS), and 610 MHz (GMRT). As mentioned earlier, 8 μm emission is seen as a prominent outer shell and an inner arc-type feature. 24 μm emission shows enhanced distribution mostly in three localized regions. These are (1) near the eastern limb of the outer shell coincident with the position of the IRAS point source, (2) toward the centre of the bubble with the inner 8 μm arc enveloping it, and (3) beyond the periphery of the broken western part of the bubble. The 8 μm emission shows a rupture in the outer shell, which seems to be aligned (at a PA of $\sim 50^{\circ}$ north of east) with the opening direction of the inner arc-type feature as is seen clearly in the right panel of Figure 3.16. The arc-type inner structure and the ruptured outer shell morphology is also clearly seen at 5.8 μm. The ionized emission at 610 MHz displays a fan-like morphology aligned in this direction. Though less extended, the 1280 MHz map also reveals similar structure (see Figure 3.3). The radio emission displays a picture wherein a flow of ionized gas is seen

from the position of the radio peak (considered to be the position of the ionizing star) toward lower density regions and further leaking out of the rupture in the outer shell. This interesting morphology prompted us to investigate the presence of a bow-wave, but at shorter wavelengths compared to the 24 μm arcs discussed in Ochsendorf et al. (2014a,b). This is supported by the fact that the likely ionizing star responsible for S10 falls in the 'weak-wind' category with an estimated log ($L/L_{\odot}$) lying between 4.04 (B0.5) and 4.40 (B0).

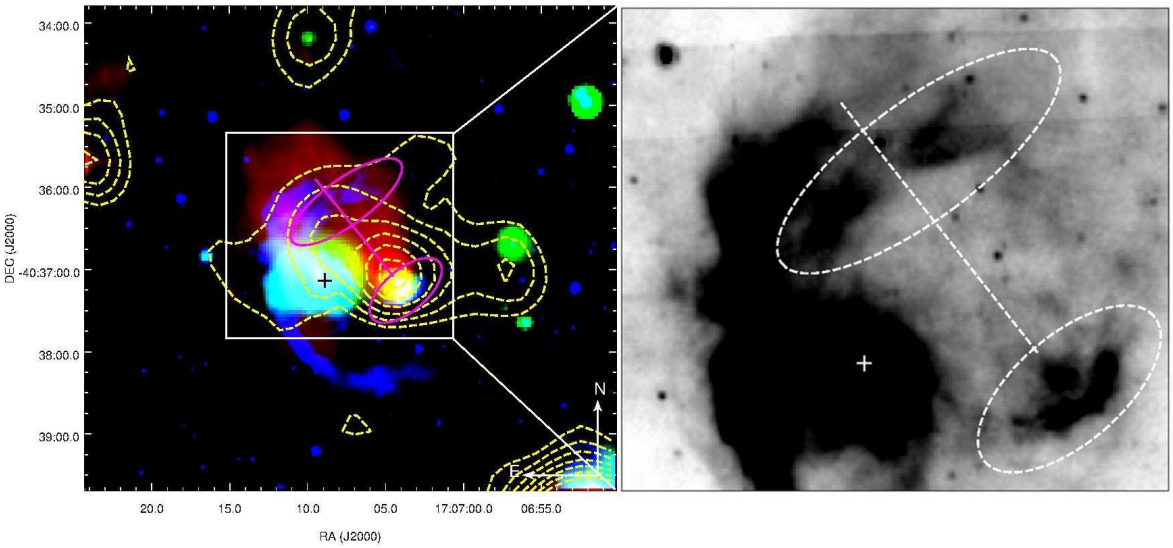

Figure 3.16: Left panel: Three-color composite image of the region associated with the bubble S10 with 8 μm Spitzer-GLIMPSE (blue), 24 μm MIPSGAL (green), and 610 MHz GMRT (red). Low resolution radio emission at 843 MHz from SUMSS is shown as contours. Right panel: Enlarged view of the outer shell rupture and the arc-type feature in the 8 μm image.

We assume the expansion of the H II region around the massive B0.5 – B0 star (located at the radio peak) to be responsible for the formation of the bubble that is seen as the outer (and larger) shell. This implies that the 8 μm band emission seen in this outer shell is largely due to PAH emission in the PDR with contribution from thermal emission from dust as well (Watson et al., 2008; Pomarès et al., 2009). It is well known that intense UV radiation close to the ionizing star destroys the PAH molecules (Watson et al., 2008). Hence, the 8 μm inner arc-type feature close to the possible ionizing star is likely to be due to thermal emission from dust alone. As seen in the figure, a bright 24 μm blob overlaps the radio emission towards the centre of the bubble. 24 μm emission arises mostly near the hot star when the dust is heated to $\sim$ 100 K. The 8 μm arc-type emission is also seen to be coupled to the ionized gas. As discussed in Ochsendorf et al.

(2014b), the gas and dust coupling depends on the efficiency of momentum transfer between gas and dust, which would result in either a dust-wave (gas and dust decoupled) or a bow-wave (gas and dust spatially correlated). The gas and dust couple well in relatively slower flow of ionized gas. The bow-wave is similar in appearance to the stellar-wind bow-shock (van Buren et al., 1990). However, in case of the bow-wave, the dust grains are stalled at a distance (r_{min}) exceeding the stand-off distance (r_s) of the bow-shock in the flow direction (Ochsendorf et al., 2014a).

The stand-off distance, r_s, is determined using the following expressions based on Mac Low et al. (1991), which equates the momentum flux of the stellar wind with the ram pressure of the star moving through the ISM.

$$r_s = 1.78 \times 10^3 \sqrt{\frac{\dot{M} v_w}{\mu_{\rm H}\, n_{\rm H}\, v^2_{\star-{\rm ISM}}}}\ {\rm pc} \tag{3.5}$$

$$\dot{m} = 2.0 \times 10^{-7}\, (L/L_\odot)^{1.25} \tag{3.6}$$

$$\log v'_w = -38.2 + 16.23 \log T_{\rm eff} - 1.70\, (\log T_{\rm eff})^2 \tag{3.7}$$

where, $\dot{M}(= \dot{m} \times 10^{-6} {\rm M}_\odot\, {\rm yr}^{-1}$) is the mass-loss rate from the star and $v_w(= v'_w \times 10^3\, {\rm km\, s^{-1}})$ is the terminal velocity of the stellar wind, $\mu_{\rm H}$ is the mean mass per hydrogen nucleus, $n_{\rm H}$ is the hydrogen gas density in ${\rm cm^{-3}}$, $v_{\star-{\rm ISM}}$ is the velocity of star with respect to the ISM in ${\rm km\, s^{-1}}$, L is the stellar luminosity, $L_\odot$ is the solar luminosity, and $T_{\rm eff}$ is the effective temperature of star, respectively. The hydrogen gas density $n_{\rm H}$ is determined from the column density maps obtained using the *Herschel* images (see Section 3.2.4). Assuming uniform density in a spherical region within $\sim 15''$ of the peak of radio emission (position of the ionizing source), we estimate $n_{\rm H}$ to be $1.6 \times 10^4\, {\rm cm^{-3}}$. This is of the same order obtained for the clumps by Beltrán et al. (2006a). Taking $\mu_{\rm H} = 1.4$ and assuming a typical velocity, $v_{\star-ISM}$ of 10 ${\rm km\, s^{-1}}$, we get a stand-off distance between $(0.8 - 1.5) \times 10^{-2}$ pc, which corresponds to $0.3'' - 0.5''$ at a distance of 5.7 kpc for spectral type of B0.5 - B0 estimated for the ionizing star. The values for L and $T_{\rm eff}$ are taken from Panagia (1973). From the 5.8 and 8 μm images, we estimate the arc to be at a distance

(r_{min}) of $\sim 15''$ from the radio peak, which corresponds to ~ 0.4 pc, far exceeding the stand-off distance, r_s. This is consistent with what is expected for a bow-wave to occur. In Ochsendorf et al. (2014a), a similar dust structure qualifying as a dust-wave is seen at a distance of 0.1 pc from σ Orionis AB. Further, Fig. 13 of Ochsendorf et al. (2014a) shows r_s and r_{min} as a function of the ISM density for the strong and weak wind regimes and clearly shows that the formation of dust and bow-waves are more efficient around weak-wind stars. The ratio r_{min}/r_s roughly estimated from the figure for the $n_{\rm H}$ value of S10 (1.6×10^4 cm^{-3}) is around 45. This is fairly consistent with the range $\sim 25 - 50$ obtained in our case.

Driven by the radio and MIR morphology and based on the above calculations, we propose that the inner arc-type structure seen in the mid-infrared bands at 5.8 and 8 μm surrounding the weak-wind ionizing star is a radiation-pressure driven dust structure: a bow-wave. The radiation pressure of the ionizing star of S10 stops the dust that is being dragged along the flow of the ionized gas at a distance that exceeds the stand-off distance. This inference is further supported by the radio maps at 610, 1280, and 843 MHz, which associates the ionized emission with the bubble that is traced by the outer shell. In addition, the orientation of the inner arc and the rupture on the outer shell and the proximity of the inner arc to the ionizing star mostly excludes the possibility of the inner arc being part of a different bubble. However, our simplistic arguments in favour of the bow-wave fail to convincingly explain the following aspects. (1) The bow-wave is not revealed in the 24 μm emission, which appears almost spherical in our case. (2) An incomplete or broken morphology is seen toward the western part of the bubble. If we assume the bubble formation to proceed as proposed by Ochsendorf et al. (2014a,b), then the western limb also needs to be blown out by the flow of ionized gas in that direction. Hence, one would expect the ionized gas morphology to be consistent with the above. Our results do not clearly show this. However, it should be noted that the lowest 1280 MHz contour (see Fig. 3.3) shows a small protrusion and the low resolution 843 MHz radio emission shows an extension in the direction of the broken western part of the bubble. (3) It is not clear why the likely bow-wave is seen only towards the narrower rupture and no such feature is in the eastern side facing the larger western opening. However, it is possible that the direction of the flow of ionized gas and hence the dust drag is dictated by the local density gradient close to the ionizing source. The aforementioned discrepancies suggest that a detailed study of the dust grain characteristics

and its wavelength dependence is necessary before we can address conclusively the possibility of occurrence of a bow-wave at shorter MIR wavelengths.

3.3 Summary

In this chapter, we have done a multiwavelength study towards southern infrared bubble S10. We probed two regions, S10 and EGO345 and arrive at the following conclusions.

1. The radio maps at 610 and 1280 MHz show the presence of ionized emission in the interior of the bubble with the emission being more extended at 610 MHz. A steep density gradient is also evident from the 610 MHz emission, which increases towards the likely centre of the bubble. Assuming optically thin, free-free emission from a single ionizing star, the spectral type of it is determined to be B0.5 – B0. The region associated with EGO345 also shows the presence of ionized emission at both the above radio frequencies. The morphology is compact and nearly spherical at 610 MHz compared to a relatively clumpier and extended one at 1280 MHz. The spectral type of the ionizing source responsible for this emission is estimated to be B0 – O9.5.

2. An intermediate-mass YSO of Class I/II, IRS1, with estimated mass of 6.2 $M_{\odot}$ lies $\sim$ 7″ to the west of the radio peak of S10. It is unlikely that this is the NIR counterpart of the ionizing star. The massive star responsible for the ionized region could likely be a deeply embedded source.

3. Dust temperature and column density maps are generated using SED modelling of the thermal dust emission from *Herschel* FIR data. The distribution of ionized gas traced by the radio emission is found to be consistent with location of warmer dust. The column density map reveals the presence of several high density clumps and filaments. The map further shows a filamentary structure extending from the north-east to the south-west connecting the two complexes. Further studies are required to explore the connection between this filament and the regions of high-mass star formation in S10 and EGO345.

4. Using the 250 μm image and the 2D variation of the *clumpfind* algorithm, eight clumps are detected in both the regions. The masses of clumps as derived from the column density maps range between $\sim$ 337 – 1564 $M_{\odot}$. The mass and effective radii of the clumps place

them in the high-mass star-forming clumps regime. Clumps 3, 4, and 7 show signatures of active star formation with Clumps 4 and 7 coincident with the radio peaks of S10 and EGO345, respectively.

5. SED modelling for sources towards these clumps show that they harbour high luminosity, high envelope accretion rate, massive YSOs. Based on the fitted values of mass of star and envelope, these clumps are seen to lie in the accelerating accretion phase of massive YSOs.

6. The MIR images show the presence of an arc-like feature near the likely centre of the bubble aligned with a rupture seen in the outer shell of the bubble. The arc encompasses the radio emission on the south-west side. The ionized emission at both the radio frequencies is consistent with the picture of a flow of ionized gas towards the outer shell originating from the centre of the bubble. The above scenario indicates at a possible detection of a bow-wave at the MIR wavelengths. This is supported by the stand-off distance which is estimated to be much smaller than the distance of the arc from the radio peak as is the case with bow-waves.

Chapter 4

Infrared dust bubble CS51 and its interaction with the surrounding interstellar medium

4.1 Introduction

In this chapter, we focus on the southern IR bubble, CS51, which is centered at α_{2000} = $17^{h}31^{m}14.90^{s}$, δ_{2000}=−33°52′55.00″ and displays a closed ring morphology with an effective radius of 2.1′ (Churchwell et al., 2007; Simpson et al., 2012). A bright IRAS source, IRAS 17279−3350, with bolometric luminosity of 1.6×10^{5} $L_{\odot}$ (Beltrán et al., 2006a) is found to be associated with the bubble. Several kinematic distance estimates to this source are found in the literature. The near and far distance estimates vary between 5.1 – 6.5 kpc and 11.7 – 13.4 kpc, respectively (Caswell & Haynes, 1987; Peeters et al., 2002; Beltrán et al., 2006a; Churchwell et al., 2007; Sánchez-Monge et al., 2013a; Urquhart et al., 2013a). In this work, we have adopted the near kinematic distance of 5.3 kpc from Churchwell et al. (2007). The justification for adopting the near kinematic distance is the presence of H I self-absorption towards the CO emission peak as observed by Garwood & Dickey (1989) (see Fig. 1 of their paper for source G354.188−0.073 which is associated with the bubble). This feature resolves the kinematic distance ambiguity and places objects at the near distance (Kolpak et al., 2003; Roman-Duval et al., 2009).

The region associated with the bubble has been probed in radio bands by a few authors. Radio continuum observations at 4.8 and 8.6 GHz by Martín-Hernández et al. (2003b) reveal the presence of three components (named A, B, and C), with A being associated with IRAS point source. These components are also studied at 5-GHz (Becker et al., 1994) and at 1.4 GHz (Zoonematkermani et al., 1990). From the 1.2-mm observation, using the SEST 15-m telescope, Beltrán et al. (2006a) identified two massive dust clumps of masses 665 and 764 $M_{\odot}$. The peak positions of these clumps correlate with that of the components A and C, respectively. Non-detection of H_2O, OH, and CH_3OH masers towards IRAS 17279−3350 was reported in Chan

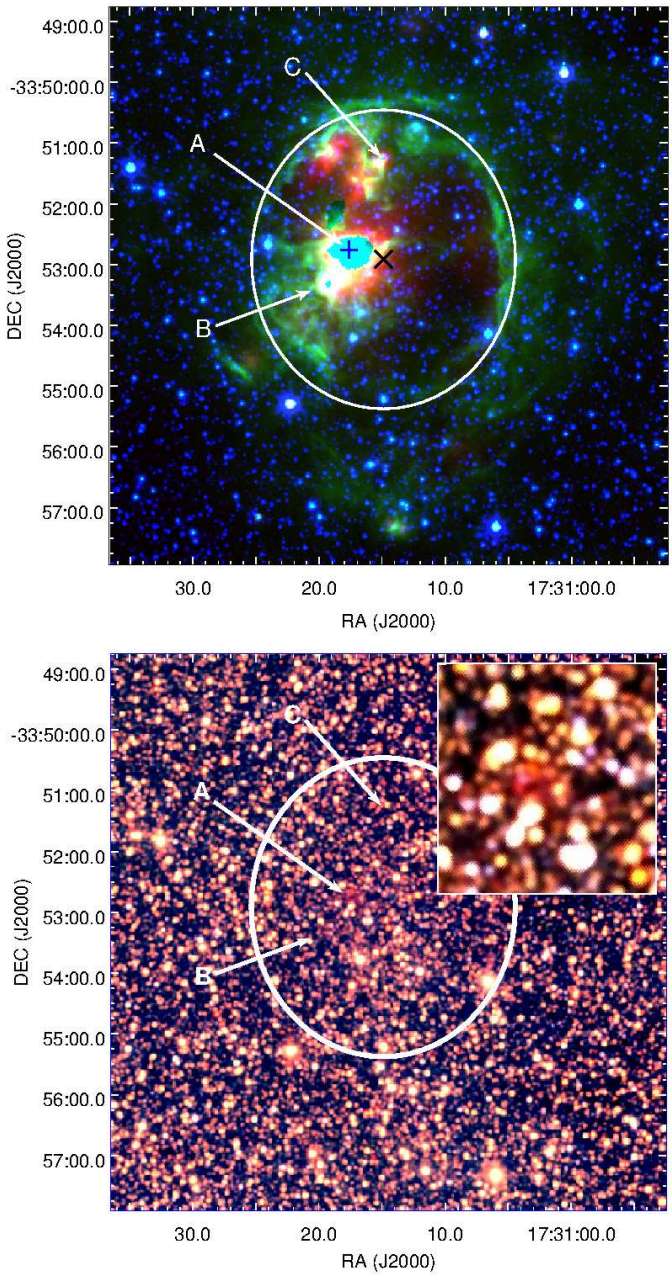

Figure 4.1: IR colour-composite images of the region towards CS51. Top: The IRAC-MIPSGAL MIR colour-composite image with 24 μm (red), 8 μm (green), and 4.5 μm (blue). The cross mark ($\times$) shows the position of the bubble center (Churchwell et al., 2007; Simpson et al., 2012). The position of IRAS 17279−3350 associated with the bubble is shown as a '+' symbol in blue. The 24-μm emission is saturated at this location. The locations of the three identified components are also highlighted with arrows, where the arrow heads are the positions of the components (Martín-Hernández et al., 2003b). The ellipse shows the extent of the bubble as described Churchwell et al. (2007). Bottom: 2MASS NIR colour-composite image with K_s band (red), H band (green), and J band (blue). The inset shows the faint nebulosity seen towards A.

et al. (1996), and references therein. However, in a later survey, the 6.7-GHz methanol maser was detected towards component C (Caswell et al., 2010).

Figure 4.1 shows the MIR and NIR view of the region associated with CS51. The displayed morphology in the MIR is similar to those observed in other bubbles (Watson et al., 2008; Ji et al., 2012; Sidorin et al., 2014; Liu et al., 2016). 24 μm emission sampling the hot dust is enclosed within the bright-rimmed 8 μm emission which shows a broken morphology towards the south. The 8 μm emission is seen to be extended in the form of an envelope beyond the identified bubble boundary. However, the NIR colour-composite image does not reveal any bubble signature and the region is seen to be densely populated. A faint, compact K_s-band nebulosity is seen towards IRAS 17279−3350 (see inset).

In presenting our study on the GLIMPSE bubble CS51, we have organized this chapter in the following way. In Section 4.2, we discuss the results obtained using various datasets. Section 4.3 focuses on the feedback of the high-mass star responsible for the formation of CS51 and its impact on the surrounding ISM and in Section 4.4, we summarize our results.

4.2 Results and Discussion

4.2.1 Ionized emission

In order to sample the ionized emission associated with our region of interest, low frequency radio observations at 610 and 1300 MHz were carried out with the GMRT on 8 and 14 August 2014. Table 4.1 provides the details regarding the radio continuum observations. Data reduction is done using `AIPS`, following the standard procedures explained in Section 2.1.2 of Chapter 2. As discussed in Section 2.1.2 of Chapter 2, we have estimated the scaling factor to be 2.26 and 1.27 at 610 and 1300 MHz, respectively. Using these values the final radio maps have been generated.

Radio emission, mapped at 610 and 1300 MHz, probing the ionized gas associated with CS51 is shown in Figure 4.2. Emission at both frequencies display complex morphology. Apart from an elongated cavity (a void in emission) seen towards the south-west, the bubble interior is filled with diffuse emission. The cavity is much more pronounced in the 1300 MHz map. This gives the radio emission a broken shell-like morphology. Faint, diffuse emission extends beyond the

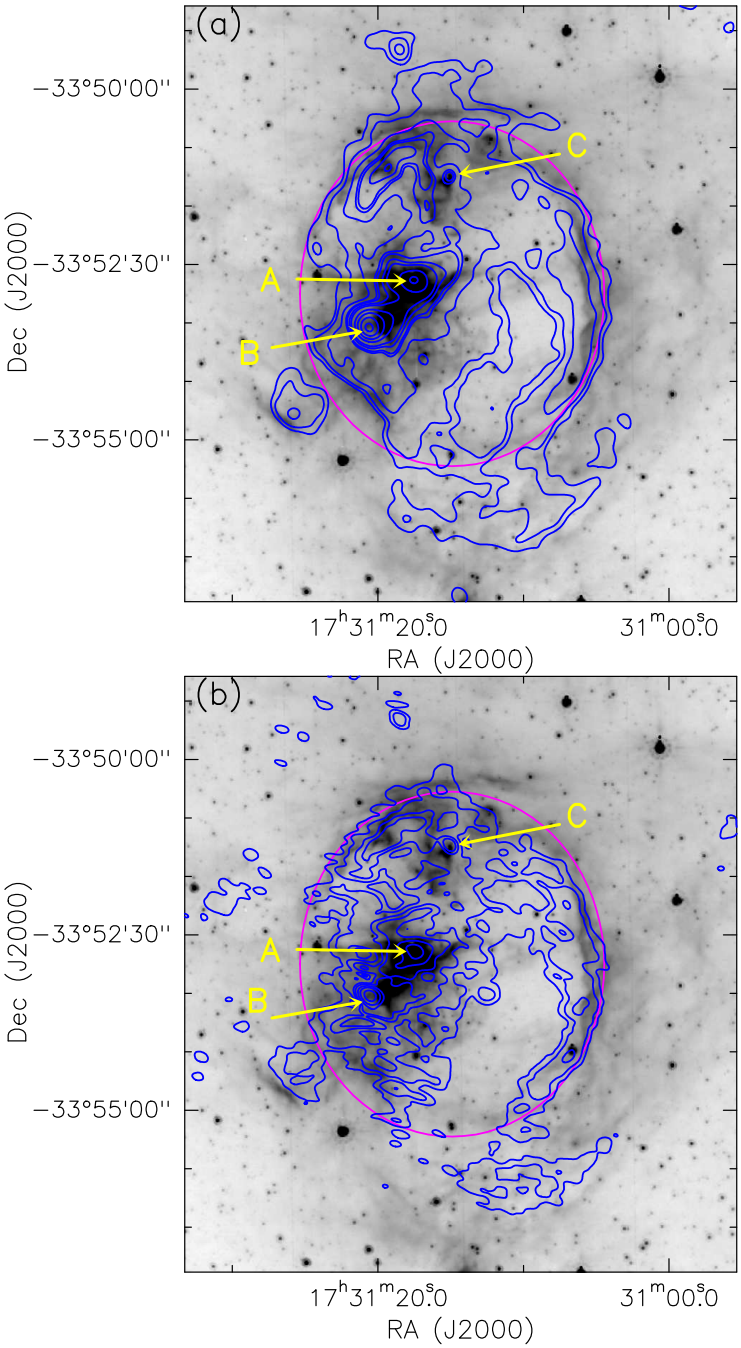

Figure 4.2: Ionized emission associated with the bubble CS51. Top: Radio continuum emission at 610 MHz associated with CS51 shown as contours overlaid on the 8 μm IRAC image. Bottom: Same as the left figure for the 1300 MHz emission. In both the figures, the contour levels are 0.3, 1.0, 2.5, 5, 12, 25, 40, 60, and 90% of the peak values. The peak fluxes at 610 and 1300 MHz are 0.34 and 0.38 Jy/beam, respectively. The positions of the identified compact components A, B, and C (see the text) are marked. The magenta ellipse shows the extent of the bubble as described in Churchwell et al. (2007).

Table 4.1
Details of the radio interferometric continuum observations towards CS51.

Details	610 MHz	1300 MHz
Date of Obs.	08 August 2014	14 August 2014
Flux Calibrators	3C286,3C48	3C286,3C48
Phase Calibrators	1714−252	1714−252
Integration time	∼ 5 hr	∼ 5 hr
Synth. beam	11.5″×9.9″	9.9″×6.5″
Position angle. (deg)	29.8	64.7
rms noise (mJy/beam)	0.5	0.3

identified bubble rim especially towards the south. The maps also reveal three compact regions of enhanced emission. Out of these, one is closer to the likely centre of the bubble, the second (and brightest of them) is more towards the south-east periphery, and the third one is located in the north-west rim of the bubble. The peak positions of these components at 610 and 1300 MHz coincide within ∼ 4″.

The overall structure described above is consistent with the 4.8 and 8.6 GHz maps obtained using the Australian Telescope Compact Array (ATCA) and presented in Martín-Hernández et al. (2003b). Their 4.8 GHz map shows patchy, diffuse emission extending in the north-south direction. Spatial correlation with the MIR images clearly shows that most of this emission lies within the confines of the bubble. As mentioned in the introduction, Martín-Hernández et al. (2003b) have also identified three distinct components namely A, B, and C with A being extended and B and C as compact. The components B and C appear detached from the main complex A. The locations of these components agree excellently (within 2.5″ from the peak positions in the 1300 MHz map) with the peaks of the detected compact components in the GMRT maps and hence we retain the same nomenclature. Their higher resolution 8.6 GHz map probes only the core of component A as most of the diffuse emission is resolved out. The flux densities and the sizes of the bubble as well as the three components determined from the GMRT and ATCA maps are listed in Table 4.2. To estimate the flux and size of the components, we use the following procedure outlined in Nandakumar et al. (2016). We first determine the threshold above which the diffuse emission becomes significant. Starting from the peak flux density, we sequentially plot contours as a percentage of the peak flux density and go upto the level where the contribution from the diffuse emission becomes apparent. This occurs at 40,

Table 4.2

GMRT and ATCA (Martín-Hernández et al., 2003b) results. The peak coordinates, peak and integrated flux densities, and sizes of CS51 and the individual components are listed.

	Peak Coordinates		Radius	Peak flux (Jy/beam)				Integrated flux (Jy)			
	RA (J2000) (hh:mm:ss.ss)	DEC (J2000) (dd:mm:ss.ss)	(arcsec)	610 MHz	1300 MHz	4.8 GHz	8.6 GHz	610 MHz‡	1300 MHz‡	4.8 GHz	8.6 GHz
CS51 (entire bubble)	17:31:20.58	−33:53:24.39	126†	0.34	0.38	–	–	5.62±0.56	4.07±0.40	–	–
Components											
A	17:31:17.53	−33:52:43.39	7.3*	0.15	0.13	0.02	0.01	0.35±0.03	0.45±0.04	–	0.52
B	17:31:20.58	−33:53:24.39	4.8*	0.34	0.38	0.09	0.05	0.96±0.09	0.51±0.05	0.10	0.06
C	17:31:15.04	−33:51:14.40	4.1*	0.02	0.03	0.08	0.05	0.03±0.003	0.04±0.004	0.12	0.11

† Effective radius from Churchwell et al. (2007), * Estimated from 2D *clumpfind* algorithm output, ‡ Error in integrated flux has been calculated following the equation from Sánchez-Monge et al. (2013b) $[(2\sigma(\theta_{\rm source}/\theta_{\rm beam})^{1/2})^2 + (2\sigma_{\rm flux-scale})^2]^{1/2}$, where σ is the *rms* noise level of the map, $\theta_{\rm source}$ and $\theta_{\rm beam}$ are the size of the source and the beam, respectively, and $\sigma_{\rm flux-scale}$ is the error in the flux scale, which takes into account the uncertainty on the calibration applied to the integrated flux of the source. For GMRT maps, uncertainty in the flux calibration is taken to be 5% (Lal & Rao, 2007).

20, and 50% of the peak flux density for the components A, B, and C, respectively. Next, this threshold emission level is given as input in the 2D *clumpfind* code of Williams et al. (1994) to determine the sizes and integrated flux densities of the components which are considered as individual clumps in this algorithm. The size is taken as the geometric mean of the full width half maximum ($FWHM$) for x axis, $FWHM_x$ and for y axis, $FWHM_y$. It should be noted here that completely decoupling the contribution of diffuse emission is difficult. Except for a larger (factor of $\sim$ 3) peak flux density for component A, our estimated values of peak and integrated flux densities of the three components at 1300 MHz are consistent with that obtained by Zoonematkermani et al. (1990) at 1400 MHz.

We derive various physical parameters associated with the ionized emission of the bubble. Assuming the radio emission at 1300 MHz to be optically thin and emanating from a homogeneous, isothermal medium, we derive the Lyman continuum flux (N_{lyc}) required to maintain ionization in the nebula, the number density of electrons (n_e), and the emission measure (EM) using the following expressions (Schmiedeke et al., 2016)

$$\left(\frac{N_{Lyc}}{sec^{-1}}\right) = 4.771 \times 10^{42} \left(\frac{S_\nu}{Jy}\right)\left(\frac{T_e}{K}\right)^{-0.45} \left(\frac{\nu}{GHz}\right)^{0.1} \left(\frac{D}{pc}\right)^2 \tag{4.1}$$

$$\left(\frac{n_e}{cm^{-3}}\right) = 2.576 \times 10^6 \left(\frac{S_\nu}{Jy}\right)^{0.5} \left(\frac{T_e}{K}\right)^{0.175} \left(\frac{\nu}{GHz}\right)^{0.05} \left(\frac{\theta_{source}}{arcsec}\right)^{-1.5} \left(\frac{D}{pc}\right)^{-0.5} \tag{4.2}$$

$$\left(\frac{EM}{pc\ cm^{-6}}\right) = 3.217 \times 10^7 \left(\frac{S_\nu}{Jy}\right)\left(\frac{T_e}{K}\right)^{0.35} \left(\frac{\nu}{GHz}\right)^{0.1} \left(\frac{\theta_{source}}{arcsec}\right)^{-2} \tag{4.3}$$

where, N_{lyc} is the Lyman continuum photons per second, T_e is the electron temperature, ν is the frequency, S_ν is the integrated flux, D is the kinematic distance to the bubble, θ refers to the angular size of the region considered (the entire bubble or the components). We determine the electron temperature adopting the following expression (Quireza et al., 2006)

$$T_e = (5780 \pm 350) + (287 \pm 46)\, R_G \tag{4.4}$$

From the estimated Galactocentric distance (R_G) of 3.3 kpc to CS51, we determine the electron temperature to be 6700 ± 380 K. This is higher than the value of 5300 K quoted in Caswell & Haynes (1987) derived using radio recombination line measurements. These authors derived the electron temperature for the radio source, which is located at an angular distance of ∼43″ from the IRAS source. For further analysis, we use the electron temperature estimate of 6700±380 K. Table 4.3 lists the derived radio properties of the bubble as well as the three components. The table also lists results from Martín-Hernández et al. (2003b).

The estimated Lyman continuum photon flux of $1.1 \times 10^{49} s^{-1}$ indicates that atleast one O6V – O5.5V star or a cluster of less massive stars are required to produce this flux (using Table 1 of Martins et al. 2005a) and maintain ionization in the nebula associated with the bubble CS51. This estimate is with the assumption of optically thin emission and hence serves as a lower limit as the emission could be optically thick at 1300 MHz. Various studies in the literature have also shown that dust absorption of Lyman continuum photons can be very high (Inoue, 2001; Arthur et al., 2004; Paron et al., 2011). Assuming a uniform distribution and taking the derived value of electron density as a representative average value for the entire bubble, we estimate the mass of ionized gas ($M_{ion} = \frac{4}{3}\pi r_{Hii}^3 n_e m_p$, where r_{Hii} is taken to be the radius of the bubble and m_p is mass of proton) to be ∼300 $M_\odot$. However, it should be noted that some ionized gas is seen beyond the defined bubble radius and its contribution has not been taken into account. The components A, B, and C could be harbouring massive stars and thus internally

Table 4.3
Physical parameters of the bubble and the three components. The values given in parenthesis are from Martín-Hernández et al. (2003b).

	log N_{lyc} (sec^{-1})	n_e ($\times 10^3$ cm^{-3})	EM ($\times 10^6$ pc cm^{-6})	Spectral Type
CS51 (entire bubble)	49.03	0.08	0.04	O6V – O5.5V
		Components		
A	48.07 (47.88)	2.00 (1.10)	1.50 (0.6)	O9 – O8.5
B	48.12 (47.15)	3.94 (9.70)	3.89 (6.3)	O8.5 – O8
C	47.02 (47.23)	1.42 (7.60)	0.43 (4.8)	B0.5 – B0[a]

[a] spectral type obtained using Table II from Panagia (1973)

ionized. The derived Lyman continuum photon flux values suggest spectral types of O9 – O8.5, O8.5 – O8, and B0.5 – B0 for A, B, and C, respectively. Component C is more likely internally

heated as there exists a 70 μm point source (Marton et al., 2017) coinciding with the peak position. However, for components A and B we cannot rule out the possibility of these being externally ionized clumps due to density inhomogeneities. Such compact ionized objects are seen in several extended H II regions (Garay et al., 1998; Kim & Koo, 2001, 2003).

4.2.2 Spectral index maps

To probe the nature of the radio emission in the region associated with the bubble, we construct a spectral index map from the 610 and 1300 MHz data. This requires a pixel-by-pixel estimation of the spectral index, α, defined as $S_\nu \propto \nu^\alpha$, where S_ν is the flux density at the frequency ν. Since we are interested in studying the variation of the spectral index over the entire region associated with CS51, we need to sample the large-scale diffuse ionized emission. GMRT is not a scaled array between the observed frequencies implying that each frequency is sensitive to different spatial scales. Hence, to ensure that the contribution of diffuse emission is same at both frequencies, we generate a new map at 1300 MHz from visibilities in the *uv* range of 0.1 – 43 Kλ which is consistent with the *uv* coverage in the 610 MHz map. The new 1300 MHz map is regridded to the pixel size of 1″of the 610 MHz map. Both maps are then convolved to a common lower resolution of $20'' \times 20''$ to exclude any small-scale statistical fluctuation in the estimated spectral index values. The above two steps are performed in the `AIPS` environment using the tasks `LGEOM` and `CONVL`. Retaining pixels above 5σ ($\sigma \sim 1$ mJy/beam) in both maps, the spectral index map is obtained using the task `COMB`. The error map is also retrieved from the task output to get the pixel uncertainties. The spectral index map and the corresponding error map is shown in Figure 4.3. The low-resolution 610 MHz contours are overlaid on the spectral index map. The spectral index values in the map vary between -1.75 to 1.5 and the estimated errors are less than ~ 0.4. However, a careful examination of the maps suggest that in the bubble interior the range is mostly between -1.0 to 1.0 with errors less than ~ 0.1. There are few patches showing extreme negative spectral index values and those are seen towards the eastern side of the component B and also towards the circular void seen north-west of component A. The observed range indicates the simultaneous presence of thermal free-free emission and non-thermal synchrotron emission which further suggest varying physical conditions. As discussed in Rodriguez et al. (1989), when only free-free emission and absorption mechanisms are involved, the spectral index lies between -0.1 and +2. Spectral indices < -0.25 are at-

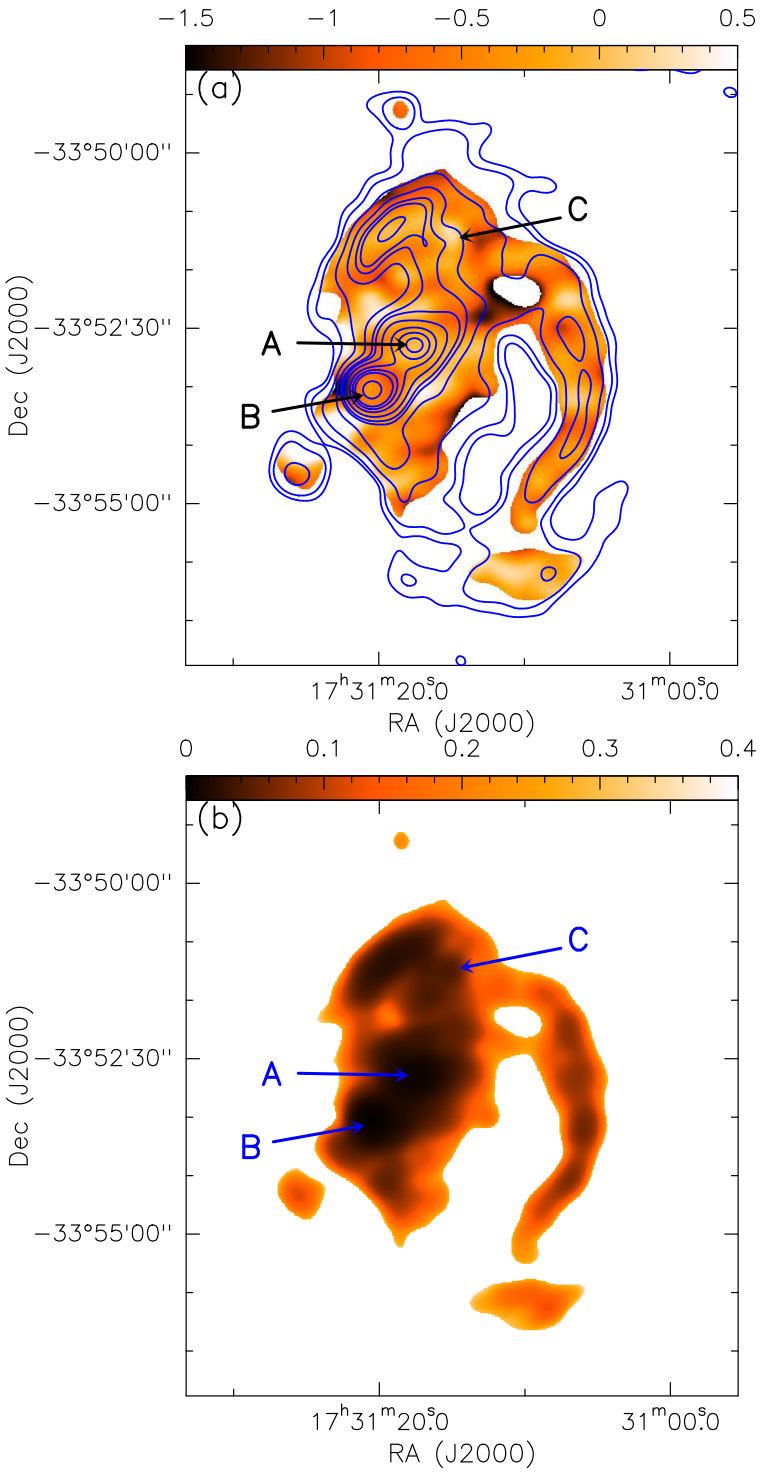

Figure 4.3: Top: Spectral index map of the region associated with CS51. The low-resolution ($20'' \times 20''$) 610 MHz contours are overlaid. The contour levels are 0.5, 1, 2.5, 5, 10, 15, 25, 35, 45 and 80% of the peak value (0.67 mJy/beam). The components A, B, and C are marked. Bottom: The corresponding error map retrieved from the `AIPS` task `COMB`.

tributed to non-thermal emission (Curiel et al., 1993; Rosero et al., 2016). Radio spectral index maps of several Galactic H II regions have shown similar co-existing thermal and non-thermal components (Nandakumar et al., 2016; Russeil et al., 2016; Veena et al., 2016). This has been attributed to shocks induced by outflows and/or winds. Such colliding wind interpretation is also cited for negative spectral indices seen towards Wolf-Rayet nebula (Benaglia et al., 2005).

In Table 4.4, we list the spectral indices obtained from the map at the peak positions of A, B, and C. The table also gives the spectral index values obtained from the integrated flux densities. The later values for components B and C are fairly consistent with that obtained by Martín-Hernández et al. (2003b). From the above estimates, we infer thermal free-free emission to be associated with components A and C, whereas the emission from component B shows spectral signature for non-thermal emission. Compact radio sources exhibiting such large negative spectral index have been discussed in Russeil et al. (2016) and Rodríguez et al. (2014) where the latter study puts forth a viable scenario of colliding winds of a massive binary system which produces a shocked region between the components where electrons can reach relativistic speeds by Fermi acceleration thus producing synchrotron emission. Similar interpretation has been discussed by Luque-Escamilla et al. (2011) for the extended non-thermal radio emission detected towards the W43 cluster. Protostars with an active magnetosphere could also give rise to such negative spectral indices (Deller et al., 2013). Detailed study of component B is required to ascertain its exact nature.

Table 4.4
Spectral indices of components A, B, and C.

Components	Spectral Index		
	GMRT 610 – 1300 MHz		ATCA 4.8 – 8.6 GHz
	From map[a]	From Int. flux[b]	From Int. flux [c]
A	−0.01±0.006	0.19±0.06	–
B	−0.33±0.004	−0.78±0.06	−0.87
C	0.19±0.040	−0.14±0.07	−0.16

[a] relates to peak positions from spectral index map; [b] obtained from the integrated flux densities of the final convolved ($20'' \times 20''$) maps; [c] from Martín-Hernández et al. (2003b).

4.2.3 Identifying the ionizing stars

A careful literature survey shows that there has been no identification of the ionizing source responsible for the H II region associated with the bubble CS51. In this section, we attempt to identify and propose the possible exciting source(s) responsible for CS51. As discussed in Churchwell et al. (2006, 2007), the association of H II regions with IR bubbles indicate that these are formed by O- and/or B-type of stars. The Lyman continuum photon flux estimated from the GMRT radio maps suggest a spectral type of O6V – O5.5.

Identification of candidate exciting star(s) has been carried out in several bubbles based on MIR and NIR photometry of sources enclosed within the bubbles (Pomarès et al., 2009; Petriella et al., 2010; Ji et al., 2012; Dewangan & Ojha, 2013; Baug et al., 2016). We have followed the method adopted in a recent paper by Ortega et al. (2016). As we expect the candidate ionizing star(s) to be located within the CS51 PDR, we consider 2MASS sources with good quality photometry located within a radius of 2.1′ of the central coordinate of CS51. Inspite of the proper motion of the exciting star(s), they are still likely to be within the PDR given that these IR bubbles are young objects. However, they need not always be located at the geometrical centre of the bubble.

In our search for O stars within the CS51 PDR, we follow the BJHK colour criteria of Comerón & Pasquali (2012). The criteria adopted by these authors is highly efficient in filtering out late-type contaminants. The B magnitudes of the retrieved sources are taken from the NOMAD1 catalog (Zacharias et al., 2004). Since the bubble CN20 studied by Ortega et al. (2016) is at a similar distance as CS51, we apply the same K_s magnitude cut of 11 to exclude out reddened early-type stars in the background of CS51. This is based on the assumption of $A_v \sim 1$ per kpc of foreground extinction. We identify 17 sources satisfying the criteria of Comerón & Pasquali (2012). These sources are marked in Figure 4.4 which shows the 8 μm image overlaid with the contours showing the 610 MHz radio emission. Except one, the sources fall in the region of the Class III population in the 2MASS CCP. The ones which have IRAC band magnitudes are also seen to populate the region occupied by Class III objects (Petriella et al., 2010). In their study of similar IR bubbles, Baug et al. (2016); Liu et al. (2016); ; Ortega et al. (2016) have discussed the likely association of the location of the ionizing star(s) and bright 24 μm emission in the

bubble interior which also correlates with peak of the free-free radio emission. Following this argument, we identify five candidates labeled 1 – 5 in Figure 4.4. Considering their associated visual extinctions from the 2MASS (H − K_s) and (J − H) CCP, we derive their absolute K magnitudes and estimate the spectral type from Martins & Plez (2006). The details of these five sources are given in Table 4.5. The location of star number 5 is towards the bubble periphery and hence it is less likely to qualify as a candidate exciting source. Similarly, star number 2 falls in the Class II YSO region in the 2MASS CCP. Thus, based on their nature and position inside the bubble, we identify source numbers 1, 3, and 4 as the most promising candidates for ionization of CS51. Optical and NIR spectroscopy of these candidate exciting sources are required to qualify the above discussion.

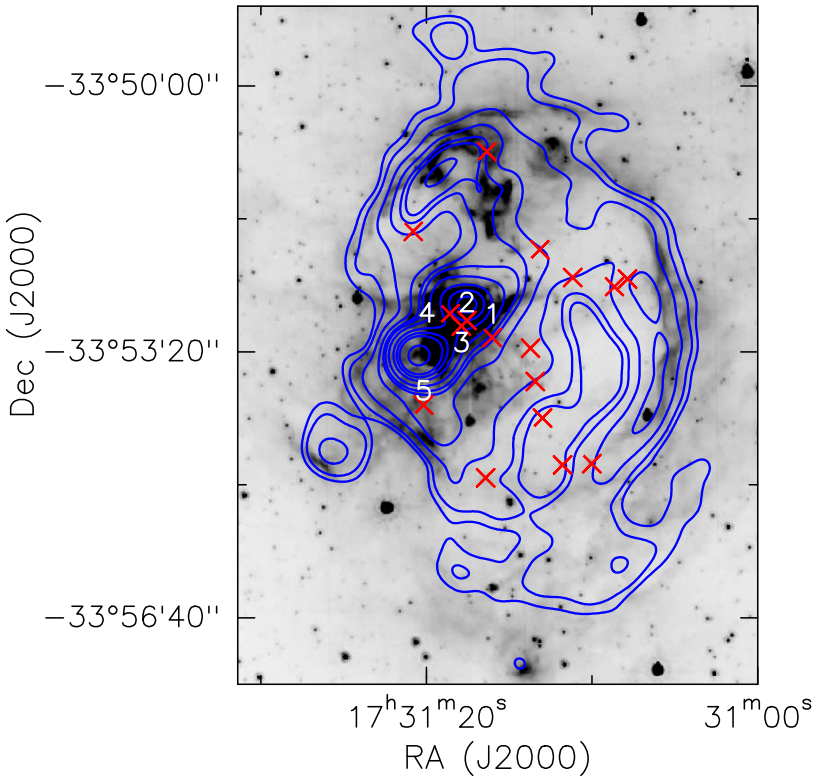

Figure 4.4: This figure displays the 8 μm image on which is shown the distribution of O- and B-type stars (red crosses) in the bubble interior which satisfy the criteria discussed in Comerón & Pasquali (2012). Low-resolution 610 MHz contours are overlaid. The contour levels are same as in Figure 4.3. The candidate ionizing stars are labelled as numbers 1 – 5. Refer to the text for further discussion.

Table 4.5
Exciting star candidates associated with CS51.

#	RA (J2000) (hh:mm:ss.ss)	DEC (J2000) (dd:mm:ss.ss)	B (mag)	J (mag)	H (mag)	K (mag)	A_V	M_J (mag)	M_H (mag)	M_K (mag)	Spectral type
1	17:31:16.01	−33:53:09.27	17.51	10.19	9.09	8.72	10.19	−6.30	−6.31	−6.04	> O3V
2	17:31:17.56	−33:52:56.50	19.52	11.73	10.51	9.79	12.39	−5.38	−5.27	−5.21	> O3V
3	17:31:17.88	−33:53:00.72	16.07	12.28	10.96	10.28	12.92	−4.98	−4.92	−4.78	O4V – O3V
4	17:31:18.58	−33:52:51.46	17.91	11.91	10.93	10.60	9.22	−4.30	−4.30	−4.04	O6.5V – O6V
5	17:31:20.17	−33:53:59.88	18.61	12.13	11.13	10.75	9.53	−4.17	−4.15	−3.93	O7V – O6.5V

4.2.4 Emission from cold dust component

Figure 4.5 shows the dust emission toward the regions associated with bubble CS51 as seen in the IRAC, MIPSGAL, Hi-Gal, and ATLASGAL images. These images reveal different dust emission features of the bubble. The 3.6 and 4.5 μm bands detect mostly the bright sources, since these bands are dominated by emission from stellar photospheres. As we move to the longer wavelengths, the flux density of the arc and the associated diffuse emission increases. At 5.8 and 8.0 μm, the bubble morphology becomes clearly visible. The 24 μm emission is much more localized and bright towards the center and the north. Emission at longer wavelengths starts to be dominated by cold dust and show extended features, as is seen the in the *Herschel* and ATLASGAL wavebands.

Temperature and column density maps

We study the nature of the cold dust emission using 160 – 500 μm *Herschel* data. The procedure followed to generate column density and temperature maps is discussed in Chapter 2. Following the procedure explained in Chapter 3, we estimate the background flux, I_{bkg}, in each band from a region located at an angular distance of $\sim 20'$ from the bubble and centered at $\alpha_{2000} = 17^h32^m14.46^s$, δ_{2000}=−34°01′21.90″. I_{bkg} is estimated to be −0.82, 2.81, 1.27, and 0.45 Jy pixel^{-1} at 160, 250, 350, and 500 μm, respectively.

The generated column density and temperature maps are shown in Figure 4.6, along with the corresponding χ^2 map. We have overlaid the low resolution ($20'' \times 20''$) 610 MHz radio map on the dust temperature map to correlate the ionized and dust components. As mentioned in Chapter 2, we fix the value of $\beta = 2$ in generating these maps.

As seen in Figure 4.6, the pixel fits are good with $\chi^2 < 6$ in the map. The column density map shows a fragmented shell-like structure with low values tracing the inner region of the

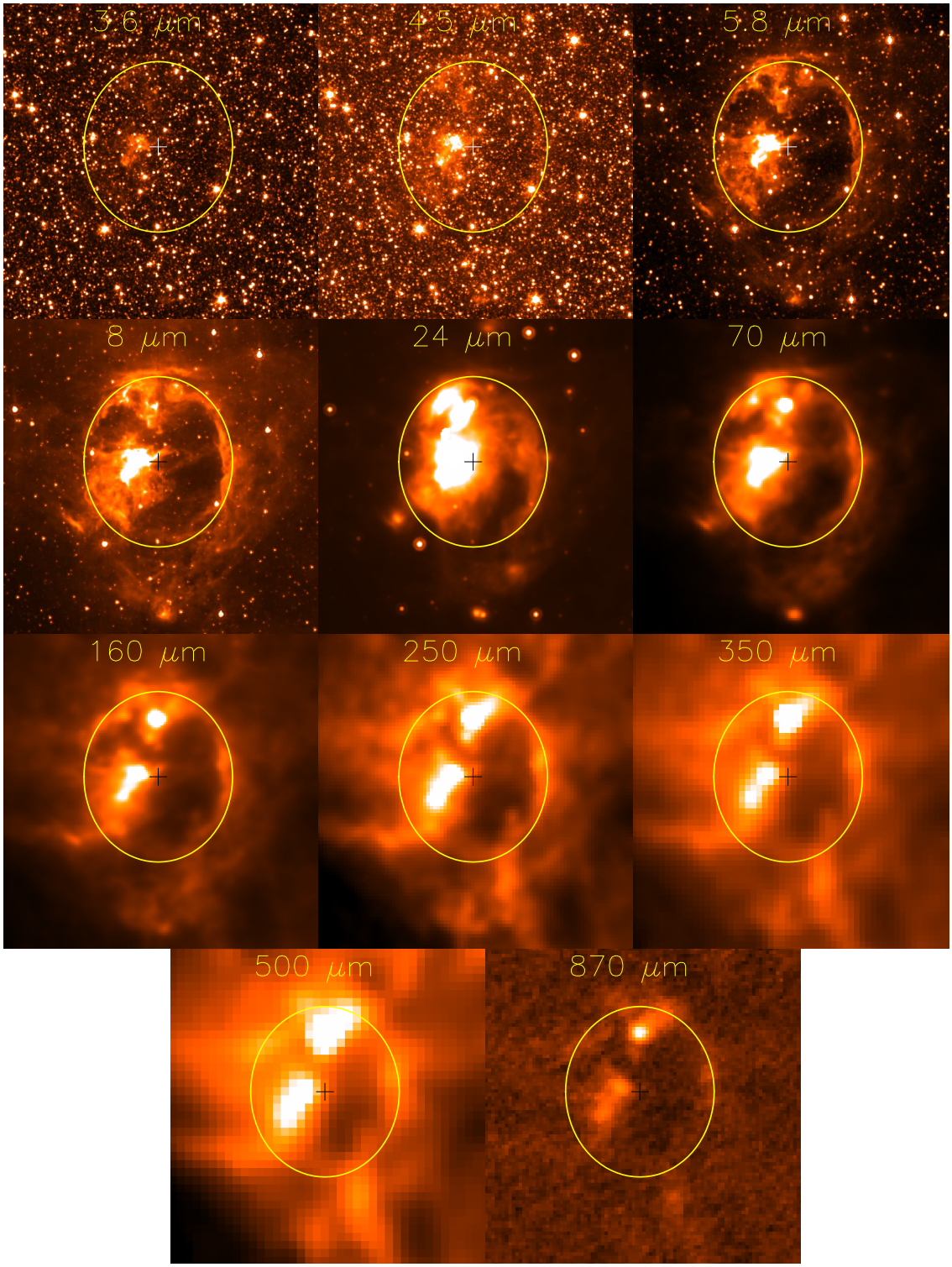

Figure 4.5: Dust emission associated with bubble CS51 is shown. Emissions at wavelengths of IRAC bands (3.6, 4.5, 5.8 and 8.0 μm), MIPSGAL (24 μm), PACS (70, 160 μm), SPIRE (250, 350, 500 μm), and ATLASGAL (870 μm) are displayed. The '+' mark shows the position of associated IRAS point source.

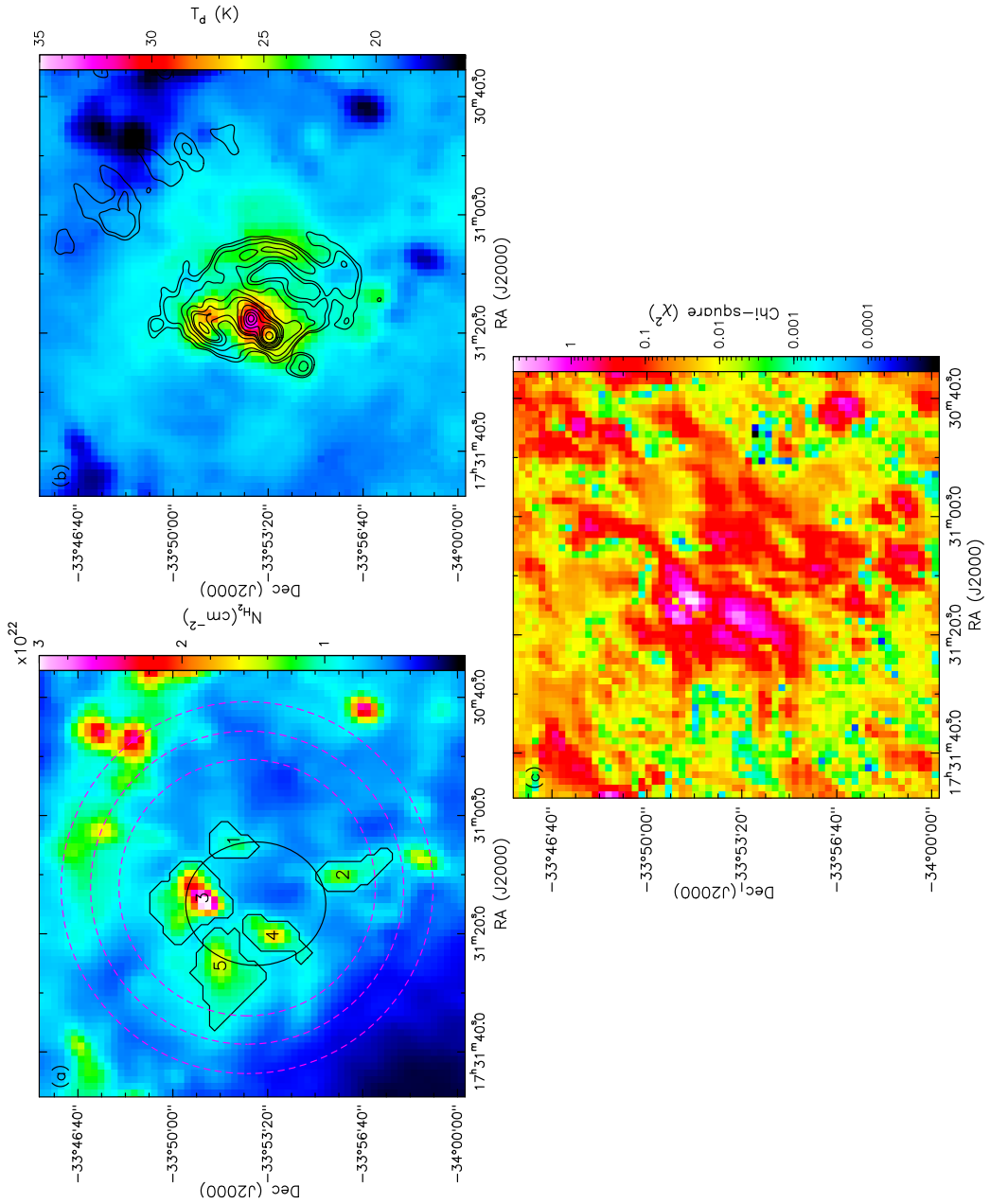

Figure 4.6: (a) Column density, (b) dust temperature, and (c) chi-square maps generated using *Herschel* FIR data are shown. In plot (a), the black ellipse shows the extent of the bubble and the five identified cold dust clumps are shown as black contours. This plot also shows three concentric circles (dashed magenta) which are used in the study of column density PDFs (see Section 4.3.2). 610 MHz radio contours are overlaid in plot (b) to correlate the dust temperature with the ionized gas distribution. The contour levels are same as in Figure 4.3.

bubble. The bubble rim is seen to contain clumpy regions of enhanced column density. One clump is located relatively close to the centre of the bubble coincident with the radio peaks. Apart from this clump, the rest fit well into a picture of fragmented swept-up molecular shell. The peak column density (3.6×10^{22}cm^{-2}) is located towards the northern part of the bubble. Several clumpy structures and high density regions are also seen on the periphery and beyond the bubble. Correlating the ionized emission with the dust temperature map, we see high dust temperature towards the three components and the entire region associated with the bubble CS51 is clearly warmer than the surrounding region.

Properties of dust clumps

As shown in Figure 4.6, five cold dust clumps associated with CS51 are detected from the column density map. Instead of using the visual inspection followed by fitting ellipses to characterize the clumps (Liu et al., 2016), we use the *astrodendro* algorithm (Rosolowsky et al., 2008; Goodman et al., 2009). The original concept of this algorithm is discussed in Houlahan & Scalo (1992). The dendrogram is composed of leaves and branches. So to create dendrograms of an image, the first step is to identify the local maxima, which is the top of the dendrogram hierarchy. Contours are generated for separation of maxima points. A local maxima can be eliminated if the host isosurface has the volume less than a certain number of pixels (N). The isosurfaces merge at certain contour levels and form a branch, which contain multiple leaves. This elimination of leaves and branches, will continue and eventually, all branches and leaves will merge at a certain minimum level, which forms the trunk of the tree structure. The minimum level or threshold level is usually set with certain multiples of the noise level. In our case, we set a threshold column density of 8.0×10^{21} cm^{-2} and detect clumps above this by specifying a minimum of 5 pixels for a potential clump.

Mass of the dust clumps is calculated using the following equation

$$M_{clump} = \mu_{H_2} m_H A_{pixel} \Sigma N(H_2) \tag{4.5}$$

where, m_H is the mass of hydrogen, A_{pixel} is the pixel area in cm^2, μ_{H_2} is the mean molecular weight and $\Sigma N(H_2)$ is the integrated column density. Assuming the clumps to be spherical, the apertures retrieved from *astrodendro* are used to estimate the physical sizes ($r = (A/\pi)^{0.5}$;

Table 4.6
Physical parameters of the clumps associated with CS51. The peak position, radius, mean dust temperature, mean column density, mass, and volume density for each clump is listed.

Clump No.	RA (2000) (hh:mm:ss.ss)	DEC (2000) (dd:mm:ss.ss)	Radius (pc)	Mean T_d (K)	Mean $N(H_2)$ ($\times 10^{21} cm^{-2}$)	$\sum N(H_2)$ ($\times 10^{23} cm^{-2}$)	Mass ($M_\odot$)	n_{H_2} ($\times 10^3 cm^{-3}$)
1	17:31:05.27	−33:52:25.35	1.0	22.7	9.4	2.3	810	2.7
2	17:31:09.68	−33:55:54.26	1.2	20.7	10.5	3.8	1340	2.5
3	17:31:15.29	−33:51:15.10	1.9	22.9	18.4	13.3	4600	2.2
4	17:31:19.75	−33:53:35.20	1.2	26.8	10.1	4.2	1460	2.9
5	17:31:24.48	−33:51:15.10	1.9	20.9	11.4	9.8	3420	1.7

(Kauffmann & Pillai, 2010)). The derived physical properties of the dust clumps are listed in Table 4.6. The volume number density is derived as, $n_{H_2} = 3\Sigma\, N(H_2)\,/4r$, r being the radius of the clump. The two clumps detected from the 1.2 mm emission by Beltrán et al. (2006a) are likely to be associated with our Clumps 3 and Clump 4. However, the masses derived in this work are larger by a factor of 2 – 7 compared to the estimates of Beltrán et al. (2006a). The possible reasons for this could be the different κ_ν and dust temperature values used by these authors and/or the large sizes of the clumps retrieved from the column density map. One also cannot exclude the effect of flux loss associated with ground based observations (Liu et al., 2017a).

4.2.5 Associated stellar population

To understand the star formation activity associated with CS51, we study the nature of the stellar population. We use *Spitzer* GLIMPSE and MIPSGAL data to identify and classify potential YSOs towards the bubble. For this, we choose a region of radius 5′ centered on the bubble. We retrieve 1060 sources with photometric data in all the IRAC bands. We also explore the catalogue of Gutermuth & Heyer (2015) to include 24 μm point sources which have 3.6 μm photometry. From the distribution of IRAC sources extracted from the catalogue, we see a dearth of point sources towards regions of bright MIR emission located in the bubble centre and periphery. Hence, to ensure a more complete sample of sources associated with the bubble we also make use of good photometric data from the 2MASS Point Source Catalog. A total of 1418 sources have good quality data in all three JHK_s bands.

The identification and classification of YSOs are carried out using the procedures detailed in Chapter 2. In this study we have followed the criteria discussed in Lada (1987), Allen et al. (2004), Chavarría et al. (2008), Guieu et al. (2010), and Rebull et al. (2011). Following the criteria of Allen et al. (2004), we have identified 21 YSOs, out of which 5 are Class I, 12 are Class II, and 4 are Class I/II. Adopting the criteria of Guieu et al. (2010), and Rebull et al. (2011), 20 YSOs are identified, out of which 9 are Class I, 8 are Class II, and 3 are flat-spectrum YSOs. Following Chavarría et al. (2008) and Lada (1987) we estimated the spectral index and identify 38 YSOs out of which 8 are Class I and 30 are Class II sources. In addition, using the JHK_s CCPs we identify 31 YSOs, out of which 2 are Class I YSOs and 29 are Class II YSOs. Figure 4.7 shows the various plots for these schemes.

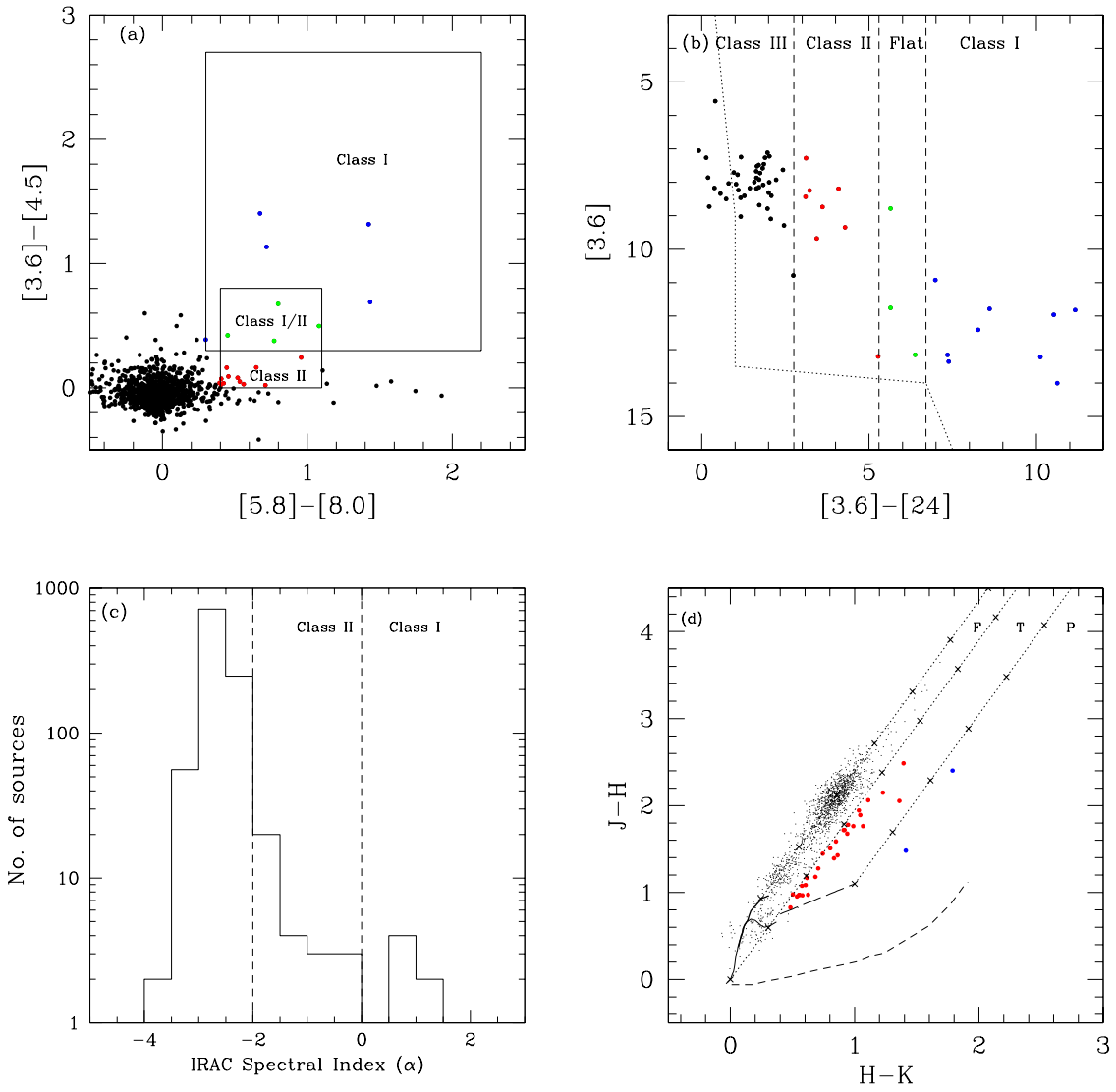

Figure 4.7: (a) IRAC CCP plot following the method of Allen et al. (2004). The boxes on the plot, adapted from Vig et al. (2007) shows the region for YSOs of different evolutionary classes. (b) [3.6] − [24] vs [3.6] CMP on which the vertical lines adopted from Guieu et al. (2010) and Rebull et al. (2011) demarcate the regions for different classes of YSOs. (c) Histogram plot of the variation of number of sources with IRAC spectral index. The regions for Class I and Class II sources labeled on the plot are adapted from Chavarría et al. (2008). (d) 2MASS J−H vs H−K CCP , in which the three separate regions are labelled as 'F', 'T', and 'P' (explained in Chapter 2). The colour coding for YSOs are as follows: Class I – blue, Class II – red, and Class I/II – green.

Compiling the YSOs identified in the above methods, we have 17, 70, and 6 Class I, Class II, and Class I/II sources, respectively, in the region of 5′ radius centered on CS51. For YSOs

identified in more than one scheme, methods (a), (b), (c), and (d) are given preference in this order to assign their class. Figure 4.8 shows the distribution of the identified YSOs on the 8 μm image and Table A.1 (given in Appendix A) lists the coordinates, NIR and MIR magnitudes and classification. The spatial distribution of YSOs do not show any particular pattern except a dearth in the bubble interior and an overdensity of Class I YSOs towards the northern periphery of the bubble. Two Class II YSOs are placed in projection towards the central clump thus hinting at a more evolved region compared to the clump towards the northern rim. Without spectroscopic confirmation, it is difficult to conclude on the physical association of the identified YSOs with CS51.

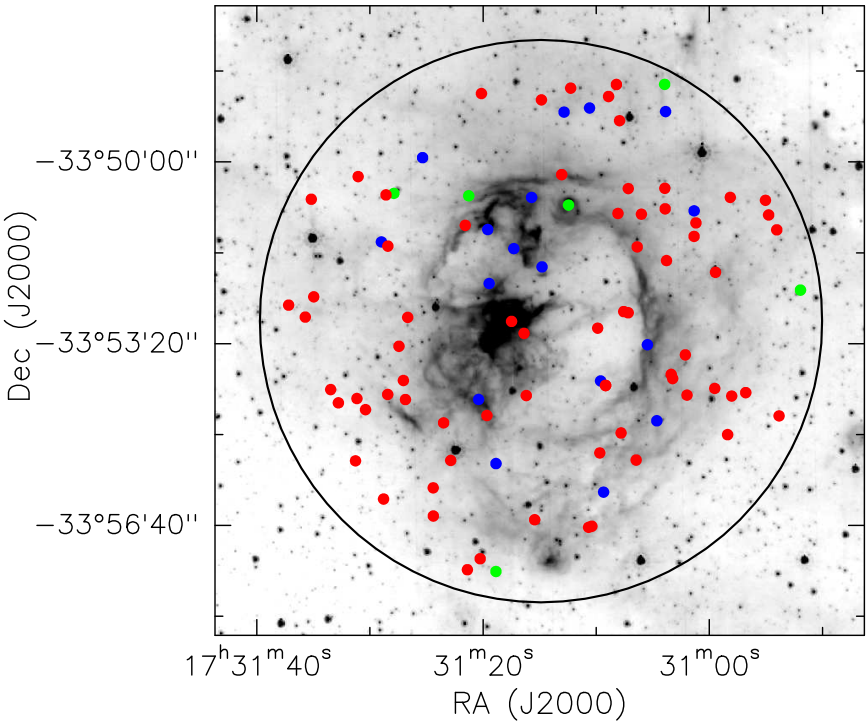

Figure 4.8: Gray scale is 8.0 μm image on which the distribution of YSOs are shown. The colour coding for YSOs are as follows: Class I – blue, Class II – red, and Class I/II – green.

4.2.6 Molecular line emission towards CS51

In order to investigate the properties of the clumps associated with the bubble, we have used molecular line data from the MALT90 and ThrUMMS survey. The available data from MALT90 survey covers two of the *Herschel* clumps (3 and 4), whereas the ThrUMMS survey covers all the clumps. Study of these molecular lines will enable us to probe the physical, chemical prop-

erties and throw light on the evolutionary states of these dense star-forming clumps. Of the 16 molecular-line transitions covered in the MALT90 survey, only five molecular species (C_2H, HCN, HCO^+, HNC, and N_2H^+) are detected towards these two clumps. The details of the transitions taken from Foster et al. (2011) and Miettinen (2014) are listed in Table 4.7. Both the papers, especially the latter, give a nice review on the environment in which these molecules exist and the physical conditions required for their formation. Out of the four molecular species probed in the ThrUMMS survey, only data for $C^{18}O$ and CN are available towards CS51. However, both molecules are not detected towards any of the five clumps.

Table 4.7
Summary of detected spectral-line transitions. E_u and n_{crit} are the excitation energy and critical density for the transitions. These are calculated adopting values from the Leiden Atomic and Molecular Database (LAMD; Schöier et al. 2005) and Cologne Database for Molecular Spectroscopy (CDMS; Müller et al. 2001, 2005), assuming a gas temperature of 20 K.

Transition	Frequency (ν) (GHz)	E_u/k_B (K)	n_{crit} (cm^{-3})	Remarks
C_2H (1 – 0) 3/2 – 1/2	87.316925	4.19	2×10^5	Tracer of photodissociation region $N_J = 1_{3/2} - 0_{1/2}$ is split into three hf components
HCN (1 – 0)	88.631847	4.25	3×10^6	tracer of high column density, optical depth. J = 1 – 0 is split into three hf components
HCO^+ (1 – 0)	89.188526	4.28	2×10^5	High column density, kinematics
HNC (1 – 0)	90.663572	4.35	3×10^5	High column density, cold gas tracer Three hf components
N_2H^+ (1 – 0)	93.173772	4.47	3×10^5	High column density, depletion resistant, optical depth. J = 1 – 0 line has 15 hf of components out which seven have a different frequency

Figure 4.9 shows the observed line-spectra at the peak positions for the two clumps from MALT90 survey. We use the hyperfine structure (`hfs`) method of CLASS90 to fit the observed spectra for C_2H, HCN, HNC, and N_2H^+ transitions and retrieve the line parameters. As described in Table 4.7, the molecule HCO^+ has no hyperfine structure thus a single Gaussian profile was used to fit the spectra. Figure 4.9 also shows the `hfs` and Gaussian (for HCO^+) fits for the detected transitions. The positions of the hyperfine components are marked in the plots. Figure 4.10 shows the spectra retrieved for $C^{18}O$ and CN for the five clumps from the ThrUMMS survey. As is clearly evident there is no detection above the noise level. Thus for

Table 4.8
Parameters of molecular transitions detected towards the two dust clumps. The LSR velocity (V_{LSR}), line width (ΔV), main-beam temperature (T_{mb}), and velocity integrated intensity ($\int T_{mb} dV$) are obtained from the `hfs` fitting method of CLASS90. The column density (N) values are estimated using RADEX and the fractional abundances (x) are derived using mean H_2 column density of 1.8×10^{22} cm^{-2} and 1.0×10^{22} cm^{-2} for Clump 3 and Clump 4, respectively (refer Section 4.2.4).

Transition	V_{LSR} (km s^{-1})	ΔV (km s^{-1})	T_{mb} (K)	$\int T_{mb} dV$ (K km s^{-1})	N ($\times 10^{14}$ cm^{-2})	x (10^{-9})
Clump 3						
C_2H	−30.10	2.61	0.27	0.33	3.59	19.90
HCN	−30.80	3.31	0.38	1.25	6.05	33.63
HCO^+	−30.54	3.36	0.75	2.69	0.52	2.89
HNC	−30.20	4.18	0.69	3.18	2.62	14.57
N_2H^+	−29.50	2.38	0.77	2.46	3.11	17.29
Clump 4						
C_2H	−32.40	1.96	0.36	0.86	2.47	23.97
HCN	−32.40	1.90	0.31	0.76	1.71	16.64
HCO^+	−32.71	4.33	0.52	2.38	0.28	2.75
HNC	−32.50	3.18	0.38	1.50	0.69	6.70
N_2H^+	−31.70	2.41	0.23	0.61	0.45	4.35

further analysis, we use the MALT90 data alone. The retrieved parameters are peak velocity (V_{LSR}), width of velocity (ΔV), main beam temperature (T_{mb}), and velocity integrated intensity ($\int T_{mb} dV$), which are listed in Table 4.8. Beam correction is applied to the antenna temperature to obtain the main beam temperature, $T_{mb} = T_A/\eta_{mb}$ (Rathborne et al., 2014) with an assumed value of $\eta_{mb} = 0.49$ (Ladd et al., 2005). As revealed in the figure, the signal-to-noise ratio of the observed spectra are less than optimal with several hyperfine components being marginally detected and few others fitting to appreciably large widths (see C_2H profile for Clump 3 and HCN profile for Clump 4). In view of this, it should be noted that the retrieved parameters would have significant uncertainties associated. The zeroth moment (velocity integrated) contours of two molecules, HNC and N_2H^+, are shown in Figure 4.11 overlaid on the *Spitzer* 8 μm image. The maps of the other molecules have poor signal-to-noise ratio and hence are not presented. Both molecules show extended emission towards Clump 3 as compared to Clump 4. The plots also show the 610 MHz contours that enable us to correlate the emission from molecular and ionized gas.

We have used RADEX (van der Tak et al., 2007), a one-dimensional non-LTE radiative transfer

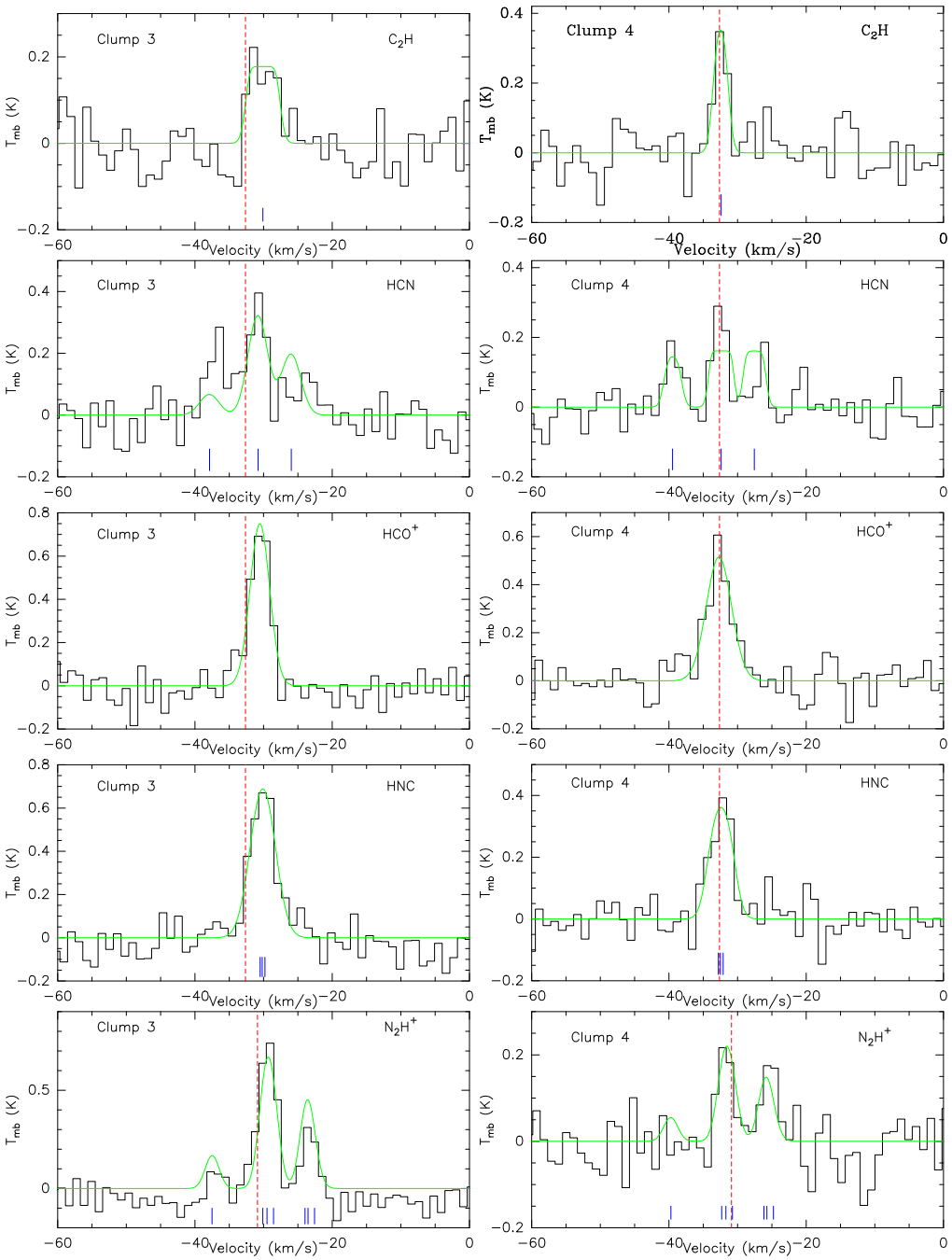

Figure 4.9: Spectra toward Clumps 3 and Clump 4 associated with CS51. The green curves show the `hfs` and Gaussian (for HCO^+) fits to the spectra. The dashed, vertical red line marks the average peak velocity (V_{LSR}) of all detected molecules of Clump 4 that is used as the systematic velocity. The hyperfine components of the respective molecules are indicated with blue lines.

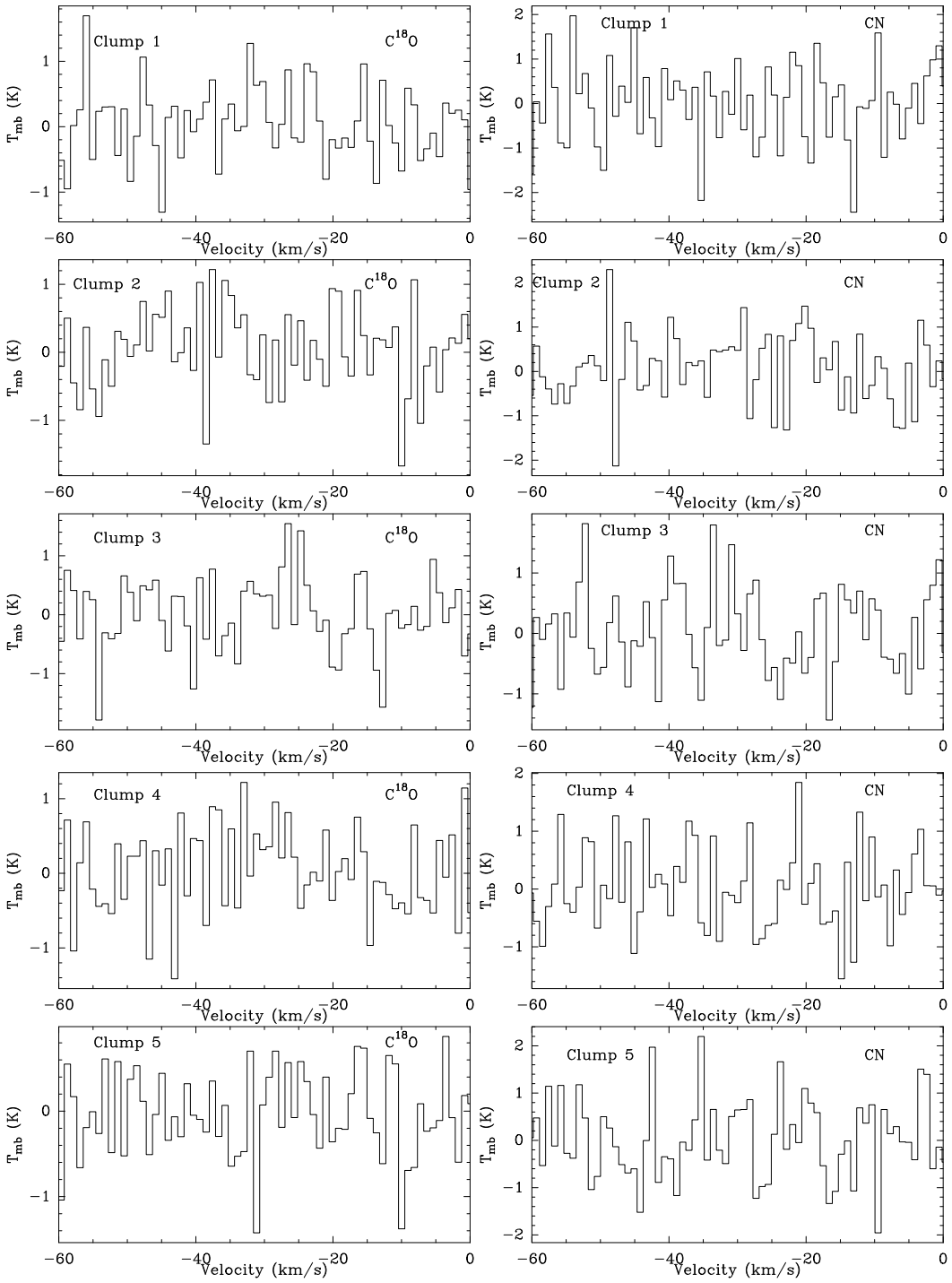

Figure 4.10: Retrieved spectra of molecules $C^{18}O$ and CN towards the clumps associated with CS51, in the velocity range of MALT90 data.

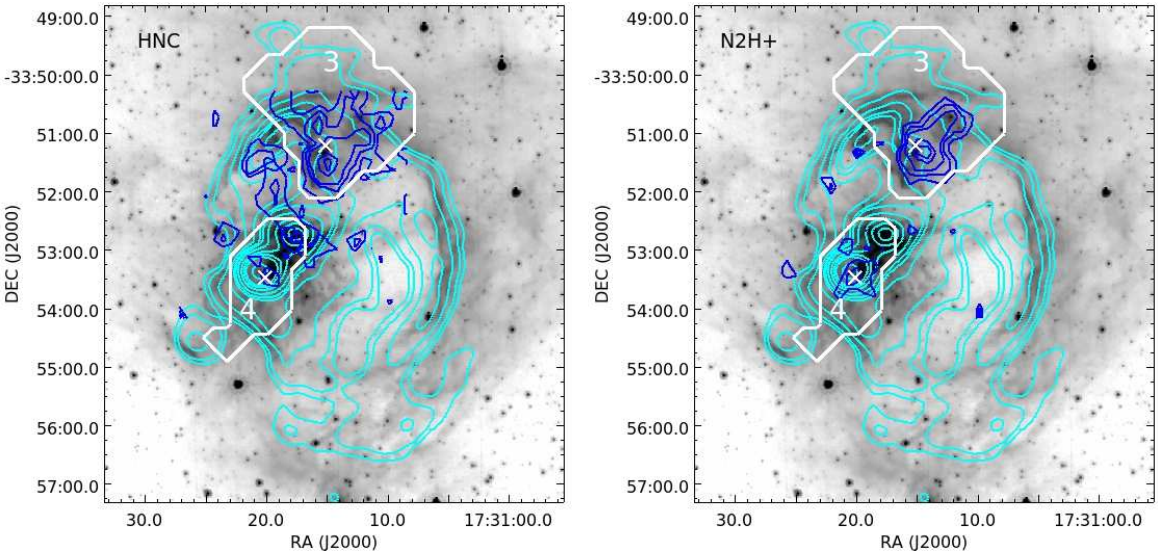

Figure 4.11: *Spitzer* 8 μm is shown in gray scale. Blue contours are the integrated intensity maps. The contour levels starts from 3σ, where σ = 0.4 K km s^{-1} for both the molecules. 610 MHz radio contours in cyan shows the distribution of ionized gas. The contour levels are same as in Figure 4.3. The white crosses are the pointing of MALT90 observation. The retrieved clump apertures (see section 4.2.4) are also shown.

code, to compute the column density of the detected molecular transitions. The input parameters to RADEX are the peak main beam temperature, background temperature (2.73 K from Purcell et al. (2006); Yu & Wang (2015)), kinetic temperature, line width, and H_2 volume density. We assume the kinetic temperature to be same as dust temperature (Sanhueza et al., 2012; Yu & Xu, 2016; Liu et al., 2016). The H_2 volume density and dust temperature values are taken from Section 4.2.4 which are estimated using the *Herschel* maps. Using the mean N(H_2) for the clumps (listed in Table 4.6), we estimate the fractional abundances (x) of the detected molecules. The derived column densities and fractional abundances are listed in Table 4.8. The values estimated for Clumps 3 and 4 are in the range derived for a large sample of clumps associated with IRDCs in the work by Miettinen (2014). Similar comparison holds with the results from Vasyunina et al. (2011).

From Figure 4.11, it is evident that N_2H^+ and HNC molecular line emission is appreciably more extended towards Clump 3 in comparison with Clump 4. This is supported by the derived column density values which shows a clear decrease towards Clump 4. Further for N_2H^+, the fractional abundances and the integrated line intensities also decrease by more than a factor of 4 towards the central Clump 4. These indicate that Clump 4 is possibly at a later evolutionary

stage as compared Clump 3 (Miettinen, 2014; Yu & Wang, 2015; Yu & Xu, 2016). The radio peaks A and B fall within Clump 4 with B being close to the peak in the *Herschel* column density map. Radio peak C is located in Clump 3. The estimated C_2H and N_2H^+ abundances show a decreasing trend with the increasing Lyman continuum photon flux of the clumps further suggesting an earlier evolutionary stage for Clump 3 (Yu & Wang, 2015; Yu & Xu, 2016). Parameters derived from the other detected molecular transitions are fairly consistent with the above picture of evolutionary stage. However, it should be noted here that better signal-to-noise ratio spectral observations are required before conclusively ascertaining the evolutionary stages of the two clumps.

4.3 Feedback of high-mass stars and origin of CS51

Massive stars can influence the parental cloud via various feedback mechanisms. In this section, we attempt to understand this in connection with the origin of the bubble CS51 and possible triggered star formation.

4.3.1 IRAC band ratio images

The general bubble structure is a PDR visible at 5.8 and 8 μm and an evacuated cavity within this (Churchwell et al., 2006, 2007; Watson et al., 2008, 2009; Anderson et al., 2010; Zavagno et al., 2010; Deharveng et al., 2010; Kendrew et al., 2012). The 5.8 and 8 μm emission is attributed to PAH molecules, which are excited by the soft UV photons permeating the PDR, with contribution from thermal emission from dust as well (Watson et al., 2008; Pomarès et al., 2009). In their detailed study on M17, Povich et al. (2007), proposed the use of IRAC band ratio images to understand the interaction of massive stars with their surrounding and delineate regions of PAH destruction. They further confirmed the disappearance of PAH in the destruction zone from spectroscopic data. Following this pioneering work, Watson et al. (2008) used this technique in several bubbles to locate the PDR around them. This technique exploits the fact that three of the four IRAC bands (at 3.6, 5.8, 8.0 μm) sample several PAH emission features (see Table 5 of Povich et al. 2007), whereas the 4.5 μm band is PAH-free.

We adopt the same procedure described in Povich et al. (2007) of using residual images (after removing point sources) followed by median filtering and smoothening before taking the ratios. Figure 4.12, shows the ratio images. Figure 4.12 (a) and (b) show the ratio of 8.0 μm and

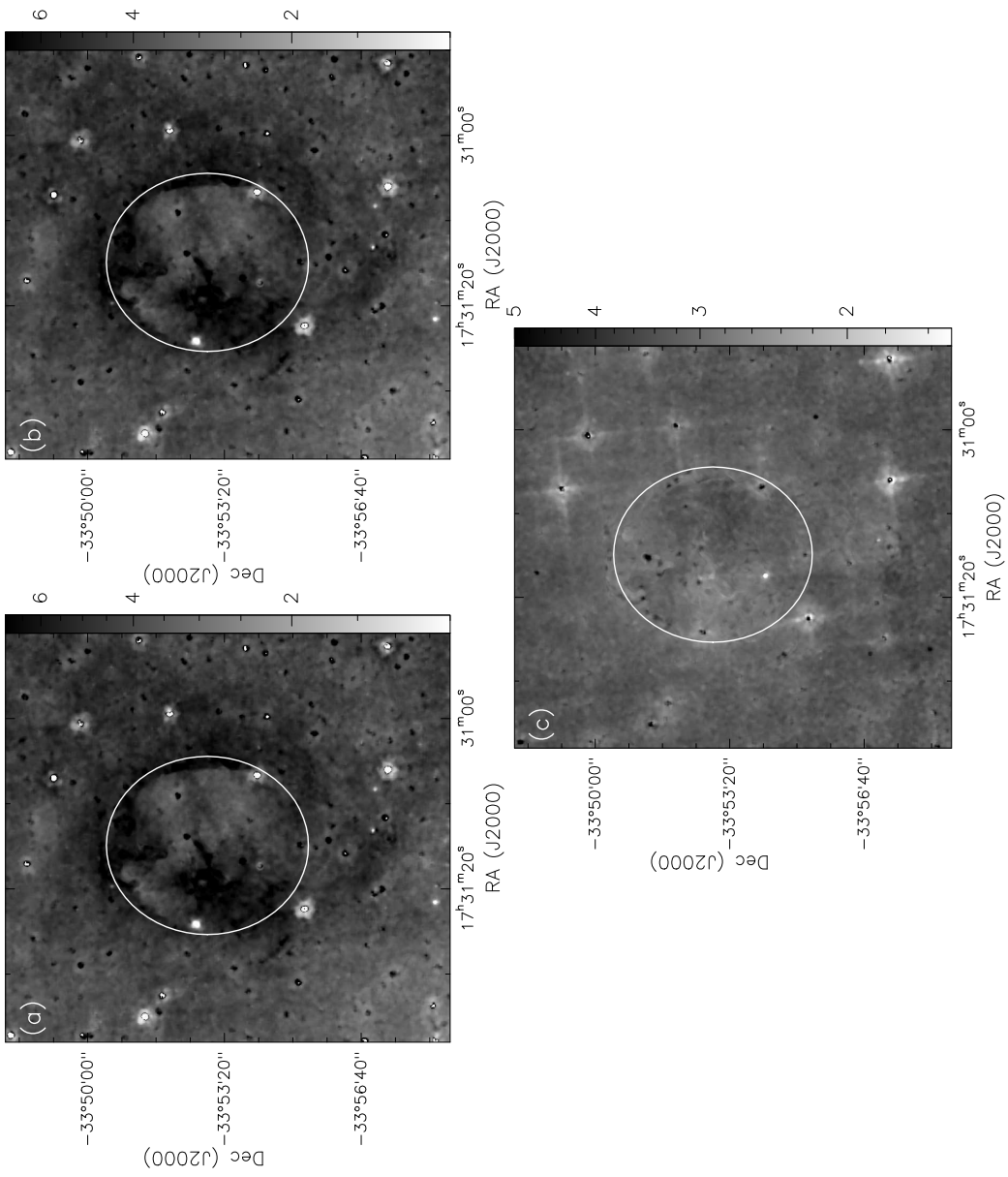

Figure 4.12: IRAC ratio maps (a) 8.0 μm/4.5 μm, (b) 5.8 μm/4.5 μm, and (c) 8.0 μm/5.8 μm of the region associated to bubble CS51. The bright emission in (a) and (b) show the PAH emission regions. The extent of the bubble is shown as a white ellipse. Point source removal at 4.5 μm is not very good, since the region is densely populated. The residuals show up in the ratio images (a) and (b).

5.8 μm images, respectively, with the PAH-free 4.5 μm image. The bright emission (seen as dark in the colour inverted plots) towards the bubble rim in these ratio maps show the location of the PAH zones thus defining the PDR related to CS51. This is similar to the results obtained by Watson et al. (2008) and Dewangan et al. (2012). However, it should be noted that the ratio maps also show enhanced emission towards the likely centre of the bubble coinciding with the region of bright radio emission. Given that PAH would be destroyed in the harsh radiation field close to the ionizing star (Watson et al. 2008; Deharveng et al. 2010, and references therein), this bright region could possibly be from the thermal dust continuum which is supported by the bright 24 μm emission that arises mostly near the hot star when the dust is heated to $\sim$100 K. Figure 4.12 (c) shows the ratio map between two PAH bearing bands (8.0 μm/5.8 μm). As expected, the rim emission is invisible here. It is to be noted that while these ratio images give the overall picture of PAH emission in the PDR, it should be kept in mind that the contribution from thermal dust and other atomic and molecular features would also be present. Thus, these ratio maps should be taken as illustrative unless confirmed with spectroscopy. Nevertheless, the ratio maps do confirm with the generally accepted picture of bubbles.

4.3.2 Column density probability distribution function

Structures in the form of clumps or condensations at the border of IR dust bubbles, pillars, and protrusions pointing towards the ionizing source have been observed in several studies (Pomarès et al., 2009; Petriella et al., 2010; Zavagno et al., 2010; Anderson et al., 2012b; Ji et al., 2012; Liu et al., 2015, 2016). The formation of these structures and the star formation therein are discussed invoking the 'collect and collapse' (C&C) model (Elmegreen & Lada, 1977) or the 'radiation driven implosion' (RDI) model (Bertoldi, 1989; Lefloch & Lazareff, 1994), thus probing the feasibility of triggered star formation in the 'accumulated' versus 'pre-existing' scenarios.

Understanding the role of density compression of ionized gas into a molecular cloud and that of ram pressure of turbulence of the cloud are crucial aspects in deciphering the impact of high-mass stars and this is discussed in detail by Tremblin et al. (2012a,b, 2014). They use the probability distribution function (PDF) of the column density around the ionized regions to study the feedback of the massive star. Their studies show that the column density PDF displays a single peak if turbulence dominates and the distribution becomes bimodal with a second peak

Table 4.9
Retrieved parameters from the lognormal fit to column density PDFs.

Circle	radius (′)	p_0	μ_0	σ_0	p_1	μ_1	σ_1
1	4.5	0.020	−0.215	0.131	0.027	0.152	0.206
2	5.5	0.028	−0.222	0.163	0.019	0.193	0.171
3	6.5	0.029	−0.229	0.179	0.018	0.222	0.190

forming at higher densities if the ionization pressure becomes larger than the turbulence. Liu et al. (2016, 2017a) have implemented this technique on two H II regions / bubbles. Adopting the same formulation, we investigate the nature of the column density PDFs in the region associated with CS51. We generate the PDF for the regions encircled within the three circles shown in Figure 4.6(a). These concentric circles are constructed with a separation of 1′ and for clarity we name them as Circle 1, 2, and 3 in increasing order of radius. The functional form for the bimodal PDF used to fit the column density is given by the following expression (Schneider et al., 2012; Tremblin et al., 2014; Liu et al., 2016)

$$p(\eta) = \frac{p_0}{\sqrt{2\pi\sigma_0^2}} exp\left(\frac{-(\eta-\mu_0)^2}{2\sigma_0^2}\right) + \frac{p_1}{\sqrt{2\pi\sigma_1^2}} exp\left(\frac{-(\eta-\mu_1)^2}{2\sigma_1^2}\right) \tag{4.6}$$

where, $\eta = \ln(N/\bar{N})$, N is the column density and $\bar{N}$ is the average column density taken over Circle 3. p_i, μ_i, and σ_i are the integral, mean, and dispersion of each component. In the above expression, the first lognormal component at low column density is associated with the initial turbulent molecular cloud and the second component at high column density is attributed to compression by the ionized gas pressure (Tremblin et al., 2014; Liu et al., 2016).

Figure 4.13 shows the column density PDFs in the three identified circles covering the ionized emission associated with CS51 and the surrounding cloud. The fitted parameters are listed in Table 4.9. The PDFs fit fairly well and all of them clearly show the second peak consistent with the results obtained for the bubbles N4, RCW 79 and RCW 120 (Tremblin et al., 2014; Liu et al., 2016, 2017a). Similar trend of p_0 increasing and p_1 decreasing as we move outwards is seen for CS51. As noted by Liu et al. (2016) and discussed by Tremblin et al. (2014), the decrease in p_1 with increasing radius indicates decreasing effect of compression due to ionized gas for larger regions. The results obtained reiterates the strong influence of the expanding bubble on its immediate surrounding. The second lognormal form suggesting compression from ionized gas

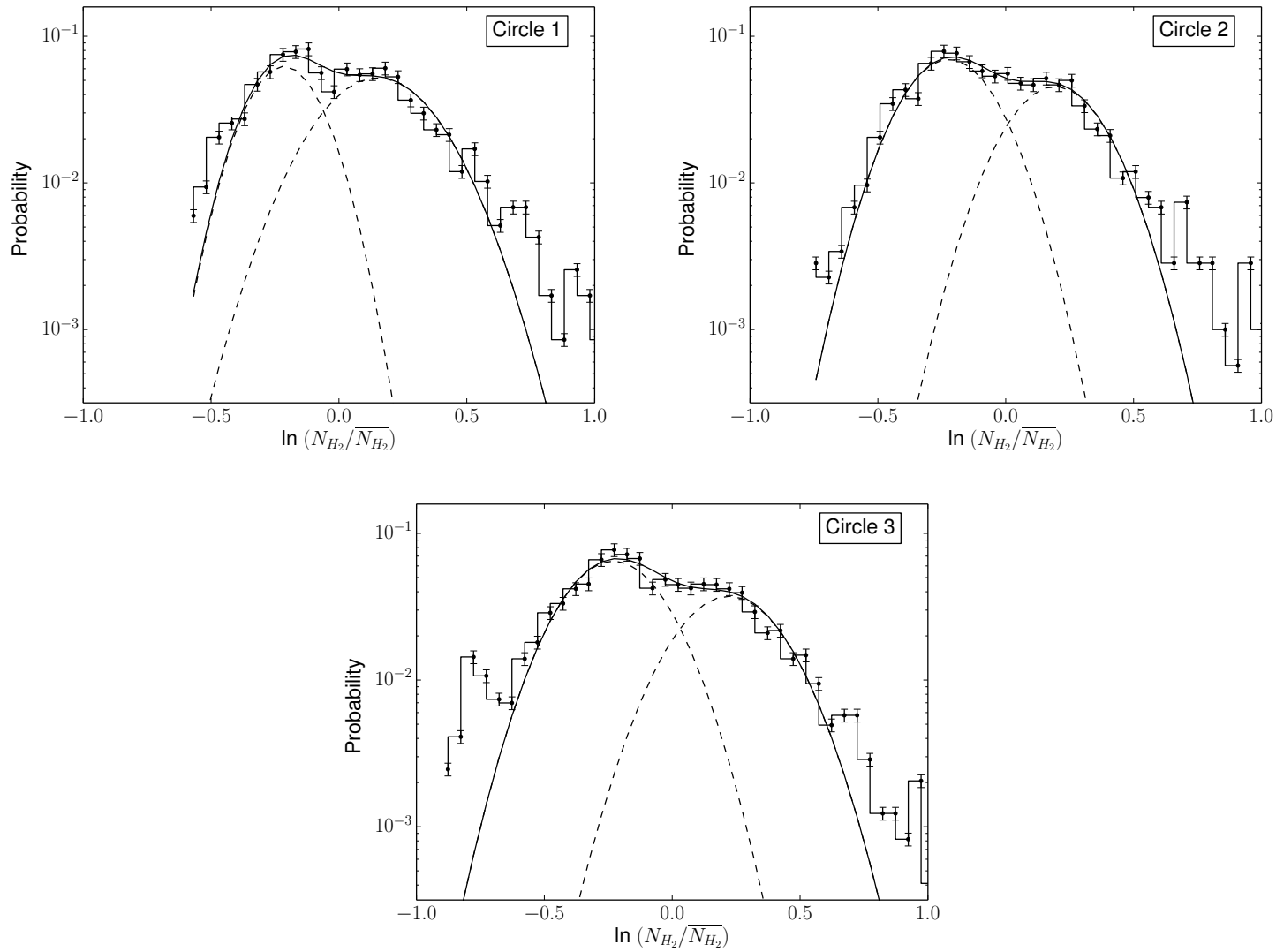

Figure 4.13: Plots of column density PDFs over the three circular regions. The dashed lines are the two lognormal components and the best fit (black solid line) is the sum of these two. $\overline{N_{H_2}}$ is the mean column density computed over the largest region.

would likely account for the condition required for triggered star formation. The high column density region shows signature of a power-law tail, which is generally attributed to on-going star formation (Schneider et al., 2012; Russeil et al., 2013; Schneider et al., 2013, 2015a; Liu et al., 2017a). Insufficient data points and low signal-to-noise ratio prevents us from fitting a power-law and attempting a more quantitative comparison with the above studies.

4.3.3 Collect and collapse scenario

The previous sub-section showed the role of ionization compression in CS51. The effect of this in triggered star formation has been in focus, since the pioneering work by Elmegreen & Lada (1977). As mentioned earlier, several studies have focused on the mechanism behind this triggering process - C&C or RDI. The detection of five dense clumps in the PDR region suggest that the shocked molecular layer is mostly swept up and accumulated during the bubble expansion. Thus, we explore the possibility of the C&C model at work around CS51. To examine this, we estimate the dynamical age of the bubble and compare the same with the fragmentation time of the surrounding cloud.

Assuming that the H II region expands in a homogeneous molecular cloud, the dynamical age of the H II region is estimated from the following well-known expressions (Spitzer, 1978; Dyson & Williams, 1980)

$$R_{st} = \left[\frac{3\ N_{Lyc}}{4\ \pi\ n_0^2\ \alpha_B}\right]^{1/3} \tag{4.7}$$

$$t_{dyn} = \frac{4}{7}\ \frac{R_{st}}{C_{Hii}}\left[\left(\frac{R_{if}}{R_{st}}\right)^{7/4} - 1\right] \tag{4.8}$$

where, R_{st} is the Strömgren radius, N_{Lyc} is the Lyman continuum photons flux responsible for the H II region and n_0 is the initial particle density of the ambient gas. α_B is the coefficient of radiative recombination and it is calculated from Kwan (1997), to be $2.6{\times}10^{-13}$ $(10^4$ K/T$)^{0.7}$ cm^3 sec^{-1}. t_{dyn} is the dynamical age of the H II region, C_{Hii} is the isothermal sound speed (assumed to be 10 km s^{-1}), R_{if} is the radius of H II region which is approximately taken as the radius of the bubble (2.1′). To estimate n_0, we take the total mass of the swept up molecular shell which is the sum of the masses of the five detected clumps on the bubble periphery (11630 $M_\odot$) and assume that it was distributed homogeneously within the bubble radius. To this, we add the mass of the ionized component (300 $M_\odot$). This gives an estimate of $n_0 = 2.4 \times 10^3$ cm^{-3} which

defines a lower limit, since it does not take into account the ionized gas that probably would have escaped through the rupture of bubble or absorbed by dust. From the estimated parameters of the clumps (see Table 4.6), we get an average number density of $n_0 = 4.8 \times 10^3$ cm^{-3} which can be considered as the upper limit. Using the above values, we estimate the dynamical age of CS51 to be 0.9 – 1.3 Myr. This estimate should be taken with caution, since the assumption of expansion in a uniform medium is not realistic.

We proceed further to investigate fragmentation of the collected shell material using the model of Whitworth et al. (1994b). They give the following expression to estimate the fragmentation time.

$$t_{frag} = 1.56\ a_s^{7/11}\ N_{49}^{-1/11}\ n_3^{-5/11}\ \text{Myr} \tag{4.9}$$

where, a_s is the sound speed in the shocked layer (the turbulent velocity) in units of 0.2 km sec^{-1}, N_{49} is the ionizing photon in units of 10^{49} photons sec^{-1}, and n_3 is the initial particle density of the ambient gas (n_0) in units of 10^3 cm^{-3}. Taking a_s to be 0.3 km s^{-1} at the derived dust temperatures, we estimate the fragmentation time, t_{frag}, to be 0.5 Myr for $n_0 = 2.4 \times 10^3$ cm^{-3} and 0.4 Myr for $n_0 = 4.8 \times 10^3$ cm^{-3}. The estimated fragmentation time is shorter (by a factor of 2) than the dynamical age of the H II region implying that the shell of collected material has enough time to gravitationally fragment during the expansion of the bubble. Similar results are obtained for N4, G8.14+0.23, and G24.136+00.436, where the fragmentation time is less than the dynamical time (Dewangan et al., 2012; Liu et al., 2015, 2016). In contrast, Ji et al. (2012) derive fragmentation time significantly larger than the dynamical age for bubble N22 and they discard the C&C process. The above estimates of the timescales involved support the C&C process as the likely mechanism for the formation of the identified clumps and the associated star formation. It should however be kept in mind that, this simple model does not conclusively exclude the RDI process and thus higher resolution observations are required to probe the dense cores within these clumps and compare their masses, radii, and separation with the theoretical predictions of the C&C mechanism (Whitworth et al., 1994b; Liu et al., 2017b).

4.3.4 What do the clumps reveal?

As discussed in Section 4.2.6, the Clumps 3 and 4 show trends of different evolutionary stages with Clump 4 being more evolved. Association with radio peaks and 24 μm emission indicate

that these are active star-forming clumps. Further, the NIR and MIR colours have shown the presence of YSOs likely to be associated with the clumps with an overdensity of Class I YSOs seen towards Clump 3.

From the derived centroid velocities of the molecular transitions in the clumps, it is seen that the lines related to Clump 3 are red-shifted by ~ 2 km s^{-1} with respect to a systematic velocity of -32.34 km s^{-1} which is taken as the average of velocities of detected molecular line emission in Clump 4. Clump 4 is located within the bubble (and closer to the centre) correlating well with the likely location of the exciting star(s). The above is consistent with the picture of the formation of CS51 where the shell of dust and gas seen is presumably swept up by the expanding H II region. Hence, Clump 3 that is located towards the northern rim is expected to be moving away from the central clump indicating the expansion of the bubble. Similar expansion is revealed from the molecular line data of bubble N4 where the clumps towards the south-east and north-west part of N4 are seen to have blue-shifted and red-shifted velocities, respectively, compared to a systematic velocity. It should be noted here that we do not have molecular line data for Clumps 1, 2, and 5 to strengthen the picture of expansion.

From the mass and size estimates of the five clumps discussed in Section 4.2.4, Clumps 2 – 5 qualify as potential high-mass forming ones as they satisfy the threshold criteria of m(r) $\geqslant$ 870 $M_\odot$ $(r/pc)^{1.33}$, where m(r) is mass of clump and r is the effective radius of clump, discussed in Kauffmann & Pillai (2010). We have also investigated the gravitational state of Clumps 3 and 4 by deriving the virial parameter (α) defined as the ratio between virial mass to dust mass. This parameter indicates whether a clump is gravitationally bound or not. Clumps are likely to undergo gravitational collapse if $\alpha < 1$ and in the absence of magnetic field can be considered as bound. If the value of α exceeds unity, then in all likelihood expansion is possible unless some external mechanism constrains the cloud. Virial mass of each clump is derived from the following equation (Contreras et al., 2016).

$$M_{vir} = \frac{5\, r\, \Delta V^2}{8\, \ln(2)\, a_1\, a_2\, G} \sim 209\, \frac{1}{a_1\, a_2} \left(\frac{\Delta V}{\text{km s}^{-1}}\right)^2 \left(\frac{r}{pc}\right) M_\odot \tag{4.10}$$

where, the constant a_1 is the correction for power-law distribution, which can be expressed as $a_1 = (1-p/3)/(1-2p/5)$, for $p < 2.5$ (Bertoldi & McKee, 1992). We adopt a power-law density

distribution of p=1.8 (Contreras et al., 2016). The constant a_2 is correction for non-spherical shape. We assume the clumps to be spherical and take a_2 as 1. ΔV and r are the line width and radius (listed in Table 4.6) of the clumps. To derive virial mass and virial parameter, we use the optically thin N_2H^+ emission because an optically thick line would overestimate the virial mass (Sanhueza et al., 2012). Thus, using the above equation and the line width obtained in Section 4.2.6, we derive virial masses of $\sim$ 1100 and 835 $M_\odot$ for Clumps 3 and 4, respectively. Taking the ratio with the mean dust masses of the clumps (see Table 4.6), we estimate the virial parameter to be 0.2 and 0.6 for Clumps 3 and 4, respectively. These estimates are consistent with the nature of the clumps where signature of active star formation is observed.

4.4 Summary

In this work, we have carried out a detailed multi-wavelength study towards the southern IR bubble CS51 which is associated with IRAS 17279−3350. Our main results are the following.

1. The associated ionized emission probed at 610 and 1300 MHz displays a complex morphology. The ionized emission mostly fills the bubble interior with a cavity towards the south-west, which is more pronounced at 1300 MHz. The observed Lyman continuum photon flux translates to a spectral type of O6V – O5.5V for the exciting source under the assumption of optically thin, free-free emission. The mass of this associated ionized gas within the bubble is estimated to be $\sim$ 300 $M_\odot$.

2. The GMRT radio maps reveal the presence of three components (A, B, and C) associated with CS51. They show up as compact regions of enhanced emission. The component A is located towards the likely center of the bubble, the component B (brightest among them) is towards the south-east periphery and the component C is located in the north-west rim of the bubble.

3. The 610 − 1300 MHz spectral index map shows the coexistence of both thermal free-free emission and non-thermal synchrotron emission. The compact regions A and C are seen to be associated with thermal emission and component B shows signature of non-thermal emission.

4. From the optical (B-band) and NIR colours, we identify three sources as potential can-

didate exciting star(s) from a sample of sources located towards the radio and 24 μm emission peaks.

5. The column density and dust temperature maps are generated by pixel-wise SED modelling of the thermal dust emission using FIR *Herschel* data. The column density map shows a fragmented shell like structure harbouring four clumps towards the periphery of the bubble and one clump is detected within the bubble close to the likely centre. Dust temperature map shows the presence of warmer dust in the bubble interior consistent with the presence of ionized emission.

6. Five molecular transitions (C_2H, HCN, HCO^+, HNC, and N_2H^+) are detected towards two clumps (3 and 4). The hyperfine components of C_2H, HCN, HNC, and N_2H^+ are clearly detected above noise level. The velocity integrated (zeroth moment) map for N_2H^+ and HNC are seen to be appreciably extended towards Clump 3. Within the uncertainties due to low signal-to-noise ratio of the observed spectra, the derived line parameters, column density, and fractional abundance suggest a possible earlier evolutionary phase of Clump 3 as compared to Clump 4.

7. The IRAC ratio maps involving PAH-bearing and PAH-free bands show the presence of PAH emission associated with the PDR of CS51, thus confirming the generally accepted bubble formation mechanism and related MIR emission.

8. The column density PDFs display a bimodal distribution thus demonstrating the strong influence of expanding bubble on its surrounding where compression due to ionized gas pressure dominates the effect of turbulence.

9. Assuming the expansion of the associated H II region to occur in a uniform medium, the dynamical age is estimated to be 0.9 – 1.3 Myr, which is higher than the derived fragmentation time of 0.4 – 0.5 Myr. This indicates that the C&C mechanism is possibly at work around the bubble CS51 and responsible for triggering star formation towards the border of the bubble.

10. The estimated values of mass and radius of the clumps, that lie between 810 – 4600$M_\odot$ and 1.0 – 1.9 pc, respectively, indicate all except Clump 1 to be high-mass star-forming

clumps.

11. The centroid velocities of the molecular transitions detected show signatures of expansion of the bubble. The Clump 3 located towards the northern rim is seen to have red-shifted velocities with respect the central Clump 4.

12. The above results present a picture of a conventional dust bubble formed due to the interaction of a massive star(s) and the surrounding medium. The compression of the ionized gas is seen to trigger star formation in the bubble rim.

Chapter 5

Two compact southern HII regions G346.056−0.021 and G346.077−0.056

5.1 Introduction

In the study presented in this chapter, we focus on two southern H II regions and probe them from IR through radio wavelengths. These are G346.056−0.021 and G346.077−0.056. IRAS 17043−4027, with IRAS colors consistent with UC H II regions (Bronfman et al., 1996), is associated with G346.077−0.056. From the ^{13}CO observations of candidate massive young stellar objects (YSOs) in the southern Galactic plane, Urquhart et al. (2007b) give the kinematic distance estimate of 5.7 kpc (near) and 10.8 kpc (far) for G346.056−0.021 and 5.8 kpc (near) and 10.7 kpc (far) for G346.077−0.056. In a later paper (Urquhart et al., 2014a), they resolve the kinematic distance ambiguity by using H I self-absorption analysis and place both the sources at the far-distance of 10.9 kpc. We adopt this distance in our study. As part of the Green Bank Telescope (GBT) H II Region Discovery Survey, hydrogen radio recombination line (RRL) emission was detected towards G346.056−0.021 and G346.077−0.056 (Anderson et al., 2011) and helium and carbon RRLs were observed towards G346.056−0.021 (Wenger et al., 2013). From their 1400 MHz Galactic plane survey, Zoonematkermani et al. (1990) listed G346.056−0.021 and G346.077−0.056 as small diameter radio sources with sizes of 18.8″ and 9″, respectively. Apart from this, G346.077−0.056 was observed at 4800 and 8640 MHz by Urquhart et al. (2007a) as part of the Red MSX Sources (RMS) survey to obtain radio observations of candidate massive YSOs. Other than the ^{13}CO survey mentioned above, a few other molecular line studies have been conducted toward G346.077−0.056 (Bronfman et al., 1996; Hoq et al., 2013; Yu et al., 2015). G346.077−0.056 has been part of a 6.7 GHz methanol maser detection survey which yielded negative results (van der Walt et al., 1995). A similar result was also obtained from the recent 6.7 GHz methanol maser survey (Caswell et al., 2010). Further, a sparsely populated embedded cluster, VVV CL094, is reported to be associated with

G346.077−0.056 (Borissova et al., 2011; Morales et al., 2013). As is evident from the literature survey, there have been no dedicated studies of either of these two H II regions.

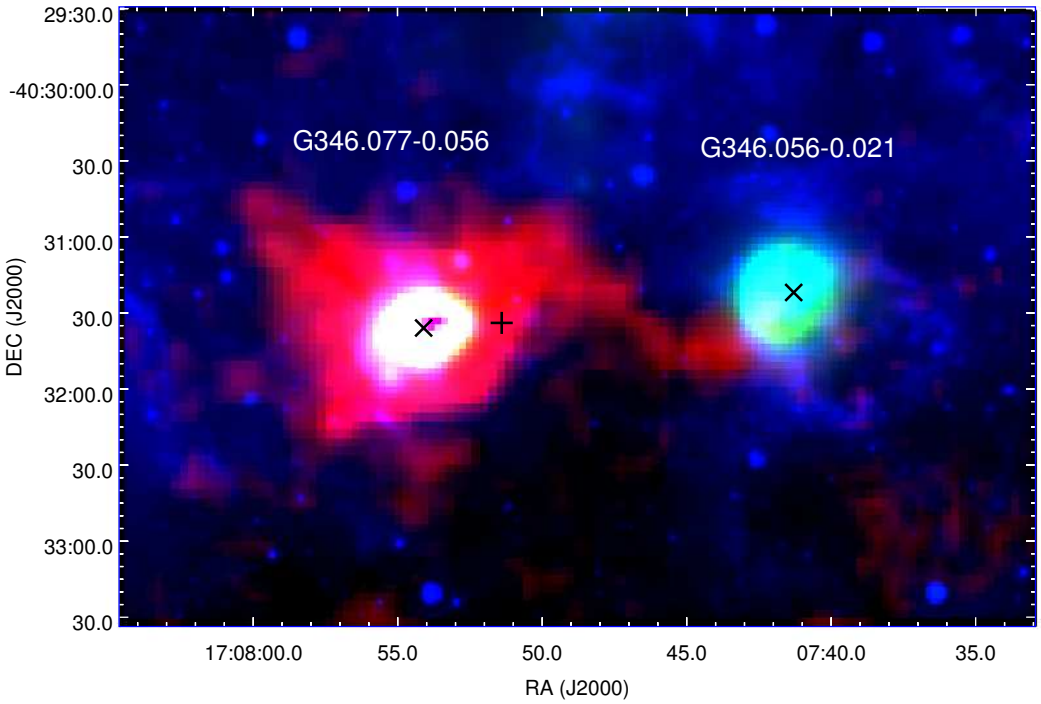

Figure 5.1: Color composite image of the region associated with G346.056−0.021 and G346.077−0.056 using IRAC 8.0 μm band (blue), MIPS 24 μm (MIPSGAL Survey; Carey et al. 2009) (green), and ATLASGAL 870 μm (red). Positions of the H II regions as listed in Anderson et al. (2011) are shown with the '×' symbols. The + symbol shows the position of IRAS 17043−4027. It should be noted here that a few pixels toward the central part of the 24 μm emission associated with G346.077−0.056 are saturated.

Figure 5.1 displays a color-composite image of the associated region showing the location and the dust environment. The 8 μm emission is relatively localized towards the center of G346.077−0.056 as compared to G346.056−0.021 where it displays an extended bubble-type morphology towards the south-west. Probing the warm dust component, 24 μm emission is seen predominantly towards G346.056−0.021 and the central portion of G346.077−0.056. The 870 μm component which traces the cold dust environment is seen as a prominent, large clump enveloping G346.077−0.056 with a distinct filamentary structure towards the west connecting to G346.056−0.021.

Presenting a multiwavelength study of the complex associated with these two H II regions, we have organized the chapter in the following way. Results and discussion from the study of the

ionized and the dust component and the associated stellar population are presented in Section 5.2. Possible mechanisms responsible for the morphology of the ionized emission for both H II regions are explored in Section 5.3. The summary of the results obtained are compiled in Section 5.4.

5.2 Results and Discussion

5.2.1 Emission from ionized gas

To probe the ionized emission associated with our regions of interest, low frequency radio observations were carried out with the GMRT on 17 and 20 July 2011. Data reduction is performed using AIPS. Chapter 2 outlines the details of observations with GMRT and the data reduction procedure. G346.056−0.021 and G346.077−0.056 are located north-east of the IR dust bubble S10 which is studied in detail in Chapter 3. Both these H II regions were observed as part of the same field with S10 being at the phase centre. Thus to generate the final maps we use the same scaling factors of 1.2 (1280 MHz) and 1.7 (610 MHz) derived in Chapter 2. This rescaling takes care of the contribution of the Galactic diffuse emission to the system temperature for the target. The radio emission associated with the two H II regions mapped at 610 and 1280 MHz is shown in Figure 5.2. These maps are generated by setting the 'robustness' parameter to −5 (on a scale where +5 represents pure natural weighting and −5 is for pure uniform weighting of the baselines) while running the task `IMAGR` and considering the entire *uv* coverage. However, for probing the larger spatial scales of the extended diffuse, ionized emission in these regions we also generate continuum maps by setting the 'robustness' parameter to +1 and weigh down the long baselines using the task `UVTAPER`. These lower resolution maps are shown in Figure 5.3. The details of observation and the generated maps are listed in Table 5.1. The positional offsets of the peaks in these maps are within $\sim 2''$.

As seen from the figures, the ionized emission associated with the H II region G346.056−0.021 displays a distinct cometary morphology at both 610 and 1280 MHz with a steep intensity gradient towards the east. A faint, broad and diffuse tail is seen towards the west-south-west. The observed morphology suggests that this H II region is density bounded towards the south-west and ionization bounded towards the north-east. The emission from G346.077−0.056 is also seen to be cometary in nature with the signature being more pronounced at 1280 MHz. The higher-

Table 5.1
Details of the radio interferometric continuum observations and generated maps. Values in parentheses are for the maps generated with 'robustness parameter' −5 and no *uv* tapering.

Details	610 MHz	1280 MHz
Date of Obs.	17 July 2011	20 July 2011
Flux Calibrators	3C286,3C48	3C286,3C48
Phase Calibrators	1626−298	1626−298
On-source Integration time	∼ 4 hr	∼ 4 hr
Synth. beam	14.4″×8.5″	8.8″×4.4″
	(6.4″×3.1″)	(3.6″×1.5″)
Position angle. (deg)	10.6	15.0
	(6.6)	(3.3)
rms noise (mJy/beam)	2.1	0.5
	(0.3)	(0.2)

resolution maps more closely corroborate the above picture. The higher-resolution 1280 MHz map displays an interesting morphology where a compact, cometary structure is seen towards the west of G346.077−0.056. This could possibly be another H II region with its cometary head facing that of G346.077−0.056. However, we cannot rule out the other possibility of an externally ionized clump arising due to density inhomogeneities. An extended low-intensity (at 3σ level) detached component is also seen at 1280 MHz in Figure 5.3. It is difficult to ascertain the physical association of this feature with G346.077−0.056. Using the Australia Telescope Compact Array, Urquhart et al. (2007a) observed the two regions at 3.6 cm (8640 MHz) and 6.0 cm (4800 MHz) with a spatial resolution of $\sim 1 - 2''$ and sensitivity $\sim$ 0.3 mJy. Radio emission is detected at both frequencies for G346.077−0.056 with the peak positions in good agreement (within 2.5″) with the GMRT maps. They classified this H II region as one displaying a cometary morphology which is consonant with the GMRT maps. However, G346.056−0.021 is not listed under the RMS sources having associated radio emission. This non-detection is investigated and presented in Appendix B. Table 5.2 allows a comparison of GMRT results with that of Urquhart et al. (2007a) and Zoonematkermani et al. (1990). The integrated flux densities derived from the GMRT 1280 MHz map is larger than that from the 1400 MHz VLA observations obtained by Zoonematkermani et al. (1990). This is understandable considering the fact that the integration time for their observation was only 120 seconds and hence not expected to be sensitive to the extended, faint diffuse emission. Similarly, the high-resolution ATCA maps would have also resolved out a good fraction of the diffuse emission.

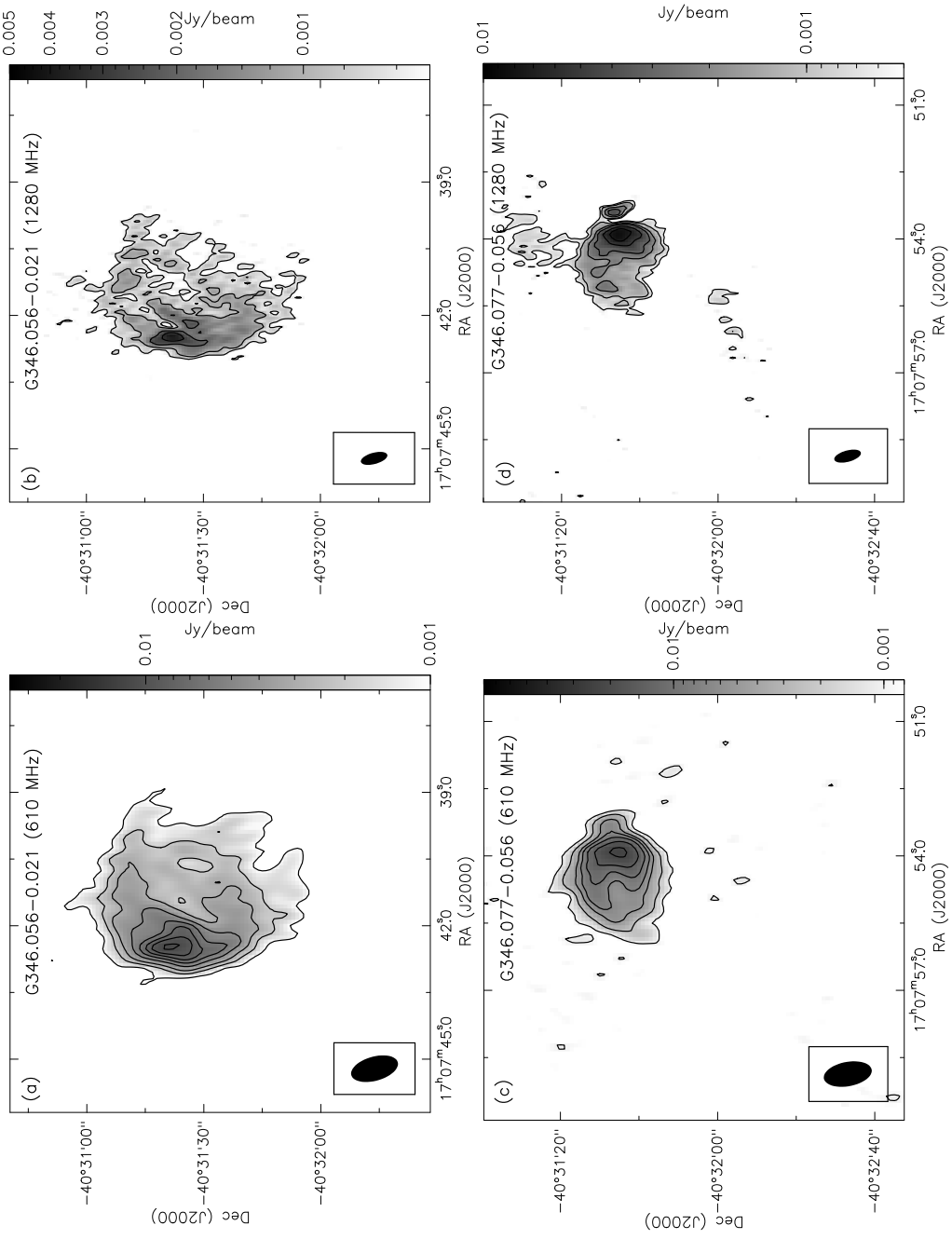

Figure 5.2: Ionized emission associated with the H II regions - (a) and (b) 610 and 1280 MHz maps for the region associated with G346.056−0.021; (c) and (d) 610 and 1280 MHz emission for the region around G346.077−0.056. The contour levels are 3, 5, 10, 15, 20, 25, 30, and 35 times σ , where σ is equal to 0.3 mJy/beam and 0.2 mJy/beam at 610 MHz and 1280 MHz, respectively. Beam in each band is shown as filled ellipse. These maps are generated by setting the 'robustness parameter' to −5 and without any *uv* tapering.

For deriving the physical parameters of the two H II regions, we use the lower-resolution GMRT maps which sample most of the associated ionized emission. For this we first convolve the 1280 MHz map to the resolution of the 610 MHz map. From the peak flux densities at 610 and 1280 MHz, we estimate the radio spectral index α ($F_\nu \propto \nu^{\alpha}$) to be -0.1 ± 0.06 and 0.01 ± 0.004 for G346.056−0.021 and G346.077−0.056, respectively. Taking the integrated flux densities, we estimate spectral index values of -0.3 ± 0.06 and -0.4 ± 0.06 for G346.056−0.021 and G346.077−0.056, respectively. Here, we have sampled the same region defined by the 3σ contour of the 610 MHz map. The spectral index values obtained from the peak flux densities are consistent with optically thin free-free emission. However, the values obtained from the integrated flux densities are indicative of non-thermal emission (Rodriguez et al., 1993; Kobulnicky & Johnson, 1999; Rosero et al., 2016). Thus a scenario of co-existing free-free and non-thermal emission can be visualized for the H II regions as has been addressed by several authors (Mücke et al., 2002; Russeil et al., 2016; Veena et al., 2016; Nandakumar et al., 2016; Das et al., 2017). The above interpretation should be taken with caution because GMRT is not a scaled array between the observed frequencies and the observed visibilities span different *uv* ranges. This implies that the generated maps at 610 and 1280 MHz are sensitive to different spatial scales thus rendering the estimated spectral indices uncertain.

Following the method discussed in Quireza et al. (2006); Anderson et al. (2015); Luisi et al. (2016), we derive the electron temperature, T_e, towards both these regions. This formulation assumes local thermodynamic equilibrium for the RRL lines, and is given by the following expression

$$T_e[K] = \left\{ 7103.3 \left(\frac{\nu}{\mathrm{GHz}}\right)^{1.1} \left(\frac{T_C}{T_L(\mathrm{H}^+)}\right) \left(\frac{\Delta V(\mathrm{H}^+)}{\mathrm{km\ s^{-1}}}\right)^{-1} \left(1 + \frac{\mathrm{n}(^4\mathrm{He}^+)}{\mathrm{n}(\mathrm{H}^+)}\right)^{-1} \right\}^{0.87} \tag{5.1}$$

where, ν is the observing frequency for the RRL lines, T_C is the peak continuum antenna temperature, T_L is the peak antenna temperature for hydrogen RRL line, $\Delta V(\mathrm{H}^+)$ is the full width at half maximum (FWHM) line width for the RRL line and $\mathrm{n}(^4\mathrm{He}^+)/\mathrm{n}(\mathrm{H}^+) = \mathrm{y}^+$ is the helium ionic abundance ratio. The hydrogen RRL line parameters for both the H II regions are taken from Anderson et al. (2011). The helium ionic abundance ratio has been derived from the hydrogen and helium RRL line properties and using the following equation (Quireza et al., 2006;

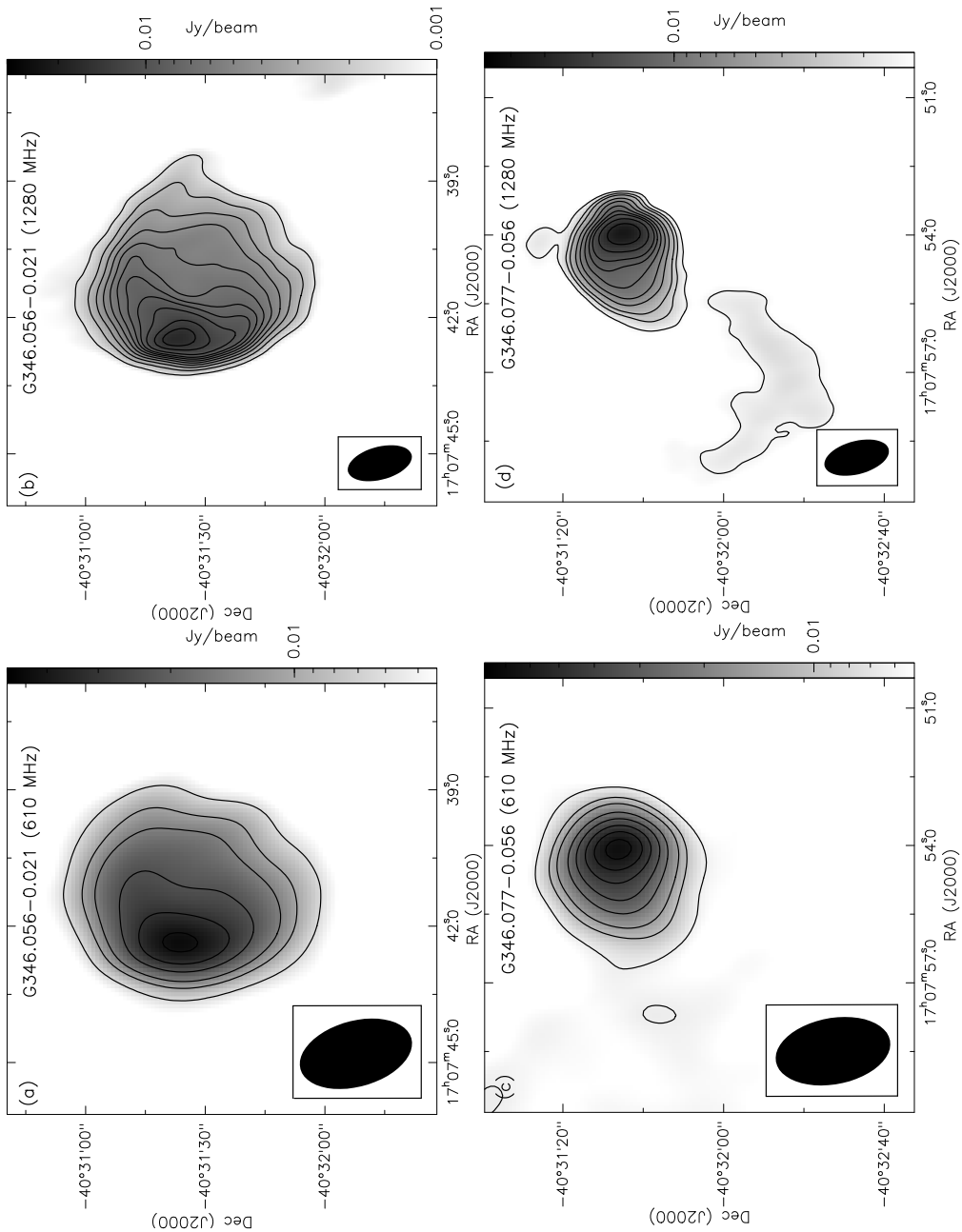

Figure 5.3: Same as in Figure 5.2, but for maps generated with 'robustness parameter' +1 and appropriate uv tapering to weigh down long baselines. The contour levels are 3, 5, 7, 11, 15, 20, 25, 30, 40, and 55 times σ where σ is 2.1 mJy/beam and 0.5 mJy/beam at 610 MHz and 1280 MHz, respectively. Beam in each band is shown as filled ellipse.

Table 5.2

GMRT, ATCA (Urquhart et al., 2007a) and 1.4 GHz (Zoonematkermani et al., 1990) results. The peak coordinates (from 1280 MHz map*), peak and integrated flux densities of the two H II regions are listed. The integrated flux density in GMRT maps are calculated by integrating above 3σ level. Values for the convolved 1280 MHz map are listed in the second line. For the integrated flux densities, the area probed is kept same as in 610 MHz. Values in parentheses are from the radio maps, generated by setting the 'robustness parameter' to −5 and no *uv* tapering.

Peak Coordinates		Peak flux (mJy/beam)					Integrated flux (mJy)				
RA (J2000)	DEC (J2000)	610 MHz	1280 MHz	1400 MHz	4.8 GHz	8.6 GHz	610 MHz‡	1280 MHz‡	1400 MHz	4.8 GHz	8.6 GHz
G346.056−0.021											
17:07:42.50	−40:31:23.00	44.7	17.3	22	–	–	339±34	271±27	101	–	–
			40.4					268±27			
		(11.37)	(4.02)				(245±24.5)	(178±18)			
G346.077−0.056											
17:07:54.00	−40:31:35.40	67.8	35.7	36	8.3	3.2	225±22	173±17	62	46.2	15.7
			68.6					174±17			
		(23.7)	(8.47)				(197±19)	(159±16)			

* The peak positions of the GMRT maps are consistent with the 1400 MHz (VLA) map (within 5.5″) and the 4.8 and 8.6 GHz (ATCA) maps (within 2.5″).

‡ Error in integrated flux has been calculated following the equation from Sánchez-Monge et al. (2013b), $[(2\sigma(\theta_{\rm source}/\theta_{\rm beam})^{1/2})^2 + (2\sigma_{\rm flux--scale})^2]^{1/2}$, where σ is the rms noise level of the map, $\theta_{\rm source}$ and $\theta_{\rm beam}$ are the size of the source and the beam, respectively, and $\sigma_{\rm flux-scale}$ is the error in the flux scale, which takes into account the uncertainty on the calibration applied to the integrated flux of the source. For GMRT maps uncertainty in the flux calibration is 5% (Lal & Rao, 2007)

Wenger et al., 2013)

$$y^{+} = \frac{T_L(^4He^+)\Delta V(^4He^+)}{T_L(H^+)\Delta V(H^+)}, \tag{5.2}$$

where T_L is the peak line intensity and ΔV is the FWHM line width. We have derived the value of y^+ to be 0.11 for the H II region G346.056−0.021 using the hydrogen and helium RRL line parameters from Wenger et al. (2013). For G346.077−0.056, no helium RRL observation is available, hence we use an average value of $y^+ = 0.07$ estimated from a sample of H II regions (Wenger et al., 2013). From the above expressions and observed parameters, we estimate the electron temperature to be 5500 K and 8900 K for the H II regions G346.056−0.021 and G346.077−0.056, respectively. These values fall within the range of ∼ 5000 to ∼ 10000 K seen for Galactic H II regions (Quireza et al., 2006). In order to derive the other physical properties of the ionized emission associated with the two H II regions, we adopted the expressions from Schmiedeke et al. (2016). Lucid explanations coupled with rigorous derivations of physical properties of H II regions can be found in the original papers of Mezger & Henderson (1967); Rubin (1968); Schraml & Mezger (1969); Panagia (1973). The H II regions are considered as Strömgren's spheres which are fully ionized spherical regions of uniform electron density. Assuming the radio emission at 1280 MHz to be optically thin and emanating from a homogeneous, isothermal medium, the electron density, n_e, the emission measure, EM, and the number of Lyman-continuum photons per second, N_{Ly}, are estimated using the following equations (Schmiedeke et al., 2016)

$$\left(\frac{\mathrm{EM}}{\mathrm{pc\ cm^{-6}}}\right) = 3.217 \times 10^7 \left(\frac{\mathrm{F}_\nu}{\mathrm{Jy}}\right)\left(\frac{T_e}{\mathrm{K}}\right)^{0.35}\left(\frac{\nu}{\mathrm{GHz}}\right)^{0.1}\left(\frac{\theta_{\mathrm{source}}}{\mathrm{arcsec}}\right)^{-2} \tag{5.3}$$

$$\left(\frac{n_e}{\mathrm{cm^{-3}}}\right) = 2.576 \times 10^6 \left(\frac{\mathrm{F}_\nu}{\mathrm{Jy}}\right)^{0.5}\left(\frac{T_e}{\mathrm{K}}\right)^{0.175}\left(\frac{\nu}{\mathrm{GHz}}\right)^{0.05}\left(\frac{\theta_{\mathrm{source}}}{\mathrm{arcsec}}\right)^{-1.5}\left(\frac{\mathrm{D}}{\mathrm{pc}}\right)^{-0.5} \tag{5.4}$$

$$\left(\frac{N_{Ly}}{\mathrm{Sec^{-1}}}\right) = 4.771 \times 10^{42} \left(\frac{\mathrm{F}_\nu}{\mathrm{Jy}}\right)\left(\frac{T_e}{\mathrm{K}}\right)^{-0.45}\left(\frac{\nu}{\mathrm{GHz}}\right)\left(\frac{\mathrm{D}}{\mathrm{pc}}\right)^{2} \tag{5.5}$$

where, F_ν is the integrated flux density of ionized region, T_e is the electron temperature, ν is the frequency, θ_{source} is the angular diameter of the H II region, and D is the distance to these

regions. The angular extents of the ionized emission associated with G346.056−0.021 and G346.077−0.056 are estimated from the 1280 MHz map to be $61'' \times 49''$ and $34'' \times 32''$, respectively. These values are the $\mathrm{FWHM_x} \times \mathrm{FWHM_y}$ obtained using the 2D *Clumpfind* algorithm (Williams et al., 1994) for a 3σ threshold level. Chapter 3 briefly outlines the prominent features of this algorithm. Applying beam corrections, we derive the deconvolved sizes to be $33'' \times 38''$ and $17'' \times 19''$ for G346.056−0.021 and G346.077−0.056, respectively. For θ_{source}, we have taken the geometric mean of the deconvolved FWHM. The physical parameters thus derived are listed in Table 5.3.

Table 5.3
Derived physical parameters of H II regions.

Source	T_e (K)	θ_{source} (arcsec)	n_e ($\mathrm{cm^{-3}}$)	EM ($\mathrm{cm^{-6}}$ pc)	log N_{Ly}	Spec. Type	$\mathrm{t_{dyn}}$ (Myr)
G346.056−0.021	5500	35	4.2×10^2	2.5×10^5	48.50	O7.5V - O7V	0.5
G346.077−0.056	8900	18	1.0×10^3	7.1×10^5	48.21	O8.5V - O8V	0.2

If single ZAMS stars are responsible for the ionization of the H II regions, then using Table I of Martins et al. (2005a), the estimated Lyman continuum flux translates to spectral types O7.5V – O7V and O8.5V – O8V for G346.056−0.021 and G346.077−0.056, respectively. Similar spectral types are obtained if we use the results of Davies et al. (2011) and Mottram et al. (2011). If we consider the compact, cometary H II region seen in the higher-resolution 1280 MHz map to be internally ionized, then the integrated flux density implies a massive star of spectral type B0.5 – B0. The spectral type estimate for the ionizing star of G346.077−0.056 remains the same if we subtract out the flux density of this component. Taking the bolometric luminosities from the RMS survey paper by Lumsden et al. (2013) and comparing the same with the tables of Mottram et al. (2011), we obtain consistent spectral type estimates of O8 – O7.5 for both the H II regions. As mentioned earlier, this estimate is with the assumption of optically thin emission and hence serves as a lower limit as the emission could be optically thick at 1280 MHz. Several studies have shown that dust absorption of Lyman continuum photons can be very high (Inoue et al., 2001; Arthur et al., 2004; Paron et al., 2011). With limited knowledge of the dust properties, we have not accounted for the dust absorption in the above estimates. The Lyman continuum fluxes suggest massive stars of masses $\sim$ 25 and $\sim 20\mathrm{M_\odot}$ responsible for the ionized emission of G346.056−0.021 and G346.077−0.056, respectively (Davies et al., 2011).

We use a simple model discussed in Spitzer (1978); Dyson & Williams (1980) to estimate the dynamical ages of the two H II regions. If an H II region evolves in a homogeneous medium then its dynamical age can be estimated from the following expressions

$$R_{st} = \left[\frac{3N_{Ly}}{4\,\pi\,n_{H,0}^2\,\alpha_B}\right]^{1/3} \tag{5.6}$$

$$t_{dyn} = \frac{4}{7}\,\frac{R_{st}}{C_{Hii}}\left[\left(\frac{R_{if}}{R_{st}}\right)^{7/4} - 1\right] \tag{5.7}$$

where, R_{st} is the Strömgren radius, N_{Ly} is the Lyman continuum photons coming from the ionizing source, $n_{H,0}$ is the particle density of the neutral gas, and α_B is the coefficient of radiative recombination and is taken to be 2.6 $\times 10^{-13}$ $(10^4$ K/T$)^{0.7}$ cm^3 sec^{-1} from Kwan (1997). In the second expression, t_{dyn} is the dynamical age, C_{Hii} is the isothermal sound speed of ionized gas (assumed to be 10 km s^{-1}), and R_{if} is the radius of the H II region. For R_{if}, we use the deconvolved sizes of 17″ (0.9 pc) and 9″ (0.5 pc) for G346.056−0.021 and G346.077−0.056, respectively. $n_{H,0}$ is estimated from the column density map (refer to Sect. 5.2.3) and is found to be 6.2×10^4cm^{-3} and 4.8×10^4cm^{-3} for G346.056−0.021 and G346.077−0.056, respectively. For G346.077−0.056, the estimated values of $n_{H,0}$ is higher than that obtained by Yu et al. (2015) by a factor of approximately 6. Using these values in the above equations, we estimate the dynamical ages for G346.056−0.021 and G346.077−0.056 to be 0.5 and 0.2 Myr, respectively. The derived age should however be treated with caution since the assumption of expansion in a homogeneous medium is not a realistic one.

5.2.2 Associated stellar population

Figure 5.4 shows the NIR view of the region associated with the two H II regions. The region is seen to be densely populated. The zoom of the region associated with G346.077−0.056 shows the presence of faint K-band nebulosity harboring the IR cluster VVVCL094 (Borissova et al., 2011). These authors have estimated the cluster radius to be 20″. After a statistical decontamination of field star population, they propose 20 probable members for this cluster. As part of another statistical study of clusters in the inner Galaxy, Morales et al. (2013) classified VVVCL094 as an embedded cluster whose estimated center coincides with the ATLASGAL peak. Given the correlation of the cluster with the probed ionized region, it is likely that the most

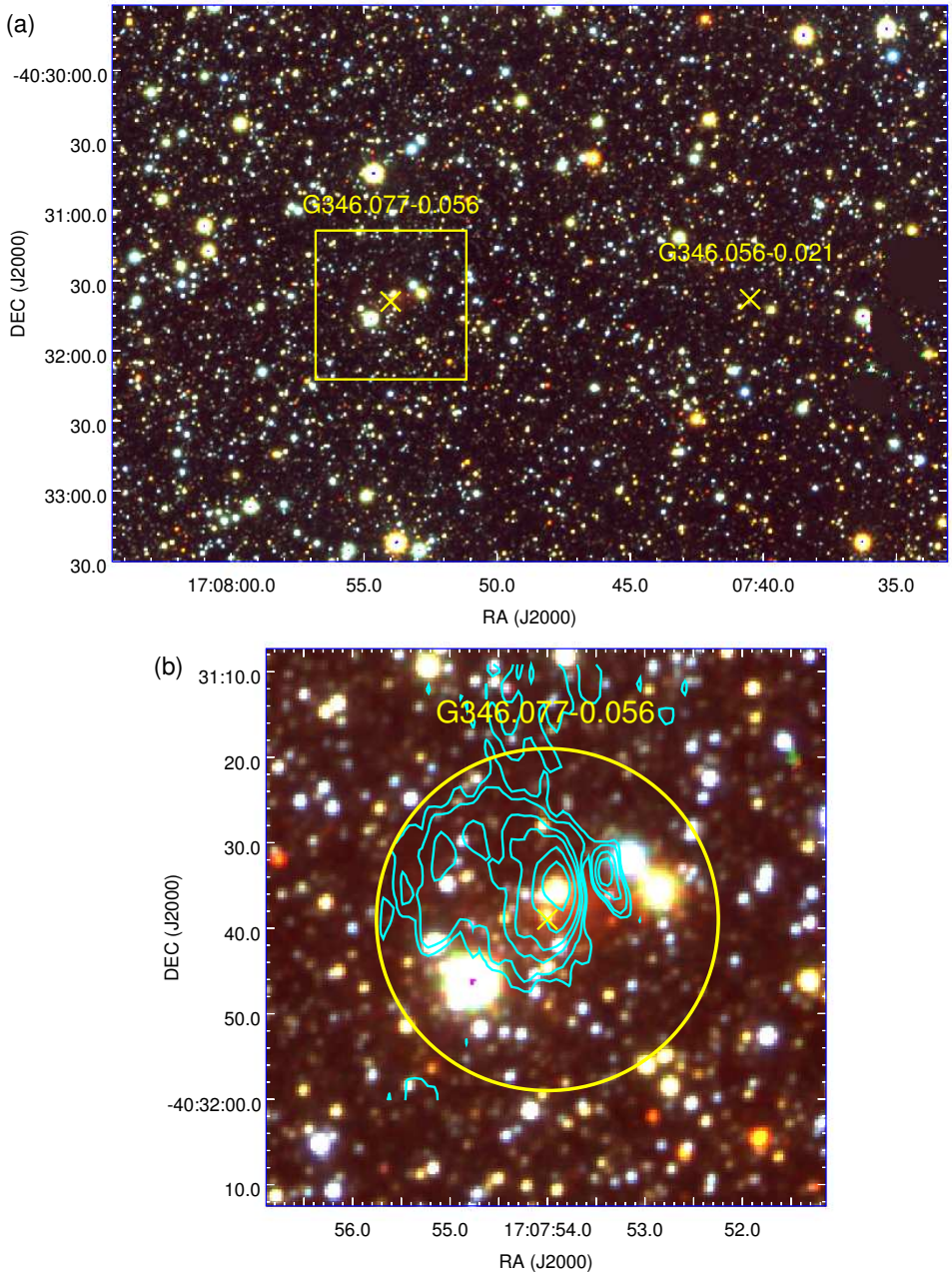

Figure 5.4: (a) NIR color composite image of the region associated with the H II regions using VVV JHK band images (red – K; green – H; blue – J). '×' marks show the location of the H II regions. (b) Zoomed in view of indicated region related to G346.077−0.056. The yellow circle denotes the size of the cluster as estimated by Borissova et al. (2011). The cyan contours show the higher-resolution 1280 MHz radio emission with the levels same as those plotted in Figure 5.2.

massive members of it are responsible for the detected H II region. Using the NIR data from the VVV and 2MASS surveys, we attempt to identify candidate ionizing star(s) responsible for the H II regions and study the distribution of the associated YSOs. We probe the region shown in Figs. 5.1 and 5.4. Adopting the set of criteria described in Chapter 2, we generate a good photometry quality merged catalog of 2013 sources with 1927 and 86 sources from the VVV catalog and the 2MASSPSC, respectively. Figure 5.5 shows the (J − H) versus (H − K) CCP and K versus (H − K) color-magnitude plot (CMP) for the sources in our merged catalog. In our search for the candidate ionizing stars, we take into account two points - (i) the ionizing stars are likely to be located within the radio contours and (ii) the Lyman continuum photon flux estimates from the GMRT radio maps (see Sect. 5.2.1) sets lower limits on the spectral types of O7.5V – O7V and O8.5V – O8V for G346.056−0.021 and G346.077−0.056, respectively. Hence, on the CCP and CMP we highlight the sources falling within the 3σ contours of the radio emission for G346.056−0.021 and G346.077−0.056, respectively and also lying above the reddening vector for spectral type O9. The identified sources are labeled # 1 to # 6 (black filled circles) for G346.056−0.021 and # 7 to # 11 (black open circles) for G346.077−0.056. Table 5.4 lists the position and photometric magnitudes of these sources and Figure 5.6(a) shows the location of these sources on the MIR 8 μm IRAC image with overlaid radio contours. The ATLASGAL clumps, discussed in the following section are also

Table 5.4
Details of the candidate ionizing star(s) for the H II regions.

#	RA (J2000) (hh:mm:ss.ss)	DEC (J2000) (dd:mm:ss.ss)	J (mag)	H (mag)	K / K_s (mag)
1*	17:07:39.81	−40:31:41.43	13.91	11.37	10.21
2	17:07:40.16	−40:31:51.95	16.57	14.22	13.11
3*	17:07:40.46	−40:31:11.82	14.51	12.84	12.15
4	17:07:40.99	−40:31:39.97	15.61	13.37	12.25
5	17:07:41.65	−40:31:24.00	17.71	14.46	12.73
6	17:07:43.02	−40:31:33.92	15.90	14.09	13.17
7*	17:07:52.93	−40:31:34.40	12.96	12.36	11.05
8*	17:07:53.25	−40:31:30.87	12.02	10.97	10.51
9*	17:07:53.98	−40:31:34.85	14.23	12.21	11.13
10	17:07:54.85	−40:31:45.17	10.71	9.39	8.87
11	17:07:55.24	−40:31:40.80	13.67	12.84	11.84

* Photometric magnitude are from 2MASSPSC.

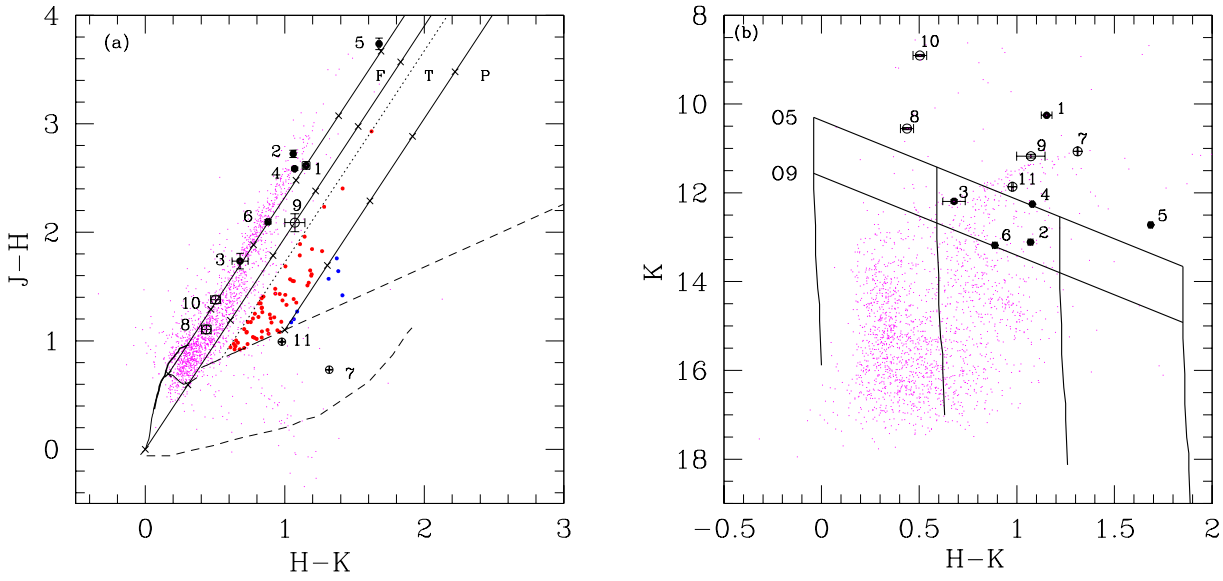

Figure 5.5: (a) (J − H) vs. (H − K) CCP for the region associated with the H II regions. The loci of main sequence (thin line) and giants (thick line) are taken from Bessell & Brett (1988). The classical T Tauri locus (long dashed line) is adopted from Meyer et al. (1997) and that for the Herbig AeBe stars (short dashed line) is from Lada & Adams (1992). The parallel lines are the reddening vectors where cross marks indicate intervals of 5 mag of visual extinction. The interstellar reddening law assumed is from Rieke & Lebofsky (1985). The colors and curves in the CCP are all converted into Bessell & Brett (1988) system. The regions 'F', 'T', and 'P' are discussed in the text. The dotted line parallel to the reddening vector accounting for an offset of three times the photometric error in the bands. On the CCP, the Class I sources (blue) and Class II sources (red) are shown as filled circles. The candidate ionizing stars are shown as filled black circles (for G346.056−0.021) and open circles (for G346.077−0.056) on both CCP and CMP. The individual error bars on the colors and magnitude are also plotted. (b) K vs. (H − K) CMP for the region associated with the H II regions. The nearly vertical solid lines represent the ZAMS loci with 0, 10, 20 and 30 magnitudes of visual extinction corrected for the distance. The slanting lines show the reddening vectors for spectral types O9 and O5. The magnitudes and the ZAMS loci are all plotted in the Bessell & Brett (1988) system.

shown in this figure. Figures 5.6(b) and (c) show the zoomed-in region for G346.077−0.056 and G346.056−0.021, respectively, on the K-band VVV image.

As seen from the CCP, apart from sources # 7 and # 11, the rest of the likely candidates earlier than O9 fall in the region occupied by main sequence or Class III sources. The location of sources # 7 and # 11 indicates that they are mostly reddened Herbig AeBe stars. Further, given the distance of 10.9 kpc to the H II regions and assuming a foreground extinction of $A_V \sim 1$ per kpc, the CMP suggests that sources # 8 and # 10 are unlikely to be associated with the H II regions. This makes the source # 9, which coincides with the radio peak (within 1″) a promising candidate ionizing star responsible for G346.077−0.056. In case of G346.056−0.021, all the early-type stars within the ionized region lie close to the left-most reddening vector. Within the photometric errors and the uncertainty involved in defining the reddening vector itself, sources # 1, # 3, # 5, and # 6 may be considered as Class III sources. However, one cannot rule out the possibility of these being highly reddened giants. Looking at their distribution within the ionized region, source # 5 has a better chance of qualifying as the ionizing source. This corroborates well with the fact that G346.056−0.021 is a young, compact H II region and thus one expects the ionizing star to be close to the radio peak. Another likely candidate would be the Class II source (located at $\alpha_{2000} = 17^{\rm h}07^{\rm m}41.13^{\rm s}$, δ_{2000}=−40°31′19.67″ with J = 17.16, H = 16.14, and K = 15.22) located close to source # 5. This can also be considered as a massive, embedded exciting source. In their study of the IR dust bubble S51, Zhang & Wang (2012) identified a Class II massive (O-type) source as the candidate ionizing star. One needs to also keep in mind that there could be multiple sources masquerading as single sources given the large distance to this complex. Detailed spectroscopy and spectral energy distribution (SED) modeling is required to confirm the identified candidates.

To understand the star formation activity towards the H II regions, we examine the spatial distribution of YSOs using the *Spitzer* GLIMPSE, VVV, and 2MASS point source photometry. To identify candidate YSOs, we adopt the schemes proposed by Allen et al. (2004) and Chavarría et al. (2008) which are based on IRAC photometry. In addition, we also explore the 2MASS CCP. Refer to Section 2.3.1 of Chapter 2 for detailed discussion on the above YSO identification methods. From the sources in our sample, we estimate a mean photometric error of ∼ 0.06 mag in all three NIR bands. To account for this photometric uncertainty and the error involved

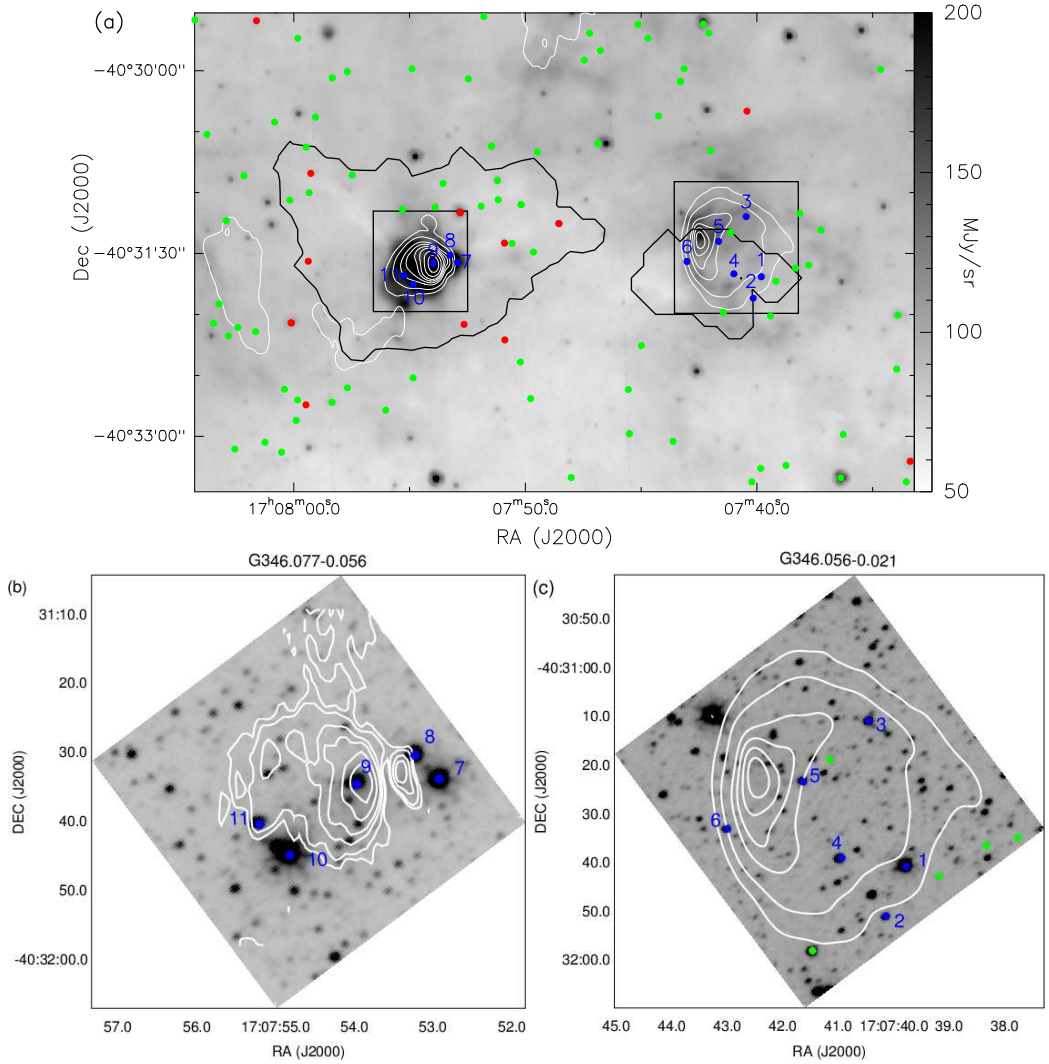

Figure 5.6: (a) Distribution of candidate ionizing stars and YSOs on the *Spitzer* 8.0 μm image. Identified YSOs have the following color coding - Class I (red), Class II (green). The ionizing stars are shown in blue. The detected clump apertures (see Sect. 5.2.3) are displayed in black. 1280 MHz (low resolution) radio contours are overlaid with levels of 3, 9, 13, 25, 30, 40, and 50 times σ. (b) and (c) are zooms of regions (marked as black rectangles in (a)) associated with G346.077−0.056 and G346.056−0.021, respectively, on the K-band VVV image. In (b), we have overlaid the high-resolution 1280 MHz radio contours shown in Figure 5.2 to reveal the finer structures.

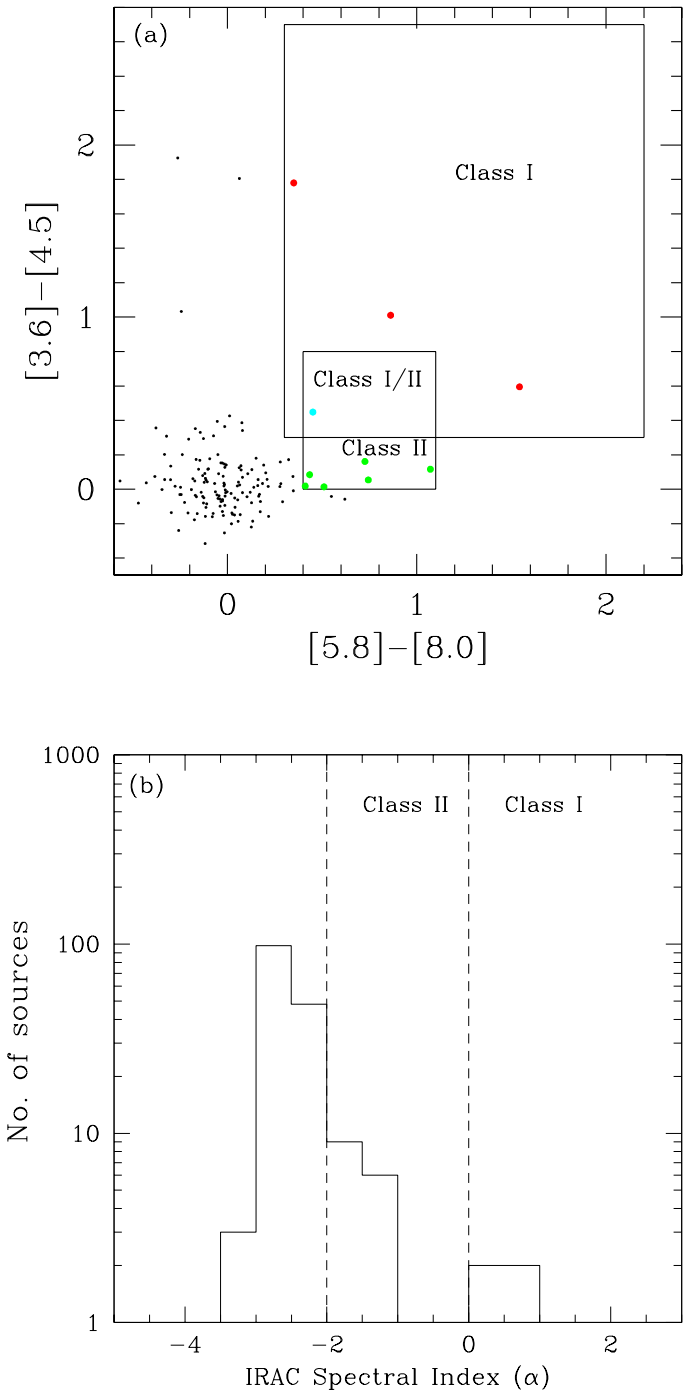

Figure 5.7: (a) IRAC CCP for the sources in the H II regions. The boxes demarcate the location of Class I (larger box) and Class II (smaller box) (Vig et al., 2007). Sources falling in the overlapping area are designated as Class I/II. The identified YSOs have the following color coding - Class I (red), Class II (green) and Class I/II (cyan). (b) The histogram showing the number of sources within specified spectral index bins. The regions demarcated on the plot are adopted from Chavarría et al. (2008) for classification of YSOs.

in defining the reddening vector, in the 2MASS CCP, we take a conservative offset of three times the photometric error to eliminate contamination to the Class II sample from the field star population. This is shown as the dotted line in Figure 5.5. It should be noted here that there might be a few genuine Class II sources which get filtered out in this process.

Based on the above three criteria, we identify 12 Class I and 80 Class II sources in the probed region, and Figure 5.6(a) shows their distribution on the MIR 8.0 μm IRAC image. The distribution is random with a marginal overdensity of Class I sources within the dust clump associated with G346.077−0.056 and the absence of Class I sources in the region related to G346.056−0.021. Figures 5.6(b) and (c) zoom in to the respective H II regions. Spectroscopic studies are essential to ascertain the nature of these identified YSOs and their association with the H II regions. It should be kept in mind that our YSO sample is not complete. The overwhelming MIR diffuse emission associated with the H II regions, especially G346.077−0.056, renders the detection and photometry of point sources impossible which reflects a lack of point sources in the GLIMPSE catalog.

5.2.3 Emission from dust component

Figure 5.8 shows the MIR and FIR emission sampled in the IRAC, MIPSGAL, and Hi-Gal images. Diffuse emission is seen towards the H II regions in all four IRAC bands. As discussed in Watson et al. (2008), various processes contribute to the emission in each IRAC band. These include thermal emission from the circumstellar dust heated by the stellar radiation and emission due to excitation of polycyclic aromatic hydrocarbons (PAHs) by UV photons in the Photo Dissociation Regions. In H II regions there would be significant contribution from trapped Lyα heated dust as well (Hoare et al., 1991). Apart from this, diffuse emission in the Brα and Pfβ lines and H_2 line emission from shocked gas would also exist (Watson et al., 2008). The shorter IRAC bands (3.6, 4.5 μm) reveal the point sources, since emission here is dominated by the stellar photosphere. As seen in the figure, the two H II regions show up as faint, compact nebulosities. The extent and brightness of the diffuse emission increases from 3.6 μm to 8.0 μm. Further, at 5.8 and 8.0 μm, G346.056−0.021 shows an extended bubble-type morphology towards the south-west. G346.077−0.056 shows an extended, diffuse morphology with an irregular distribution of MIR emission (see Figure 5.12). This will be discussed in more detail in a later section. The comparison of the [5.8] band, which is mostly a dust tracer, and the

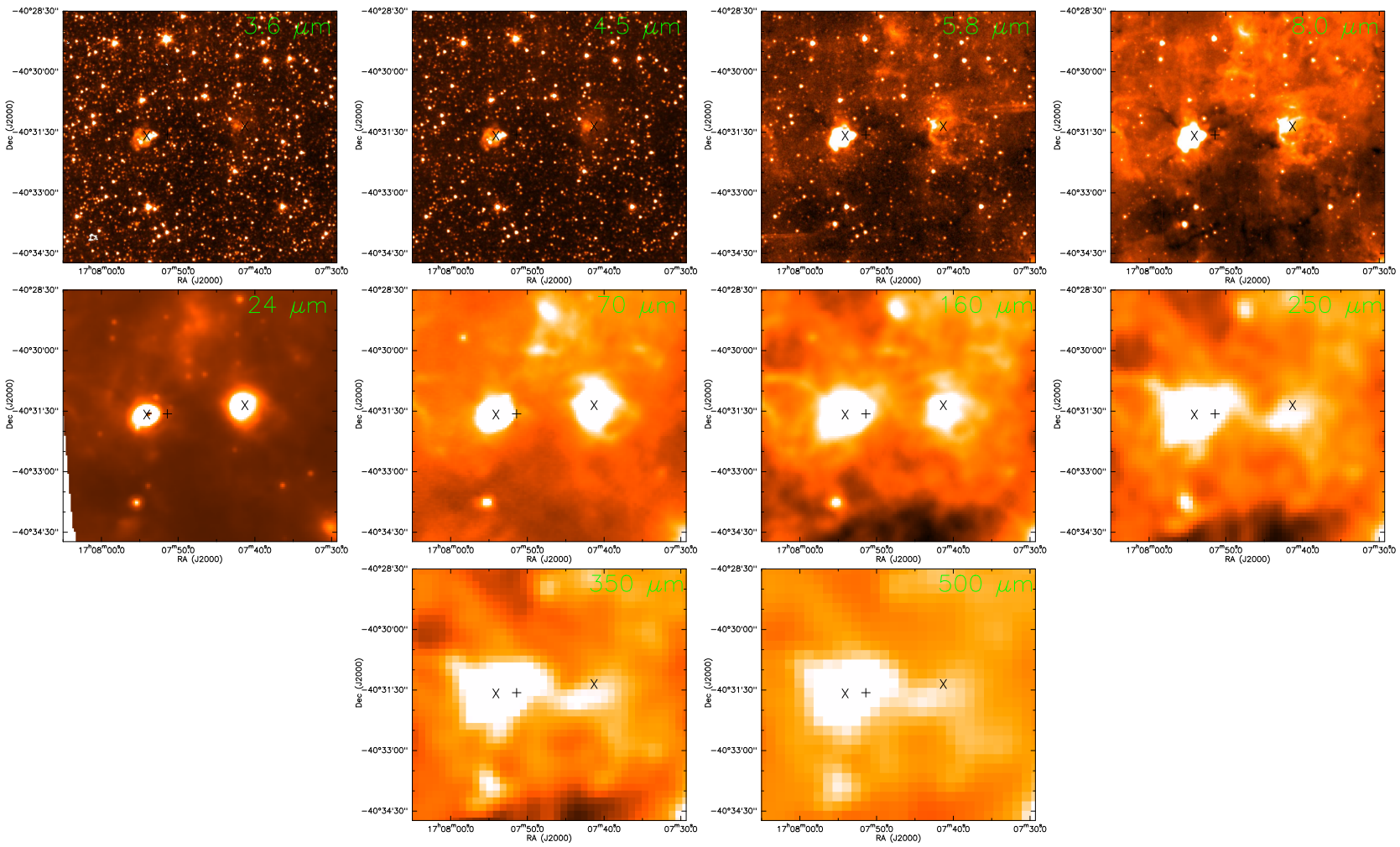

Figure 5.8: Dust emission associated with the H II regions is shown: top panel from left 3.6, 4.5, 5.8, 8.0 μm; middle panel from left 24, 70, 160, 250 μm ; bottom panel from left 350, 500 μm. The '×' marks are the positions of the H II regions. The '+' mark shows the position of the associated IRAS point source, IRAS 17043−4027.

[4.5] band, which has significant contribution from Brα emission (H^+ tracer) (Churchwell et al., 2004) shows that the two H II regions are dominated by dust emission. The 24 μm emission is in unison with the radio free-free emission. This emission which spatially correlates well with the ionized component can be attributed to Lyα heating of normal-size dust grains that could maintain the temperatures close to 100 K in the ionized region (Hoare et al., 1991). Few authors also associate the 24 μm emission in H II regions with either Very Small Grains or Big Grain replenishment (Everett & Churchwell, 2010b; Paladini et al., 2012). As we move towards the cold dust sampled with the *Herschel* bands, filamentary structures are prominent and seem to connect the two H II regions. The extent and brightness of G346.056−0.021 decreases and that of G346.077−0.056 increases as we go longward of 160 μm suggesting the dominance of warm dust in G346.056−0.021 and cold dust in G346.077−0.056.

Column density and dust temperature maps

We study the nature of the cold dust emission using the *Herschel* FIR bands. Following the formulation described in Section 2.3.2 of Chapter 2, line-of-sight average molecular hydrogen column density, and dust temperature maps are generated by pixel-wise modified single temperature blackbody fits using the background-corrected fluxes and assuming the emission at these wavelengths to be optically thin. As mentioned earlier, given the limited number of data points confined to the Raleigh-Jeans part of the emission, we prefer to fix the value of β to 2 (Hildebrand, 1983; Beckwith et al., 1990; André et al., 2010) which is also a typical value estimated for a large sample of H II regions (Anderson et al., 2012b). Following the procedure explained in Chapter 3 we have estimated the background flux, I_{bkg}, in each band from the region which is located at an angular distance of $\sim 1^\circ$ from the H II regions and centered at $\alpha_{2000} = 17^h11^m57.17^s$, δ_{2000}=−41°06′38.99″. I_{bkg} is estimated to be −3.22, 1.45, 0.72, 0.26 Jy pixel^{-1} at 160, 250, 350, and 500 μm, respectively. As discussed in Chapter 2 and adopted in several studies (Peretto et al., 2010; Anderson et al., 2010; Battersby et al., 2011; Liu et al., 2016) we have also excluded the 70 μm emission.

The generated column density, dust temperature maps, and the corresponding χ^2 map are shown in Figure 5.10. We have overlaid the 1280 MHz radio map to correlate the emission from ionized gas and the cold dust component. The fitting uncertainties are small as is evident from the χ^2 map where the maximum value for individual pixel fits is ~ 1. The χ^2 map clearly reveals

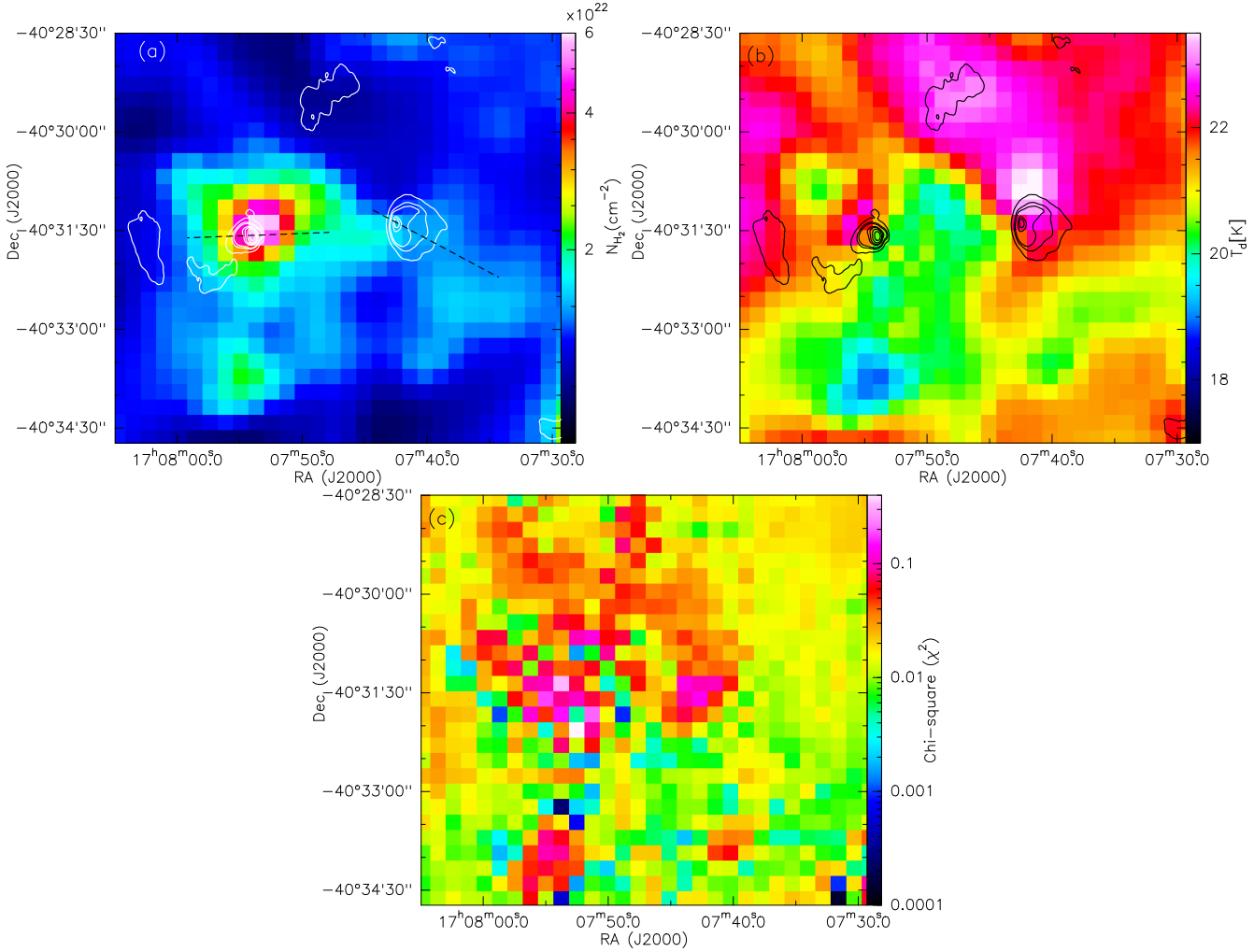

Figure 5.10: Column density (a), dust temperature (b) and chi-square (χ^2) (c) maps of the region associated to H II regions. 1280 MHz GMRT radio emission is shown as contours. The contour levels are same as those plotted in Figure 5.6. The dashed line on the H II regions shows the projections, the column density variation which is used to understand the morphology of the ionized region in a later Section.

that the pixels towards the H II regions fit better to the SED model. In Figure 5.9, we show the model fitting of two pixels having the minimum and maximum χ^2 values. The one with the maximum χ^2 is located toward the H II region G346.077−0.056 and the pixel with lowest χ^2 is located toward the south of G346.056−0.021. The column density map shows a large clump

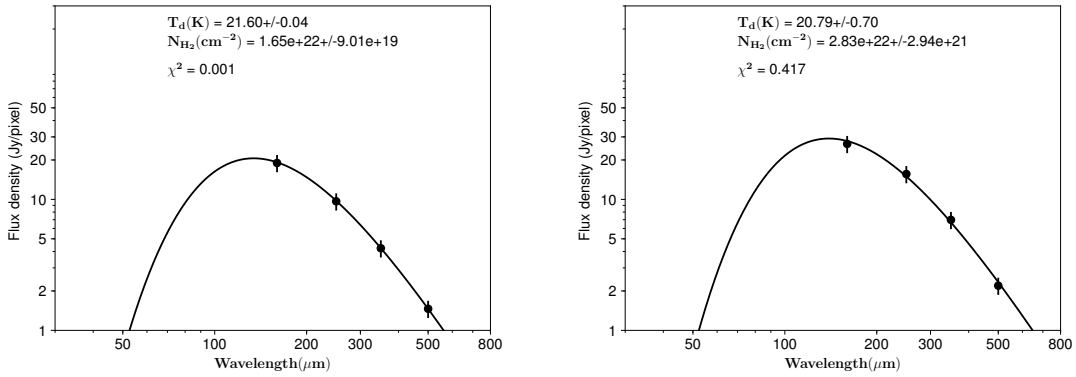

Figure 5.9: Modified black body fitting for two individual pixels having the best (0.001) and the worst (0.42) χ^2 values.

enveloping the H II region G346.077−0.056 with the previously mentioned western filamentary structure visible. The region associated with G346.056−0.021 shows relatively low column density which is indicative of a less significant cold dust component. The peak (5.9×10^{22} cm^{-2}) is located close to the radio peak of G346.077−0.056. Apart from the H II regions, a compact, spherical clump is seen to the south of G346.077−0.056. The association of this clump with the H II regions is not certain as there is no supporting literature available. As expected, we see regions of higher dust temperature toward both the H II regions. The dust temperature map shows extended warm distribution towards the north-east of G346.056−0.021 with the dust temperature distribution peaking just north of G346.056−0.021. This extended distribution coincides with a faint diffuse ionized structure (detected at the 3σ level of the 1280 MHz emission). The southern compact clump displays the coldest dust temperature.

Properties of dust clumps

To identify and study the cold dust clumps, we use the ATLASGAL 870 μm map because this wavelength is sensitive to the colder dust components and also the emission is optically thin. Further, the resolution of the ATLASGAL map is better (18″.2) compared to the column density map (35″.7). We use the two-dimensional (2D) *Clumpfind* algorithm (Williams

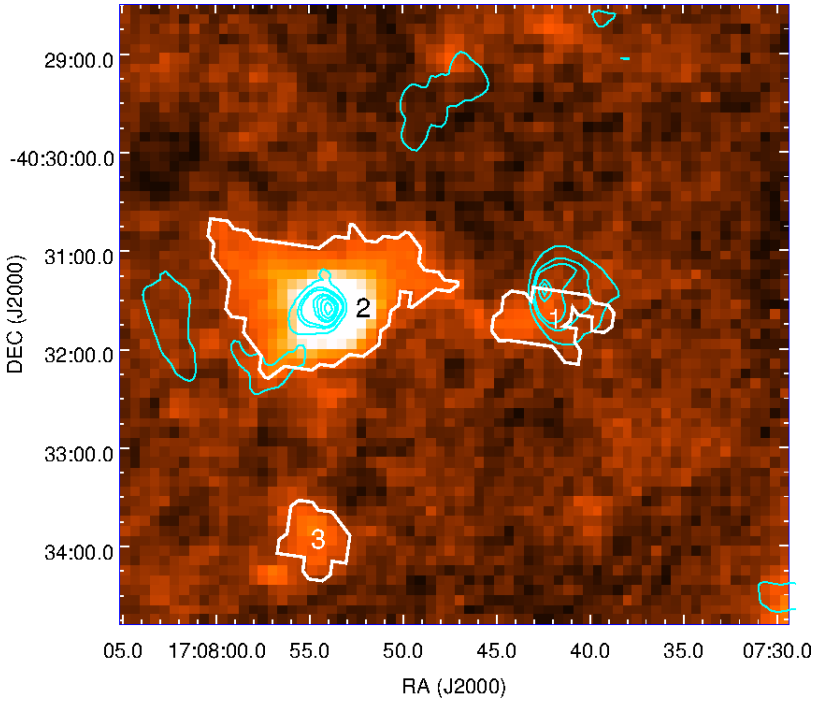

Figure 5.11: ATLASGAL image shown, on top of which the clump apertures are overlaid. The clumps are labeled as 1, 2, and 3. 1280 MHz GMRT radio emission is shown as cyan contours with the same levels as those plotted in Figure 5.6.

et al., 1994) with a 2σ (where, σ = 0.06 Jy/beam) threshold and optimum contour levels to detect the clumps. Chapter 3 briefly outlines the prominent features of this algorithm. Using this threshold three clumps are detected, the retrieved apertures of which are shown overlaid on the ATLASGAL image in Figure 5.11. Clump 1 overlaps with the southern part of the H II region G346.056−0.021 and is mostly part of the filamentary structure. Clump 2 is seen to be associated and enveloping G346.077−0.056. Clump 3 is located towards the south of G346.077−0.056. Masses of the clumps are estimated using the following expression

$$M_{clump} = \mu_{H_2} m_H A_{pixel} \Sigma N(H_2) \tag{5.8}$$

where, m_H is the mass of hydrogen, A_{pixel} is the pixel area in cm^2, μ_{H_2} is the mean molecular weight and $\Sigma N(H_2)$ is the integrated column density over the pixel area. Clump apertures retrieved from the *Clumpfind* algorithm are used to determine $\Sigma N(H_2)$ from the column density map. Location of 870 μm peaks, deconvolved sizes, mean dust temperature, mean column density, integrated column density, masses, and number density ($n_{H_2} = 3\Sigma\, N(H_2)\,/4r$, r being the

radius) of the clumps are estimated and listed in Table 5.5. Clump 2 has been studied by Yu et al. (2015). They have estimated the mass of the clump from 870 μm integrated flux density. Assuming a dust temperature of 30 K, they obtain a mass of 13013 $M_{\odot}$. This is a factor of $\sim$ 1.2 lower than the estimates from our column density map. The possible reason for the higher mass estimate in our work could be the lower dust temperature (21 K) and different dust opacity assumed. One also cannot exclude the effect of flux loss associated with ground-based observations (Liu et al., 2017a)

5.3 Morphology of the HII regions

As mentioned in Sect. 5.2.1, both the H II regions show signature of cometary morphology in the radio. This morphology shows up as a bright, arc-type head and a diffuse, broad tail emission. In Figure 5.12, we compare the radio morphology with the MIR emission in IRAC 8.0 μm band. The radio and MIR emission associated with G346.056−0.021 is seen to spatially correlate towards the head but there is a void in the MIR emission towards the tail implying that the H II region is density-bounded towards the south-west. The picture presented by G346.056−0.021 is similar to that of the cometary H II region G331.1465+00.1343 shown in Figure 1 of Hoare et al. (2007). In contrast, the MIR emission associated with G346.077−0.056 is extended and envelopes most of the ionized region. The radio peak and the possible second H II region is seen to coincide with the enhanced MIR emission towards the east.

In this Section, we attempt to understand the origin of such cometary morphologies that are commonly seen in H II regions (Wood & Churchwell, 1989). Several models have been proposed in the literature to address this, of which the frequently used ones are (i) the bow-shock model and (ii) the champagne-flow model. The former is due to the interaction of a supersonically moving, wind-blowing, ionizing star with the dense surrounding molecular gas. The latter model is a result of a steep density gradient encountered by an expanding H II region around a nearly stationary, ionizing source. Here, the ionizing star is possibly located at the edge of a dense clump where the ionized gas expands asymmetrically out towards regions of minimum density. Initial papers by Israel (1978); Tenorio-Tagle (1979); Reid & Ho (1985); van Buren et al. (1990); Mac Low et al. (1991) offer a detailed insight into these two models and the related physical conditions favoring one over the other. Recently, more involved

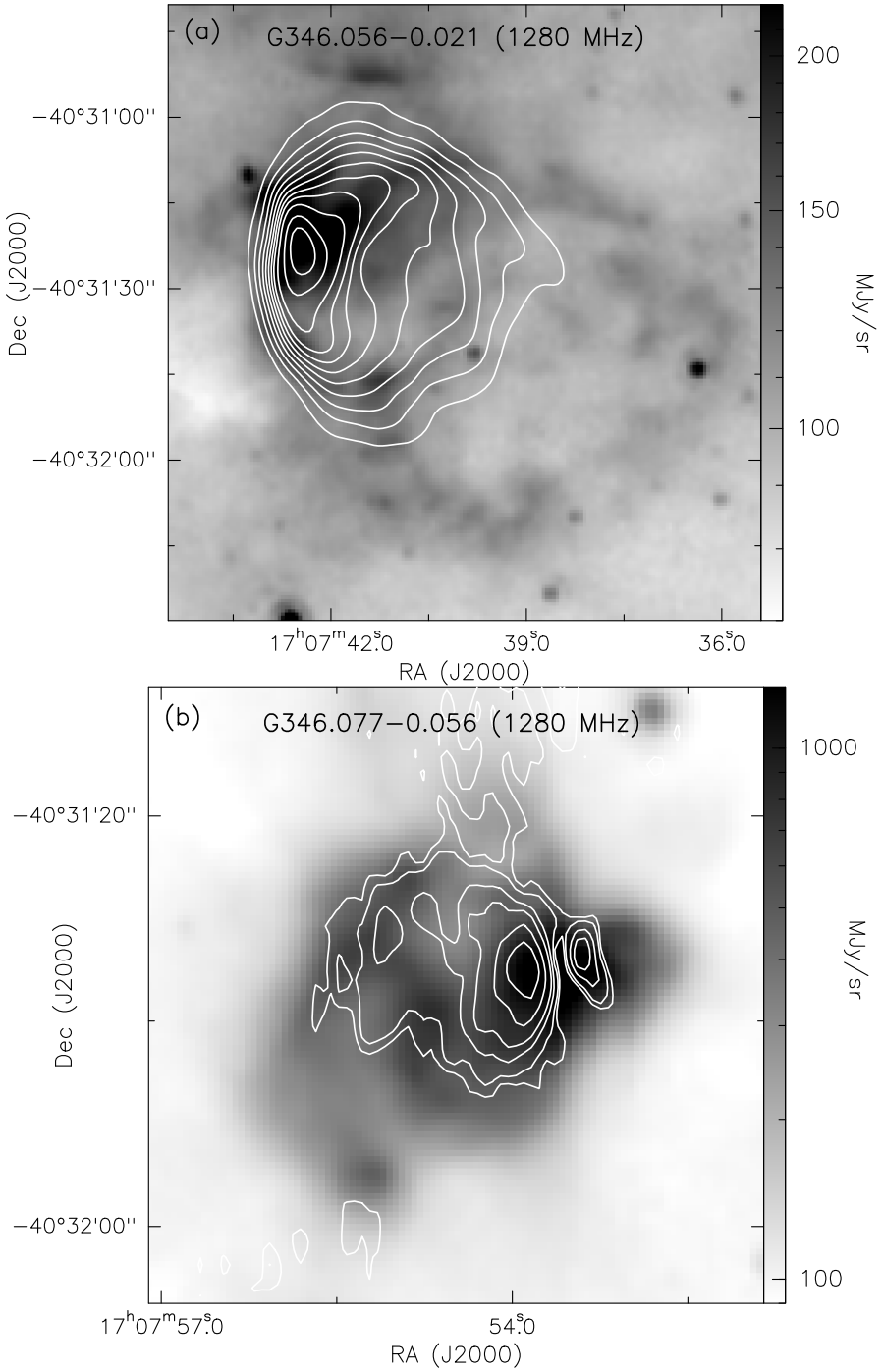

Figure 5.12: 1280 MHz radio contours overlaid on the 8.0 μm gray-scale image of (a) G346.056−0.021 and (b) G346.077−0.056. In (a) we have overlaid the lower-resolution contours presented in Figure 5.3 and in (b) to show the finer structures, we plot the higher-resolution contours as shown in Figure 5.2.

Table 5.5
Physical parameters of the clumps. The columns refer to location of 870 μm peaks, deconvolved sizes, mean dust temperature, mean column density, integrated column density, mass and number density ($n_{H_2} = 3\Sigma\, N(H_2)\,/4r$)

Clump No.	RA (2000) (hh:mm:ss.ss)	DEC (2000) (dd:mm:ss.ss)	Radius (pc)	Mean T_d (K)	Mean $N(H_2)$ ($\times10^{22}$cm^{-2})	$\sum N(H_2)$ ($\times10^{23}$cm^{-2})	Mass ($M_\odot$)	n_{H_2} ($\times10^{4}$cm^{-3})
1	17:07:43.32	−40:31:47.77	0.6	21.6	1.5	1.6	1922	3.1
2	17:07:12.02	−40:36:57.00	1.3	21.0	2.9	12.5	15248	2.4
3	17:07:09.40	−40:37:09.09	0.2	19.1	1.9	1.2	1412	45.9

radiation-hydrodynamic models have been proposed that include density gradient in the surrounding medium and a stellar wind contribution from an ionizing star in addition to its supersonic motion within the ambient cloud (Arthur & Hoare, 2006). Another recent paper by Roth et al. (2014) explores a quasi-one-dimensional, steady-state wind model to explain the cometary morphology of UCH II regions. High spatial and spectral resolution observations of the MIR [Ne II] fine structure line in a sample of H II and UCH II regions by Zhu et al. (2005, 2008) have shed further light on the various models. These studies show the co-existence of H II regions with dense and massive molecular cores where the ionized emission displays parabolic shells with the open end facing away from the dense cores and the kinematics reveal gas flow tangential to these shells. RRL studies of cometary H II regions have also invoked 'hybrid' (combination of bow-shock and champagne-flow) models to explain the observed velocity structure (Immer et al., 2014)

Based on simple analytic expressions and arguments, we aim at interpreting the observed morphology of the ionized emission and the column density distribution associated with our H II regions. We first consider the bow-shock model and derive the bow-shock parameters along the lines discussed in Reid & Ho (1985); van Buren et al. (1990); Mac Low et al. (1991). In this model, the stellar wind freely streams in all directions until it encounters a terminal shock. In the direction of motion, the shock occurs at a distance l_s (stand-off-distance) from the star, where the momentum flux of the wind equals ram pressure of the surrounding ambient ISM. This 'bow-shock' gives rise to a H II region resembling a thin paraboloidal shell in the plane of the sky.

The stand-of distance l_s is estimated using the following expressions (van Buren et al., 1990; Mac Low et al., 1991)

$$l_s = 5.50 \times 10^{16}\ \dot{m}_{*,-6}^{1/2}\ v_{w,8}^{1/2}\ \mu_H^{-1/2}\ n_{H,5}^{-1/2}\ v_{*,6}^{-1}\ \mathrm{cm} \tag{5.9}$$

$$\dot{m}_{*,-6} = 2 \times 10^{-7}\ (L/L_\odot)^{1.25}\ M_\odot\ \mathrm{yr}^{-1} \tag{5.10}$$

$$\log v_w = -38.2\ + 16.23\ \log T_{eff}\ - 1.70\ (\log T_{eff})^2 \tag{5.11}$$

where, $\dot{m}_{*,-6} = \dot{m}_* \times 10^6\ M_\odot\ \mathrm{yr}^{-1}$ is the stellar wind mass-loss rate, $v_{w,8} = v_w \times 10^8 \mathrm{cm\ sec}^{-1}$ is the

terminal velocity of the wind, μ_H is the mean mass per hydrogen nucleus, $n_{H,5} = n_H \times 10^5$ cm^{-3} is the hydrogen gas density, $v_{*,6} = v_* \times 10^6$ cm sec^{-1} is the relative velocity of star, L and $L_\odot$ are the luminosity of star and sun, respectively, and T_{eff} is the effective temperature of the star. The medium through which the star moves would be a combination of ionized and neutral medium. We consider a neutral medium here and take $\mu_H = 1.4\ m_H$, where m_H is taken as one atomic mass unit. We estimate n_H to be 6.2×10^4 cm^{-3} and 4.8×10^4 cm^{-3} for G346.056−0.021 and G346.077−0.056, respectively, from the column density maps (refer Sect. 5.2.3). For the estimated spectral type of the ionizing stars, we assume luminosities in the range 1.0×10^5 - $1.3 \times 10^5 L_\odot$ and 6.6×10^4 - $8.0 \times 10^4 L_\odot$ for G346.056−0.021 and G346.077−0.056, respectively, from Martins et al. (2005a). We further assume a typical velocity of 10 km sec^{-1} (van Buren & Mac Low, 1992) for the ionizing star. Plugging in these values in the above equations, we calculate the expected stand-off distances. For G346.056−0.021 we obtain a value of 0.4″ (0.02 pc) - 0.5″ (0.03 pc) and for G346.077−0.056 we estimate 0.2″ (0.01 pc) - 0.3″ (0.016 pc). In the image plane, the stand-off distance is defined as the distance between the steep density gradient at the cometary head and the radio peak (assuming this to be the location of the ionizing star). Hence from the the radio maps, we estimate l_s to be $\sim$ 9″ (0.5 pc) and $\sim$ 11″ (0.6 pc) for G346.056−0.021 and G346.077−0.056, respectively. These values are significantly larger than the expected theoretical values. The discrepancies between the theoretical and observed stand-off distance estimates narrows down if we consider ionizing stars to move slower, with a velocity of $\sim$ 1 km sec^{-1}. It should be noted here that the ionizing star need not always be at the location of the radio peak (Martín-Hernández et al., 2003a) and that the viewing angle would also play a role in the estimated stand-off distance.

Further light can be shed by deriving the trapping parameter (τ_{bs}). As discussed in Mac Low et al. (1991), the dense shells swept up by the supersonically moving, ionizing star trap the H II region and the ram pressure inhibits their further dynamical expansion. This parameter is so defined that its inverse gives the ionization fraction. The shell thus traps the H II region when there are more recombinations in the shell compared to ionizing photons. This happens when $\tau_{bs} > 1$. This parameter is shown to be much larger ($\tau_{bs} >> 1$) as computed by Mac Low et al. (1991) for a sample of cometary H II regions. We estimate τ_{bs} for G346.056−0.021 and G346.077−0.056 using the following expression from Mac Low et al. (1991)

$$\tau_{\rm bs} = 0.282\ \dot{m}_{*,-6}^{3/2}\ v_{w,8}^{3/2}\ n_{H,5}^{1/2}\ T_{e,4}^{-1}\ N_{Ly49}^{-1}\ \mu_{H}^{-1/2}\ \gamma^{-1}\ \alpha_{-13} \tag{5.12}$$

where, $T_e = T_{e,4} \times 10^4$ is the temperature of ionized gas, $N_{Ly} = N_{Ly49} \times 10^{49}$ is the ionizing photon flux, γ is the ratio between specific heats, α is the hydrogen recombination rate to all levels but the ground state, given in units of 10^{-13}cm^3 sec^{-1}, and N_{Ly} is 3.2×10^{48} photons sec^{-1} and 1.6×10^{48} photons sec^{-1} for G346.056−0.021 and G346.077−0.056, respectively (refer Sect. 5.2.1). The temperature of ionized gas is 5500 K and 8900 K for G346.056−0.021 and G346.077−0.056, respectively, and the value of γ is 5/3. The value of α is estimated to be 4.3×10^{-13}cm^3 sec^{-1} and 3.0×10^{-13}cm^3 sec^{-1} at 5500 K and 8900 K, respectively, by a linear interpolation of the optically thick case from Osterbrock (1989). The derived values of $\tau_{\rm bs}$ lie in the range 4.3 – 2.7 and 1.8 – 1.2 for G346.056−0.021 and G346.077−0.056, respectively. These values suggest weak or no bow shock.

Considering the above, it is less likely that the bow-shock mechanism is in play in G346.056−0.021 and G346.077−0.056. Given this, we explore the alternate model of champagne flow. Here, the morphology of the H II region is mostly dictated by the density structure of the molecular cloud. The H II region expands preferentially toward low-density regions resulting in a champagne flow. To probe this, we try to understand the variation in ionized emission and correlate with the column density distribution along the respective cometary axes which are marked in Figure 5.10. We choose the 1280 MHz map. These projected lines also pass through the respective radio peaks of G346.056−0.021 and G346.077−0.056. The profiles are displayed in Figure 5.13. Here, the *x*-axis shows the positional offset from the radio peak increasing towards the direction of the 'tail'. The *y*-axis of the top panels which shows the variation in radio flux density is normalized to the peak values. In the bottom panels, the column density values are given in terms of 10^{22} cm^{-2}. The ionized emission profiles are characteristic of cometary morphology (Wood & Churchwell, 1989). What is interesting is the correlation with the density structure. As visible from the plots, the column density distribution peaks ahead of the ionized emission for both the regions implying that dense molecular gas is located at the head of the cometary arc of the H II regions which stalls the ionization front thus keeping the H II regions pressure and ionization bounded in the north-east and east directions for G346.056−0.021 and G346.077−0.056, respectively. On the other side, ionized gas streams away into the more rar-

efied environment which reveals itself as a decreasing column density distribution. These are signatures of a champagne flow. Thus it is likely that the cometary morphology is due to the density gradient rather than the supersonic motion of the ionizing star. It should be noted here that the above discussions are based on the projected morphology of the ionized and molecular gas where we have not considered the effect of viewing angle. One also has to keep in mind that the resolution and pixel sizes of the two maps used here are very different and hence crucial small-scale correlation is not possible. Though the analytical calculation based on simple assumptions do not present a strong case for a bow-shock scenario and the observed morphology agrees well with the champagne-flow model, it is necessary to study in detail the gas kinematics with the highest spectral and spatial resolution in order to understand the physical mechanism responsible for the cometary structure of the ionized regions.

5.4 Summary

We have carried out a detailed study of the complex associated with the two southern galactic H II regions, G346.056−0.021 and G346.077−0.056. Based on our analysis we deduce the following.

1. Radio continuum emission is detected towards both H II regions at 610 and 1280 MHz. The ionized emission morphology shows a cometary structure for G346.056−0.021. The morphology for G346.077−0.056 is mostly compact and spherical with a faint cometary signature.

2. The ZAMS spectral type of the ionizing sources are estimated to lie in the range O7.5V - O7V and O8.5V - O8V for G346.056−0.021 and G346.077−0.056, respectively. The dynamical ages of G346.056−0.021 and G346.077−0.056 are similar and estimated to be $\sim 0.5 - 0.2$Myr.

3. Emission from the dust component shows cold dust to be predominantly located near G346.077−0.056 and the region associated with G346.056−0.021 contains relatively warmer dust. The column density map shows the presence of a dense clump towards G346.077−0.056. Two additional clumps are detected in the 870 μm image, one of which is towards G346.056−0.021.

4. Assuming the clumps to be physically associated and hence at the same distance, the masses are estimated to be 1922, 15248, and 1412 $M_{\odot}$ for clumps 1, 2, and 3, respectively, from the column density map.

5. Simple analytical calculations show that the bow-shock mechanism is less likely to be responsible for the observed cometary morphology. The variation of the ionized gas and the column density along the cometary axis favors the champagne-flow model for both H II regions.

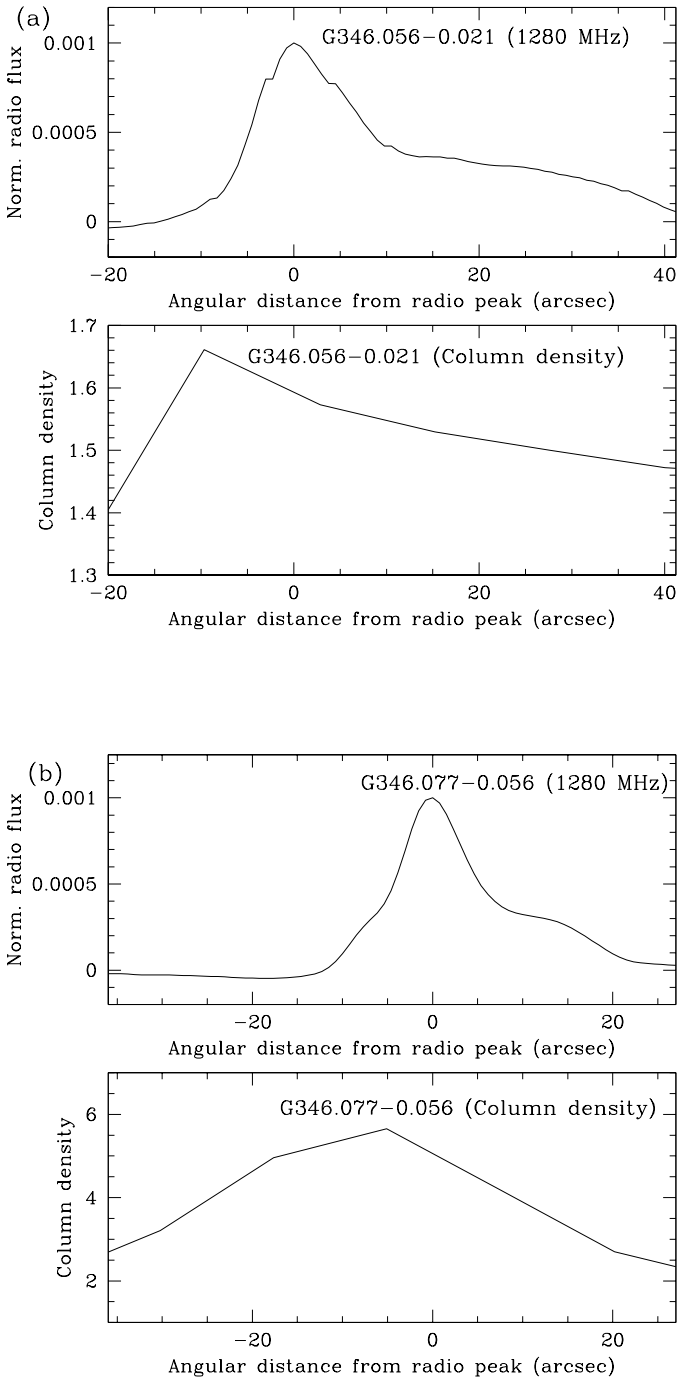

Figure 5.13: Relative distribution of radio emission and column density with respect to the radio peaks for G346.056−0.021 and G346.077−0.056 along the projections shown in the column density map in Figure 5.10. Zero on the x-axis corresponds to the position of the radio peaks increasing towards the direction of the tail (south-west for G346.056−0.021 and east for G346.077−0.056). The radio flux densities plotted are normalized to the peak flux densities and the column density is given in terms of 10^{22} cm^{-2}.

Chapter 6

Probing the cold dust emission associated with a sample of IR dust bubbles

6.1 Introduction

Star formation initiates in cold dense cores. To understand the star formation activity associated with IR dust bubbles, we need to probe the cold dust emission and study the nature of the detected dust clumps.

In this chapter, we present the study of cold dust emission associated with a sample of seventeen IR dust bubbles. These bubbles with varied morphologies are selected from the catalogue of Churchwell et al. (2006). We have selected 'northern' bubbles which belong to the northern ($l = 10^{\circ} - 65^{\circ}$) region as discussed by these authors. IR dust bubbles are ideal laboratories to investigate not only the influence of high-mass stars on the surrounding medium but also delve into understanding triggered star formation in the bubble periphery. For this identifying potential dust clumps and studying their properties is crucial.

6.2 Presenting the sample

We have done a careful literature survey and present the relevant details of each bubble.

1. **N10**

   N10 is classified as a complete or bipolar bubble by Churchwell et al. (2006). This bubble is also identified by Simpson et al. (2012) in the Milky Way project. N10 is also associated with IRAS 18111-1729. The near kinematic distance estimates to the bubble varies between 4.1 – 4.9 kpc (Szymczak et al., 2000; Churchwell et al., 2006; Pandian et al., 2008; Watson et al., 2008; Beaumont & Williams, 2010; Gama et al., 2016). Pandian et al. (2008) have resolved the kinematic distance ambiguity (KDA), towards the source through H I self absorption (HISA) spectra. They place the source at the near

kinematic distance of 4.6 kpc. Using CO observations towards the bubble, Gama et al. (2016) have calculated the near and far kinematic distance to be 4.7 and 11.3 kpc, respectively. Since the bubble lies in the inner disk of the Galaxy, these authors have adopted the near kinematic distance with 10% uncertainty and placed the source at 4.7±0.05 kpc. Based on the above, we have used a distance of 4.7 kpc for N10. Two compact radio sources (G13.180+0.050 and G13.189+0.039) are observed towards the bubble in the 5 GHz survey (Becker et al., 1994). Cold dust emission from SCUBA observations reveal the presence of three sub-mm components towards the bubble. Detection of H_2O and CH_3OH masers are reported by Braz & Epchtein (1983) and Szymczak et al. (2000), respectively. 6.7 MHz methanol maser is also detected towards the bubble by Pestalozzi et al. (2005).

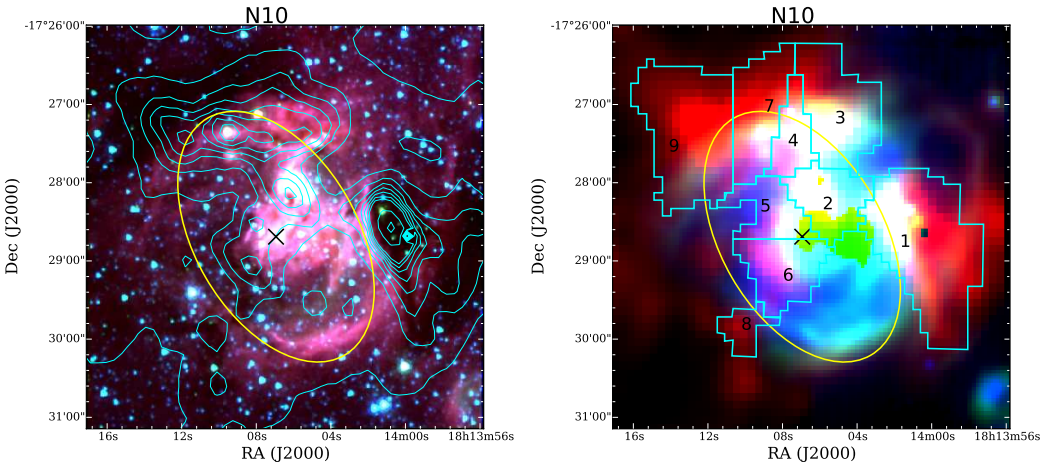

Figure 6.1: Left: MIR *Spitzer*-IRAC color composite image of bubble N10, with 8.0 μm (red), 4.5 μm (green), and 3.6 μm (blue). Cyan contours show 250 μm emission from *Herschel*. Right: FIR *Herschel* color composite image with 250 μm (red), 70 μm (green), and 24 μm (blue). White contours are the retrieved apertures for the detected cold dust clumps (see text). On both images '×' shows the position of the bubble center and the ellipse shows the extent of the bubble (Churchwell et al., 2006).

Figure 6.1 shows the MIR and FIR color composite images of N10. The figure shows the diffuse emission traced by 8 μm towards the border as well as the center of the bubble. As opposed to Churchwell et al. (2006) N10 shows a broken morphology. The warm dust emission seen at 24 μm is saturated towards the center of the bubble and the 70 μm emission is mostly seen on the periphery of the bubble. 250 μm cold dust emission displays

fragmented structures outside of the bubble.

2. **N32**

Morphologically, N32 is classified as a broken bubble by Churchwell et al. (2006). Simpson et al. (2012) have also identified this bubble. The bubble is associated with IRAS 18319-0802. The near and far kinematic distance estimates to the source vary between 2.4 – 4.6 and 11.0 – 13.1 kpc, respectively (Churchwell et al., 2006; Anderson & Bania, 2009; Schlingman et al., 2011). The KDA towards the source has been resolved through HISA method and the source has been placed at 13.1 kpc (Anderson & Bania, 2009). A millimeter source is detected towards the bubble from the Bolocam Galactic Plane Survey (BGPS) by Schlingman et al. (2011). Several masers (H_2O, CH_3OH, NH_3) are detected towards this bubble (Codella et al., 1994; Xu et al., 2008; Urquhart et al., 2011). The region associated with the bubble has also been observed as part of many radio surveys at various frequencies (Garwood et al., 1988; Zoonematkermani et al., 1990; Becker et al., 1994; Kuchar & Clark, 1997; Urquhart et al., 2009).

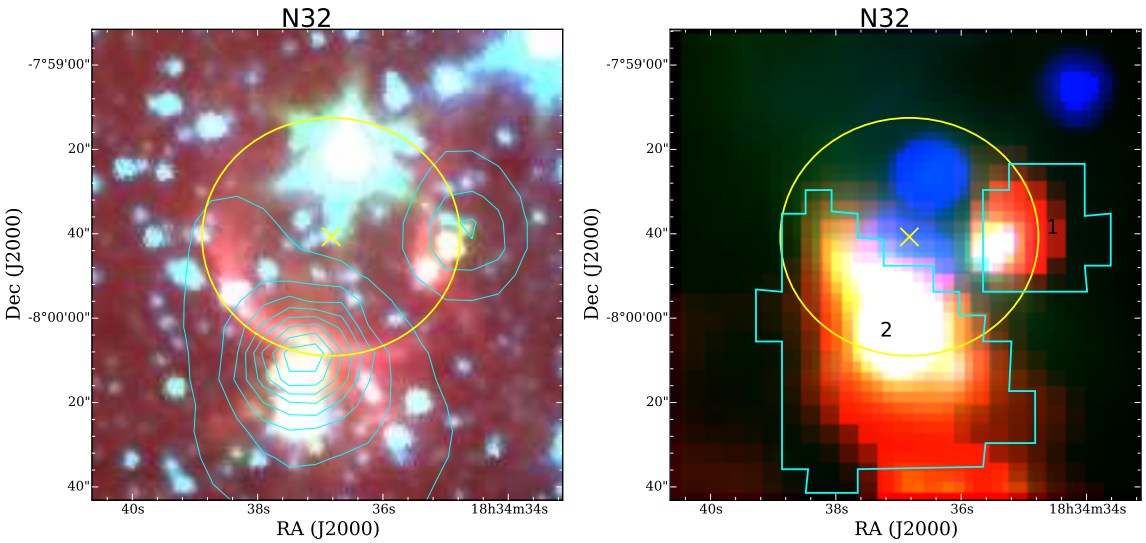

Figure 6.2: Same as Figure 6.1, but for bubble N32.

The distribution of MIR and FIR dust emission toward the bubble is shown in Figure 6.2. The broken morphology of the bubble is clearly seen from the 8 μm IRAC band. The bubble shows an opening towards the north. A bright source is seen at IRAC bands

towards the opening of the bubble. The 24 μm band shows localized emission peaks, towards the center and outside the bubble. Associated clumps are seen from the cold dust emission at 250 μm.

3. **N33**

N33 is classified as one with a broken morphology (Churchwell et al., 2006). This bubble has also been detected by Simpson et al. (2012). N33 is associated with IRAS 18328-0748. Distance to the IRAS source is resolved through the HISA spectra method and the source is found to be located at its far distance of 10.4 kpc (Jones & Dickey, 2012). Four ATLASGAL (870 μm) compact sources are identified towards the bubble by Urquhart et al. (2014b). The region associated with N33 has been part of 1.1 mm BGPS, which shows the presence of dust clumps towards the bubble (Rosolowsky et al., 2010). Radio sources in the 5 GHz VLA survey and 4.85 GHz survey are detected towards N33 (Becker et al., 1994; Kuchar & Clark, 1997). Massive YSO candidates located towards the bubble have been observed in the 6 cm radio band by Urquhart et al. (2009). Radio recombination line (RRL) observations have been made towards the region associated with the bubble (Lockman, 1989).

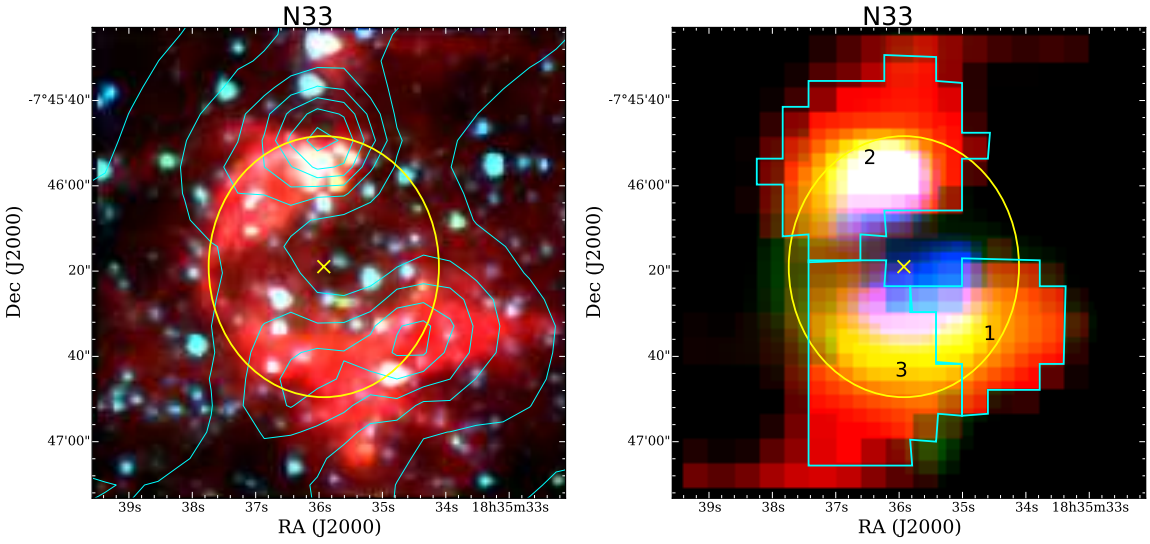

Figure 6.3: Same as Figure 6.1, but for bubble N33.

The MIR and FIR view of the bubble are shown in Figure 6.3. The broken morphology of the bubble is clearly seen at 8 μm emission, which traces the PDR of the bubble. Warm

dust emission at 24 μm is seen in the inner region of the bubble, at two localized positions and the 70 μm emission is almost unison with the 24 μm. The 250 μm band, tracing the cold dust emission, shows filamentary structures towards the north and southern part of the bubble.

4. **N37**

This bubble N37 is classified as one with a broken ring morphology by Churchwell et al. (2006) and also detected by Simpson et al. (2012). A H II region (G025.292+0.293) is associated with the bubble (Churchwell et al., 2006; Deharveng et al., 2010; Beaumont & Williams, 2010). N37 is found to be located in the direction of the H II region RCW 173 (Marco & Negueruela, 2011). The near and far kinematic distance estimates for the bubble are 2.6 – 3.3 and 12.3 – 12.6, respectively (Churchwell et al., 2006; Beaumont & Williams, 2010; Deharveng et al., 2010). However, the KDA has been resolved using the HISA method by Anderson & Bania (2009), who place the source at the far kinematic distance of 12.6 kpc. Though in a recent work, Baug et al. (2016) have used the near kinematic distance of 3.3 kpc, but in our study, we use 12.6 kpc. Deharveng et al. (2010) reveal the association of condensations (clumps) with N37 and the association with an IRDC has been reported by Peretto & Fuller (2009). The cold dust properties in the region of N37 has been explored using the molecular line emission data by Yan et al. (2016). The region has also been observed in the sub-mm bands by many authors (Schlingman et al., 2011; Dunham et al., 2011; Urquhart et al., 2014b).

Colour composite images using MIR and FIR bands of the region are shown in Figure 6.4. The 8 μm emission clearly shows broken ring morphology. From the 3.6 and 4.5 μm bands there is an over density of stellar sources seen in the inner region of the bubble. The 24 μm is seen to fill the interior of the bubble, whereas the 70 μm traces the boundary of the bubble. The cold dust emission at 250 μm is dominant on and outside of the northern periphery of the bubble. A large clumpy structure also seen towards the south of the bubble, however, it is difficult to probe its association with N37.

5. **N39**

As classified by Churchwell et al. (2006), N39, appears to have a broken or multiple

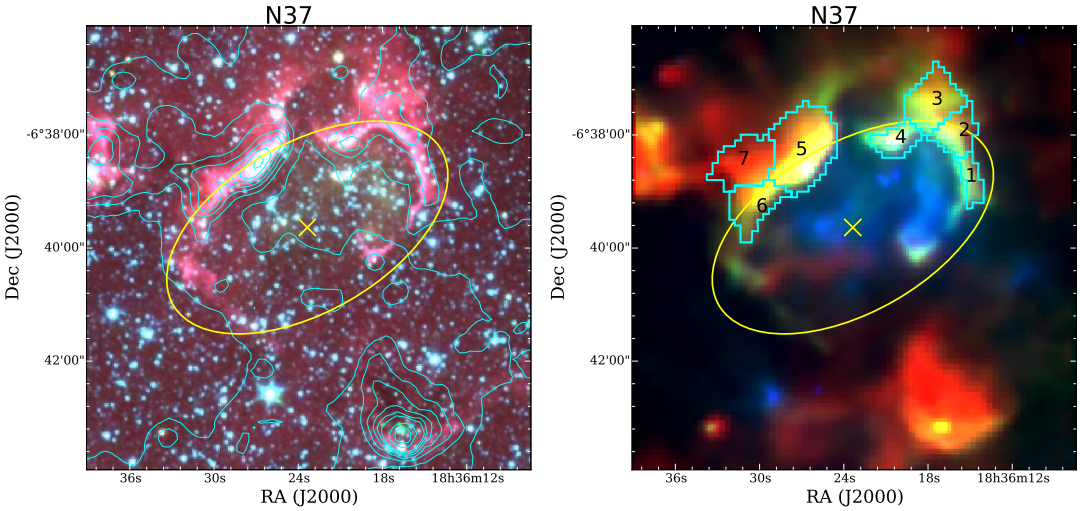

Figure 6.4: Same as Figure 6.1, but for bubble N37.

bubble morphology. Identification of the bubble has also been made by Simpson et al. (2012). The bubble is associated with a massive star-forming region W42 (G25.38-0.18) and an IR source IRAS 18355-0650. Several kinematic distance estimates are available in literature for this source. The KDA towards the bubble has been resolved by Anderson & Bania (2009) and the source has been placed at a near distance of 3.8 kpc. In our analysis, we have used this estimate. N39 is reported as a bipolar H II region by Deharveng et al. (2010) with the presence of an UC H II on the border. The bubble shows several clumps on its rim.

MIR and FIR views of the region associated with N39 are shown in Figure 6.5. The morphology is broken and open towards the west. The eastern rim of the bubble shows diffuse filamentary emission at 8 μm. The bubble interior is filled with warm dust seen at 24 μm. The 24 μm emission is saturated towards the east. 70 μm emission is localized towards the north and the eastern arm of the bubble. The 250 μm emission is clumpy.

6. **N40**

Morphologically, N40 is a broken bubble (Churchwell et al., 2006). Simpson et al. (2012) has also identified the bubble. N40 is associated with an IR source IRAS 18361-0655. The KDA towards the bubble has been resolved by Anderson & Bania (2009) and the bubble has been placed at a far distance of 11.3 kpc. This distance has been used by other

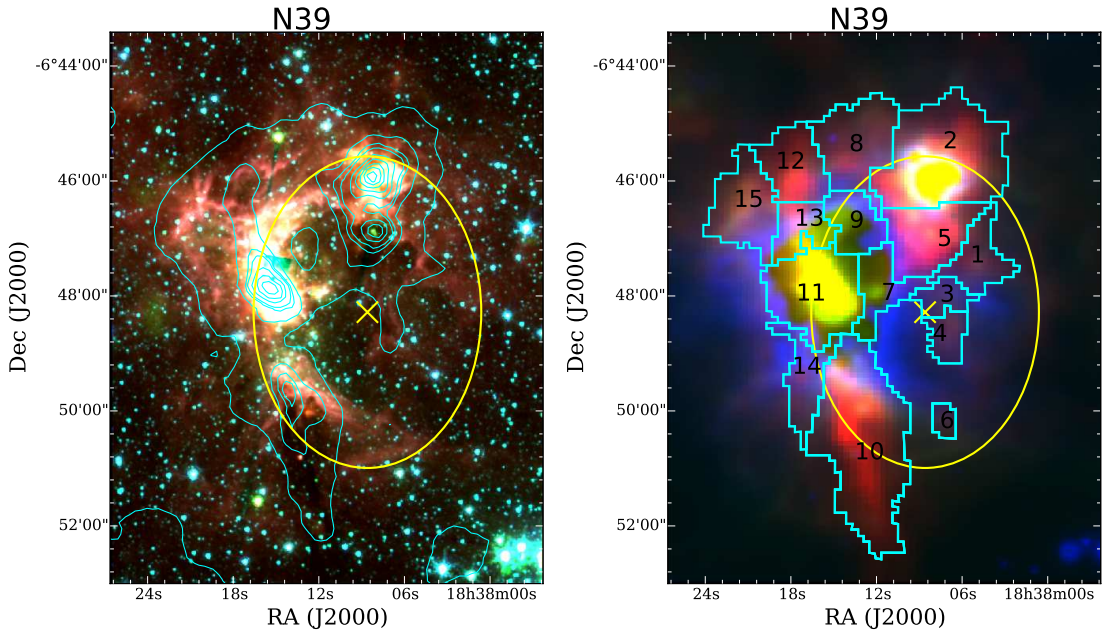

Figure 6.5: Same as Figure 6.1, but for bubble N39.

authors (Deharveng et al., 2010; Hattori et al., 2016) and in our analysis, we have also adopted this distance. N40 is found to be associated with an IRDC (Peretto & Fuller, 2009) and two distinct H II regions (Deharveng et al., 2010).

Figure 6.6 demonstrates the MIR and FIR dust distribution towards N40. The ring structure of the bubble N40 is clearly seen at 8 μm with a filament seen extending from the bubble towards the north. The warm dust emission at 24 μm is seen mostly in the northern half of the bubble. An arc type feature is also seen at 24 μm towards the north of bubble. The 70 and 250 μm emission trace the ring morphology of the bubble.

7. **N53**

N53 is classified as a complete bubble by Churchwell et al. (2006), with the effective radius of ∼1′ and is associated with IRAS 18461−0142. This bubble has also been detected by Simpson et al. (2012). Deharveng et al. (2010) have suggested that the near circular morphology of the bubble could be due to its evolution within a homogeneous medium, where the effect of turbulence is low. The near and far kinematic distances to the bubble are estimated to be 3.2 and 11.3 kpc respectively (Russeil et al., 2011). However, these authors have placed the source at the far distance by resolving the KDA adopting the

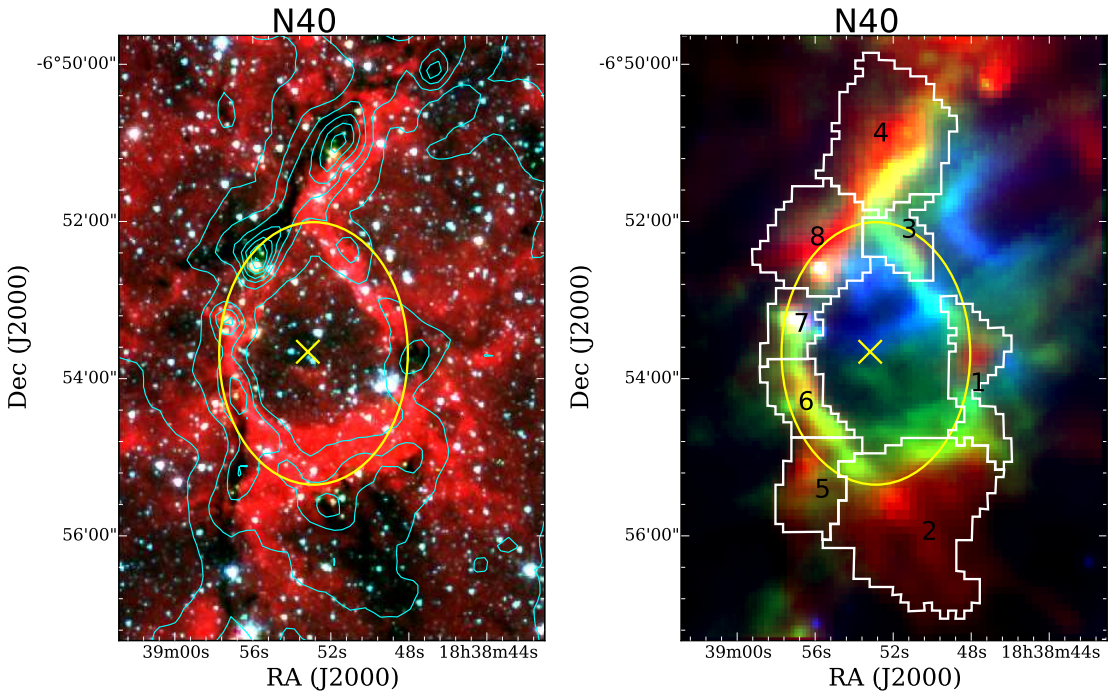

Figure 6.6: Same as Figure 6.1, but for bubble N40.

HISA method. Also, the near and far kinematic distance estimates obtained by Anderson & Bania (2009) are 2.6 and 11.9 kpc, and they have also resolved the KDA and placed the bubble at the far distance. In the study of a large sample of bubble, Deharveng et al. (2010) have adopted 11.6 kpc as the distance to N53. In our analysis the adopted distance is 11.6 kpc. The bubble N53 lies on the border of a large H II region, G31.165−0.127. Both are probably linked because they show similar velocities (Deharveng et al., 2010). The region associated with N53 is investigated at *Herschel* wavebands and reported to have a 70 μm counterpart (Russeil et al., 2011). 6.7 GHz methanol maser emission has been detected towards the bubble by Sun et al. (2014).

Figure 6.7 displays the MIR and FIR dust distribution towards the bubble N53. The bubble N53 appears as a bright arc with an opening in the west, which is clearly visible at 8 μm. Diffuse emission on the arc as well as in the interior of the bubble is also seen at 8 μm. The 24 μm emission is traced in the inner region with a faint arc-like feature seen close to the center. The 70 μm band displays similar morphology as the emission at 8 μm band. The 250 μm band shows clumpy localized structures around the bubble rim.

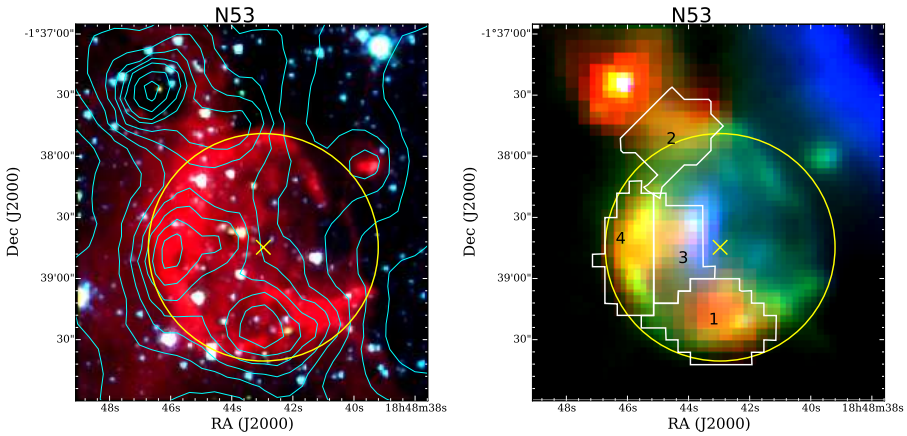

Figure 6.7: Same as Figure 6.1, but for bubble N53.

8. **N73**

N73 is classified as a broken bubble by Churchwell et al. (2006) and it is also detected by Simpson et al. (2012). The bubble is associated with IRAS 19000+0501. Near and far kinematic distance estimates to the bubble are obtained to be 4.1 and 9.2 kpc by Anderson et al. (2012a). By resolving the KDA, they place the bubble at its far distance of 9.2 kpc. Deharveng et al. (2010) have also adopted 9.2 kpc as distance to the bubble. We also use this estimate in our study.

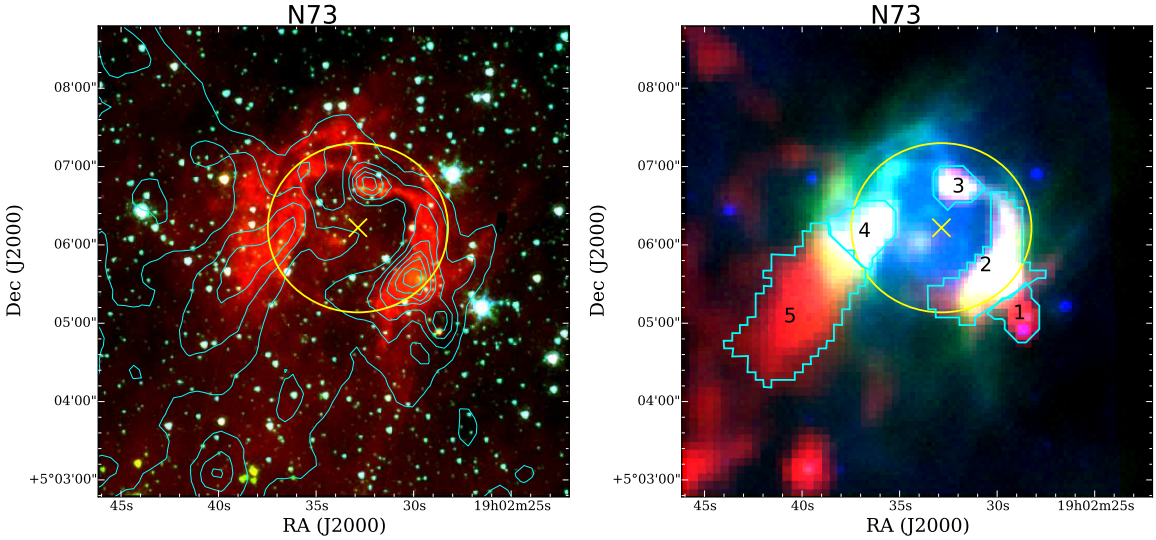

Figure 6.8: Same as Figure 6.1, but for bubble N73.

MIR and FIR dust emission in the region associated with N73 are shown in Figure 6.8.

The broken morphology of N73 is clearly seen at 8 μm. Emission at 24 and 70 μm are seen to be morphologically matching. The 250 μm displays clumps distributed on the bubble rim. One large clumpy structure is seen extending from the bubble rim and to the south-west direction.

9. **N82**

As classified by Churchwell et al. (2006), this bubble N82, has a complete ring morphology. This bubble is also detected by Simpson et al. (2012). N82 is located on the border of another large bubble N81 and from the morphology it is clearly associated with N81 (Deharveng et al., 2010). The near and far kinematic distance estimates to the bubble are 4.5 and 8.1 kpc, (Anderson & Bania, 2009), but the authors have been able to resolve the KDA using the HISA method and place the bubble at the far distance of 8.1 kpc. This far distance has been adopted by us in our analysis. N82 is also reported to have an association with an IRDC (Peretto & Fuller, 2009). Sub-mm emission properties associated with the bubble have been studied by various authors (Anderson et al., 2009; Shirley et al., 2013; Ellsworth-Bowers et al., 2015). CO molecular line emission has been observed towards the bubble and found to be distributed along the bright rim of the bubble (Yan et al., 2016). Distribution of cold atomic hydrogen in the region associated with N82 has been studied using 21 cm VLA observation (Kolpak et al., 2002). N82 is likely to have triggered star formation on the rim as deduced from the distribution of YSOs (Watson et al., 2010).

Figure 6.9 displays the MIR and FIR dust distribution in N82. The bubble is circular and shows a closed ring morphology which is clearly visible from the 8 μm emission. Relatively faint 8 μm emission is also seen in the inner region of the bubble. 24 μm emission is seen to be present in the interior. 70 μm emission shows similar morphology as of 24 μm. The 250 μm map shows a clear clumpy ring structure surrounding the 24 μm emission.

10. **N84**

The bubble N84 is classified as having a broken ring morphology by Churchwell et al. (2006) and also detected by Simpson et al. (2012). The bubble is associated with IRAS

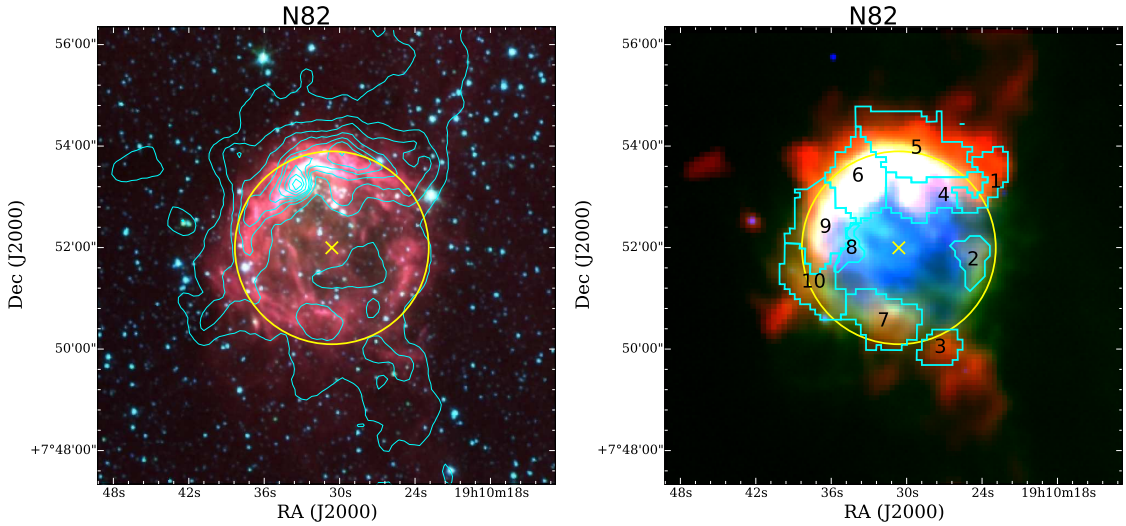

Figure 6.9: Same as Figure 6.1, but for bubble N82.

19077+0839. This bubble is located in the direction of an IR star cluster G42.834−0.151 (Solin et al., 2012). Kinematic distance to the bubble is estimated to be 1.1 kpc (Watson et al., 2010). We adopt the same distance. Deharveng et al. (2010) suggested that the bubble is associated with two condensations and the association with an IRDC has been reported by Peretto & Fuller (2009). 6.7 MHz methanol maser is detected towards the bubble by Szymczak et al. (2000). Associated cold dust with N84 have been explored at 850 and 1200 μm by Matthews et al. (2009).

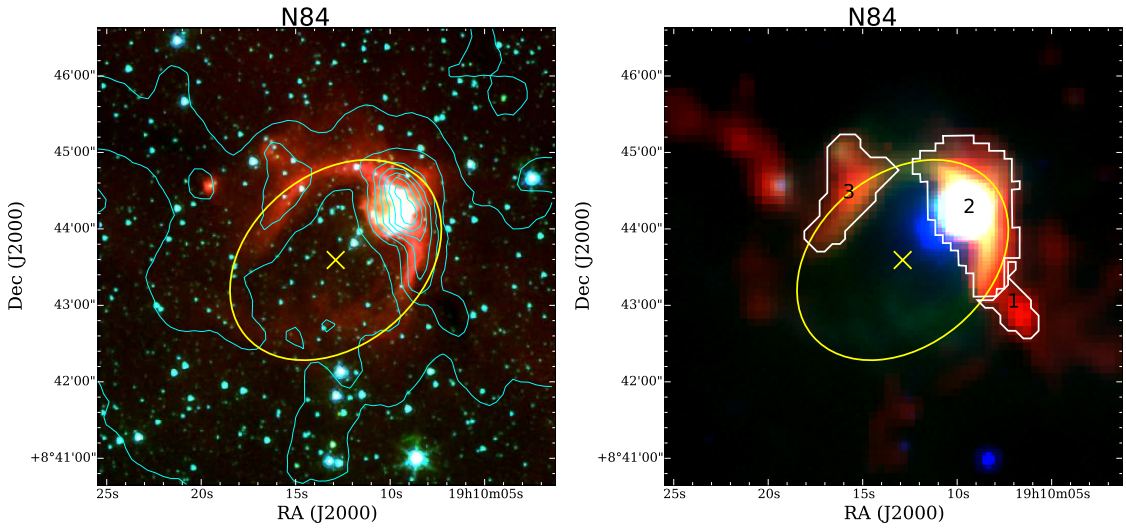

Figure 6.10: Same as Figure 6.1, but for bubble N84.

Colour composite images using MIR and FIR bands of the region associated with bubble N84 are shown in Figure 6.10. The 8 μm band clearly traces the ring morphology of the bubble, with an enhanced emission towards the north-west. The 24 μm and 70 μm maps also show enhanced emission at the same location as the 8μm band. 250 μm band displays fragmented structures on the bubble rim.

11. **N92**

N92 is classified as a broken bubble by Churchwell et al. (2006). Simpson et al. (2012) have also reported the detection of this bubble. The near and far kinematic distance estimates to the bubble are 4.9 and 7.2 kpc, (Anderson et al., 2012a), but the authors have been able to resolve the KDA by finding that the bubble is a tangent-point source. They place the bubble at the distance of 6.1 kpc. This distance has been adopted by Deharveng et al. (2010) and we use the same distance. According to Deharveng et al. (2010), N92 is associated with a filamentary condensation and an IRDC. At the MIR wavelengths the bubble appears to be open in one direction and this could be because of the evolution of nebula in a low density medium (Deharveng et al., 2010). N92 has been studied in more detail to explore the triggered star formation using MIR and molecular line data by Dirienzo et al. (2012). Sub-mm emission have been observed toward the bubble by many authors (Schlingman et al., 2011; Urquhart et al., 2014b).

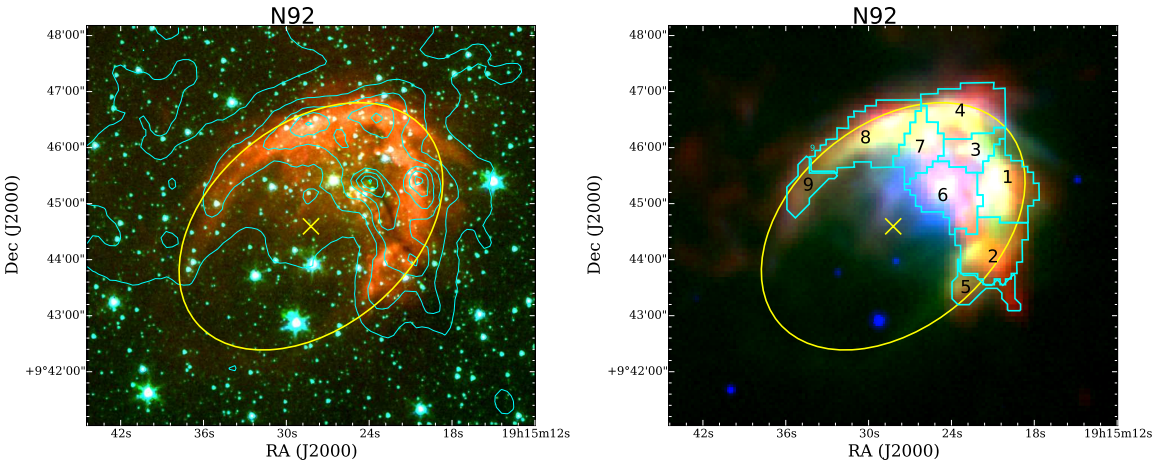

Figure 6.11: Same as Figure 6.1, but for bubble N92.

Figure 6.11 displays the dust emission at MIR and FIR bands. N92 shows up as an arc at

8 μm band. The point sources seen at 3.6 and 4.5 μm bands show a higher density near the arc compared to the other locations. 24 and 70 μm emissions are brighter near the arc. Cold dust emission at 250 μm also appears to be associated with the arc.

12. **N95**

N95 is classified as a broken ring bubble by Churchwell et al. (2006), which is also detected by Simpson et al. (2012). An IR star cluster G45.397−0.709 is found to be located in the direction of the bubble (Solin et al., 2012). The near and far kinematic distance estimates to the bubble are 3.9 and 8.0 kpc, (Anderson et al., 2012a), but these authors have resolved the KDA and they place the bubble at the far distance of 8.0 kpc. The same distance has been adopted by Deharveng et al. (2010) and we also use this distance estimate for our analysis. N95 has been reported to be associated with several condensations along the bright PDR (Deharveng et al., 2010). Association of the bubble with IRDC has also been reported by Peretto & Fuller (2009).

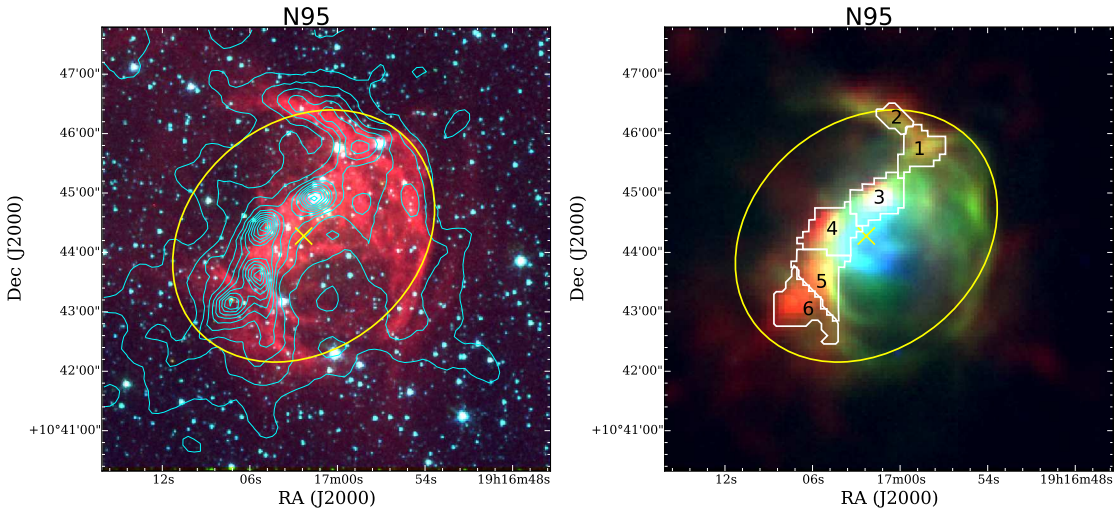

Figure 6.12: Same as Figure 6.1, but for bubble N95.

The MIR and FIR view of the region towards N95 are shown in Figure 6.12. At 8 μm the bubble displays a bipolar morphology. The interesting morphology resembles two broken and connected bubbles. As displayed in Figure 6.12, the 8 μm emission shows an arc type feature towards the north-west corner of the bubble and it is connected to a thin

filament extending towards the south-east. The lower half is more prominent at 8 μm and also at 24 and 70 μm bands. The cold dust emission at 250 μm is brighter on the filament passing through the center part of the bubble. The lower half itself displays morphology of a broken bubble.

13. **N101**

Bubble N101 is classified as a broken bubble by Churchwell et al. (2006). Simpson et al. (2012) have also identified the bubble in their project. N101 is part of GMC W51 and associated with H II region G49.20−0.30. The bubble is also found to be associated with an IRDC (Peretto & Fuller, 2009). The KDA towards N101 has been resolved by finding the bubble to be located on the tangent plane and the distance towards the bubble is estimated to be 5.6 kpc. However, Watson et al. (2010) estimated the distance to be 5.1 kpc. In our analysis, we have adopted the value from Watson et al. (2010). Water maser has been detected towards N101 by Nagayama et al. (2015). Dense clumps have been detected in the filament towards N101 and their nature has been investigated using FIR and mm data by Mookerjea et al. (2014). Several molecular line observations have been carried out to understand the nature of cold dust in the large W51 complex by many authors (Koo, 1999; Sorai et al., 2008; Kang et al., 2010; Parsons et al., 2012).

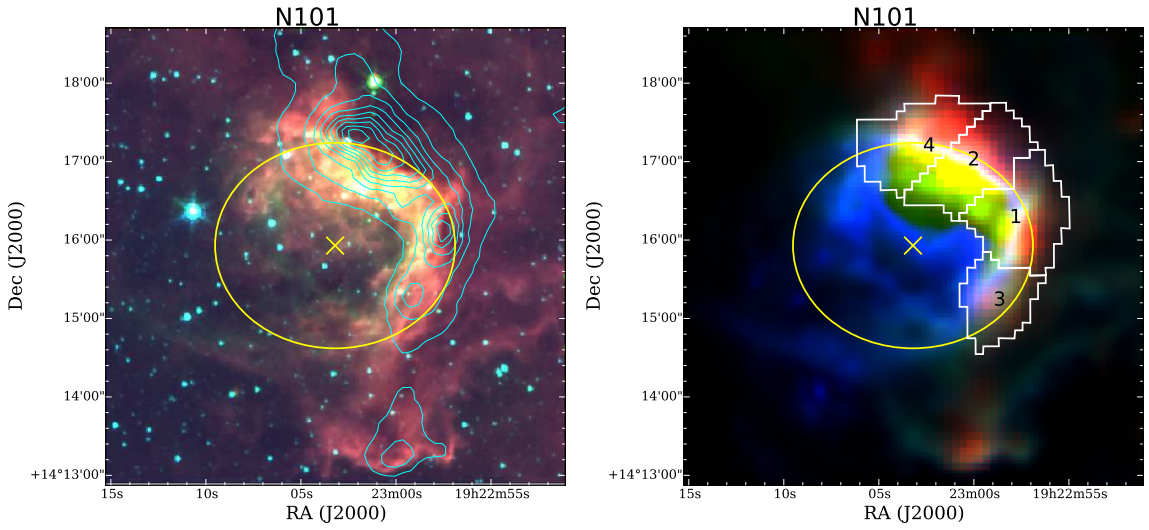

Figure 6.13: Same as Figure 6.1, but for bubble N101.

Figure 6.13 displays the MIR and FIR dust distribution of the region associated with N101. It clearly shows enhanced diffuse emission at 8 μm in the north part of the bubble. Morphologically, the bubble is broken towards on the south-east. Emission at 24 μm fills the bubble interior and it is saturated towards the arc of the bubble. 70 μm emission is associated with the arc with faint emission seen towards the south of the bubble. Emission at 250 μm is strongly associated with the rim of the bubble.

14. **N105**

N105 is classified as a complete ring bubble by Churchwell et al. (2006), which is also detected by Simpson et al. (2012). The far kinematic distance to the bubble is estimated to be 11.2 kpc and using the HISA method, the KDA has been resolved and the bubble is found to be located at its far distance (Anderson et al., 2012a). In our study, we have adopted 10.6 kpc as the distance (Watson et al., 2010). Dust emission properties associated with the bubble have been studied at sub-mm wavebands by various authors (Anderson et al., 2011; Urquhart et al., 2014b; Ellsworth-Bowers et al., 2015). Cold dust environment associated with the bubble has been explored using the molecular line information by Yan et al. (2016).

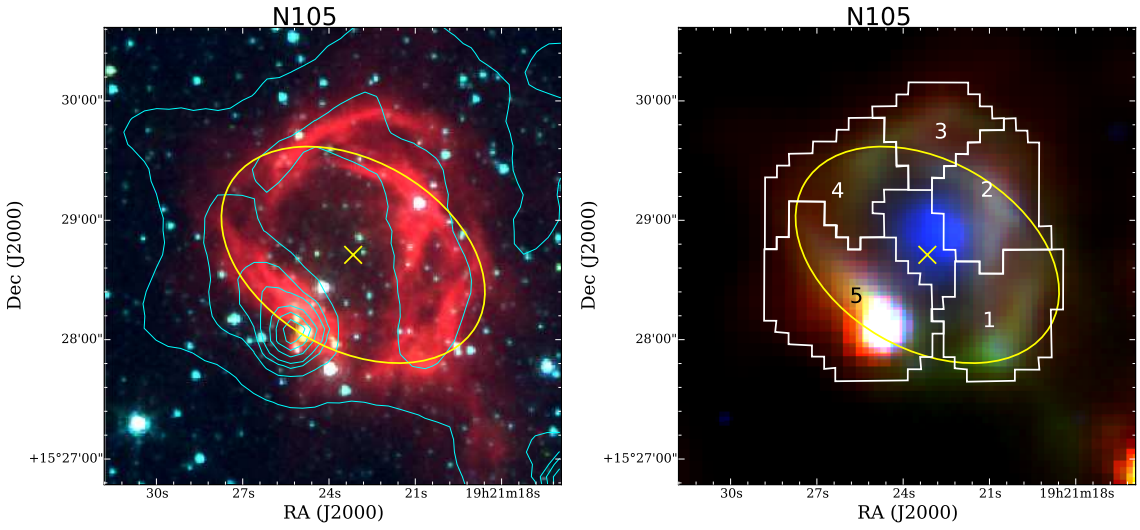

Figure 6.14: Same as Figure 6.1, but for bubble N105.

Figure 6.14 displays the MIR and FIR dust emission picture in N105. The closed ring morphology of N105 is clearly seen from the emission at 8 μm. The presence of filamen-

tary structures and ruptures in the 8 μm emission band are also seen. The 3.6 and 4.5 μm bands tracing stellar sources, reveal an overdensity of the stars on the south-east rim of the bubble, where the cold dust emission is also prominent. As seen from the figure the 24 μm emission is seen towards the center of the bubble, with 70 μm emission around it. The cold dust emission at 250 μm follows the periphery of the bubble.

15. **N115**

This bubble is classified as having a complete ring morphology by Churchwell et al. (2006). It has also been detected by Simpson et al. (2012). The bubble is associated with the H II region G53.54−0.01(Sh2-82). The near and far kinematic distances estimated towards the bubble are 1.8 and 8.3 kpc (Anderson et al., 2012a). However, these authors are unable to resolve the KDA to the bubble because of the faint emission from the bubble. Watson et al. (2010) adopt the estimated distance to the bubble to be 2.6 kpc and we use this in our analysis too. The region towards the bubble has been suggested to be formed as a result of collisions of larger bubble N115 with N116+N117 and it has been proposed that such collision will lead to triggered star formation (Zychová & Ehlerová, 2016). While investigating the region in the IR and with molecular line emission, Xu & Ju (2014) suggest that the bubble is associated with active star formation and the distribution of YSOs on the border could be formed because of the collect-and-collapse process. Hydrogen RRLs have been detected towards the bubble by Anderson et al. (2011) and cold dust environment have been explored using the molecular line information by Yan et al. (2016).

Colour composite images using MIR and FIR bands of the region associated with bubble N115 are shown in Figure 6.15. The broken morphology (Churchwell et al., 2006) of bubble N115 is clearly evident from the 8 μm emission. Extended emission at 8 μm is also seen in the northern part of the bubble. Warm dust emission at 24 μm is prominent within the bubble and also seen on the northern periphery. 70 μm emission displays the rim of the bubble and also appears on the northern region. Emission from cold dust is dominant on the north and north-western region of the bubble.

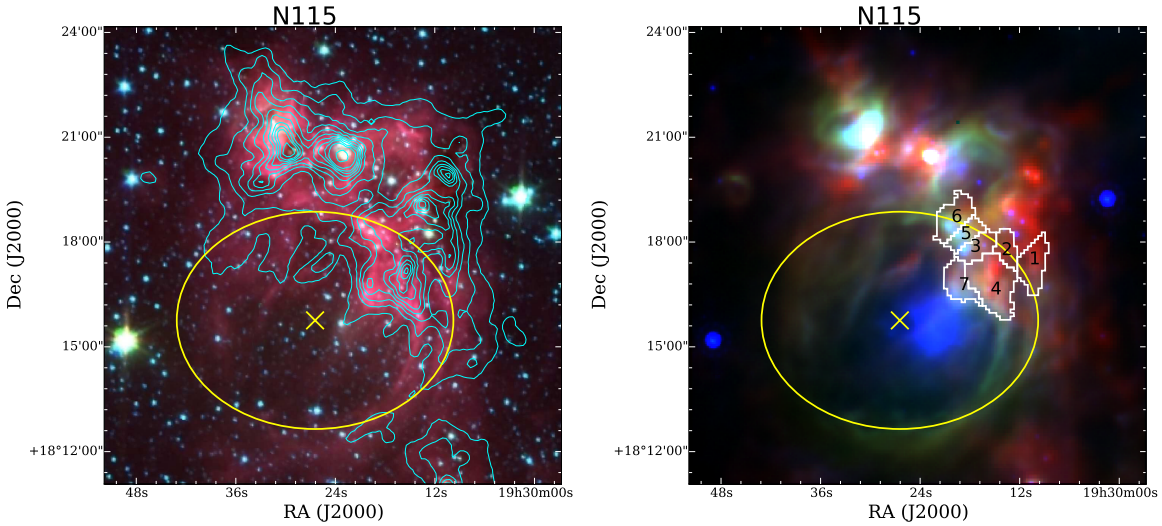

Figure 6.15: Same as Figure 6.1, but for bubble N115.

16. **N124**

As classified by Churchwell et al. (2006), this bubble N124, appears to have a broken ring morphology at MIR wavelengths. Identification of the bubble has also been made by Simpson et al. (2012). Two IR sources IRAS 19362+2251 and IRAS 19364+2252 are located in the direction of the bubble. N124 is located at the kinematic distance of 3.2 kpc (Watson et al., 2010). No other distance estimates towards the bubble are found in the literature. The bubble region has been investigated at FIR wavebands to study the star formation activity by many authors (Chapin et al., 2008; Veneziani et al., 2013).

Figure 6.16 demonstrates the dust emission as seen in the MIR and FIR bands. The morphology at 8 μm shows an extended filament stretching in the south-east and south-west direction of the bubble. The bubble is broken and open towards the east. As is clear from the figure, the cold dust emission at 250 μm matches well with the 8 μm emission. Localized emission is seen in the 24 μm band. Close to the filament, a 24 μm emission blob is clearly seen. 70 μm band shows very faint diffuse emission near the filament.

17. **N133**

N133 is classified as a complete ring bubble by Churchwell et al. (2006). This bubble is also detected by Simpson et al. (2012). The bubble is associated with the H II region Sh2−90. Distance to the H II region complex has been discussed by Samal et al. (2014)

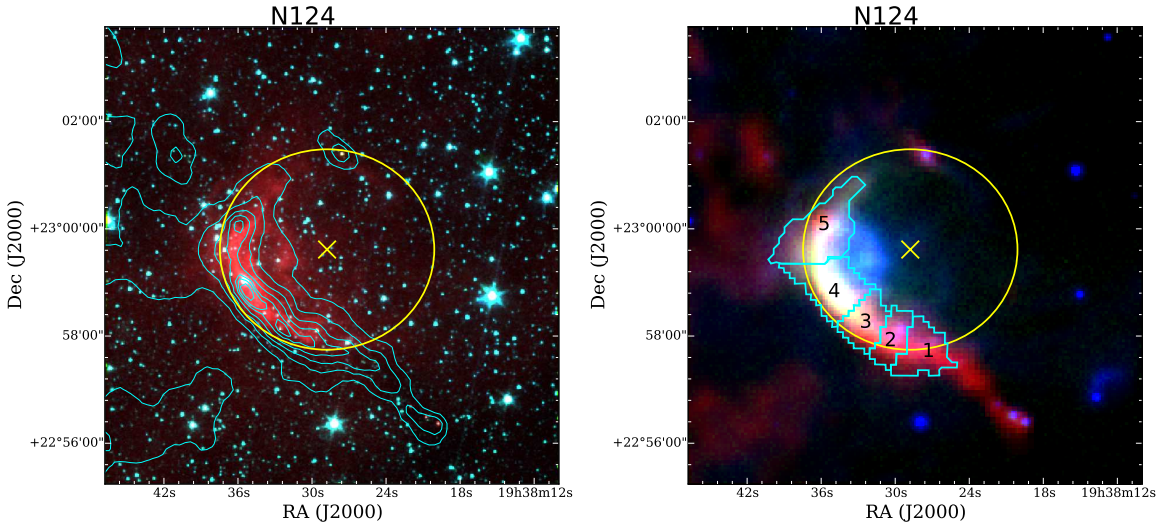

Figure 6.16: Same as Figure 6.1, but for bubble N124.

and they give an estimate in the range 2.1 – 2.5 kpc which is consistent with the value adopted by Watson et al. (2010). In our analysis, we use the value of 2.1 kpc. Physical properties of the associated molecular cloud to N133 has been investigated using the molecular line emission data by Yan et al. (2016). The molecular cloud complex Sh2−90 has been studied in sub-mm wavebands by various authors (Beuther et al., 2002; Di Francesco et al., 2008).

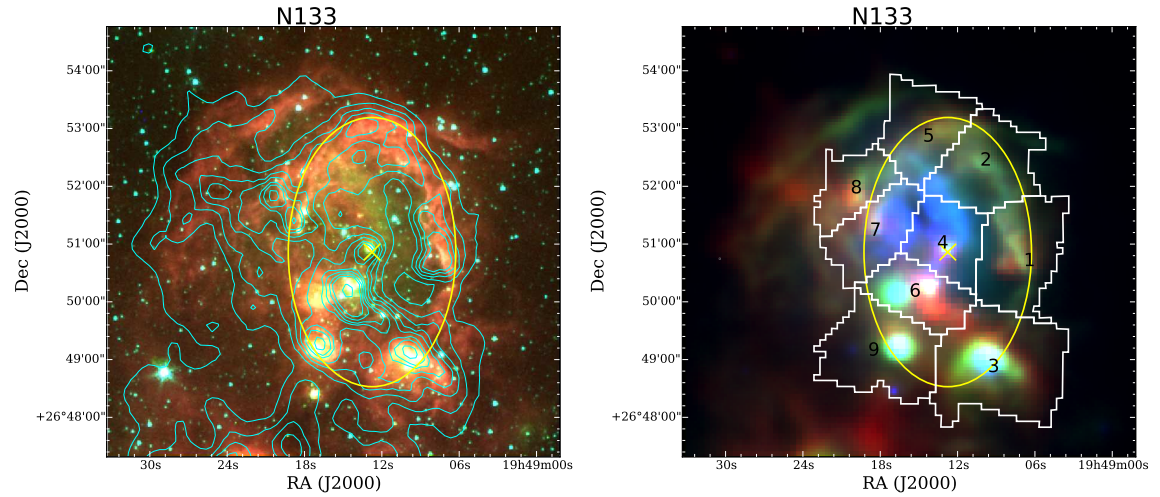

Figure 6.17: Same as Figure 6.1, but for bubble N133.

Colour composite images of MIR and FIR bands for the region associated with the bubble

N133 are shown in Figure 6.17. The 8 μm band displays large scale diffuse emission towards the northern part of the bubble. Localized enhanced emission is also visible, and a large number of point sources are seen to be associated with the enhanced emission. The warm dust emission at 24 μm band is present within the bubble interior and also shows localized distribution. 70 μm band emission is similar to that of the 24 μm band. The 250 μm band reveals the cold dust emission as fragmented structures inside and around the bubble.

Table 6.1 list the position, size, distance and the morphological classification from Churchwell et al. (2006).

Table 6.1
Details of the sample of IR bubbles. The table lists the bubble names, central coordinates, effective radius, and morphology from Churchwell et al. (2006). Distances to the bubbles have been taken from literature (see text). The morphology type listed in column 6 is as follows: C – complete or closed ring; B – broken or incomplete ring; CC – probable enclosed central star cluster; MB – multiple bubbles; BP – bipolar bubble or a double bubble whose lobes are in contact.

Bubble	RA (J2000) (hh:mm:ss.ss)	DEC (J2000) (dd:mm:ss.ss)	Radius ($'$)	Distance (kpc)	Morphology
N10	18:14:06.94	-17:28:41.43	1.22	4.7	C, CC, BP
N32	18:34:36.82	-07:59:40.73	0.42	13.1	B
N33	18:35:35.92	-07:46:18.96	0.42	10.4	B
N37	18:36:23.35	-06:39:38.18	1.77	12.6	B
N39	18:38:08.59	-06:48:16.94	1.99	3.8	B, MB
N40	18:38:53.18	-06:53:39.48	1.23	11.3	B
N53	18:48:42.96	-01:38:44.67	0.84	11.6	C
N73	19:02:32.85	+05:06:13.15	0.93	9.2	B
N82	19:10:30.62	+07:51:59.78	1.68	8.1	C, CC
N84	19:10:12.88	+08:43:35.59	1.16	1.1	C
N92	19:15:28.21	+09:44:35.70	1.94	6.1	C, CC
N95	19:17:02.31	+10:44:16.61	2.02	8.0	C
N101	19:23:03.20	+14:15:55.79	1.17	5.1	C
N105	19:21:23.16	+15:28:42.64	0.84	10.6	C
N115	19:30:26.44	+18:15:45.56	3.17	2.7	C
N124	19:38:28.77	+22:59:36.91	1.74	3.2	B
N133	19:49:12.76	+26:50:51.75	1.64	2.1	C

6.3 Cold dust emission

6.3.1 Column density and dust temperature maps

The procedure followed to generate column density and temperature maps are discussed in Chapter 2. Following the same, the background flux density I_{bkg} has been estimated in each band from regions close to the bubbles and the details are given in Table 6.2. Figure 6.18 and

Table 6.2
Background values obtained at different wavebands for the bubble sample. Column 2 and 3 list the center RA and DEC of the background region, Column 4 gives the angular separation of background from the bubble center and Columns 5 - 8 list the background values.

Bubble	RA (J2000)	DEC (J2000)	Ang. separation from	Background value (Jy/pix)			
	(hh:mm:ss.ss)	(dd:mm:ss.ss)	bubble (degree)	160 μm	250 μm	350 μm	500 μm
N10	18:11:17.74	-16:54:35.36	0.9	-3.02	1.65	0.79	0.36
N32	18:40:31.00	-07:43:30.75	1.5	-0.02	1.11	0.55	0.19
N33	18:40:31.00	-07:43:30.75	1.2	-0.02	1.11	0.55	0.19
N37	18:40:31.00	-07:43:30.75	1.5	-0.02	1.11	0.55	0.19
N39	18:40:31.00	-07:43:30.75	1.1	-0.02	1.11	0.55	0.19
N40	18:40:31.00	-07:43:30.75	0.9	-0.02	1.11	0.55	0.19
N53	18:46:12.89	-01:13:25.24	0.7	-0.82	3.60	1.77	0.66
N73	18:59:58.55	05:37:24.98	0.8	-0.01	1.97	1.06	0.42
N82	19:12:51.16	08:07:21.60	0.6	-0.82	1.33	0.71	0.27
N84	19:14:11.72	08:41:34.06	0.9	-1.53	0.86	0.48	0.18
N92	19:14:11.72	08:41:34.06	1.1	-1.53	0.86	0.48	0.18
N95	19:19:10.09	10:57:04.86	0.6	-0.88	1.17	0.65	0.26
N101	19:24:33.65	13:59:58.83	0.5	-0.38	1.24	0.67	1.26
N105	19:27:15.47	15:12:42.13	1.4	-1.06	1.22	0.68	0.27
N115	19:31:51.75	17:46:37.95	0.6	-0.57	1.06	0.58	0.23
N124	19:42:59.97	22:18:06.80	1.2	-0.41	0.79	0.44	0.18
N133	19:48:15.65	27:22:11.42	0.6	-0.23	0.54	0.31	0.13

the figures in Appendix C display the column density, dust temperature and the corresponding χ^2 maps of the region associated with the bubbles. In generating these maps, we consider relatively large regions towards the bubbles to understand the dust temperature and column density distribution in the bubble vicinity. The minimum, maximum and mean dust temperature and column density estimated from the maps are listed in 6.3. The table also lists the χ^2 statistics which shows the quality of the modified black body fits to the flux densities.

6.3.2 Cold dust clumps

In order to identify dust clumps or condensations that are likely to be associated with the bubbles, we use the 250 μm image which has an optimum resolution of 18″. After inspecting the

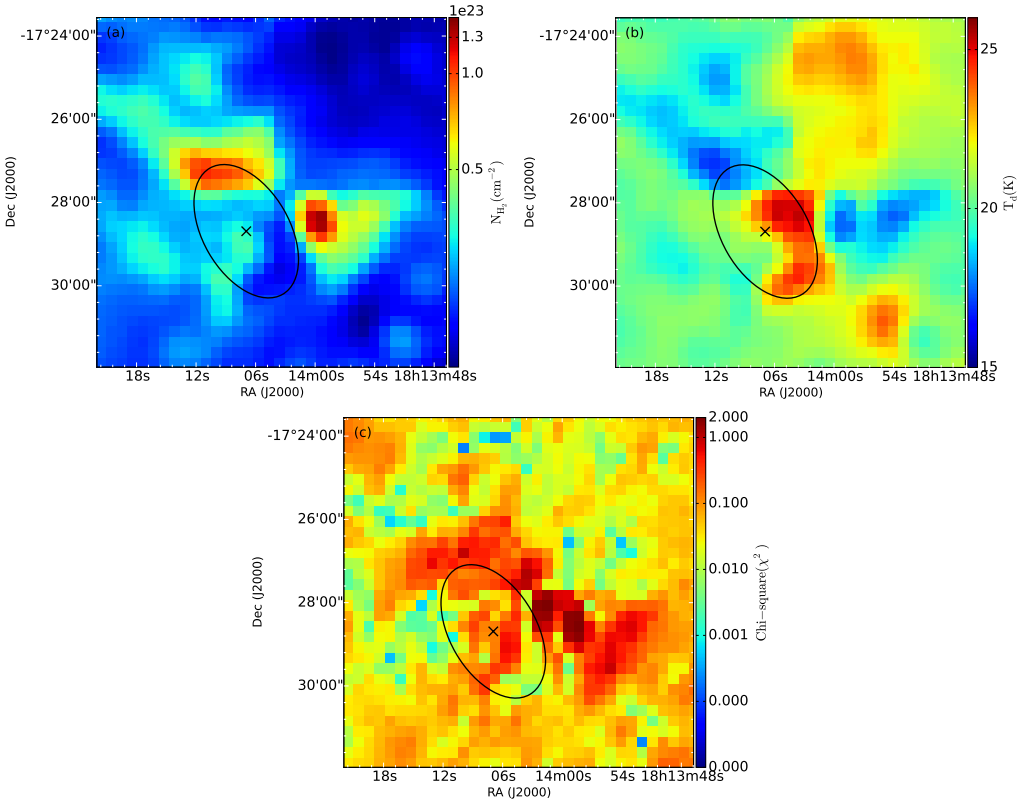

Figure 6.18: Column density (a), dust temperature (b) and chi-square (χ^2) (c) maps of the region associated with bubble N10. The '×' shows the position of bubble center and the ellipse shows the extent of the bubble (Churchwell et al., 2006).

250 μm images, threshold values are set for detecting the clump peaks and these values are listed in Table 6.4. In identifying the clumps, we follow the following procedure. The positions of peak intensities in the map are determined by identifying the pixels having the highest value in 3×3 pixel matrices, with flux density values above the defined threshold. Subsequent to the peak identification, contours are generated to isolate the clumps around these peaks. The generated contours are given as input to the *clumpfind* routine which was introduced in Chapter 3. Figure 6.1 to 6.17 shows the distribution of the detected clumps overlaid on the color composite image of 24 μm (blue), 70 μm (green), and 250 μm (red). It should be noted that the defined threshold results in the detection of many clumps in the selected field of column density and dust temperature maps. We retain only those clumps that lie within or on the bubble periphery. This goes with the assumption that they are associated and at the same distance as the bubble. This assumption may not always be realistic but the formation mechanism and studies of several bubbles (Liu et al., 2016; Gama et al., 2016; Das et al., 2017) have shown clumps within and on

Table 6.3
Statistics of column density and dust temperature and χ^2 from the maps for each bubble.

Bubble	$N(H_2)(\times 10^{22}cm^{-2})$			T_d (K)			χ^2		
	min	max	mean	min	max	mean	min	max	mean
N10	1.2	13.8	2.3	16.9	25.4	20.7	2.0×10^{-4}	2.3	0.1
N32	3.4	8.1	4.9	12.4	20.2	14.0	0.1	14.4	8.1
N33	3.3	6.1	4.5	13.2	19.0	15.7	0.9	9.4	4.9
N37	0.7	6.6	1.3	15.4	23.9	17.2	0.01	8.9	4.3
N39	1.4	11.4	2.4	13.2	35.3	17.1	0.02	13.1	4.7
N40	0.6	4.9	1.7	13.7	21.4	16.7	0.4	10.9	4.6
N53	0.3	1.7	0.7	21.4	28.0	25.0	4.0×10^{-4}	1.0	0.3
N73	0.6	1.7	1.0	18.2	22.5	19.6	4.0×10^{-5}	0.3	0.03
N82	0.5	2.2	0.8	14.9	27.3	18.9	2.0×10^{-4}	1.3	0.1
N84	0.6	1.7	1.0	17.6	28.6	19.3	4.0×10^{-4}	0.9	0.1
N92	0.2	1.2	0.4	15.2	25.5	18.2	5.2×10^{-7}	1.5	0.1
N95	0.2	1.8	0.4	15.5	23.2	18.3	1.0×10^{-3}	2.8	0.2
N101	0.1	8.9	0.9	18.7	31.5	24.9	1.0×10^{-3}	2.8	0.5
N105	0.01	1.5	0.4	14.9	27.8	18.3	6.0×10^{-4}	9.1	0.5
N115	0.1	3.3	0.5	16.4	29.1	21.9	0.1	2.6	0.5
N124	0.04	0.8	0.3	14.3	23.3	17.3	1.0×10^{-4}	2.3	0.2
N133	0.1	3.8	0.3	14.3	28.1	19.3	2.0×10^{-4}	7.8	0.3

the bubble rims are associated. Independent kinematic studies of individual clumps are required to ascertain the physical association. Table 6.4 gives the number of detected clumps associated with each bubble.

Mass estimation of clumps

Mass of the dust clumps are estimated using the following equation which was introduced in previous chapters.

$$M_{clump} = \mu_{H_2} m_H A_{pixel} \Sigma N(H_2) \tag{6.1}$$

where, m_H is the mass of hydrogen, A_{pixel} is the pixel area in cm^2, μ_{H_2} is the mean molecular weight and $\Sigma N(H_2)$ is the integrated column density. The clump apertures retrieved are used to estimate the physical radius ($r_p = (A/\pi)^{0.5}$; (Kauffmann & Pillai, 2010)). Apart from the physical size, we have derived the deconvolved radius (r_d) following the method outlined in Beltrán et al. (2006a). The geometric mean of the largest and smallest values of FWHM of the contour level upto which the flux density is integrated gives another estimate of the size and hence the radius r_g. For further analysis, we use the deconvolved radius, r_d as the effective

radius of the clump. The volume number density is derived as, $n_{H_2} = 3\Sigma N(H_2)/4r$, r being the radius of the clump. The estimated physical properties of the dust clumps are listed in Table 6.5.

Table 6.4
rms noise of the maps and the threshold defined and given as input to the *clumpfind* algorithm are listed. The last column gives the number of detected clumps towards each bubble.

Bubble	Noise level (σ) (MJy/sr)	Threshold ($\times\sigma$)	No. of detected clumps
N10	115.24	30	9
N32	104.03	30	2
N33	93.59	35	3
N37	65.18	25	7
N39	74.28	35	15
N40	74.28	25	8
N53	66.35	35	4
N73	40.58	40	5
N82	37.08	30	10
N84	43.67	30	3
N92	36.03	20	9
N95	38.94	25	6
N101	51.31	50	4
N105	35.37	25	5
N115	36.40	30	7
N124	20.91	25	5
N133	17.68	30	9

SED modelling of the dust clumps

In order to understand the nature of the sources towards these clumps, we use the offline SED model fitting tool of Robitaille et al. (2007) to fit the clump flux densities with the inbuilt YSO models. This is along the lines discussed in Zavagno et al. (2010). Here, we make a rather simplistic assumption that each clump would form only a single massive star. Given the large estimated masses of some of the clumps, this assumption would be unrealistic for these. More on this is discussed in later sections. Flux densities from the MIPS and *Herschel* data are used for the model fitting. We use the clump apertures retrieved from the *clumpfind* algorithm to obtain flux densities in all wavelengths. Same apertures are used on nearby 'smooth' and 'dark' regions to estimate the background emission which is subtracted out from the clump flux densities. We take a conservative uncertainty of 10% on the background subtracted flux densities. Figure 6.19 and figures in Appendix C show the results of the SED fits. In Table

Table 6.5
Clump parameters estimated from the maps. Peak positions, estimated radius (r_d, r_g, r_p), mean dust temperature and column density, total column density, mass and number density of clumps are listed.

Clump No.	RA (J2000) (hh:mm:ss.ss)	DEC (J2000) (dd:mm:ss.ss)	Radius (pc) r_d	r_g	r_p	Mean T_d (K)	Mean $N(H_2)$ ($\times10^{22}$cm^{-2})	$\sum N(H_2)$ ($\times10^{23}$cm^{-2})	Mass ($M_\odot$)	No. density (n_{H_2}) ($\times10^4$cm^{-3})
						N10				
1	18:14:01.50	-17:28:45.65	0.6	0.7	1.1	20.6	5.9	23.9	5429	7.7
2	18:14:05.63	-17:28:16.78	0.3	0.4	0.7	24.3	2.8	3.4	772	7.1
3	18:14:04.96	-17:27:10.91	0.5	0.5	0.8	21.0	4.0	8.4	1910	6.4
4	18:14:07.47	-17:27:28.40	0.1	0.3	0.5	20.2	6.4	5.1	1156	136.9
5	18:14:08.98	-17:28:18.46	0.3	0.4	0.6	22.8	2.8	2.5	557	5.2
6	18:14:07.75	-17:29:11.56	0.4	0.4	0.7	22.0	3.0	4.5	1022	7.4
7	18:14:08.78	-17:27:01.92	0.4	0.5	0.8	18.9	6.3	10.7	2430	14.6
8	18:14:09.98	-17:29:49.20	0.2	0.3	0.4	19.7	3.4	2.0	461	36.5
9	18:14:13.87	-17:27:32.51	0.6	0.6	1.0	18.4	6.2	22.3	5066	9.1
						N32				
1	18:34:34.57	-07:59:38.72	0.1	0.6	0.9	16.9	4.6	1.7	3035	673.2
2	18:34:37.22	-08:00:03.05	0.9	1.1	1.9	18.9	4.3	5.9	10571	5.0
						N33				
1	18:35:34.60	-07:46:34.88	0.1	0.5	0.8	18.3	3.5	1.4	1546	195.0
2	18:35:36.48	-07:45:53.61	0.5	0.7	1.1	17.7	4.0	3.6	4037	12.6
3	18:35:35.98	-07:46:43.43	0.4	0.6	1.1	18.5	3.6	2.2	2391	13.6
						N37				
1	18:36:15.05	-06:38:44.14	0.6	0.7	1.0	19.9	1.0	0.3	504	3.0
2	18:36:16.19	-06:37:55.68	0.7	0.9	1.4	21.1	1.1	0.9	1565	1.7
3	18:36:17.45	-06:37:22.50	0.9	1.1	1.9	21.2	1.1	1.5	2432	1.0
4	18:36:20.01	-06:38:02.96	0.5	0.8	1.3	22.2	0.9	0.7	1113	3.0
5	18:36:27.11	-06:38:15.96	1.3	1.4	2.5	22.1	1.1	3.1	5028	1.0
6	18:36:29.91	-06:39:16.19	0.9	1.1	1.6	20.3	1.4	1.6	2547	1.2
7	18:36:31.23	-06:38:26.03	0.9	1.1	1.8	18.7	1.8	2.6	4294	1.6
						N39				
1	18:38:05.07	-06:47:18.35	0.4	0.4	0.6	19.4	2.8	4.4	657	3.9
2	18:38:06.95	-06:45:19.19	0.7	0.7	1.1	24.4	2.9	18.2	2702	2.6
3	18:38:07.16	-06:47:59.37	0.2	0.3	0.4	19.8	2.6	2.1	304	14.3
4	18:38:07.63	-06:48:40.29	0.2	0.3	0.5	19.5	2.3	2.1	311	12.3
5	18:38:07.35	-06:47:01.15	0.4	0.4	0.8	21.0	5.9	17.1	2539	13.0
6	18:38:07.15	-06:50:11.21	0.1	0.2	0.3	18.6	2.4	0.5	71	20.7
7	18:38:11.27	-06:47:57.47	0.4	0.4	0.6	20.9	2.8	5.4	797	4.2
8	18:38:13.50	-06:45:22.26	0.5	0.5	0.9	20.6	2.7	9.4	1394	3.8
9	18:38:13.48	-06:46:42.08	0.3	0.4	0.6	22.8	2.3	4.3	637	6.5
10	18:38:12.62	-06:50:43.81	0.7	0.7	1.3	20.2	3.2	25.6	3801	3.6
11	18:38:16.74	-06:47:58.10	0.5	0.5	0.9	27.9	2.3	9.6	1427	4.9
12	18:38:18.18	-06:45:40.49	0.4	0.4	0.7	19.0	3.7	8.3	1226	8.1
13	18:38:16.86	-06:47:01.07	0.3	0.4	0.5	24.6	2.6	3.2	469	5.2
14	18:38:17.00	-06:49:14.50	0.4	0.5	0.6	21.7	2.3	3.7	543	2.8
15	18:38:21.11	-06:46:20.35	0.4	0.5	0.8	21.4	2.5	7.1	1058	4.4
						N40				
1	18:38:47.77	-06:54:04.17	1.2	1.3	1.9	16.9	2.2	4.1	5436	1.2
2	18:38:50.25	-06:55:57.66	2.0	2.1	3.4	17.4	2.2	13.8	18121	0.7
3	18:38:51.28	-06:52:07.01	0.9	1.0	1.5	17.4	2.1	2.5	3296	1.7
4	18:38:52.69	-06:50:53.49	1.7	1.8	2.8	17.0	2.9	11.8	15495	1.1
5	18:38:55.72	-06:55:25.40	1.0	1.1	1.8	18.7	1.9	3.5	4635	1.6
6	18:38:56.54	-06:54:18.46	0.9	1.0	1.5	18.0	2.0	2.9	3926	1.9
7	18:38:56.80	-06:53:18.83	0.7	0.8	1.4	17.8	2.1	2.3	3059	3.5
8	18:38:55.97	-06:52:12.76	1.2	1.3	2.3	16.5	3.2	9.0	11871	2.3
						N53				
1	18:48:43.22	-13:92:03.70	0.6	0.8	1.4	24.9	0.9	0.9	1169	1.9
2	18:48:44.60	-13:75:17.60	0.6	0.8	1.3	22.2	1.2	0.7	1011	1.7
3	18:48:44.21	-13:85:02.20	0.4	0.6	1.0	25.0	0.8	0.4	585	3.9
4	18:48:46.24	-13:84:07.20	0.5	0.7	1.1	25.1	0.9	0.8	1090	3.4

Table 6.5
continued

Clump No.	RA (J2000) (hh:mm:ss.ss)	DEC (J2000) (dd:mm:ss.ss)	Radius r_d	r_g	(pc) r_p	Mean T_d (K)	Mean $N(H_2)$ ($\times10^{22}$cm^{-2})	$\sum N(H_2)$ ($\times10^{23}$cm^{-2})	Mass ($M_\odot$)	No. density (n_{H_2}) ($\times10^4$cm^{-3})
						N73				
1	19:02:28.95	+05:05:07.33	0.4	0.6	0.7	19.8	1.4	0.7	587	4.6
2	19:02:30.66	+05:05:44.05	1.1	1.1	1.5	21.5	1.1	2.0	1749	0.5
3	19:02:32.06	+05:06:44.34	0.2	0.4	0.7	20.9	1.1	0.5	392	17.2
4	19:02:36.84	+05:06:10.24	0.5	0.6	1.0	21.9	1.0	0.9	793	2.4
5	19:02:40.69	+05:05:04.92	1.3	1.4	2.1	20.2	1.3	4.5	3943	0.6
						N82				
1	19:10:24.06	+07:53:17.14	0.8	0.8	1.1	21.7	0.9	1.1	769	0.6
2	19:10:24.83	+07:51:45.18	0.3	0.5	0.8	23.9	0.5	0.4	292	2.7
3	19:10:27.43	+07:50:01.81	0.4	0.6	0.9	20.9	0.9	0.8	525	2.6
4	19:10:26.28	+07:54:47.54	0.8	0.9	1.5	24.7	0.8	1.6	1079	0.6
5	19:10:33.97	+07:53:24.39	1.2	1.2	1.9	21.5	1.3	4.9	3279	0.8
6	19:10:33.97	+07:53:24.39	0.8	0.9	1.6	25.7	0.9	2.5	1700	1.2
7	19:10:31.96	+07:50:33.05	0.8	0.9	1.5	23.7	0.6	1.5	998	0.6
8	19:10:34.47	+07:51:59.01	0.4	0.6	0.7	25.2	0.5	0.1	70	0.5
9	19:10:36.54	+07:52:23.86	0.9	0.9	1.6	24.7	0.7	1.9	1335	0.7
10	19:10:37.54	+07:51:19.01	0.9	0.9	1.4	23.6	0.7	1.2	789	0.4
						N84				
1	19:10:07.11	+08:43:02.48	0.1	0.1	0.1	18.8	1.4	0.9	10	9.7
2	19:10:09.44	+08:44:16.67	0.1	0.1	0.2	23.4	0.9	2.9	36	5.1
3	19:10:15.81	+08:44:28.26	0.1	0.1	0.2	21.1	0.9	1.6	19	6.6
						N92				
1	19:15:20.05	+09:45:27.39	0.5	0.6	1.0	21.6	0.6	1.3	505	1.1
2	19:15:21.09	+09:44:02.30	0.6	0.6	0.9	20.8	0.7	1.3	478	0.9
3	19:15:22.33	+09:45:56.52	0.4	0.5	0.7	22.7	0.6	0.5	195	1.3
4	19:15:23.43	+09:46:38.64	0.6	0.6	1.1	22.4	0.5	1.1	436	0.9
5	19:15:21.55	+09:43:29.61	0.2	0.4	0.7	20.8	0.5	0.4	144	4.3
6	19:15:24.70	+09:45:08.05	0.6	0.6	1.1	20.6	0.8	1.5	589	1.0
7	19:15:26.37	+09:45:59.94	0.4	0.5	0.8	23.8	0.5	0.6	244	1.2
8	19:15:30.30	+09:46:09.86	0.8	0.8	1.2	23.8	0.4	1.1	405	0.3
9	19:15:34.45	+09:45:19.19	0.4	0.5	0.6	22.2	0.4	0.3	121	0.6
						N95				
1	19:16:58.80	+10:45:43.66	0.4	0.6	0.9	20.7	0.7	0.6	362	1.7
2	19:17:00.35	+10:46:15.36	0.1	0.4	0.6	20.7	0.6	0.1	84	52.3
3	19:17:01.52	+10:44:54.57	0.5	0.6	0.9	21.3	0.7	0.7	436	1.6
4	19:17:04.72	+10:44:22.97	0.5	0.6	1.0	19.5	1.0	1.2	756	2.4
5	19:17:05.47	+10:43:29.66	0.4	0.6	1.0	19.1	1.2	1.3	842	3.9
6	19:17:06.37	+10:43:01.95	0.4	0.6	1.1	17.9	1.3	1.7	1125	5.3
						N101				
1	19:22:57.89	+14:16:17.10	0.5	0.5	0.9	27.7	1.9	4.7	1267	4.0
2	19:23:00.09	+14:17:01.14	0.5	0.5	0.9	27.2	2.9	6.3	1671	5.8
3	19:22:58.72	+14:15:13.90	0.4	0.4	0.8	28.2	1.4	2.4	633	4.2
4	19:23:02.60	+14:18:02.70	0.5	0.5	0.9	27.5	2.8	6.8	1840	6.4
						N105				
1	19:21:21.08	+15:28:09.24	0.8	0.9	1.6	22.9	0.5	0.8	1019	0.6
2	19:21:21.14	+15:29:14.78	0.8	0.9	1.6	21.5	0.7	0.9	1061	0.7
3	19:21:22.74	+15:29:44.09	0.6	0.8	1.3	20.6	0.6	0.8	887	1.2
4	19:21:26.31	+15:29:14.31	0.9	1.0	1.5	20.2	7.1	1.1	1236	0.6
5	19:21:25.68	+15:28:21.41	1.1	1.2	2.1	20.8	0.9	2.5	2888	0.8
						N115				
1	19:30:10.38	+18:17:30.14	0.2	0.3	0.4	20.8	0.9	1.6	118	3.3
2	19:30:13.71	+18:17:45.90	0.2	0.2	0.3	21.3	1.0	0.9	67	6.5
3	19:30:17.46	+18:17:51.64	0.2	0.2	0.4	23.3	0.8	0.9	72	3.1
4	19:30:14.94	+18:16:38.39	0.3	0.4	0.6	22.5	0.9	3.2	237	2.1
5	19:30:18.61	+18:18:13.54	0.2	0.2	0.3	23.5	0.8	0.7	54	2.5
6	19:30:19.70	+18:18:42.76	0.3	0.3	0.4	23.7	0.7	1.4	101	1.7
7	19:30:18.85	+18:16:45.97	0.2	0.3	0.4	25.4	0.5	0.8	60	1.7

Table 6.5
continued

Clump No.	RA (J2000) (hh:mm:ss.ss)	DEC (J2000) (dd:mm:ss.ss)	Radius (pc) r_d	r_g	r_p	Mean T_d (K)	Mean $N(H_2)$ ($\times10^{22}$cm^{-2})	$\sum N(H_2)$ ($\times10^{23}$cm^{-2})	Mass ($M_\odot$)	No. density (n_{H_2}) ($\times10^4$cm^{-3})
						N124				
1	19:38:27.46	+22:57:42.58	0.3	0.3	0.4	18.0	0.5	0.7	76	1.4
2	19:38:30.51	+22:57:54.63	0.2	0.2	0.4	19.3	0.4	0.3	29	1.6
3	19:38:32.51	+22:58:15.27	0.2	0.3	0.4	20.3	0.4	0.5	48	1.8
4	19:38:35.02	+22:58:49.51	0.3	0.4	0.6	22.2	0.3	0.6	60	0.5
5	19:38:35.89	+23:00:04.72	0.4	0.4	0.6	20.9	0.3	0.8	82	0.4
						N133				
1	19:49:06.55	+26:50:42.36	0.3	0.3	0.5	24.2	0.4	1.9	89	1.2
2	19:49:09.92	+26:52:26.78	0.3	0.3	0.5	26.0	0.4	1.5	69	0.9
3	19:49:09.30	+26:48:52.27	0.4	0.4	0.7	23.9	0.5	3.7	166	1.2
4	19:49:13.22	+26:51:00.70	0.2	0.3	0.4	24.5	0.5	1.6	70	1.9
5	19:49:14.35	+26:52:51.67	0.3	0.3	0.5	24.6	0.5	1.8	80	1.4
6	19:49:15.38	+26:50:10.63	0.2	0.3	0.4	22.9	1.1	3.4	152	4.4
7	19:49:18.48	+26:51:13.90	0.3	0.3	0.5	23.3	0.8	2.4	108	1.8
8	19:49:19.95	+26:51:57.97	0.2	0.3	0.4	23.2	0.8	1.6	73	1.9
9	19:49:18.59	+26:49:09.33	0.3	0.3	0.6	22.8	0.6	3.2	145	1.6

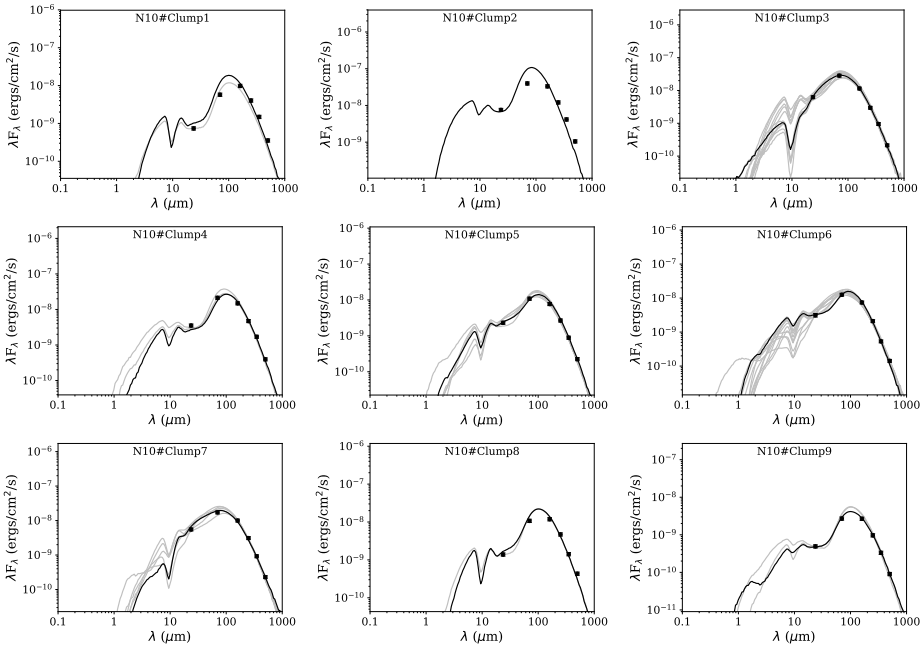

Figure 6.19: Results of the command line SED modeling of Robitaille et al. (2007) for the nine clumps associated with bubble N10. The black solid line is the best model fit and gray lines are the subsequent models satisfying criteria $\chi^2 - \chi^2_{\rm best} < 3$.

6.6, we list the range of values of various retrieved parameters from the models satisfying the criteria of $\chi^2 - \chi^2_{\rm best}$ (per data point) < 3 with the weighted mean values in parenthesis. The retrieved values of the parameters are to be used as indicative only as these models involve a large range in parameters with limited data points.

Table 6.6

Results from the SED fitting are listed in this table. Final mass of the star, envelope accretion rate, envelope mass and total luminosity of the clumps are given in columns 1 to 4. Values within the parenthesis are the weighted mean obtained from all the models fitted satisfying the criteria of $\chi^2 - \chi^2_{\rm best} < 3$.

Clump No.	$M_\star$ ($M_\odot$)	$\dot{M}_{\rm env}$ (10^{-3}M$_\odot$ yr^{-1})	$M_{\rm env}$ (M$_\odot$)	$L_\star$ (10^3 L$_\odot$)	Maximum mass (M$_{\rm max}$ in M$_\odot$) 30%†	6.5%†	30%‡	6.5%‡
			N10					
1	25 – 25 (25)	9 – 9 (9)	4356 – 4356 (4356)	69 – 69 (69)	70	22	59	18
2	14 – 20 (16)	4 – 7 (5)	2066 – 3413 (2821)	16 – 33 (24)	16	5	32	13
3	20 – 25 (22)	8 – 10 (9)	4096 – 5223 (4602)	17 – 25 (19)	31	10	61	19
4	13 – 20 (18)	6 – 9 (8)	2590 – 4672 (4040)	8 – 15 (11)	21	7	56	17
5	12 – 20 (16)	3 – 8 (5)	1086 – 2999 (1830)	9 – 14 (11)	12	4	30	9
6	15 – 19 (16)	4 – 7 (6)	2597 – 3979 (3196)	10 – 22 (14)	19	6	46	14
7	20 – 22 (21)	9 – 10 (10)	4511 – 5223 (4860)	15 – 17 (16)	38	12	64	20
8	12 – 13 (12)	4 – 6 (4)	1046 – 2791 (2484)	3 – 4 (3)	10	3	39	12
9	20 – 20 (20)	10 – 10 (10)	5223 – 5223 (5223)	17 – 17 (17)	66	20	68	21
			N32					
1	19 – 19 (19)	9 – 9 (9)	4672 – 4672 (4672)	11 – 11 (11)	45	14	73	23
2	27 – 27 (27)	3 – 3 (3)	1481 – 1481 (1481)	143 – 143 (143)	117	36	26	8
			N33					
1	13 – 20 (16)	6 – 9 (7)	2590 – 4672 (3535)	7 – 11 (9)	27	8	58	16
2	20 – 25 (22)	8 – 10 (9)	3612 – 5223 (4280)	17 – 28 (22)	56	17	60	18
3	16 – 25 (20)	7 – 10 (8)	3844 – 5223 (4428)	11 – 18 (15)	37	11	60	19
			N37					
1	9 – 18 (12)	1 – 5 (1.9)	727 – 1822 (1075)	4 – 10 (7)	11	3	20	6
2	16 – 25 (20)	7 – 8 (7.0)	3360 – 3773 (3581)	20 – 31 (27)	27	8	51	16
3	15 – 21 (18)	3 – 8 (5.9)	1719 – 4141 (3088)	30 – 58 (37)	38	12	45	14
4	15 – 18 (17)	4 – 7 (5.7)	2192 – 3773 (3045)	16 – 26 (21)	21	6	45	14
5	27 – 27 (27)	3 – 3 (3.3)	1481 – 1481 (1481)	143 – 143 (143)	66	20	26	8
6	16 – 25 (21)	6 – 8 (7.3)	3455 – 4141 (3749)	28 – 43 (33)	39	12	52	16
7	20 – 25 (22)	8 – 10 (8.2)	3612 – 5223 (4133)	17 – 43 (27)	58	18	57	18
			N39					
1	11 – 15 (13)	3 – 6 (4)	1186 – 3628 (2270)	4 – 7 (6)	14	4	36	11
2	27 – 31 (28)	3 – 9 (5)	1481 – 3584 (2016)	135 – 183 (147)	41	13	32	10
3	9 – 13 (11)	1 – 3 (2)	516 – 1538 (893)	3 – 6 (4)	8	2	17	5
4	10 – 13 (11)	1 – 3 (2)	652 – 2109 (1223)	2 – 5 (4)	8	2	22	7
5	16 – 25 (21)	6 – 8 (7)	3361 – 4141 (3661)	28 – 35 (31)	39	12	51	16
6	2 – 8 (7)	0.3 – 2 (1)	117 – 644 (233)	0.3 – 1 (1)	3	1	6	2
7	13 – 21 (16)	3 – 4 (4)	897 – 2632 (1838)	11 – 24 (16)	16	5	30	9
8	15 – 25 (18)	5 – 8 (6)	3003 – 3612 (3229)	14 – 28 (18)	25	8	47	14
9	12 – 21 (16)	2 – 6 (3)	897 – 3003 (1768)	14 – 32 (23)	13	4	29	9
10	19 – 27 (23)	3 – 9 (6)	1481 – 4356 (3032)	49 – 143 (78)	53	16	44	14
11	25 – 44 (31)	3 – 10 (7)	1481 – 4079 (2975)	99 – 234 (149)	25	8	44	14
12	13 – 19 (16)	6 – 9 (7)	2590 – 4672 (3686)	8 – 15 (10)	22	7	52	16
13	12 – 25 (15)	2 – 4 (3)	897 – 2350 (1477)	10 – 31 (19)	11	3	26	8
14	12 – 21 (14)	2 – 6 (4)	897 – 3218 (2013)	7 – 21 (11)	12	4	32	10
15	15 – 17 (16)	4 – 6 (5)	2597 – 3368 (3054)	12 – 22 (16)	20	6 45	14	
			N40					
1	20 – 25 (23)	8 – 8 (8)	3612 – 4141 (3868)	28 – 30 (29)	70	22	54	17
2	27 – 27 (27)	3 – 3 (3)	1481 – 1481 (1481)	143 – 143 (143)	177	54	26	8
3	17 – 25 (21)	7 – 8 (8)	3612 – 4141 (3834)	20 – 30 (26)	48	15	53	16
4	27 – 27 (27)	3 – 3 (3)	1481 – 1481 (1481)	143 – 143 (143)	157	48	26	8
5	20 – 20 (20)	10 – 10 (10)	5223 – 5223 (5223)	17 – 17 (17)	62	19	68	21
6	20 – 20 (20)	10 – 10 (10)	5223 – 5223 (5223)	17 – 17 (17)	55	17	68	21
7	15 – 25 (21)	5 – 10 (8)	3083 – 5223 (3861)	14 – 28 (20)	45	14	54	17
8	27 – 27 (27)	3 – 3 (3)	1481 – 1481 (1481)	143 – 143 (143)	128	39	54	17
			N53					
1	20 – 23 (21)	7 – 8 (7)	3463 – 4096 (3801)	25 – 43 (34)	22	7	53	16
2	20 – 25 (22)	9 – 10 (10)	4406 – 5223 (4903)	15 – 18 (17)	19	6	53	16
3	16 – 25 (21)	6 – 10 (8)	3315 – 5223 (4158)	15 – 25 (19)	13	4	57	18
4	20 – 25 (21)	8 – 10 (9)	4096 – 5223 (4567)	17 – 25 (20)	20	6	61	19

†Maximum mass calculated using clump mass, derived from column density and ‡using the model derived envelope mass of clumps.

Table 6.6
continued

Clump No.	$M_\star$ ($M_\odot$)	$\dot{M}_{env}$ ($10^{-3} M_\odot$ yr^{-1})	M_{env} ($M_\odot$)	$L_\star$ (10^3 $L_\odot$)	Maximum mass (M_{max} in $M_\odot$) 30%†	6.5%†	30%‡	6.5%‡
			N73					
1	12 – 14 (14)	5 – 7 (6)	2888 – 3716 (3572)	4 – 5 (4)	13	4	61	19
2	20 – 20 (20)	10 – 10 (10)	5223 – 5223 (5223)	17 – 17 (17)	29	9	68	21
3	12 – 13 (12)	4 – 6 (5)	1046 – 2791 (1795)	3 – 4 (4)	9	3	30	9
4	15 – 22 (19)	6 – 9 (8)	2199 – 4511 (2883)	11 – 15 (13)	16	5	43	13
5	20 – 20 (20)	10 – 10 (10)	5223 – 5223 (5223)	17 – 17 (17)	55	17	68	21
			N82					
1	13 – 20 (17)	6 – 9 (7)	1995 – 388 (2674)	6 – 12 (9)	16	5	41	13
2	11 – 18 (12)	2 – 5 (3)	273 – 2433 (1441)	6 – 14 (8)	7	2	25	8
3	13 – 15 (13)	4 – 6 (5)	2433 – 3716 (2901)	4 – 7 (6)	12	4	43	13
4	16 – 25 (20)	6 – 9 (7)	2564 – 4141 (3549)	28 – 35 (31)	20	6	50	16
5	25 – 25 (25)	9 – 9 (9)	4356 – 4356 (4356)	69 – 69 (69)	48	15	59	18
6	21 – 21 (21)	9 – 9 (9)	4348 – 4348 (4348)	70 – 70 (70)	29	9	59	18
7	18 – 25 (21)	6 – 9 (7)	3315 – 4406 (3723)	18 – 28 (24)	19	6	52	16
8	8 – 17 (11)	0.4 – 2 (1)	108 – 680 (302)	2 – 8 (5)	2	1	8	2
9	15 – 25 (20)	3 – 9 (7)	1719 – 4141 (3290)	28 – 64 (41)	23	7	48	15
10	16 – 25 (18)	4 – 9 (6)	1866 – 4406 (2822)	15 – 19 (17)	16	5	42	13
			N84					
1	1 – 2 (1)	1 – 1 (1)	25 – 75 (53)	0 – 0.1 (0.0)	1	0.2	2	0.6
2	6 – 11 (8)	0.3 – 3 (1)	48 – 397 (212)	1 – 3 (1)	2	0.5	6	2
3	3 – 6 (4)	1 – 2 (1)	25 – 202 (59)	0.1 – 0.3 (0.2)	1	0.3 2	0.7	
			N92					
1	11 – 18 (13)	3 – 5 (4)	1399 – 2781 (2023)	6 – 11 (8)	11	3	32	10
2	11 – 14 (12)	3 – 6 (4)	1046 – 2791 (1620)	3 – 8 (5)	11	3	28	9
3	9 – 13 (10)	1 – 4 (2)	200 – 1522 (797)	2 – 7 (5)	5	2	16	5
4	11 – 16 (14)	3 – 5 (4)	704 – 2781 (2204)	6 – 8 (6)	10	3	35	11
5	6 – 10 (8)	1 – 3 (2)	353 – 1436 (709)	1 – 2 (1)	4	1	15	5
6	24 – 38 (35)	3 – 3 (3)	1151 – 1304 (1190)	58 – 71 (61)	13	4	22	7
7	10 – 14 (11)	2 – 6 (2)	545 – 2038 (1216)	4 – 9 (6)	6	2	22	7
8	11 – 16 (14)	3 – 5 (4)	704 – 2781 (1936)	6 – 11 (7)	10	3	32	10
9	6 – 10 (8)	1 – 3 (2)	321 – 1436 (596)	1 – 2 (1)	4	1	13	4
			N95					
1	11 – 13 (12)	3 – 6 (4)	549 – 2791 (1568)	3 – 4 (4)	9	3	27	8
2	5 – 8 (7)	1 – 2 (2)	95 – 485 (293)	0.4 – 1 (1)	3	1	7	2
3	11 – 17 (14)	2 – 5 (3)	704 – 2539 (1656)	4 – 8 (6)	10	3	28	9
4	12 – 16 (14)	2 – 7 (6)	1402 – 4351 (3369)	5 – 7 (5)	15	5	48	15
5	12 – 15 (13)	4 – 7 (6)	2433 – 4351 (3377)	5 – 7 (6)	17	5	48	15
6	13 – 15 (14)	5 – 7 (6)	3297 – 4351 (3742)	4 – 5 (4) 21	6	52	16	
			N101					
1	19 – 28 (24)	6 – 9 (7)	2913 – 4356 (3398)	57 – 110 (76)	23	7 49	15	
2	23 – 29 (26)	7 – 10 (9)	3404 – 4356 (4070)	69 – 101 (78)	28	9	56	17
3	14 – 28 (20)	2 – 9 (5)	1084 – 3455 (2520)	26 – 62 (41)	13	4	39	12
4	21 – 27 (26)	3 – 9 (5)	1481 – 4356 (2243)	64 – 143 (114)	30	9	35	11
			N105					
1	16 – 25 (22)	7 – 10 (9)	3844 – 5223 (4452)	15 – 18 (17)	19	6	60	19
2	16 – 19 (17)	7 – 9 (7)	1866 – 4672 (3824)	10 – 16 (13)	20	6	53	16
3	13 – 20 (15)	6 – 7 (6)	1995 – 3882 (2855)	7 – 11 (8)	17	5	43	13
4	19 – 22 (20)	9 – 9 (9)	2199 – 4672 (3788)	11 – 15 (12)	22	7	53	16
5	23 – 23 (23)	8 – 8 (8)	3822 – 3822 (3822)	43 – 43 (43)	43	13	53	16
			N115					
1	6 – 10 (8)	1 – 3 (2)	135 – 862 (547)	1 – 2 (1)	4	1	12	4
2	7 – 8 (8)	1 – 3 (3)	135 – 410 (179)	1 – 1 (1)	2	1	5	2
3	8 – 11 (9)	1 – 3 (1)	153 – 671 (422)	1 – 3 (2)	3	1	10	3
4	9 – 14 (11)	1 – 5 (2)	200 – 1822 (977)	3 – 9 (5)	6	2	19	6
5	7 – 11 (9)	0.4 – 2 (1)	122 – 419 (283)	1 – 3 (2)	2	1	7	2
6	6 – 13 (11)	1 – 4 (1)	240 – 1032 (573)	2 – 7 (4)	3	1	12	4
7	8 – 13 (10)	0.4 – 1 (1)	223 – 671 (395)	2 – 5 (3)	2	1	9	3

†Maximum mass calculated using clump mass, derived from column density and ‡using the model derived envelope mass of clumps.

Table 6.6
continued

Clump No.	$M_\star$ ($M_\odot$)	$\dot{M}_{env}$ (10^{-3} $M_\odot$ yr^{-1})	M_{env} ($M_\odot$)	$L_\star$ (10^3 $L_\odot$)	Maximum mass (M_{max} in $M_\odot$) 30%†	6.5%†	30%‡	6.5%‡
			N124					
1	4 – 7 (5)	2 – 3 (2)	319 – 1028 (521)	0.3 – 1 (0.4)	3	1	12	4
2	3 – 6 (4)	1 – 2 (2)	66 – 303 (109)	0.2 – 0.2 (0.2)	1	0.4	3	1
3	4 – 7 (5)	2 – 2 (2)	95 – 706 (333)	0.3 – 1 (0.4)	2	0.6	8	3
4	6 – 9 (8)	1 – 3 (2)	321 – 1122 (497)	1 – 1 (1)	2	1	11	3
5	6 – 9 (7)	2 – 4 (3)	321 – 1836 (783)	1 – 1 (1)	3	1	16	5
			N133					
1	8 – 13 (10)	0.4 – 5 (1)	172 – 905 (508)	1 – 6 (3)	3	1	11	4
2	8 – 14 (10)	0.3 – 5 (1)	172 – 737 (324)	1 – 7 (4)	2	1	8	2
3	9 – 16 (11)	1 – 6 (2)	333 – 1537 (705)	2 – 10 (6)	5	1	15	5
4	8 – 14 (10)	0.3 – 2 (1)	175 – 737 (305)	1 – 7 (4)	2	1	8	2
5	8 – 10 (9)	1 – 5 (3)	172 – 654 (284)	1 – 3 (2)	3	1	7	1
6	9 – 12 (11)	1 – 4 (2)	272 – 1579 (675)	2 – 8 (4)	4	1	14	4
7	8 – 13 (10)	0.4 – 5 (1)	172 – 1084 (529)	2 – 6 (3)	3	1	12	4
8	5 – 11 (9)	0.3 – 5 (1)	172 – 654 (319)	1 – 4 (2)	3	1	8	2
9	8 – 13 (10)	1 – 4 (1)	193 – 1579 (655)	2 – 10 (5)	4	1	14	4

†Maximum mass calculated using clump mass, derived from column density and ‡using the model derived envelope mass of clumps.

6.4 Results and discussion

The column density and dust temperature distribution maps of the selected sample of bubbles display varied morphology. In general, high column density is seen towards bubble periphery and in some cases, dust clumps are seen towards the centre as well. Majority of the bubbles are associated with warmer dust compared to the surrounding. The number distribution of clumps as a function of the radius and mass are shown in Figure 6.20. The largest clumps are associated with bubble N40 having radius 2.0 pc and 1.7 pc. The three smallest clumps are associated with bubble N84, having radius $\sim$ 0.1 pc. Out of a total of 111 dust clumps detected towards the bubble sample, $\sim$90% have radius $<$ 1 pc. As discussed in Urquhart et al. (2013a), 0.15 pc and 1.25 pc are considered as rough boundaries between 'cores' and 'clumps' and 'clumps and clouds'. Majority of the clumps detected by us fall under the category of 'clumps' and hence, we retain this nomenclature that has been used so far with the caveat that it includes 'cores'. The two largest ones associated with N40 may be considered as 'clouds'. The number distribution with respect to mass reveals that around 77% dust clumps have masses $\lesssim$2000 $M_\odot$ and $\sim$ 19% dust clumps have mass between $\sim$2000 – 5000 $M_\odot$. There are four clumps that are massive having masses greater than 10000 $M_\odot$. These are Clump 2 ($\sim$ 10570 $M_\odot$) associated with bubble N32, and Clumps 2, 4, 8 associated with N40 which have masses $\sim$18120, 15500, 11870 $M_\odot$, respectively.

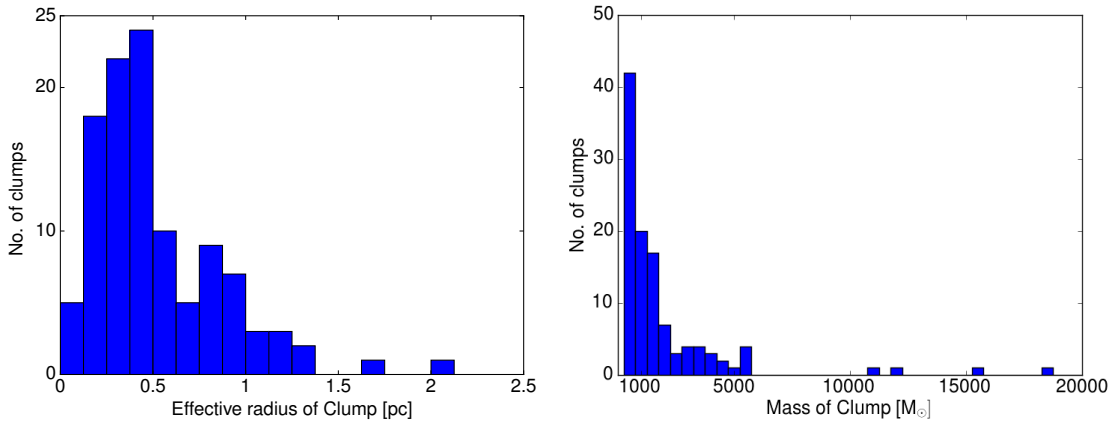

Figure 6.20: (a) Number distribution for the radius of clumps and (b) for the derived clump masses.

Cold dust clumps are regions from which stars form. Hence it is important to investigate their nature. Urquhart et al. (2013b) have studied the nature of a large sample of massive star-forming clumps (500). They obtain a relation between the mass and radius [log(m(r)) = 3.4 ± 0.013 + (1.67 ± 0.036) × log(r)] by a least square fit to their sample. In their study, these authors have used the deconvolved radius of the clumps. In an earlier work, Kauffmann & Pillai (2010) have suggested an empirical relation between the mass and radius of dust clumps, to identify potential high-mass star-forming clumps. They have derived this relation from a large number of clumps, with and without the signature of massive star formation. The mass-radius relation m(r) $\leqslant$ 870 $M_{\odot}$ $(r/pc)^{1.33}$, is shown to be satisfied by clumps devoid of massive star formation. In their study, Kauffmann & Pillai (2010) have used the effective radius of the clumps which are derived from the physical area of the clumps. To probe the nature of the detected clumps associated with our sample of bubbles, we have plotted the mass as the function of radius (deconvolved radius) in Figure 6.21. Figure 6.21 (a) shows the radius as a function of derived clump mass and Figure 6.21 (b) shows the radius as a function of the envelope mass retrieved from the SED models. In these plots, the black solid line adopted is from Kauffmann & Pillai (2010) and the dashed solid line is based on Urquhart et al. (2013b). If we consider the estimated masses of the clumps, calculated from the column density maps, majority of clumps lie above the threshold lines defined in the above studies ($\sim$ 75% if we consider the results of Kauffmann & Pillai (2010) and $\sim$ 52% if we go by the threshold defined by Urquhart et al. (2013b)). This indicates

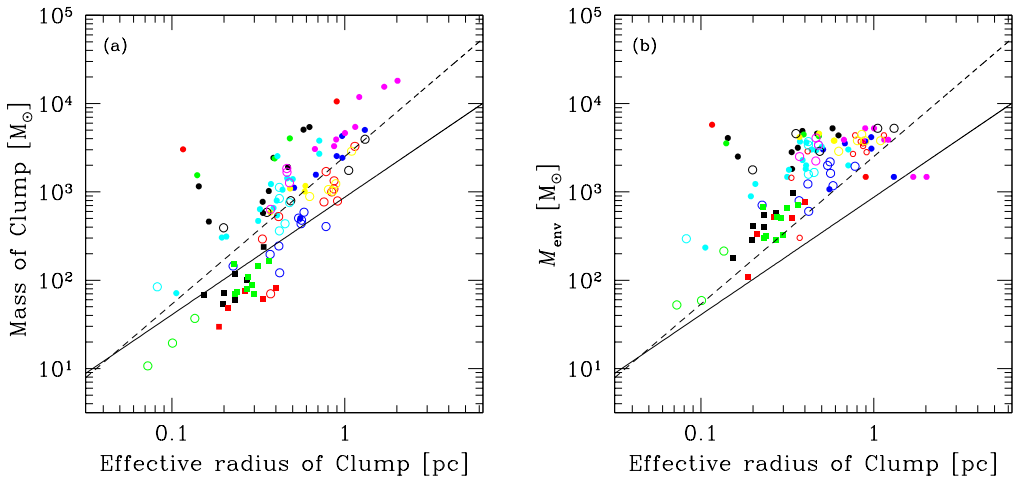

Figure 6.21: Clump masses as a function of the effective radius. (a) Derived clump masses as a fuction of effective radius and (b) envelope masses derived from SED modelling as a function of effective radius. The straight solid line shows the threshold for high-mass star formation based on the relation from Kauffmann & Pillai (2010). Also plotted as the dashed line is the slope from Urquhart et al. (2013b). The symbols used for clumps associated to different bubbles are N10 (●), N32 (●), N33 (●), N37 (●), N39 (●), N40 (●), N53 (●), N73 (○), N82 (○), N84 (○), N92 (○), N95 (○), N101 (○), N105 (○), N115 (■), N124 (■), and N133 (■).

that majority of the clumps detected and associated with these seventeen bubbles are potential high-mass star-forming clumps. The four clumps having masses greater than 10000 $M_\odot$, fall in the region occupied by massive proto-cluster candidates as shown in Fig. 15 and Fig. 20 of Urquhart et al. (2013a) and Urquhart et al. (2013b), respectively. For the model derived envelope masses the percentage increases.

As discussed in Chapter 3, we attempt to understand the evolutionary phase of these clumps associated with the bubbles. In Figure 6.22(a) and (b), we plot the clump mass and the corresponding envelope mass determined from the SED models as a function of the derived luminosity, respectively. The loci demarcating the accelerating accretion and onset of envelope clearing phases, adopted from Fig. 9 of Molinari et al. (2008), are also plotted in this figure. Figure 6.22(a) shows that most of the clumps are located close to the ZAMS loci and are possibly in their final accelerated accretion phase. This agrees well with the model predicted high envelope accretion rates given in Table 6.6. Though still in the accelerating accretion phase, distribution seems to shift downward from the ZAMS loci when the luminosity is plotted as a function of the envelope mass. In Figure 6.23(a), we plot the envelope mass as a function of the final mass of

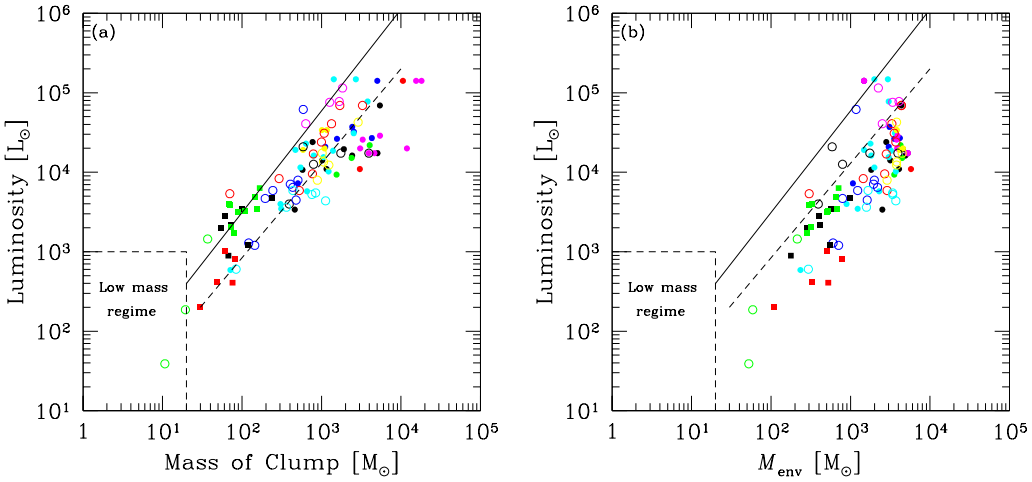

Figure 6.22: Clump luminosity as a function of mass. (a) Luminosity as a function of the derived clump masses and (b) for luminosity as a function of envelope masses derived from SED modelling. The solid and dashed lines are adopted from Fig. 9 of Molinari et al. (2008). These lines distinguish the accelerating accretion phase and the onset of envelope clearing phase. Symbols are same as given in Figure 6.21.

the star, M_* derived from the SED models. The derived envelope mass is considered here as the initial mass of the envelope given the almost vertical evolutionary track in the $L_{bol} - M_{env}$ plot of Molinari et al. (2008) where the mass of the envelope remains the same from the initial to the end of accelerating accretion phase. As seen in the figure, the final mass of the star follows a decreasing trend with the decrease in mass of the envelope. The figure also shows the log-log fit from Molinari et al. (2008). The general trend and slope seen in our clumps are consistent with their fit but shifted to the left. Based on SED model fitted values, our results also hint at a disagreement with the prediction of competitive accretion model of Bonnell et al. (2004), who opine that the final mass of a star is unrelated to the initial mass of the clump. From the estimated mass of the stars and the envelopes, we calculate the star formation efficiency, $\epsilon = [\frac{M_*}{M_{env}} \times 100]$ for all the clumps. Figure 6.23(b) shows this as a function of the envelope mass. The derived values of star-forming efficiency decreases from 6.5 % to 0.5% with increasing envelope mass which in this case is assumed to be the initial envelope mass. The highest estimated efficiency is consistent with that presented in Molinari et al. (2008) and the average star-forming efficiency across the Galaxy as discussed in Williams & McKee (1997). However, for the massive clumps in our sample, we obtain a lower estimate for the efficiency. This is not

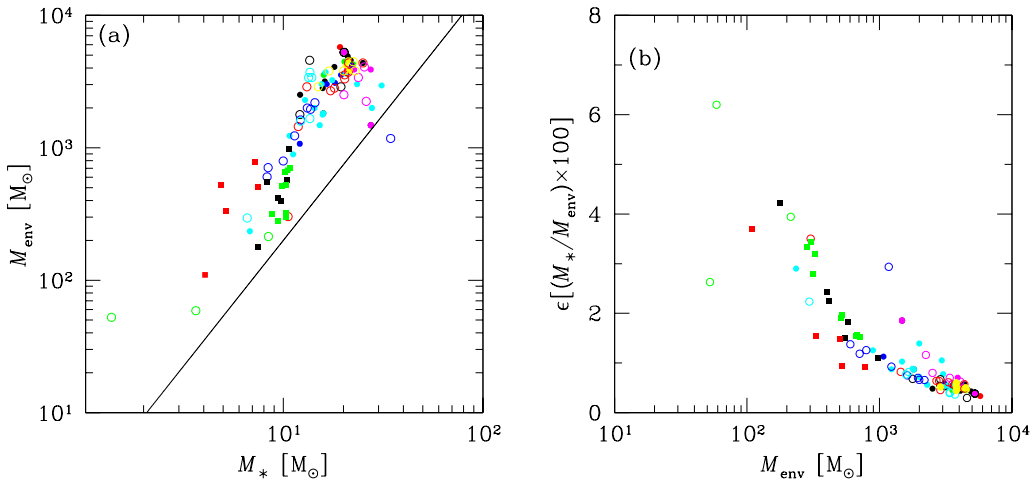

Figure 6.23: (a) The final mass of the massive star, M_* as a function of the envelope mass (assumed to be the initial mass of the envelope here). The straight line is the fit adopted from Molinari et al. (2008). (b) The star forming efficiency of the clumps as a function of the envelope mass. Symbols are same as given in Figure 6.21.

surprising since our simplistic approach assumes that these form a single star whose mass is derived from the single star SED models. In addition, as discussed in Molinari et al. (2008), the estimated values of the star-forming efficiency should be taken as a lower limit considering the fact that massive YSOs form in clusters along with low and intermediate-mass stars. The larger the clump mass, the more populous would be the cluster and hence relatively less mass goes to the most massive member. Hence, using the mass of the most massive member understates the star-forming efficiencies.

We have further explored the potential of all the clumps to form high-mass star. For this, we have estimated the most massive star (M_{max}) that can be formed by a clump, following the discussions outlined in Svoboda et al. (2016) who have used the stellar IMF from Kroupa (2001). As stated in Svoboda et al. (2016), the total stellar cluster mass is equal to the mass of the progenitor clump times the star formation efficiency (ϵ) and the relation between M_{max} and mass of clump given as follows

$$M_{max} = 20\ M_\odot \left(\frac{\epsilon\ \times\ M_{clump}}{0.3\ \times\ 1064 M_\odot} \right)^{1/1.3} \tag{6.2}$$

We consider the highest efficiency of 6.5% estimated from our samples. We have also derived the maximum mass for a higher efficiency of 30% as discussed in Lada & Lada (2003). The

maximum mass of stars derived using the above equation are listed in Table 6.6. In Figure 6.24, we plot the SED model derived final mass of the star as a function of the maximum mass estimated using (a) the derived clump mass from the column density maps and (b) model derived envelope mass. The plots show that the model derived final mass of the star is fairly consistent (slightly higher) with the estimate of maximum mass derived using the envelope mass if we take the star formation efficiency to be 6.5%. However, for a higher efficiency of 30%, the maximum mass estimates are appreciably larger than the estimated final mass of the star. Maximum mass determined from the clump mass are smaller than the predicted final mass of the star for efficiency of 6.5%. If the star formation is assumed to be more efficient (30%) then beyond around $\sim 15 M_{\odot}$, the estimated maximum mass is larger. These trends reassure that inspite of the oversimplistic assumptions that have gone in, our estimates of the final mass of stars likely harboured by the dust clumps and the predicted envelope masses are consistent with the formulation of deriving the mass of the most massive member possible from a clump of a given mass.

We detect a large number of clumps associated with these seventeen bubbles. In cases of several bubbles, these detected clumps are located in the rims thus suggesting a triggered star formation scenario. The model derived parameters suggest most to be harbouring high-mass stars. A word or two of caution is necessary here. Our simplistic assumption that each clump forms one star needs to be taken with caution. Further, many of these massive clumps may have several dense cores and those remain unresolved with the threshold set to detect the clumps.

6.5 Summary

In this chapter, we have probed the cold dust emission associated with the seventeen bubbles and analyse them statistically. The main results from our analysis are as follows.

1. Dust temperature and column density maps are generated using SED modelling of the thermal dust emission from *Herschel* FIR data. The column density maps reveal the presence of high density clumps and filaments associated with the bubbles.

2. Using the 250 μm image and the 2D variation of the *clumpfind* algorithm, cold dust clumps have detected towards the bubbles. The masses of clumps as derived from the

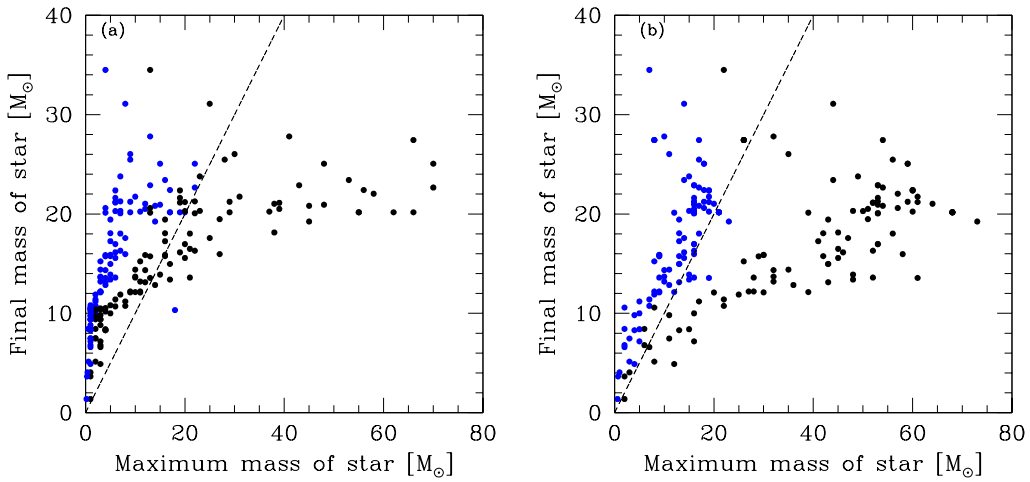

Figure 6.24: Estimated maximum mass of a star that can be formed from a clump of a given mass as a function of the model estimated final mass of the star – (a) maximum mass derived from clump mass and (b) maximum mass calculated from model derived envelope mass. In (a) we have excluded clumps with estimated masses greater than 10000 $M_\odot$. The blue and black circles show the estimates with 6.5 and 30% star formation efficiency, respectively. The dashed line is the locus of $M_\star = M_{max}$.

column density maps and we see the presence of massive clumps within our sample.

3. The mass, size and luminosity of the clumps show that they are potential high-mass star-forming clumps which are possibly in the accelerating accretion phase. This is consistent with the results obtained from SED modelling.

4. The identification of dust clumps on the bubble rims, and the evidence of star formation activity in them, confirms the scenario of triggered star formation and emphasizes the fact that IR dust bubbles are indeed ideal laboratories to probe this.

Chapter 7

Conclusion and future work

Given the importance of high-mass stars, this field involving their formation is an active research area in stellar astrophysics. In the introductory chapter, we discussed about the associated observational and theoretical challenges. Inspite of the tremendous progress seen in recent years, the understanding is still sketchy. This gap can be narrowed by exploring a large sample of star-forming regions over a wide range of wavelength bands and providing valuable observational data for addressing the theoretical concerns. In this thesis work, we have attempted to contribute to this field through extensive multiwavelength analysis of several massive star-forming regions. We selected southern regions which are not that well studied. The key findings from our study are briefly summarized in the following section.

7.1 Summary

In chapter 3, star formation towards the bubble, S10, and a possible outflow source, EGO345, has been investigated. The radio maps at 610 and 1280 MHz show the presence of ionized emission in the interior of the bubble with the emission being more extended at the lower frequency. A steep gradient towards the likely centre of the bubble is also seen at this frequency. Radio emission is also detected towards EGO345 that appears to be more extended at 1280 MHz. Assuming optically thin free-free emission, these regions are estimated to be ionized by early B to late O type stars. Using the *Spitzer* GLIMPSE MIR data, 14 and 5 YSOs are detected towards S10 and EGO345, respectively. The YSO population do not show any particular trend in the distribution. A Class-I/II-type source (IRS1) is identified ∼7″ from the radio peak of S10. By modelling the SED, the mass is estimated to be 6.2 $M_{\odot}$. This suggests that IRS1 is unlikely to be the NIR counterpart of the ionizing star of S10. The massive star responsible for the ionized region is likely to be a deeply embedded source.

Pixel-wise, modified blackbody fits to the thermal dust emission using *Herschel* FIR data was performed to construct dust temperature and column density maps. The distribution of ion-

ized gas traced by the radio emission is seen to be consistent with the location of warmer dust. The column density map also reveals the presence of several high density clumps and filaments. Eight clumps are detected in this complex using the 250 μm image. The masses and linear diameter of these clumps range between ~300 – 1600 $M_{\odot}$ and 0.2 – 1.1 pc, respectively, which qualifies them as high-mass star-forming clumps. Modeling of the SEDs of these clumps indicated the presence of high luminosity, high accretion rate, massive YSOs possibly in the accelerating accretion phase. Furthermore, based on the radio and MIR morphology, the occurrence of a possible bow wave towards the likely ionizing star was explored. This was prompted by the presence of an arc-like feature near the likely centre of the bubble aligned with a rupture seen in the outer shell of the bubble as seen in the MIR images at 5.8 and 8 m. The arc is seen to encompass the radio emission on the south-west side. The ionized emission at both the radio frequencies unravels a likely picture of a flow of ionized gas towards the outer shell originating from the centre of the bubble. The distribution of ionized emission and its correlation with the ruptured MIR bubble morphology and analytical calculations supports the bow-wave scenario.

In chapter 4, we probed the region associated with the IR dust bubble CS51. The ionized emission associated with the bubble shows complex morphology. It mostly fills the bubble interior with a cavity towards the south-west, and is seen to be pronounced at 1300 MHz. The ionized region is found to be excited by a star of spectral type of O6V – O5.5V. The mass of this associated ionized gas within the bubble is estimated to be ~300 $M_{\odot}$. The radio maps reveal the presence of three components (A, B, and C) associated with CS51. They show up as compact regions of enhanced emission. Component A is located towards the likely center of the bubble, the component B (brightest among them) is towards the south-east periphery and component C is located in the north-west rim of the bubble. To study the nature of ionized emission, we constructed the spectral index map, using the 610 and 1300 MHz radio maps. The spectral index map reveals the coexistence of both thermal free-free emission and non-thermal synchrotron emission. The compact regions A and C are seen to be associated with thermal emission and component B shows the signature of non-thermal emission. Further using the optical (B-band) and NIR colors, we identified three sources as potential candidate exciting star(s) from a sample of sources located towards the radio and 24 μm emission peaks.

The column density map shows a fragmented shell-like structure harbouring four clumps to-

wards the periphery of the bubble and one clump is detected inside the bubble close to the likely centre. Dust temperature map further shows the presence of warmer dust in the bubble interior in unison with the ionized emission. The estimated values of mass and radius of the clumps, that lie between 810 – 4600 $M_{\odot}$ and 1.0 – 1.9 pc, respectively, indicate all except one clump to be high-mass star-forming clumps. MALT90 moelcular line survey covers two of the *Herschel* clumps, the clump detected toward the northern periphery of the bubble and the clump detected close to the bubble centre. Five molecular transitions (C_2H, HCN, HCO^+ , HNC, and N_2H^+) are detected towards the two clumps. The hyperfine components of C_2H, HCN, HNC, and N_2H^+ are clearly detected above the noise level. The velocity integrated (0th moment) map for N_2H^+ and HNC are seen to be appreciably extended towards clump located near the rim. Within the uncertainties due to the low signal-to-noise ratio of the observed spectra, the derived line parameters, column density, and fractional abundance suggest a possible earlier evolutionary phase of this clump as compared to central clump. The centroid velocities of the molecular transitions detected show signatures of expansion of the bubble. The clump located towards the northern rim is seen to have red-shifted velocities with respect to the central clump.

The generated column density PDFs display a bimodal distribution thus demonstrating the strong influence of expanding bubble on its surrounding where compression due to ionized gas pressure dominates the effect of turbulence. This reveals that the expanding ionized gas has a potential influence on the surrounding medium, which could lead to triggered star formation on the boundary of the bubble. Assuming the expansion of the associated H II region to occur in a uniform medium, the dynamical age was estimated to be 0.9 – 1.3 Myr, which is higher than the derived fragmentation time of 0.4 – 0.5 Myr. This indicates that the 'collect and collapse' mechanism is possibly at work around the bubble CS51 and responsible for triggering star formation towards the border of the bubble. Further, the IRAC ratio maps involving PAH-bearing and PAH-free bands show the presence of PAH emission associated with the PDR of CS51 thus confirming the generally accepted bubble formation mechanism and related MIR emission.

We have further explored two compact southern Galactic H II regions G346.056−0.021 and G346.077−0.056 and presented the results in chapter 5. The ionized emission reveals a cometary structure for G346.056−0.021. The morphology for G346.077−0.056 is mostly compact and spherical with a faint cometary signature. Assuming the ionized emission is optically thin, free-

free emission, the ZAMS spectral type of the ionizing sources was estimated to lie in the range O7.5V – O7V and O8.5V – O8V for G346.056−0.021 and G346.077−0.056, respectively. The dynamical age of G346.056−0.021 and G346.077−0.056 are similar and is estimated to be ∼0.5 – 0.2 Myr.

Emission from the dust component shows cold dust to be predominantly located near the H II region G346.077−0.056 and the region associated with G346.056−0.021 contains relatively warmer dust. The generated column density map shows the presence of a dense clump towards G346.077−0.056. Two additional clumps are detected in the 870 μm image out of which one is located towards G346.056−0.021. Assuming the clumps to be physically associated and hence at the same distance, the masses were estimated to range between $\sim$ 1400 to 15250 $M_{\odot}$.

In this work, we also attempted to understand the origin of the cometary morphologies that were seen in the H II regions. Our analytical calculations show that the bow-shock mechanism is less likely to be responsible for the observed cometary morphology. However, the variation of the ionized gas and the column density along the cometary axis favours the champagne flow model for the cometary structure seen in both H II regions.

In chapter 6, we carried out a statistical study of cold dust emission towards a sample of seventeen IR dust bubbles selected from Churchwell et al. (2006). In order to study the properties of dust emission, we have used the *Herschel* FIR data. As done for the other sources, pixel-wise, modified blackbody fits to the thermal dust emission using FIR data was carried out to construct dust temperature and column density maps. Cold dust clumps were identified using the 250 μm image. Assuming that clumps on the periphery and within the bubble are at the same distance, we have probed the mass-radius and mass-luminosity of the dust clumps to understand their nature. Majority of clumps are seen to be potential high-mass star-forming ones. With further assumption of clumps forming single stars, SED modeling is carried out. This again reveals that most clumps harbour massive young stellar objects in the accelerated accretion phase. The star formation efficiency derived from the model derived envelope mass lies in the range of 6.5 to 0.5%. The model derived final mass of the star and mass of the envelope seem to be correlated thus negating the competitive accretion as a viable mechanism. However, we would caution against the simplistic assumption taken into consideration in this study.

7.2 Ongoing and future research work

The work done in this thesis is an initial step to understand the high-mass star formation and its influence on the ambient ISM. This is a vast field and I would like to delve deep into the subject to gain further knowledge.

7.2.1 Ongoing research work

- **Investigating the star formation activity towards the sample of IR dust bubbles using molecular line data**

  To explore triggered star formation at play at the bubble borders, we are investigating molecular line data obtained with the KVN 21 m telescope. All the dust clumps at the border of bubbles have been observed at four frequencies 22, 44, 89, and 141 GHz. The aim is to observe masers at 22 GHz (H_2O maser) and 44 GHz (CH_3OH maser) towards these clumps, which are believed to be excited by collisions. These maser emission will allow us to explore the shock front induced because of the expansion of the bubble. Apart from this, molecular line transition of HCO^+ $(1-0)$ and $H_2CO(2_{1,2}-1_{1,1})$ have also been observed towards these clumps. This data will allow us to trace the infall and outflow signature in the molecular clumps. Data reduction of this molecular line data is under progress.

- **Probing massive star formation towards IR dust bubble S6**

  S6 is classified as a complete bubble by Churchwell et al. (2006). This bubble is associated with the star-forming complex IRAS17149−3916 (RCW121) which is located at a kinematic distance of 2.6 kpc (Watson et al., 2010). This region has been part of several studies carried out in various wavebands. Radio observation at frequencies of 4.8, 18, and 22.8 GHz have been observed (Wright et al., 1994; Duronea et al., 2008; Sánchez-Monge et al., 2013a) and the complex is found to be powered by a massive star of spectral type O8.5. 22.235 and 6.7 GHz water and methanol masers respectively are detected towards the region (Walsh et al., 1997, 1998; Sánchez-Monge et al., 2013a). Association of an IR star cluster with RCW121 is reported by Dutra et al. (2003). Three distinct FIR sources are identified and from the SED modeling these dense cores are reported to be massive YSOs with luminosities of a star equivalent to B spectral type (Tapia et al., 2014).

We are in the process of a detailed multiwavelength investigation to explore the star formation activity in this complex. We have observed the region at low frequency radio bands of 610 and 1300 MHz using GMRT. Using these we aim to probe the nature of the associated H II region and the ionizing source. Further, by generating the spectral index map the mechanism of ionized emission will be investigated. The available NIR and MIR data will allow us to explore the nature of stellar sources and for the identification of YSOs to search for signatures of triggered star formation. Using these data the likely ionizing candidates will also be detected. Further plan is to obtain NIR spectra of the bright and possible ionizing candidates in the complex to throw more light on their nature.

7.2.2 Future research plan

- **Radio continuum mapping and Recombination line studies of IR bubbles**

  Low frequency GMRT observations of an extended sample of bubbles are envisaged. The radio data will allow us to explore several crucial properties such as nature of ionization zone, the exciting source(s). The variation of spectral indices will allow us to shed more light on the mechanism involved in the ionized emission emitting from different zones of the bubble. This data will further allow us to investigate the triggered star formation on the periphery of bubbles. The feedback from the high-mass stars will also be investigated using the radio continuum data.

  We also propose to probe the kinematics and dynamics of ionized regions associated with IR bubbles. Radio recombination lines (RRLs) arise from atomic transitions between large principal quantum numbers (typically $n \geq 40$), where the small difference between energy levels means that the emitted photons lie in the radio part of the electromagnetic spectrum. RRLs are excellent tracers of astrophysical plasma. RRL measurements yield several of the physical parameters of the ionized gas like the electron temperature and density (Brocklehurst & Seaton, 1972; Gordon & Sorochenko, 2002). With appropriate line selection, RRLs can be used to trace the kinematics of ionized gas from the extended low density medium in evolved H II regions to the densest parts of young compact H II regions in the bubble periphery probing the triggered star formation.

- **Brγ and H_2 mapping of IR Bubbles**

  We propose to generate a database of Brγ and H_2 line maps of IR dust bubbles to investigate the associated ionized and shocked gas. This will be rendered possible through NIR narrow band imaging in the lines and the nearby continuum.

- **Understanding early phases of high-mass star formation**

  To understand the early phases of high-mass star formation, IRDCs are the ideal sites to explore. Unlike IR dust bubbles, IRDCs are cold, dense and seen in extinction in MIR against the strong background emission of the Galactic plane (Perault et al., 1996; Rathborne et al., 2006). They serve as reservoirs of gas which is potentially available to form stars. In IRDCs, the filamentary structures of molecular gas with sizes of few parsecs (Jackson et al., 2010; Ragan et al., 2014) represent the initial phase of star formation. FIR, sub-mm, and radio-band observations reveal the fragmenting nature of IRDCs. These fragments form the dense massive cores in initial evolutionary stages of star formation. They start from prestellar, dark, cold, and quiescent cores and move to the phase of active, bright substructures with embedded sources driving outflows and H II regions (Carey et al., 2000; Ormel et al., 2005; Rathborne et al., 2005; Pillai et al., 2006; Wang et al., 2011; Sanhueza et al., 2012). Several authors have done extensive research to establish the chemistry of IRDCs (Vasyunina et al., 2011; Peretto et al., 2013, 2014; Tackenberg et al., 2014). There are questions regarding the high-mass star forming potential of IRDC(Kauffmann & Pillai, 2010). Thus to understand the global nature of these initial stages of massive star formation, it is important to investigate IRDCs in detail.

  Star formation activity in IRDCs have been investigated by several authors. Using *Herschel*, ATLASGAL and CO molecular line data Schneider et al. (2015b) have studied four IRDCs (G11.11−0.12, G18.82−0.28, G28.37+0.07, and G28.53−0.25). From the molecular line data, they reported these IRDCs to be the densest regions within GMCs and their analysis show infall signature towards G28.37+0.07 and G11.11−0.12, which supports the scenario of gravitational collapse. Irrespective of their evolutionary stages the column density PDFs towards G11.11−0.12, G18.82−0.28, G28.37+0.07 show power-law distribution over all (high) column densities indicating star formation activity, whereas G28.53−0.25 appears to be devoid of any such activity. In a recent work on IRDC

G035.39−00.33, Myers (2017) conclude that the large scale kinematics and temperature structure of the IRDC is consistent with starless dark filaments. However, on smaller scales the kinematic gas temperature profile traces the heating mechanism revealing the locations of massive protostellar cores. The nature of fragmented cores within the IRDCs has been studied by Henshaw et al. (2016). To address the chemical properties associated with IRDCs clumps, Miettinen (2014) used the molecular line data from the MALT90 survey. They conclude that the detection of SiO is possibly due to shocks driven by outflows. Their result supports the fact that C_2H molecule as a reliable tracer of cold dust gas.

Apart from IRDCs, EGOs or 'green fuzzies' (Cyganowski et al., 2008; Chambers et al., 2009) are also excellent tracers of the early stage of massive star formation. They are believed to be driven by outflows from MYSOs, the shocks from which excite the IR lines. The associated enhanced 4.5 μm emission contains many interesting lines and bandheads - Brα, [Mg IV], [Ar IV], broader bands of polycyclic aromatic hydrocarbons (PAHs), H_2 , [Fe II] and CO bandheads. The above spectral carriers suggest different mechanisms for this emission which include shocks associated with outflows from massive young stellar objects (MYSOs), circumstellar gas and dust, scattered continuum in outflow cavities, PAH emission. Majority of EGOs are associated with IRDCs and with class II Methanol masers which are signposts of massive star formation. Studies have associated the EGOs with shocked H_2 line and/or CO bandheads (Takami et al. 2012; Lee et al. 2012 and references therein) that are excited by shocks driven by bipolar outflows ramming into the ambient interstellar medium. The association with IRDCs and masers make them likely candidates tracing outflows from MYSOs. In a recent work, De Buizer & Vacca (2010) have obtained L and M band spectroscopy on two selected EGOs from the sample of Cygonowski et al. (2008). The L and M band overlap with the 4.5 μm band of IRAC. They identify the spectral carrier in one of them as the shocked H_2 line. The other source shows only continuum emission. The NIR K band includes the shocked H_2 and CO first overtone bands. EGOs have been shown to coincide with H_2 outflows traced with the narrow-band imaging at 2.122 μm which probes the H_2 1 – 0 (S1) shocked emission (Lee et al., 2012). Enhanced 4.5 μm emission tracing the H_2 outflow was also observed toward

MYSO IRAS 17527-2439 (Varricatt, 2011). From the spatial coincidence of features in 115 GHz CO maps and the 4.5 μm emission, Marston et al. (2004) suggested CO emission as the mechanism behind the 'green fuzzies'. However, De Buizer & Vacca (2010) did not detect the 4.6 μm CO feature for the outflow candidate. Apart from the K-band, the H-band also includes the 1.644 μm [Fe II] line. This emission line is also an excellent tracer of dense outflows in young and massive star-forming regions.

The future plan is to study these objects in a wide range of wavelength bands. The IRDC filaments and cores will be probed to obtain their nature in more detail. The FIR and sub-mm data from *Herschel* and ATLASGAL will help to explore the nature of such cores. SED modelling will bring more information about their nature. The properties of dust emission in IRDCs will be probed using the FIR and sub-mm data from *Herschel* and ATLASGAL. Using the MIR data from *Spitzer* Space Telescope the associated warm dust component will be probed and the YSO population in the filaments of IRDCs. Apart from these radio continuum data can be observed using GMRT to study the H II regions associated with the evolved cores. Column density PDFs along with radio continuum data will allow us to look deep into the feedback mechanism of massive protostars on their surrounding. Also, the nature of starless IRDC cores can be studied using the MIR and FIR data, which will throw more light on whether such cores are truly starless or not. Molecular line data can be used to study the kinematics and evolution of dust clumps in the IRDCs. The chemistry of cold dust can also be probed using this data. NIR imaging and spectroscopy associated EGOs will provide more valuable information. The H and K bands include lines due to [Fe II] (1.64 μm), H_2 (2.12 μm) and CO bandheads (2.3 μm). These lines could be shock excited and hence would enable us to trace and associate the EGOs with outflows. Radio continuum mapping of EGOs will further enable to probe massive protostellar jets.

References

Allen, L. E., Calvet, N., D'Alessio, P., et al. 2004, ApJS, 154, 363

Anathpindika, S. V. 2010, MNRAS, 405, 1431

Anderson, L. D., & Bania, T. M. 2009, ApJ, 690, 706

Anderson, L. D., Bania, T. M., Balser, D. S., & Rood, R. T. 2011, ApJS, 194, 32

—. 2012a, ApJ, 754, 62

Anderson, L. D., Bania, T. M., Jackson, J. M., et al. 2009, ApJS, 181, 255

Anderson, L. D., Hough, L. A., Wenger, T. V., Bania, T. M., & Balser, D. S. 2015, ApJ, 810, 42

Anderson, L. D., Zavagno, A., Rodón, J. A., et al. 2010, A&A, 518, L99

Anderson, L. D., Zavagno, A., Deharveng, L., et al. 2012b, A&A, 542, A10

Andre, P., Ward-Thompson, D., & Barsony, M. 1993, ApJ, 406, 122

—. 2000, Protostars and Planets IV, 59

André, P., Men'shchikov, A., Bontemps, S., et al. 2010, A&A, 518, L102

Aniano, G., Draine, B. T., Gordon, K. D., & Sandstrom, K. 2011, PASP, 123, 1218

Arthur, S. J., & Hoare, M. G. 2006, ApJS, 165, 283

Arthur, S. J., Kurtz, S. E., Franco, J., & Albarrán, M. Y. 2004, ApJ, 608, 282

Barnes, P. J., Muller, E., Indermuehle, B., et al. 2015, ApJ, 812, 6

Battersby, C., Bally, J., Ginsburg, A., et al. 2011, A&A, 535, A128

Baug, T., Dewangan, L. K., Ojha, D. K., & Ninan, J. P. 2016, ApJ, 833, 85

Beaumont, C. N., & Williams, J. P. 2010, ApJ, 709, 791

Becker, R. H., White, R. L., Helfand, D. J., & Zoonematkermani, S. 1994, ApJS, 91, 347

Beckwith, S. V. W., Sargent, A. I., Chini, R. S., & Guesten, R. 1990, AJ, 99, 924

Beltrán, M. T., Brand, J., Cesaroni, R., et al. 2006a, A&A, 447, 221

Beltrán, M. T., Cesaroni, R., Codella, C., et al. 2006b, Nature, 443, 427

Benaglia, P., Romero, G. E., Koribalski, B., & Pollock, A. M. T. 2005, A&A, 440, 743

Benjamin, R. A., Churchwell, E., Babler, B. L., et al. 2003, PASP, 115, 953

Bertoldi, F. 1989, ApJ, 346, 735

Bertoldi, F., & McKee, C. F. 1992, ApJ, 395, 140

Bessell, M. S., & Brett, J. M. 1988, PASP, 100, 1134

Beuther, H., Schilke, P., Menten, K. M., et al. 2002, ApJ, 566, 945

Beuther, H., Sridharan, T. K., & Saito, M. 2005, ApJ, 634, L185

Beuther, H., Tackenberg, J., Linz, H., et al. 2012, ApJ, 747, 43

Bisbas, T. G., Wünsch, R., Whitworth, A. P., & Hubber, D. A. 2009, A&A, 497, 649

Bisbas, T. G., Wünsch, R., Whitworth, A. P., Hubber, D. A., & Walch, S. 2011, ApJ, 736, 142

Blitz, L. 1993, in Protostars and Planets III, ed. E. H. Levy & J. I. Lunine, 125–161

Bodenheimer, P., Tenorio-Tagle, G., & Yorke, H. W. 1979, ApJ, 233, 85

Bonnell, I. A., Bate, M. R., & Zinnecker, H. 1998, MNRAS, 298, 93

Bonnell, I. A., Vine, S. G., & Bate, M. R. 2004, MNRAS, 349, 735

Borissova, J., Bonatto, C., Kurtev, R., et al. 2011, A&A, 532, A131

Braz, M. A., & Epchtein, N. 1983, A&AS, 54, 167

Brocklehurst, M., & Seaton, M. J. 1972, MNRAS, 157, 179

Bronfman, L., Alvarez, H., Cohen, R. S., & Thaddeus, P. 1989, ApJS, 71, 481

Bronfman, L., Nyman, L.-A., & May, J. 1996, A&AS, 115, 81

Capriotti, E. R., & Kozminski, J. F. 2001, PASP, 113, 677

Caratti o Garatti, A., Stecklum, B., Linz, H., Garcia Lopez, R., & Sanna, A. 2015, A&A, 573, A82

Carey, S. J., Clark, F. O., Egan, M. P., et al. 1998, ApJ, 508, 721

Carey, S. J., Feldman, P. A., Redman, R. O., et al. 2000, ApJ, 543, L157

Carey, S. J., Noriega-Crespo, A., Mizuno, D. R., et al. 2009, PASP, 121, 76

Caselli, P., & Myers, P. C. 1995, ApJ, 446, 665

Castor, J., McCray, R., & Weaver, R. 1975, ApJ, 200, L107

Caswell, J. L., & Haynes, R. F. 1987, A&A, 171, 261

Caswell, J. L., Fuller, G. A., Green, J. A., et al. 2010, MNRAS, 404, 1029

Cesaroni, R., Galli, D., Neri, R., & Walmsley, C. M. 2014, A&A, 566, A73

Chabrier, G. 2003, PASP, 115, 763

Chambers, E. T., Jackson, J. M., Rathborne, J. M., & Simon, R. 2009, ApJS, 181, 360

Chan, S. J., Henning, T., & Schreyer, K. 1996, A&AS, 115, 285

Chapin, E. L., Ade, P. A. R., Bock, J. J., et al. 2008, ApJ, 681, 428

Chavarría, L. A., Allen, L. E., Hora, J. L., Brunt, C. M., & Fazio, G. G. 2008, ApJ, 682, 445

Chen, X., Ellingsen, S. P., Shen, Z.-Q., Titmarsh, A., & Gan, C.-G. 2011, ApJS, 196, 9

Churchwell, E. 2002, ARA&A, 40, 27

Churchwell, E., Whitney, B. A., Babler, B. L., et al. 2004, ApJS, 154, 322

Churchwell, E., Povich, M. S., Allen, D., et al. 2006, ApJ, 649, 759

Churchwell, E., Watson, D. F., Povich, M. S., et al. 2007, ApJ, 670, 428

Churchwell, E., Babler, B. L., Meade, M. R., et al. 2009, PASP, 121, 213

Clark, B. G. 1980, A&A, 89, 377

Codella, C., Felli, M., Natale, V., Palagi, F., & Palla, F. 1994, A&A, 291, 261

Comerón, F., & Pasquali, A. 2012, A&A, 543, A101

Compiègne, M., Flagey, N., Noriega-Crespo, A., et al. 2010, ApJ, 724, L44

Contreras, Y., Garay, G., Rathborne, J. M., & Sanhueza, P. 2016, MNRAS, 456, 2041

Contreras, Y., Schuller, F., Urquhart, J. S., et al. 2013, A&A, 549, A45

Csengeri, T., Urquhart, J. S., Schuller, F., et al. 2014, A&A, 565, A75

Csengeri, T., Weiss, A., Wyrowski, F., et al. 2016, A&A, 585, A104

Curiel, S., Rodriguez, L. F., Moran, J. M., & Canto, J. 1993, ApJ, 415, 191

Cyganowski, C. J., Whitney, B. A., Holden, E., et al. 2008, AJ, 136, 2391

Dale, J. E., Bonnell, I. A., & Whitworth, A. P. 2007, MNRAS, 375, 1291

Dale, J. E., Ercolano, B., & Bonnell, I. A. 2012, MNRAS, 424, 377

—. 2013a, MNRAS, 430, 234

Dale, J. E., Ngoumou, J., Ercolano, B., & Bonnell, I. A. 2013b, MNRAS, 436, 3430

Dalton, G. B., Caldwell, M., Ward, A. K., et al. 2006, in Proc. SPIE, Vol. 6269, Society of Photo-Optical Instrumentation Engineers (SPIE) Conference Series, 62690X

Das, S. R., Tej, A., Vig, S., et al. 2017, MNRAS, 472, 4750

Davies, B., Hoare, M. G., Lumsden, S. L., et al. 2011, MNRAS, 416, 972

De Buizer, J. M., & Vacca, W. D. 2010, AJ, 140, 196

de Geus, E. J., de Zeeuw, P. T., & Lub, J. 1989, A&A, 216, 44

de Graauw, T., Helmich, F. P., Phillips, T. G., et al. 2010, A&A, 518, L6

De Pree, C. G., Wilner, D. J., Deblasio, J., Mercer, A. J., & Davis, L. E. 2005, ApJ, 624, L101

Deharveng, L., Peña, M., Caplan, J., & Costero, R. 2000, MNRAS, 311, 329

Deharveng, L., Schuller, F., Anderson, L. D., et al. 2010, A&A, 523, A6

Deharveng, L., Zavagno, A., Samal, M. R., et al. 2015, A&A, 582, A1

Deller, A. T., Forbrich, J., & Loinard, L. 2013, A&A, 552, A51

Dewangan, L. K., & Ojha, D. K. 2013, MNRAS, 429, 1386

Dewangan, L. K., Ojha, D. K., Anandarao, B. G., Ghosh, S. K., & Chakraborti, S. 2012, ApJ, 756, 151

Di Francesco, J., Johnstone, D., Kirk, H., MacKenzie, T., & Ledwosinska, E. 2008, ApJS, 175, 277

Dirienzo, W. J., Indebetouw, R., Brogan, C., et al. 2012, AJ, 144, 173

Dobbs, C. L., Bonnell, I. A., & Clark, P. C. 2005, MNRAS, 360, 2

Doyle, D., Pilbratt, G., & Tauber, J. 2009, IEEE Proceedings, 97, 1403

Dunham, M. K., Robitaille, T. P., Evans, II, N. J., et al. 2011, ApJ, 731, 90

Duronea, N. U., Arnal, E. M., & Testori, J. C. 2008, in Revista Mexicana de Astronomia y Astrofisica Conference Series, Vol. 33, Revista Mexicana de Astronomia y Astrofisica Conference Series, 161–161

Dutra, C. M., Bica, E., Soares, J., & Barbuy, B. 2003, A&A, 400, 533

Dyson, J. E., & Williams, D. A. 1980, Physics of the interstellar medium

—. 1997, The physics of the interstellar medium, doi:10.1201/9780585368115

Edgar, R., & Clarke, C. 2003, MNRAS, 338, 962

Ellsworth-Bowers, T. P., Rosolowsky, E., Glenn, J., et al. 2015, ApJ, 799, 29

Elmegreen, B. G. 1998, in Astronomical Society of the Pacific Conference Series, Vol. 148, Origins, ed. C. E. Woodward, J. M. Shull, & H. A. Thronson, Jr., 150

Elmegreen, B. G., Kimura, T., & Tosa, M. 1995, ApJ, 451, 675

Elmegreen, B. G., & Lada, C. J. 1977, ApJ, 214, 725

Everett, J., & Churchwell, E. 2010a, in Astronomical Society of the Pacific Conference Series, Vol. 438, The Dynamic Interstellar Medium: A Celebration of the Canadian Galactic Plane Survey, ed. R. Kothes, T. L. Landecker, & A. G. Willis, 69

Everett, J. E., & Churchwell, E. 2010b, ApJ, 713, 592

Faimali, A., Thompson, M. A., Hindson, L., et al. 2012, MNRAS, 426, 402

Fatuzzo, M., & Adams, F. C. 2002, ApJ, 570, 210

Fazio, G. G., Hora, J. L., Allen, L. E., et al. 2004, ApJS, 154, 10

Ferrière, K. M. 2001, Reviews of Modern Physics, 73, 1031

Fontani, F., Beltrán, M. T., Brand, J., et al. 2005, A&A, 432, 921

Foster, J. B., Jackson, J. M., Barnes, P. J., et al. 2011, ApJS, 197, 25

Franco, J., Tenorio-Tagle, G., & Bodenheimer, P. 1990, ApJ, 349, 126

Freyer, T., Hensler, G., & Yorke, H. W. 2003, ApJ, 594, 888

Froebrich, D. 2013, International Journal of Astronomy and Astrophysics, 3, 161

Fukui, Y., Torii, K., Ohama, A., et al. 2016, ApJ, 820, 26

Gama, D. R. G., Lepine, J. R. D., Mendoza, E., Wu, Y., & Yuan, J. 2016, ApJ, 830, 57

Garay, G., & Lizano, S. 1999, PASP, 111, 1049

Garay, G., Moran, J. M., Rodríguez, L. F., & Reid, M. J. 1998, ApJ, 492, 635

Garay, G., Rodriguez, L. F., Moran, J. M., & Churchwell, E. 1993, ApJ, 418, 368

Garwood, R. W., & Dickey, J. M. 1989, ApJ, 338, 841

Garwood, R. W., Perley, R. A., Dickey, J. M., & Murray, M. A. 1988, AJ, 96, 1655

Giannetti, A., Brand, J., Sánchez-Monge, Á., et al. 2013, A&A, 556, A16

Goodman, A. A., Rosolowsky, E. W., Borkin, M. A., et al. 2009, Nature, 457, 63

Gordon, M. A., & Sorochenko, R. L., eds. 2002, Astrophysics and Space Science Library, Vol. 282, Radio Recombination Lines. Their Physics and Astronomical Applications

Greene, T. P., Wilking, B. A., Andre, P., Young, E. T., & Lada, C. J. 1994, ApJ, 434, 614

Griffin, M. J., Abergel, A., Abreu, A., et al. 2010, A&A, 518, L3

Guieu, S., Rebull, L. M., Stauffer, J. R., et al. 2010, ApJ, 720, 46

Güsten, R., Nyman, L.-A., Menten, K., et al. 2006a, The Messenger, 124

Güsten, R., Nyman, L. Å., Schilke, P., et al. 2006b, A&A, 454, L13

Gutermuth, R. A., & Heyer, M. 2015, AJ, 149, 64

Gutermuth, R. A., Myers, P. C., Megeath, S. T., et al. 2008, ApJ, 674, 336

Habe, A., & Ohta, K. 1992, PASJ, 44, 203

Haslam, C. G. T., Salter, C. J., Stoffel, H., & Wilson, W. E. 1982, A&AS, 47, 1

Hattori, Y., Kaneda, H., Ishihara, D., et al. 2016, PASJ, 68, 37

Henshaw, J. D., Caselli, P., Fontani, F., et al. 2016, MNRAS, 463, 146

Herbig, G. H. 1962, Advances in Astronomy and Astrophysics, 1, 47

Hildebrand, R. H. 1983, QJRAS, 24, 267

Hoare, M. G., Kurtz, S. E., Lizano, S., Keto, E., & Hofner, P. 2007, Protostars and Planets V, 181

Hoare, M. G., Roche, P. F., & Glencross, W. M. 1991, MNRAS, 251, 584

Hogerheijde, M. 1998, PhD thesis, Department of Astronomy, University of California, Campbell Hall, Berkeley, CA 94720, USA <EMAIL>michiel@strw.leidenuniv.nl</EMAIL>

Hoq, S., Jackson, J. M., Foster, J. B., et al. 2013, ApJ, 777, 157

Hosokawa, T., & Inutsuka, S.-i. 2005, ApJ, 623, 917

—. 2006, ApJ, 648, L131

Hosokawa, T., & Omukai, K. 2009, ApJ, 691, 823

Houck, J. R., Roellig, T. L., van Cleve, J., et al. 2004, ApJS, 154, 18

Houlahan, P., & Scalo, J. 1992, ApJ, 393, 172

Iben, Jr., I. 1965, ApJ, 141, 993

Icke, V. 1979, ApJ, 234, 615

Immer, K., Cyganowski, C., Reid, M. J., & Menten, K. M. 2014, A&A, 563, A39

Inoue, A. K. 2001, AJ, 122, 1788

Inoue, A. K., Hirashita, H., & Kamaya, H. 2001, ApJ, 555, 613

Inoue, T., & Fukui, Y. 2013, ApJ, 774, L31

Israel, F. P. 1978, A&A, 70, 769

Jackson, J. M., Finn, S. C., Chambers, E. T., Rathborne, J. M., & Simon, R. 2010, ApJ, 719, L185

Jackson, J. M., Rathborne, J. M., Foster, J. B., et al. 2013, PASA, 30, e057

Ji, W.-G., Zhou, J.-J., Esimbek, J., et al. 2012, A&A, 544, A39

Jones, C., & Dickey, J. M. 2012, ApJ, 753, 62

Kahn, F. D. 1974, A&A, 37, 149

Kang, M., Bieging, J. H., Kulesa, C. A., & Lee, Y. 2009, ApJ, 701, 454

Kang, M., Bieging, J. H., Kulesa, C. A., et al. 2010, ApJS, 190, 58

Kauffmann, J., Bertoldi, F., Bourke, T. L., Evans, II, N. J., & Lee, C. W. 2008, A&A, 487, 993

Kauffmann, J., & Pillai, T. 2010, ApJ, 723, L7

Kendrew, S., Simpson, R., Bressert, E., et al. 2012, ApJ, 755, 71

Kennicutt, R. C., & Evans, N. J. 2012, ARA&A, 50, 531

Keto, E., & Wood, K. 2006, ApJ, 637, 850

Kim, K.-T., & Koo, B.-C. 2001, ApJ, 549, 979

—. 2003, ApJ, 596, 362

Kobulnicky, H. A., & Johnson, K. E. 1999, ApJ, 527, 154

Kolpak, M. A., Jackson, J. M., Bania, T. M., Clemens, D. P., & Dickey, J. M. 2003, ApJ, 582, 756

Kolpak, M. A., Jackson, J. M., Bania, T. M., & Dickey, J. M. 2002, ApJ, 578, 868

Koo, B.-C. 1999, ApJ, 518, 760

Kraus, S., Hofmann, K.-H., Menten, K. M., et al. 2010, Nature, 466, 339

Kroupa, P. 2001, MNRAS, 322, 231

Krumholz, M. R., Klein, R. I., McKee, C. F., Offner, S. S. R., & Cunningham, A. J. 2009, Science, 323, 754

Kuchar, T. A., & Clark, F. O. 1997, ApJ, 488, 224

Kuiper, R., Klahr, H., Beuther, H., & Henning, T. 2011, ApJ, 732, 20

Kurtz, S. 2005, in IAU Symposium, Vol. 227, Massive Star Birth: A Crossroads of Astrophysics, ed. R. Cesaroni, M. Felli, E. Churchwell, & M. Walmsley, 111–119

Kurtz, S., Churchwell, E., & Wood, D. O. S. 1994, ApJS, 91, 659

Kwan, J. 1997, ApJ, 489, 284

Lada, C. J. 1987, in IAU Symposium, Vol. 115, Star Forming Regions, ed. M. Peimbert & J. Jugaku, 1–17

Lada, C. J. 1999, in NATO Advanced Science Institutes (ASI) Series C, Vol. 540, NATO Advanced Science Institutes (ASI) Series C, ed. C. J. Lada & N. D. Kylafis, 143

Lada, C. J., & Adams, F. C. 1992, ApJ, 393, 278

Lada, C. J., & Lada, E. A. 2003, ARA&A, 41, 57

Lada, C. J., & Shu, F. H. 1990, Science, 248, 564

Lada, C. J., & Wilking, B. A. 1984, ApJ, 287, 610

Ladd, N., Purcell, C., Wong, T., & Robertson, S. 2005, PASA, 22, 62

Lal, D. V., & Rao, A. P. 2007, MNRAS, 374, 1085

Launhardt, R., Stutz, A. M., Schmiedeke, A., et al. 2013, A&A, 551, A98

Lee, H.-T., & Chen, W. P. 2007, ApJ, 657, 884

Lee, H.-T., Takami, M., Duan, H.-Y., et al. 2012, ApJS, 200, 2

Lee, H.-T., Liao, W.-T., Froebrich, D., et al. 2013, ApJS, 208, 23

Lefloch, B., & Lazareff, B. 1994, A&A, 289, 559

Liu, H.-L., Wu, Y., Li, J., et al. 2015, ApJ, 798, 30

Liu, H.-L., Li, J.-Z., Wu, Y., et al. 2016, ApJ, 818, 95

Liu, H.-L., Figueira, M., Zavagno, A., et al. 2017a, A&A, 602, A95

Liu, T., Lacy, J., Li, P. S., et al. 2017b, ApJ, 849, 25

Lockman, F. J. 1989, ApJS, 71, 469

Lu, X., Zhang, Q., Liu, H. B., et al. 2018, ApJ, 855, 9

Luisi, M., Anderson, L. D., Balser, D. S., Bania, T. M., & Wenger, T. V. 2016, ApJ, 824, 125

Lumsden, S. L., Hoare, M. G., Urquhart, J. S., et al. 2013, ApJS, 208, 11

Luque-Escamilla, P. L., Muñoz-Arjonilla, A. J., Sánchez-Sutil, J. R., et al. 2011, A&A, 532, A92

Mac Low, M.-M., van Buren, D., Wood, D. O. S., & Churchwell, E. 1991, ApJ, 369, 395

Mallick, K. K., Ojha, D. K., Tamura, M., et al. 2015, MNRAS, 447, 2307

Marco, A., & Negueruela, I. 2011, A&A, 534, A114

Marcolino, W. L. F., Bouret, J.-C., Martins, F., et al. 2009, A&A, 498, 837

Marcote, B., Ribó, M., Paredes, J. M., & Ishwara-Chandra, C. H. 2015, MNRAS, 451, 59

Marston, A. P., Reach, W. T., Noriega-Crespo, A., et al. 2004, ApJS, 154, 333

Marti, J., Rodriguez, L. F., & Reipurth, B. 1993, ApJ, 416, 208

Martín-Hernández, N. L., Bik, A., Kaper, L., Tielens, A. G. G. M., & Hanson, M. M. 2003a, A&A, 405, 175

Martín-Hernández, N. L., van der Hulst, J. M., & Tielens, A. G. G. M. 2003b, A&A, 407, 957

Martins, F., & Plez, B. 2006, A&A, 457, 637

Martins, F., Pomarès, M., Deharveng, L., Zavagno, A., & Bouret, J. C. 2010, A&A, 510, A32

Martins, F., Schaerer, D., & Hillier, D. J. 2005a, A&A, 436, 1049

Martins, F., Schaerer, D., Hillier, D. J., et al. 2005b, A&A, 441, 735

Marton, G., Calzoletti, L., Perez Garcia, A. M., et al. 2017, ArXiv e-prints, arXiv:1705.05693

Matthews, H., Kirk, H., Johnstone, D., et al. 2009, AJ, 138, 1380

Mauch, T., Murphy, T., Buttery, H. J., et al. 2003, MNRAS, 342, 1117

McCray, R. 1983, Highlights of Astronomy, 6, 565

McKee, C. F., & Ostriker, E. C. 2007, ARA&A, 45, 565

McKee, C. F., & Tan, J. C. 2003, ApJ, 585, 850

Mellema, G., Arthur, S. J., Henney, W. J., Iliev, I. T., & Shapiro, P. R. 2006, ApJ, 647, 397

Meyer, M. R., Calvet, N., & Hillenbrand, L. A. 1997, AJ, 114, 288

Mezger, P. G., & Henderson, A. P. 1967, ApJ, 147, 471

Miao, J., White, G. J., Thompson, M. A., & Nelson, R. P. 2009, ApJ, 692, 382

Miettinen, O. 2014, A&A, 562, A3

Minier, V., Ellingsen, S. P., Norris, R. P., & Booth, R. S. 2003, A&A, 403, 1095

Minniti, D., Lucas, P. W., Emerson, J. P., et al. 2010, New A, 15, 433

Molinari, S., Pezzuto, S., Cesaroni, R., et al. 2008, A&A, 481, 345

Molinari, S., Swinyard, B., Bally, J., et al. 2010a, A&A, 518, L100

—. 2010b, PASP, 122, 314

Mookerjea, B., Vastel, C., Hassel, G. E., et al. 2014, A&A, 566, A61

Morales, E. F. E., Wyrowski, F., Schuller, F., & Menten, K. M. 2013, A&A, 560, A76

Motte, F., Bontemps, S., & Louvet, F. 2017, ArXiv e-prints, arXiv:1706.00118

Mottram, J. C., Hoare, M. G., Davies, B., et al. 2011, ApJ, 730, L33

Mücke, A., Koribalski, B. S., Moffat, A. F. J., Corcoran, M. F., & Stevens, I. R. 2002, ApJ, 571, 366

Müller, H. S. P., Schlöder, F., Stutzki, J., & Winnewisser, G. 2005, Journal of Molecular Structure, 742, 215

Müller, H. S. P., Thorwirth, S., Roth, D. A., & Winnewisser, G. 2001, A&A, 370, L49

Myers, P. C. 2017, ApJ, 838, 10

Myers, P. C., & Benson, P. J. 1983, ApJ, 266, 309

Myers, P. C., & Fuller, G. A. 1992, ApJ, 396, 631

Nagayama, T., Kobayashi, H., Omodaka, T., et al. 2015, PASJ, 67, 65

Nandakumar, G., Veena, V. S., Vig, S., et al. 2016, AJ, 152, 146

Nandakumar, G., Schultheis, M., Feldmeier-Krause, A., et al. 2018, A&A, 609, A109

Ochsendorf, B. B., Cox, N. L. J., Krijt, S., et al. 2014a, A&A, 563, A65

Ochsendorf, B. B., Verdolini, S., Cox, N. L. J., et al. 2014b, A&A, 566, A75

Ojha, D. K., Tamura, M., Nakajima, Y., et al. 2004a, ApJ, 616, 1042

—. 2004b, ApJ, 608, 797

Omont, A., Gilmore, G. F., Alard, C., et al. 2003, A&A, 403, 975

Ormel, C. W., Shipman, R. F., Ossenkopf, V., & Helmich, F. P. 2005, A&A, 439, 613

Ortega, M. E., Giacani, E., Paron, S., & Rubio, M. 2016, MNRAS, 458, 3684

Osorio, M., Lizano, S., & D'Alessio, P. 1999, ApJ, 525, 808

Osterbrock, D. E. 1989, Astrophysics of gaseous nebulae and active galactic nuclei

Paladini, R., Umana, G., Veneziani, M., et al. 2012, ApJ, 760, 149

Palla, F., & Stahler, S. W. 1993, ApJ, 418, 414

Panagia, N. 1973, AJ, 78, 929

Pandian, J. D., Momjian, E., & Goldsmith, P. F. 2008, A&A, 486, 191

Paron, S., Petriella, A., & Ortega, M. E. 2011, A&A, 525, A132

Parsons, H., Thompson, M. A., Clark, J. S., & Chrysostomou, A. 2012, MNRAS, 424, 1658

Patel, N. A., Curiel, S., Sridharan, T. K., et al. 2005, Nature, 437, 109

Peeters, E., Hony, S., Van Kerckhoven, C., et al. 2002, A&A, 390, 1089

Perault, M., Omont, A., Simon, G., et al. 1996, A&A, 315, L165

Peretto, N., & Fuller, G. A. 2009, A&A, 505, 405

Peretto, N., Fuller, G. A., Plume, R., et al. 2010, A&A, 518, L98

Peretto, N., Fuller, G. A., Duarte-Cabral, A., et al. 2013, A&A, 555, A112

Peretto, N., Fuller, G. A., André, P., et al. 2014, A&A, 561, A83

Pestalozzi, M. R., Minier, V., & Booth, R. S. 2005, A&A, 432, 737

Petriella, A., Paron, S., & Giacani, E. 2010, A&A, 513, A44

Pilbratt, G. L., Riedinger, J. R., Passvogel, T., et al. 2010, A&A, 518, L1

Pillai, T., Wyrowski, F., Carey, S. J., & Menten, K. M. 2006, A&A, 450, 569

Poglitsch, A., Waelkens, C., Geis, N., et al. 2010, A&A, 518, L2

Pomarès, M., Zavagno, A., Deharveng, L., et al. 2009, A&A, 494, 987

Povich, M. S., Stone, J. M., Churchwell, E., et al. 2007, ApJ, 660, 346

Preibisch, T., & Zinnecker, H. 2007, in IAU Symposium, Vol. 237, Triggered Star Formation in a Turbulent ISM, ed. B. G. Elmegreen & J. Palous, 270–277

Price, S. D., Egan, M. P., Carey, S. J., Mizuno, D. R., & Kuchar, T. A. 2001, AJ, 121, 2819

Purcell, C. R., Balasubramanyam, R., Burton, M. G., et al. 2006, MNRAS, 367, 553

Quireza, C., Rood, R. T., Bania, T. M., Balser, D. S., & Maciel, W. J. 2006, ApJ, 653, 1226

Raga, A. C., Cantó, J., & Rodríguez, L. F. 2012, Rev. Mexicana Astron. Astrofis., 48, 199

Ragan, S. E., Henning, T., Tackenberg, J., et al. 2014, A&A, 568, A73

Rathborne, J. M., Jackson, J. M., Chambers, E. T., et al. 2005, ApJ, 630, L181

Rathborne, J. M., Jackson, J. M., & Simon, R. 2006, ApJ, 641, 389

Rathborne, J. M., Longmore, S. N., Jackson, J. M., et al. 2014, ApJ, 786, 140

Rebull, L. M., Koenig, X. P., Padgett, D. L., et al. 2011, ApJS, 196, 4

Reid, M. J., & Ho, P. T. P. 1985, ApJ, 288, L17

Rieke, G. H., & Lebofsky, M. J. 1985, ApJ, 288, 618

Rieke, G. H., Young, E. T., Engelbracht, C. W., et al. 2004, ApJS, 154, 25

Robitaille, T. P., Whitney, B. A., Indebetouw, R., & Wood, K. 2007, ApJS, 169, 328

Robitaille, T. P., Meade, M. R., Babler, B. L., et al. 2008, AJ, 136, 2413

Rodriguez, L. F., Curiel, S., Moran, J. M., et al. 1989, ApJ, 346, L85

Rodriguez, L. F., Marti, J., Canto, J., Moran, J. M., & Curiel, S. 1993, Rev. Mexicana Astron. Astrofis., 25, 23

Rodríguez, L. F., Masqué, J. M., Dzib, S. A., Loinard, L., & Kurtz, S. E. 2014, Rev. Mexicana Astron. Astrofis., 50, 3

Roger, R. S., Costain, C. H., Landecker, T. L., & Swerdlyk, C. M. 1999, A&AS, 137, 7

Roman-Duval, J., Jackson, J. M., Heyer, M., et al. 2009, ApJ, 699, 1153

Rosero, V., Hofner, P., Claussen, M., et al. 2016, ApJS, 227, 25

Rosolowsky, E., Dunham, M. K., Ginsburg, A., et al. 2010, ApJS, 188, 123

Rosolowsky, E. W., Pineda, J. E., Kauffmann, J., & Goodman, A. A. 2008, ApJ, 679, 1338

Roth, N., Stahler, S. W., & Keto, E. 2014, MNRAS, 438, 1335

Rubin, R. H. 1968, ApJ, 153, 761

Russeil, D., Pestalozzi, M., Mottram, J. C., et al. 2011, A&A, 526, A151

Russeil, D., Schneider, N., Anderson, L. D., et al. 2013, A&A, 554, A42

Russeil, D., Tigé, J., Adami, C., et al. 2016, A&A, 587, A135

Saito, R., Hempel, M., Alonso-García, J., et al. 2010, The Messenger, 141, 24

Salpeter, E. E. 1955, ApJ, 121, 161

Samal, M. R., Zavagno, A., Deharveng, L., et al. 2014, A&A, 566, A122

Sánchez-Monge, Á., Beltrán, M. T., Cesaroni, R., et al. 2013a, A&A, 550, A21

Sánchez-Monge, Á., Kurtz, S., Palau, A., et al. 2013b, ApJ, 766, 114

Sanhueza, P., Jackson, J. M., Foster, J. B., et al. 2012, ApJ, 756, 60

Saraceno, P., Andre, P., Ceccarelli, C., Griffin, M., & Molinari, S. 1996, A&A, 309, 827

Schlingman, W. M., Shirley, Y. L., Schenk, D. E., et al. 2011, ApJS, 195, 14

Schmiedeke, A., Schilke, P., Möller, T., et al. 2016, A&A, 588, A143

Schneider, N., Csengeri, T., Hennemann, M., et al. 2012, A&A, 540, L11

Schneider, N., André, P., Könyves, V., et al. 2013, ApJ, 766, L17

Schneider, N., Ossenkopf, V., Csengeri, T., et al. 2015a, A&A, 575, A79

Schneider, N., Csengeri, T., Klessen, R. S., et al. 2015b, A&A, 578, A29

Schöier, F. L., van der Tak, F. F. S., van Dishoeck, E. F., & Black, J. H. 2005, A&A, 432, 369

Schraml, J., & Mezger, P. G. 1969, ApJ, 156, 269

Schuller, F., Menten, K. M., Contreras, Y., et al. 2009, A&A, 504, 415

Shirley, Y. L., Ellsworth-Bowers, T. P., Svoboda, B., et al. 2013, ApJS, 209, 2

Shu, F. H. 1977, ApJ, 214, 488

Shu, F. H., Adams, F. C., & Lizano, S. 1987, ARA&A, 25, 23

Shu, F. H., Allen, A., Shang, H., Ostriker, E. C., & Li, Z.-Y. 1999, in NATO Advanced Science Institutes (ASI) Series C, Vol. 540, NATO Advanced Science Institutes (ASI) Series C, ed. C. J. Lada & N. D. Kylafis, 193

Sidorin, V., Douglas, K. A., Palouš, J., Wünsch, R., & Ehlerová, S. 2014, A&A, 565, A6

Simon, J. D., Bolatto, A. D., Whitney, B. A., et al. 2007, ApJ, 669, 327

Simpson, R. J., Povich, M. S., Kendrew, S., et al. 2012, MNRAS, 424, 2442

Siringo, G., Weiss, A., Kreysa, E., et al. 2007, The Messenger, 129, 2

Siringo, G., Kreysa, E., Kovács, A., et al. 2009, A&A, 497, 945

Skrutskie, M. F., Cutri, R. M., Stiening, R., et al. 2006, AJ, 131, 1163

Solin, O., Ukkonen, E., & Haikala, L. 2012, A&A, 542, A3

Sorai, K., Habe, A., Nishitani, H., et al. 2008, PASJ, 60, 1285

Spitzer, L. 1978, Physical processes in the interstellar medium, doi:10.1002/9783527617722

Stahler, S. W. 2000, in ESA Special Publication, Vol. 445, Star Formation from the Small to the Large Scale, ed. F. Favata, A. Kaas, & A. Wilson, 133

Stahler, S. W., & Palla, F. 2005, The Formation of Stars

Stahler, S. W., Palla, F., & Ho, P. T. P. 2000, Protostars and Planets IV, 327

Stern, D., Eisenhardt, P., Gorjian, V., et al. 2005, ApJ, 631, 163

Sugitani, K., Matsuo, H., Nakano, M., Tamura, M., & Ogura, K. 2000, AJ, 119, 323

Sugitani, K., Tamura, M., & Ogura, K. 1999, in Star Formation 1999, ed. T. Nakamoto, 358–364

Sugitani, K., Tamura, M., Nakajima, Y., et al. 2002, ApJ, 565, L25

Sun, Y., Xu, Y., Chen, X., et al. 2014, A&A, 563, A130

Svoboda, B. E., Shirley, Y. L., Battersby, C., et al. 2016, ApJ, 822, 59

Swarup, G., Ananthakrishnan, S., Kapahi, V. K., et al. 1991, Current Science, Vol. 60, NO.2/JAN25, P. 95, 1991, 60, 95

Szymczak, M., Hrynek, G., & Kus, A. J. 2000, A&AS, 143, 269

Tackenberg, J., Beuther, H., Henning, T., et al. 2014, A&A, 565, A101

Takahira, K., Tasker, E. J., & Habe, A. 2014, ApJ, 792, 63

Takami, M., Chen, H.-H., Karr, J. L., et al. 2012, ApJ, 748, 8

Tan, J. C., Beltrán, M. T., Caselli, P., et al. 2014, Protostars and Planets VI, 149

Tan, J. C., Kong, S., Butler, M. J., Caselli, P., & Fontani, F. 2013, ApJ, 779, 96

Tan, J. C., & McKee, C. F. 2003, ArXiv Astrophysics e-prints, astro-ph/0309139

Tapia, M., Persi, P., Roth, M., et al. 2014, MNRAS, 437, 606

Tej, A., Ojha, D. K., Ghosh, S. K., et al. 2006, A&A, 452, 203

Tenorio-Tagle, G. 1979, A&A, 71, 59

Tielens, A. G. G. M. 2005, The Physics and Chemistry of the Interstellar Medium

Toalá, J. A., Guerrero, M. A., Chu, Y.-H., & Gruendl, R. A. 2015, MNRAS, 446, 1083

Torii, K., Hasegawa, K., Hattori, Y., et al. 2015, ApJ, 806, 7

Torii, K., Hattori, Y., Hasegawa, K., et al. 2017, ApJ, 835, 142

Townsley, L. K., Feigelson, E. D., Montmerle, T., et al. 2003, ApJ, 593, 874

Tremblin, P., Audit, E., Minier, V., Schmidt, W., & Schneider, N. 2012a, A&A, 546, A33

Tremblin, P., Audit, E., Minier, V., & Schneider, N. 2012b, A&A, 538, A31

Tremblin, P., Schneider, N., Minier, V., et al. 2014, A&A, 564, A106

Urquhart, J. S., Busfield, A. L., Hoare, M. G., et al. 2007a, A&A, 461, 11

Urquhart, J. S., Figura, C. C., Moore, T. J. T., et al. 2014a, MNRAS, 437, 1791

Urquhart, J. S., Busfield, A. L., Hoare, M. G., et al. 2007b, A&A, 474, 891

Urquhart, J. S., Hoare, M. G., Purcell, C. R., et al. 2009, A&A, 501, 539

Urquhart, J. S., Morgan, L. K., Figura, C. C., et al. 2011, MNRAS, 418, 1689

Urquhart, J. S., Moore, T. J. T., Schuller, F., et al. 2013a, MNRAS, 431, 1752

Urquhart, J. S., Thompson, M. A., Moore, T. J. T., et al. 2013b, MNRAS, 435, 400

Urquhart, J. S., Csengeri, T., Wyrowski, F., et al. 2014b, A&A, 568, A41

Urquhart, J. S., Moore, T. J. T., Csengeri, T., et al. 2014c, MNRAS, 443, 1555

van Buren, D., & Mac Low, M.-M. 1992, ApJ, 394, 534

van Buren, D., Mac Low, M.-M., Wood, D. O. S., & Churchwell, E. 1990, ApJ, 353, 570

van der Tak, F. F. S., Black, J. H., Schöier, F. L., Jansen, D. J., & van Dishoeck, E. F. 2007, A&A, 468, 627

van der Walt, D. J., Gaylard, M. J., & MacLeod, G. C. 1995, A&AS, 110, 81

van Dishoeck, E. F., & Blake, G. A. 1998, ARA&A, 36, 317

Varricatt, W. P. 2011, A&A, 527, A97

Vasyunina, T., Linz, H., Henning, T., et al. 2011, A&A, 527, A88

Veena, V. S., Vig, S., Tej, A., et al. 2016, MNRAS, 456, 2425

Veneziani, M., Elia, D., Noriega-Crespo, A., et al. 2013, A&A, 549, A130

Vig, S., Ghosh, S. K., Ojha, D. K., & Verma, R. P. 2007, A&A, 463, 175

Walsh, A. J., Burton, M. G., Hyland, A. R., & Robinson, G. 1998, MNRAS, 301, 640

—. 1999, MNRAS, 309, 905

Walsh, A. J., Hyland, A. R., Robinson, G., & Burton, M. G. 1997, MNRAS, 291, 261

Wang, K., Zhang, Q., Wu, Y., & Zhang, H. 2011, ApJ, 735, 64

Watson, C., Corn, T., Churchwell, E. B., et al. 2009, ApJ, 694, 546

Watson, C., Hanspal, U., & Mengistu, A. 2010, ApJ, 716, 1478

Watson, C., Povich, M. S., Churchwell, E. B., et al. 2008, ApJ, 681, 1341

Weaver, R., McCray, R., Castor, J., Shapiro, P., & Moore, R. 1977, ApJ, 218, 377

Wenger, T. V., Bania, T. M., Balser, D. S., & Anderson, L. D. 2013, ApJ, 764, 34

Werner, M. W., Roellig, T. L., Low, F. J., et al. 2004, ApJS, 154, 1

Whittet, D. C. B. 1992, Dust in the galactic environment

Whitworth, A. P., Bhattal, A. S., Chapman, S. J., Disney, M. J., & Turner, J. A. 1994a, A&A, 290, 421

—. 1994b, MNRAS, 268, 291

Whitworth, A. P., & Francis, N. 2002, MNRAS, 329, 641

Williams, J. P., Blitz, L., & McKee, C. F. 2000, Protostars and Planets IV, 97

Williams, J. P., de Geus, E. J., & Blitz, L. 1994, ApJ, 428, 693

Williams, J. P., & McKee, C. F. 1997, ApJ, 476, 166

Wolff, S. C., Strom, S. E., Dror, D., Lanz, L., & Venn, K. 2006, AJ, 132, 749

Wolfire, M. G., & Cassinelli, J. P. 1987, ApJ, 319, 850

Wood, D. O. S., & Churchwell, E. 1989, ApJS, 69, 831

Wright, A. E., Griffith, M. R., Burke, B. F., & Ekers, R. D. 1994, ApJS, 91, 111

Xu, J.-L., & Ju, B.-G. 2014, A&A, 569, A36

Xu, Y., Li, J. J., Hachisuka, K., et al. 2008, A&A, 485, 729

Xue, X. X., Rix, H. W., Zhao, G., et al. 2008, ApJ, 684, 1143

Yan, Q.-z., Xu, Y., Zhang, B., et al. 2016, AJ, 152, 117

Yu, N., & Wang, J.-J. 2015, MNRAS, 451, 2507

Yu, N., Wang, J.-J., & Li, N. 2015, MNRAS, 446, 2566

Yu, N., & Xu, J. 2016, ApJ, 833, 248

Yuan, J., Li, J.-Z., Wu, Y., et al. 2018, ApJ, 852, 12

Zacharias, N., Monet, D. G., Levine, S. E., et al. 2004, in Bulletin of the American Astronomical Society, Vol. 36, American Astronomical Society Meeting Abstracts, 1418

Zavagno, A., Deharveng, L., Comerón, F., et al. 2006, A&A, 446, 171

Zavagno, A., Pomarès, M., Deharveng, L., et al. 2007, A&A, 472, 835

Zavagno, A., Anderson, L. D., Russeil, D., et al. 2010, A&A, 518, L101

Zhang, C. P., & Wang, J. J. 2012, A&A, 544, A11

Zhu, Q.-F., Lacy, J. H., Jaffe, D. T., Richter, M. J., & Greathouse, T. K. 2005, ApJ, 631, 381

—. 2008, ApJS, 177, 584

Zoonematkermani, S., Helfand, D. J., Becker, R. H., White, R. L., & Perley, R. A. 1990, ApJS, 74, 181

Zweibel, E. G. 2002, ApJ, 567, 962

Zychová, L., & Ehlerová, S. 2016, A&A, 595, A49

Appendix A

A.1 YSO list

Table A.1
List of identified YSOs detected in region of bubble CS51. The 2MASS and IRAC photometric magnitudes of the YSOs are given.

YSO	RA (J2000)	DEC (J2000)	J	H	K	3.6	4.5	5.8	8.0	24	YSO Class			
	(hh:mm:ss.ss)	(dd:mm:ss.ss)	(mag)	(mag)	(mag)	(mag)	(mag)	(mag)	(mag)	(mag)	1	2	3	4
1	17:30:51.95	−33:52:21.04	–	–	–	12.88	12.46	11.87	11.42	–	Class I/II	–	Class II	–
2	17:30:53.83	−33:54:39.49	–	–	–	12.70	12.62	11.82	11.97	–	–	–	Class II	–
3	17:30:54.05	−33:51:14.72	14.35	12.74	12.07	11.49	11.32	11.27	10.83	–	Class II	–	–	–
4	17:30:54.77	−33:50:58.34	15.27	13.33	12.70	11.86	11.82	12.17	11.75	–	Class II	–	–	–
5	17:30:55.05	−33:50:42.22	–	–	–	13.21	13.25	–	–	7.93	–	Class II	–	–
6	17:30:56.78	−33:54:13.90	13.44	11.25	10.32	9.68	9.71	9.48	9.42	6.24	–	Class II	–	–
7	17:30:58.02	−33:54:17.63	15.11	13.41	12.42	11.54	11.46	11.32	–	–	–	–	–	Class II
8	17:30:58.15	−33:50:39.01	–	–	–	11.55	10.97	10.67	10.55	–	–	–	Class II	–
9	17:30:58.38	−33:55:00.12	–	–	–	11.83	11.67	12.22	11.57	–	Class II	–	–	–
10	17:30:59.46	−33:52:01.49	12.84	10.51	8.74	6.70	–	4.79	4.21	3.36	–	–	–	Class I
11	17:30:59.52	−33:54:09.25	14.90	12.88	12.05	11.38	11.38	11.12	10.63	–	–	–	Class II	–
12	17:31:01.19	−33:51:07.09	13.24	10.43	9.17	8.24	8.25	7.92	7.86	5.02	–	Class II	–	–
13	17:31:01.35	−33:50:53.81	–	–	–	13.22	12.60	–	–	3.10	–	Class I	–	–
14	17:31:01.35	−33:51:21.95	14.07	13.05	12.46	–	–	–	–	–	–	–	–	Class II
15	17:31:01.97	−33:54:16.62	14.57	12.58	11.23	10.19	10.05	9.71	9.82	–	–	–	–	Class II
16	17:31:02.12	−33:53:32.32	–	–	12.01	11.21	11.30	10.84	10.23	–	–	–	Class II	–
17	17:31:03.24	−33:53:58.38	14.74	12.41	11.53	10.80	10.84	10.47	10.11	–	–	–	Class II	–
18	17:31:03.37	−33:53:53.77	14.52	12.44	11.68	11.06	11.08	10.58	10.32	–	–	–	Class II	–
19	17:31:03.79	−33:51:48.56	–	–	11.64	9.66	9.06	8.56	8.68	–	–	–	Class II	–
20	17:31:03.87	−33:49:04.58	–	–	–	10.92	9.52	8.46	7.78	3.94	Class I	Class I	Class I	–
21	17:31:03.91	−33:50:51.61	15.18	13.02	12.28	11.60	11.55	11.37	10.84	–	Class II	–	Class II	–
22	17:31:03.94	−33:50:29.04	–	–	–	11.79	11.83	11.55	10.89	–	–	–	Class II	–
23	17:31:03.96	−33:48:34.63	–	–	–	13.98	13.31	11.42	10.62	–	Class I/II	–	Class I	–
24	17:31:04.63	−33:54:44.86	–	–	–	13.30	13.28	11.81	10.33	–	–	–	Class I	–
25	17:31:05.47	−33:53:21.16	–	–	–	12.41	12.34	–	–	4.15	–	Class I	–	–
26	17:31:06.01	−33:50:57.52	15.00	12.96	12.13	11.36	11.46	11.09	10.57	–	–	–	Class II	–
27	17:31:06.37	−33:51:33.52	14.74	12.66	11.79	11.23	11.20	10.43	9.30	–	–	–	Class II	–

Table A.1
Continued

YSO	RA (J2000)	DEC (J2000)	J	H	K	3.6	4.5	5.8	8.0	24	YSO Class			
	(hh:mm:ss.ss)	(dd:mm:ss.ss)	(mag)	(mag)	(mag)	(mag)	(mag)	(mag)	(mag)	(mag)	1	2	3	4
28	17:31:06.46	−33:55:28.06	–	10.68	9.84	9.34	9.43	9.04	–	5.06	–	Class II	–	–
29	17:31:07.16	−33:50:29.33	13.53	10.85	9.59	8.74	8.62	8.27	8.08	5.13	–	Class II	–	–
30	17:31:07.17	−33:52:45.98	13.66	12.89	12.39	12.22	12.13	12.06	–	–	–	–	–	Class II
31	17:31:07.57	−33:52:44.69	14.47	13.55	13.28	12.39	12.14	12.06	11.10	–	Class II	–	Class II	–
32	17:31:07.80	−33:54:58.28	12.80	10.59	9.48	8.94	8.78	8.27	8.04	–	–	–	Class II	–
33	17:31:07.94	−33:49:14.61	15.24	13.53	12.57	11.56	–	11.62	–	–	–	–	–	Class II
34	17:31:08.08	−33:50:56.72	–	–	–	8.12	7.62	7.20	7.10	–	–	–	Class II	–
35	17:31:08.22	−33:48:34.77	14.87	13.54	12.69	11.99	12.06	12.14	–	–	–	–	–	Class II
36	17:31:08.91	−33:48:47.99	–	13.73	12.70	11.87	11.98	11.78	11.15	–	–	–	Class II	–
37	17:31:09.17	−33:54:06.02	14.17	12.35	11.29	10.21	10.05	9.81	9.89	–	–	–	–	Class II
38	17:31:09.33	−33:48:53.77	12.61	11.71	11.16	10.64	10.67	10.42	10.61	–	–	–	–	Class II
39	17:31:09.34	−33:56:03.37	–	–	–	14.01	14.06	–	–	3.38	–	Class I	–	–
40	17:31:09.61	−33:54:01.04	–	–	–	13.15	12.01	10.92	10.19	–	Class I	–	Class I	–
41	17:31:09.67	−33:55:20.24	–	13.23	12.35	11.67	11.59	11.38	10.97	–	Class II	–	–	–
42	17:31:09.87	−33:53:02.93	14.38	13.35	12.73	12.23	12.05	–	–	–	–	–	–	Class II
43	17:31:10.38	−33:56:40.92	14.91	12.73	11.95	11.28	11.26	10.66	9.95	–	Class II	–	Class II	–
44	17:31:10.59	−33:49:00.66	–	–	–	13.15	13.10	11.71	10.13	–	–	–	Class I	–
45	17:31:10.67	−33:56:42.07	14.82	12.89	12.08	11.34	11.39	10.67	9.94	–	–	–	Class II	–
46	17:31:12.25	−33:48:38.81	11.64	9.34	8.19	7.27	7.15	6.86	6.76	4.16	–	Class II	–	–
47	17:31:12.44	−33:50:47.47	–	–	–	8.78	8.55	8.12	8.16	3.14	–	Class I/II	–	–
48	17:31:12.84	−33:49:05.16	–	–	–	11.78	11.79	–	–	3.18	–	Class I	–	–
49	17:31:13.04	−33:50:13.99	11.97	10.64	10.09	9.72	9.85	9.52	9.00	–	–	–	Class II	–
50	17:31:14.78	−33:51:55.48	–	–	–	13.12	12.43	10.26	8.82	–	Class I	–	Class I	–
51	17:31:14.84	−33:48:51.71	14.92	13.27	12.346	11.66	–	11.53	–	–	–	–	–	Class II
52	17:31:15.43	−33:56:33.73	13.71	12.33	11.57	–	–	–	–	–	–	–	–	Class II
53	17:31:15.71	−33:50:39.05	–	–	–	13.17	13.03	10.86	9.76	–	–	–	Class I	–
54	17:31:16.18	−33:54:17.09	15.06	13.62	12.80	11.85	–	–	–	–	–	–	–	Class II

Table A.1
Continued

YSO	RA (J2000)	DEC (J2000)	J	H	K	3.6	4.5	5.8	8.0	24	YSO Class			
	(hh:mm:ss.ss)	(dd:mm:ss.ss)	(mag)	(mag)	(mag)	(mag)	(mag)	(mag)	(mag)	(mag)	1	2	3	4
55	17:31:16.38	−33:53:08.67	12.67	11.56	10.93	–	–	–	–	–	–	–	–	Class II
56	17:31:17.28	−33:51:35.39	–	–	–	11.96	11.47	9.21	–	1.44	–	Class I	–	–
57	17:31:17.48	−33:52:55.47	11.73	10.51	9.79	–	–	–	–	–	–	–	–	Class II
58	17:31:18.85	−33:55:31.94	–	–	–	13.36	13.23	–	–	5.98	–	Class I	–	–
59	17:31:18.86	−33:57:30.69	–	–	–	13.15	13.39	–	–	6.78	–	Class I/II	–	–
60	17:31:19.45	−33:52:13.80	–	–	–	12.59	11.27	9.18	7.75	–	Class I	–	Class I	–
61	17:31:19.58	−33:51:14.40	–	13.45	12.56	11.82	11.79	–	–	0.66	–	Class I	–	–
62	17:31:19.66	−33:54:39.05	13.33	11.68	10.76	–	–	–	–	–	–	–	–	Class II
63	17:31:20.14	−33:48:44.73	11.38	10.26	9.56	–	–	–	–	–	–	–	–	Class II
64	17:31:20.26	−33:57:16.66	14.56	12.94	12.00	11.51	–	11.38	–	–	–	–	–	Class II
65	17:31:20.39	−33:54:21.39	14.51	13.09	11.68	10.51	10.28	9.74	–	–	–	–	–	Class I
66	17:31:21.26	−33:50:37.28	12.56	10.34	9.24	8.19	7.81	7.15	6.38	4.10	Class I/II	Class II	Class II	–
67	17:31:21.38	−33:57:28.76	–	–	–	11.73	11.69	11.38	10.99	–	Class II	–	Class II	–
68	17:31:21.57	−33:51:09.78	13.61	11.73	10.69	–	–	–	–	–	–	–	–	Class II
69	17:31:22.86	−33:55:28.49	14.99	12.91	11.68	–	–	–	–	–	–	–	–	Class II
70	17:31:23.48	−33:54:47.12	–	13.01	12.20	11.50	11.62	10.63	9.45	–	–	–	Class II	–
71	17:31:24.40	−33:56:29.67	14.17	12.34	11.29	–	–	–	–	–	–	–	–	Class II
72	17:31:24.41	−33:55:58.66	–	–	12.54	11.37	11.19	10.65	10.56	–	–	–	Class II	–
73	17:31:25.33	−33:49:55.31	13.29	12.56	12.19	11.84	11.45	11.59	11.29	–	Class I	–	–	–
74	17:31:26.66	−33:52:51.07	13.40	12.04	11.17	10.43	10.56	10.22	–	–	–	–	–	Class II
75	17:31:26.86	−33:54:21.49	–	13.52	12.36	11.57	11.49	11.19	10.67	–	Class II	–	Class II	–
76	17:31:27.04	−33:54:00.50	–	–	–	12.69	12.72	12.22	10.47	–	–	–	Class II	–
77	17:31:27.43	−33:53:22.86	14.27	13.36	12.76	12.02		12.09	11.81	–	–	–	–	Class II
78	17:31:27.87	−33:50:34.62	–	–	–	11.75	11.25	10.67	9.58	6.11	Class I/II	Class I/II	Class II	–
79	17:31:28.41	−33:51:32.64	15.32	13.33	12.22	10.82	10.59	10.30	10.33	–	–	–	–	Class II
80	17:31:28.43	−33:54:15.88	12.30	10.16	9.18	8.43	8.36	7.99	7.91	5.33	–	Class II	–	–
81	17:31:28.57	−33:50:36.28	13.85	12.94	12.37	11.86	11.87	11.89	–	–	–	–	–	Class II

Table A.1
Continued

YSO	RA (J2000)	DEC (J2000)	J	H	K	3.6	4.5	5.8	8.0	24	YSO Class			
	(hh:mm:ss.ss)	(dd:mm:ss.ss)	(mag)	(mag)	(mag)	(mag)	(mag)	(mag)	(mag)	(mag)	1	2	3	4
82	17:31:28.80	−33:56:10.96	12.59	11.68	11.04	10.57	10.61	10.45	10.46	–	–	–	–	Class II
83	17:31:28.98	−33:51:28.01	–	–	–	13.16	13.08	–	–	5.81	–	Class I	–	–
84	17:31:30.39	−33:54:32.58	13.33	12.41	11.88	–	–	–	–	–	–	–	–	Class II
85	17:31:31.03	−33:50:16.12	15.13	12.72	11.34	10.27	10.18	9.81	9.96	–	–	–	–	Class II
86	17:31:31.15	−33:54:20.38	–	13.22	12.41	11.79	11.89	11.19	11.18	–	–	–	Class II	–
87	17:31:31.27	−33:55:28.96	12.52	11.82	11.34	10.83	10.58	10.33	10.07	–	–	–	Class II	–
88	17:31:32.79	−33:54:25.12	13.80	12.88	12.31	–	–	–	–	–	–	–	–	Class II
89	17:31:33.47	−33:54:10.51	11.38	10.26	9.57	–	–	–	–	–	–	–	–	Class II
90	17:31:34.96	−33:52:28.45	13.28	12.19	11.76	11.46	11.43	11.29	10.89	–	Class II	–	–	–
91	17:31:35.17	−33:50:41.06	–	–	–	12.38	12.44	12.53	10.60	–	–	–	Class II	–
92	17:31:35.71	−33:52:50.74	–	13.03	11.01	9.27	9.18	9.09	8.63	–	Class II	–	–	–
93	17:31:37.18	−33:52:37.60	–	–	–	12.41	12.38	11.95	11.39	–	Class II	–	Class II	–

Appendix B

B.1 GMRT results with different UV range

In this section, we have attempted to investigate the reason for non-detection of the H II region G346.077−0.056 in the RMS source list using GMRT. In order to do so we have generated radio maps with different UV range values and setting the robustness parameter to −5 are shown in the following figures. Figure B.1 shows emission from maps generated with UV range 25 to maximum, Figure B.2 shows emission from maps generated with UV range 15 to maximum, and Figure B.3 shows emission from maps generated with UV range 5 to maximum. The details of the radio maps are given in Table B.1. So based on our analysis we conclude the following about the detection of G346.077−0.056.

1. The resolution of the new 1280 MHz map is $3.6'' \times 1.5''$ which is similar to the resolution of 1.5 – 3″ quoted in Urquhart et al. (2007a). Given this**,** we would expect the ATCA observations to detect this source.

2. Further taking the spectral index estimated from the GMRT maps (−0.1 for G346.056−0.021), we predict the peak flux density at 3.6 and 6 cm to be 3.3 and 3.5 mJy/beam. This is $\sim 10\sigma$ (σ = 0.3 mJy/beam) and thus the compact peak distribution is expected to be detected.

3. It is possible that this ATCA field is re-imaged by excluding shorter baselines to limit the contribution of large-scale diffuse emission. As quoted in Urquhart et al. (2007a), the largest well-imaged structure possible at 3.6 and 6 cm, given their limited *uv* coverage and integration time, is ∼ 20″ and ∼ 30″, respectively.

   We re-imaged the GMRT maps by removing shorter baselines to exclude diffuse emission larger than (i) 50″ (ii) 15″ and (iii) 10″. And in all maps**,** we detect G346.056−0.021.

From the above, it is likely that the *uv* coverage was limited in the ATCA observations resulting in non-detection of G346.056−0.021. With denser *uv* sampling, the region is likely to be detected. In addition, the limited integration time of ∼10 minutes may not be enough to detect the faint diffuse emission.

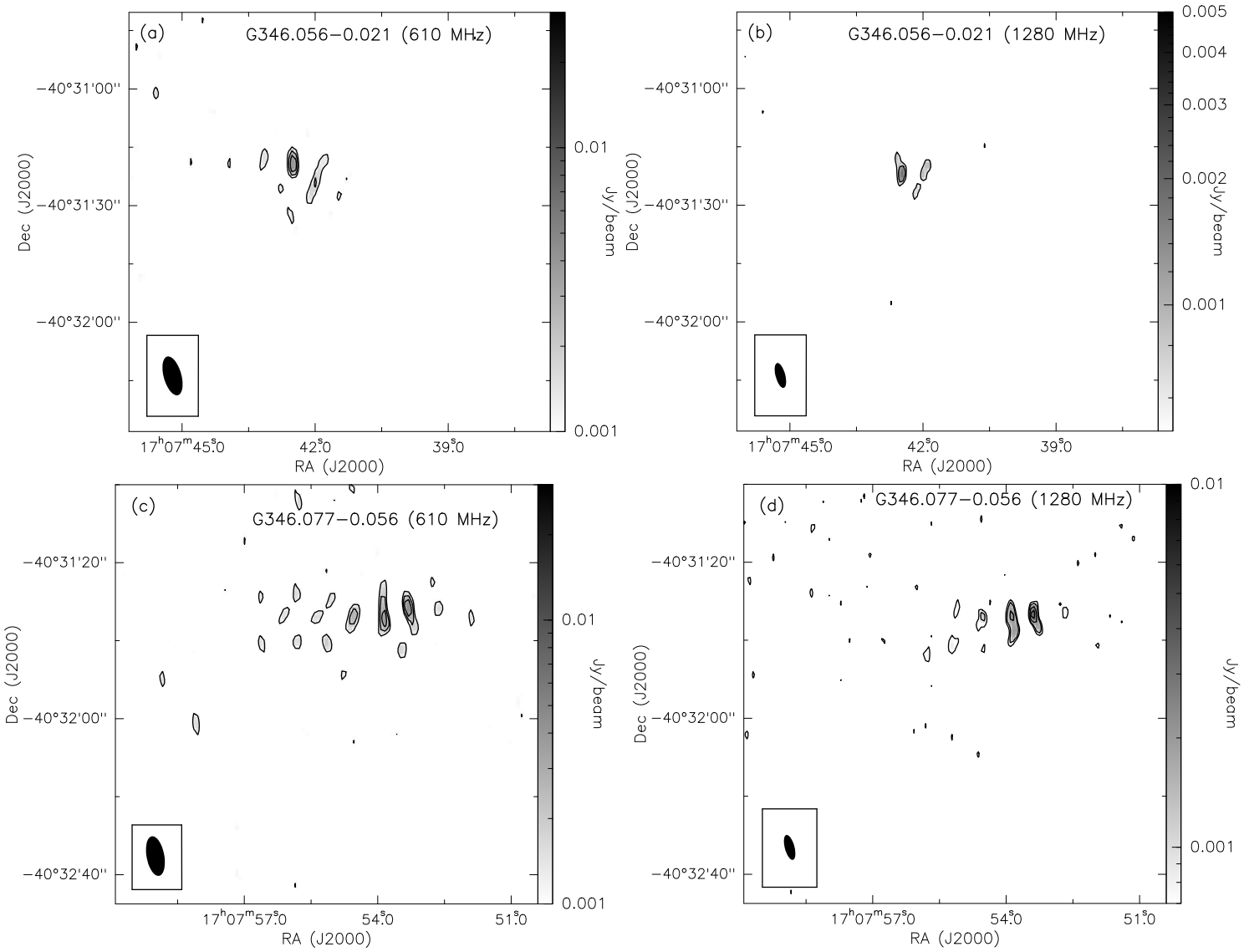

Figure B.1: Radio emission from maps generated by setting UV range from 25 to maximum and robustness parameter -5. (a) and (b) 610 and 1280 MHz maps for the region associated with G346.056−0.021; (c) and (d) 610 and 1280 MHz emission for the region around G346.077−0.056. The contour levels start from 3σ level. Beam in each band is shown as filled ellipse.

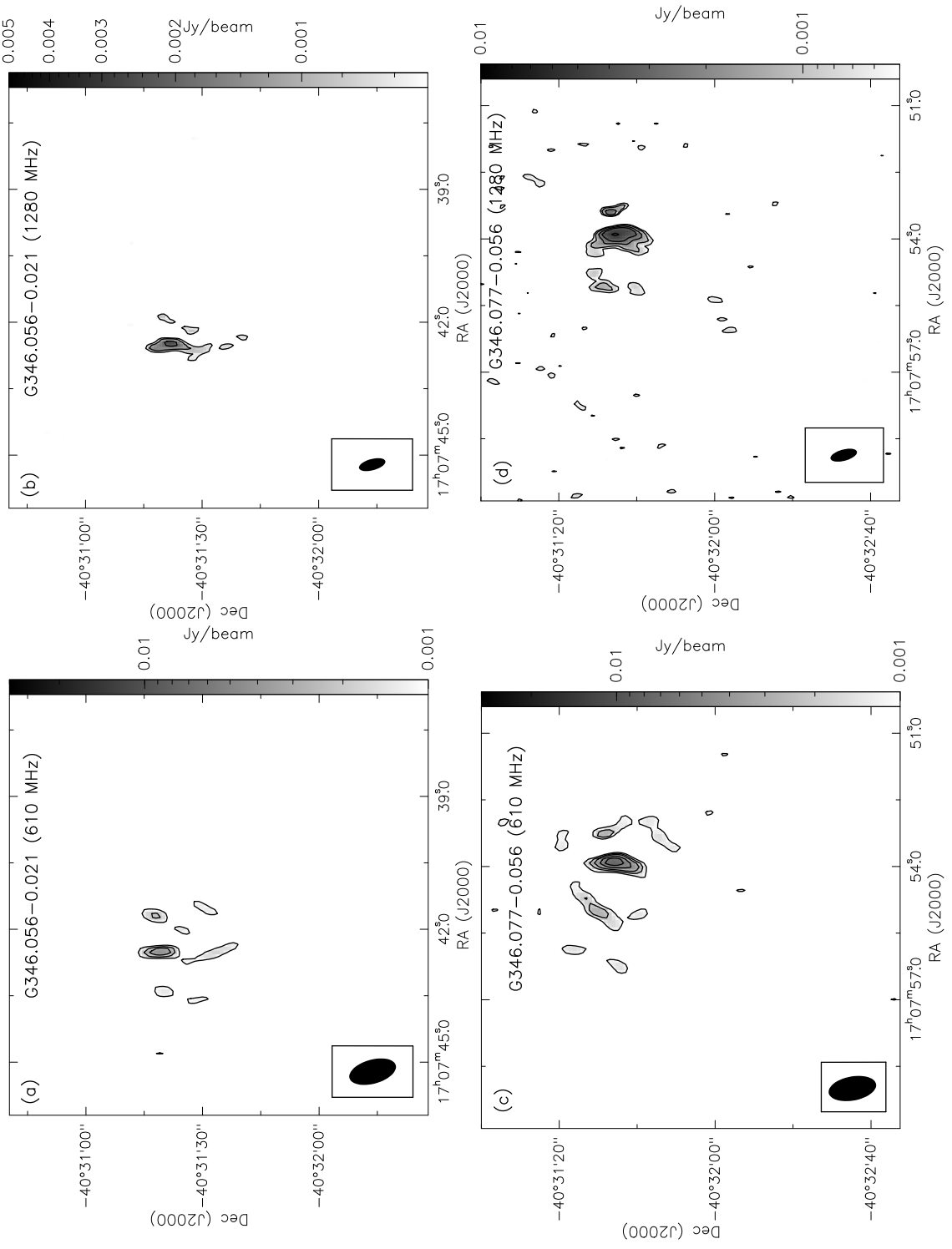

Figure B.2: Same as Figure B.1, but from radio maps generated by setting UV range from 15 to maximum and robustness parameter −5.

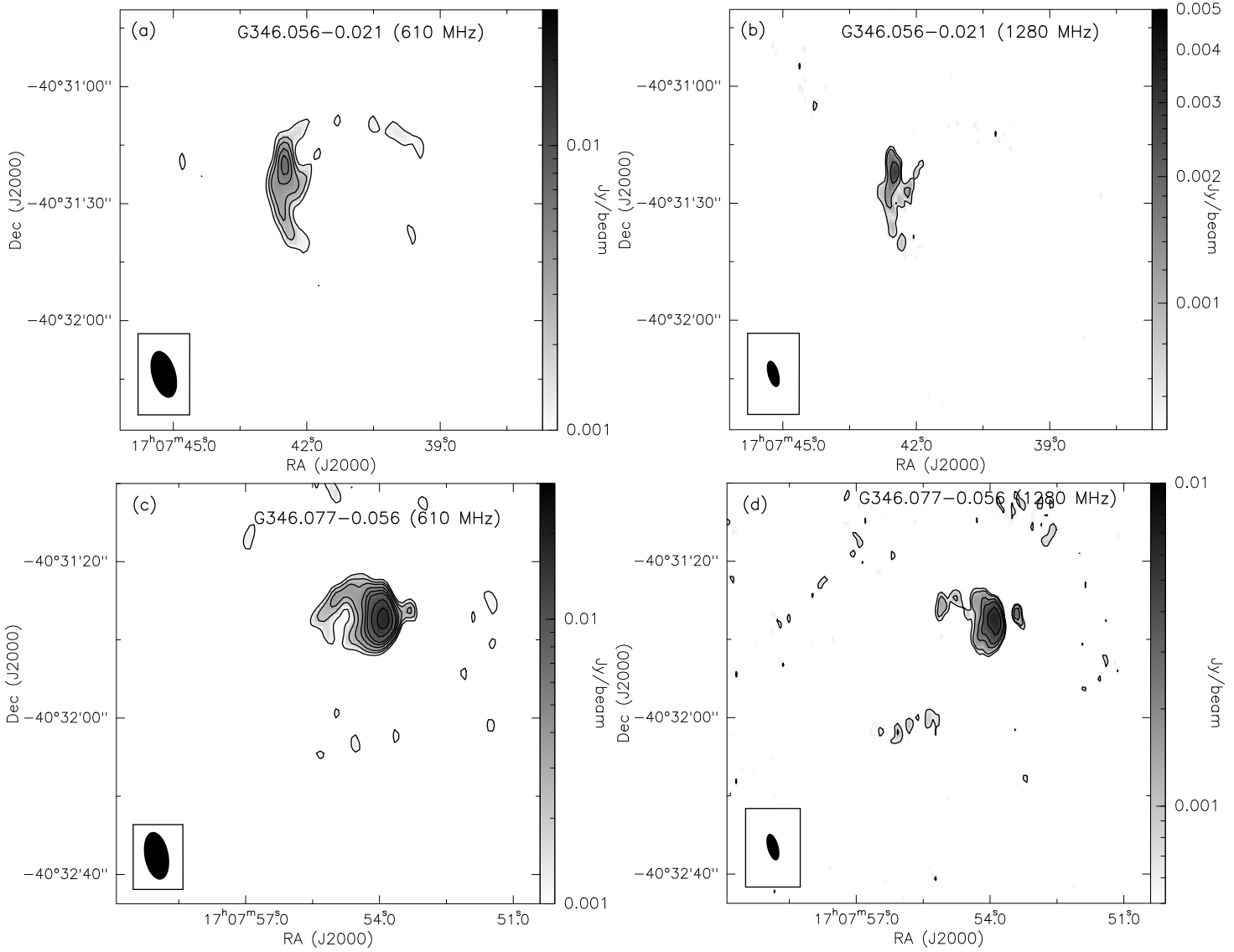

Figure B.3: Same as Figure B.1, but from radio maps generated by setting UV range from 5 to maximum and robustness parameter −5.

Table B.1
Details of the radio maps generated with different UV range values.

	Peak flux(mJy/beam)		Synth. beam		*rms* noise (mJy/beam)	
	610 MHz	1280 MHz	610 MHz	1280 MHz	610 MHz	1280 MHz
UV range (25 to maximum)						
G346.056−0.021	4.13	1.84	5.2″×2.2″	3.2″×1.3″	0.37	0.17
G346.077−0.056	4.48	3.57	5.2″×2.2″	3.2″×1.3″	0.37	0.17
UV range (15 to maximum)						
G346.056−0.021	4.24	2.50	5.7″×2.7″	3.5″×1.5″	0.28	0.17
G346.077−0.056	7.47	5.22	5.7″×2.7″	3.5″×1.5″	0.28	0.17
UV range (5 to maximum)						
G346.056−0.021	7.06	3.00	6.3″×3.0″	3.5″×1.5″	0.29	0.19
G346.077−0.056	17.56	6.92	6.3″×3.0″	3.5″×1.5″	0.29	0.19

Appendix C

C.1 Column density and dust temperature maps

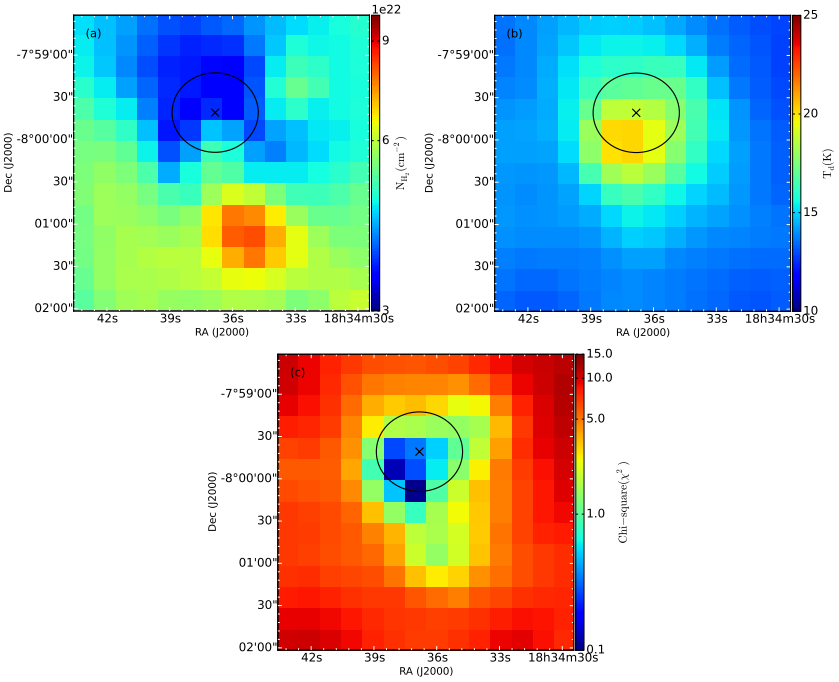

Figure C.1: Same as Figure 6.18, but for bubble N32.

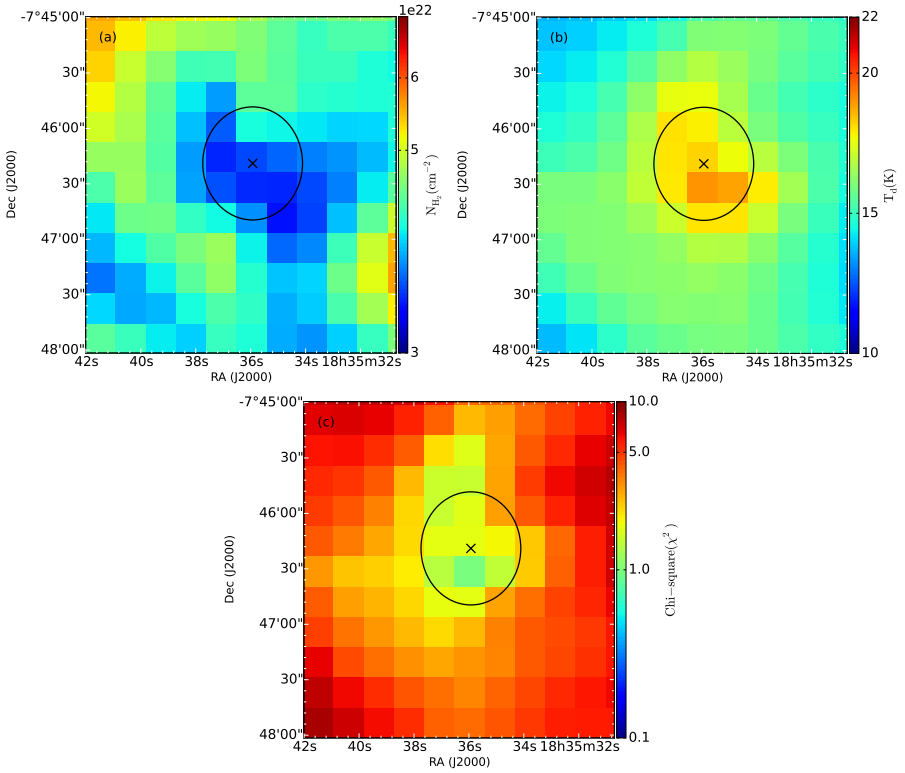

Figure C.2: Same as Figure 6.18, but for bubble N33.

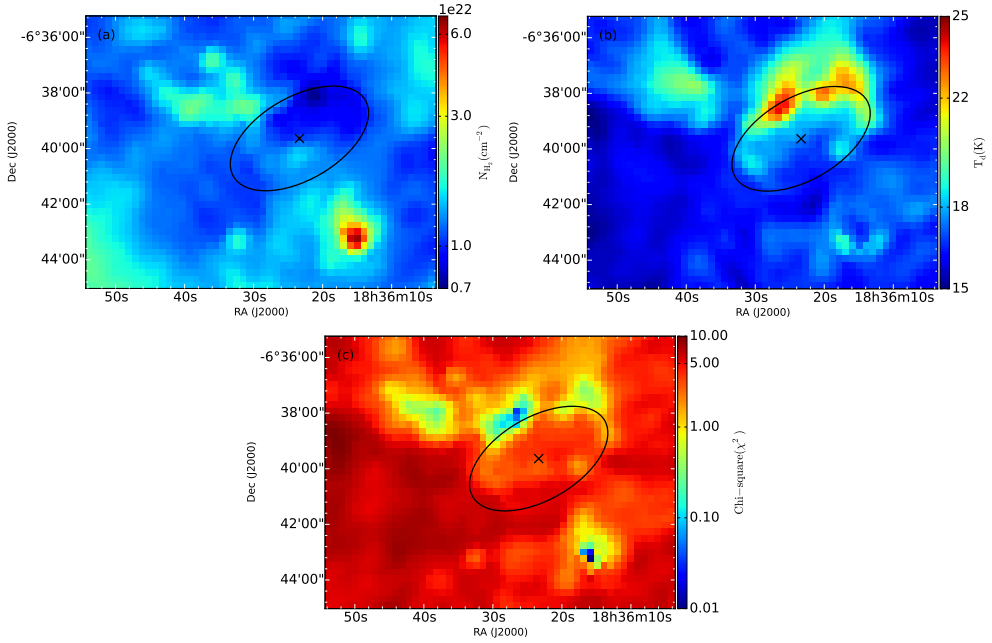

Figure C.3: Same as Figure 6.18, but for bubble N37.

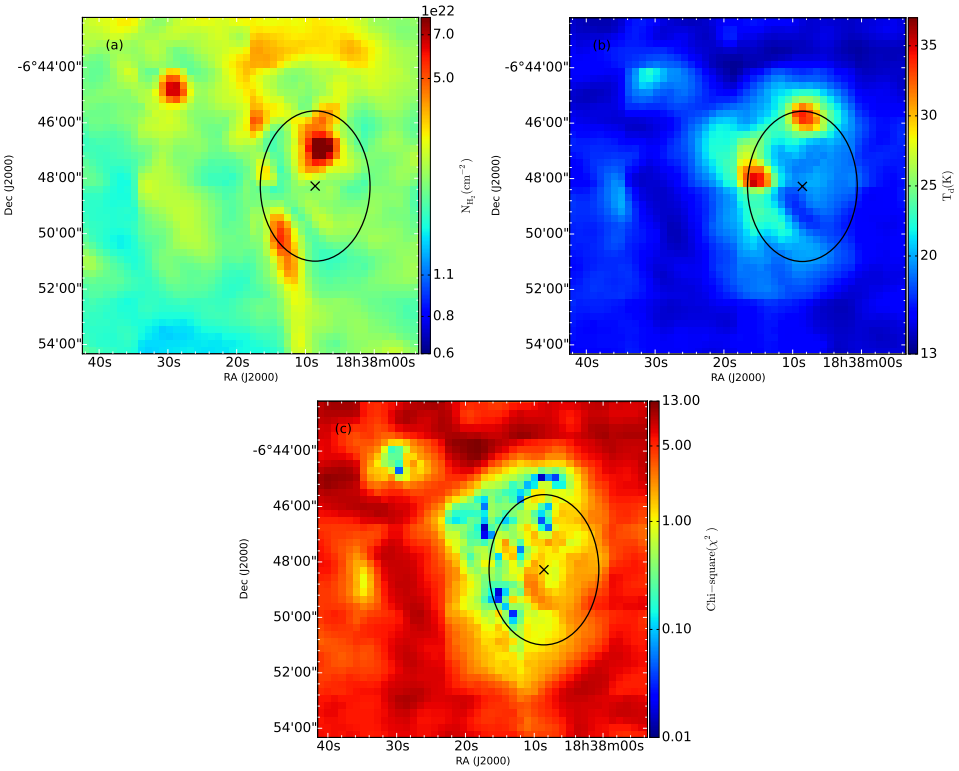

Figure C.4: Same as Figure 6.18, but for bubble N39.

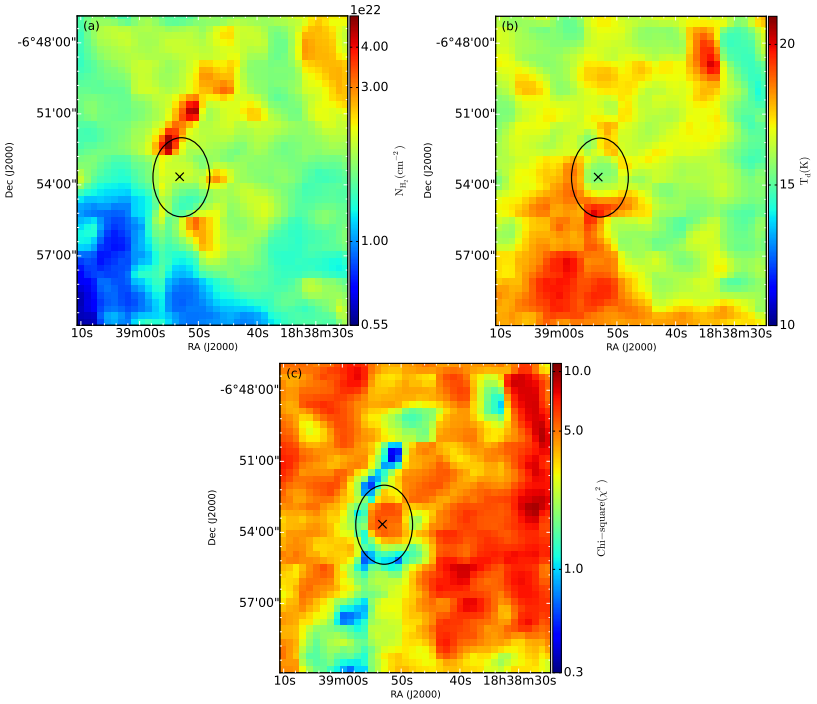

Figure C.5: Same as Figure 6.18, but for bubble N40.

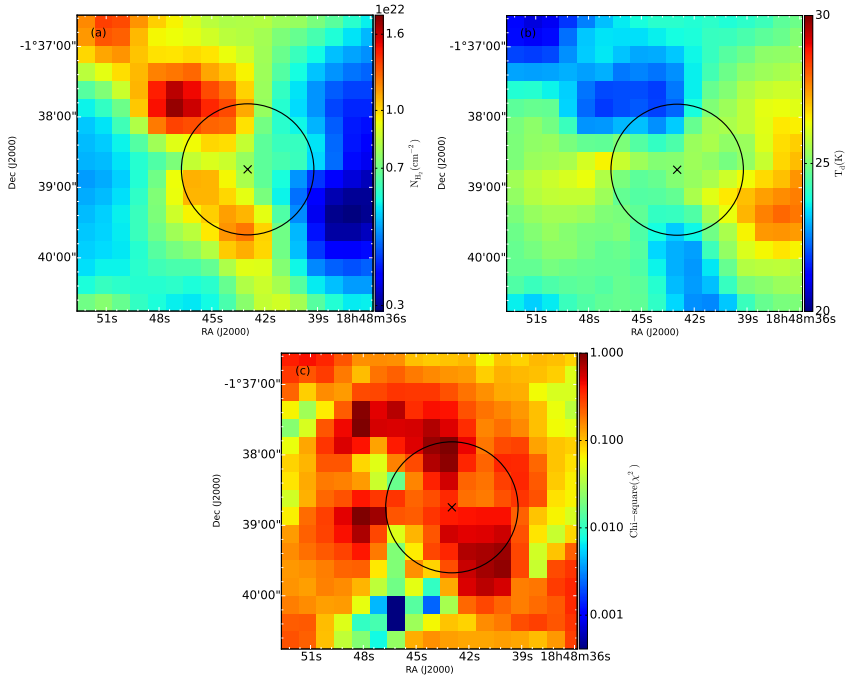

Figure C.6: Same as Figure 6.18, but for bubble N53.

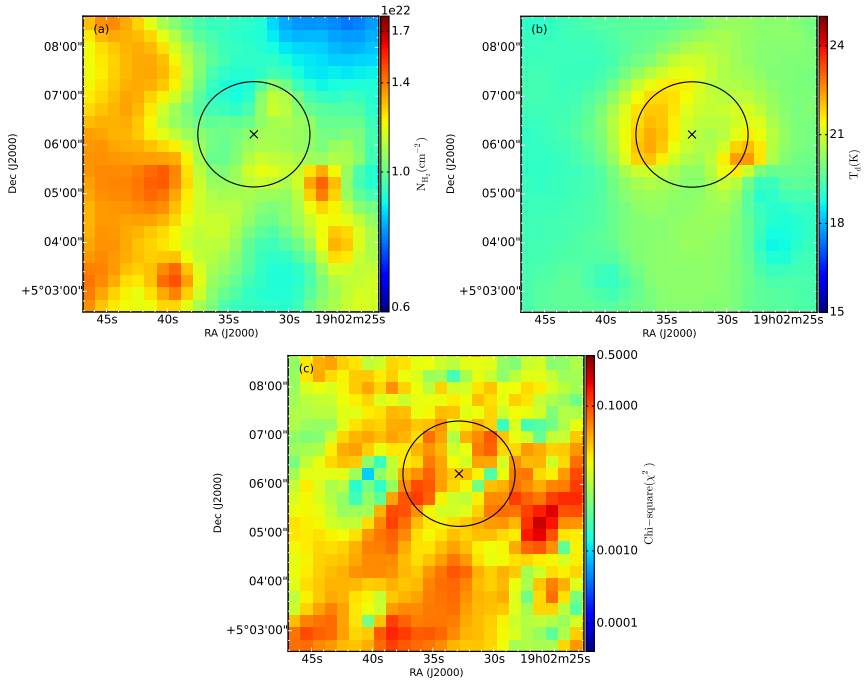

Figure C.7: Same as Figure 6.18, but for bubble N73.

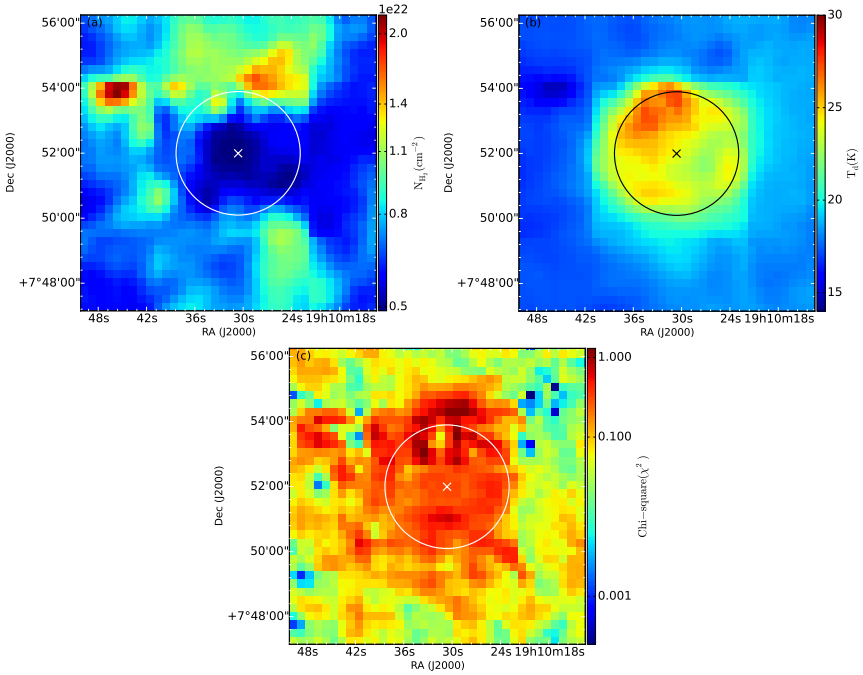

Figure C.8: Same as Figure 6.18, but for bubble N82.

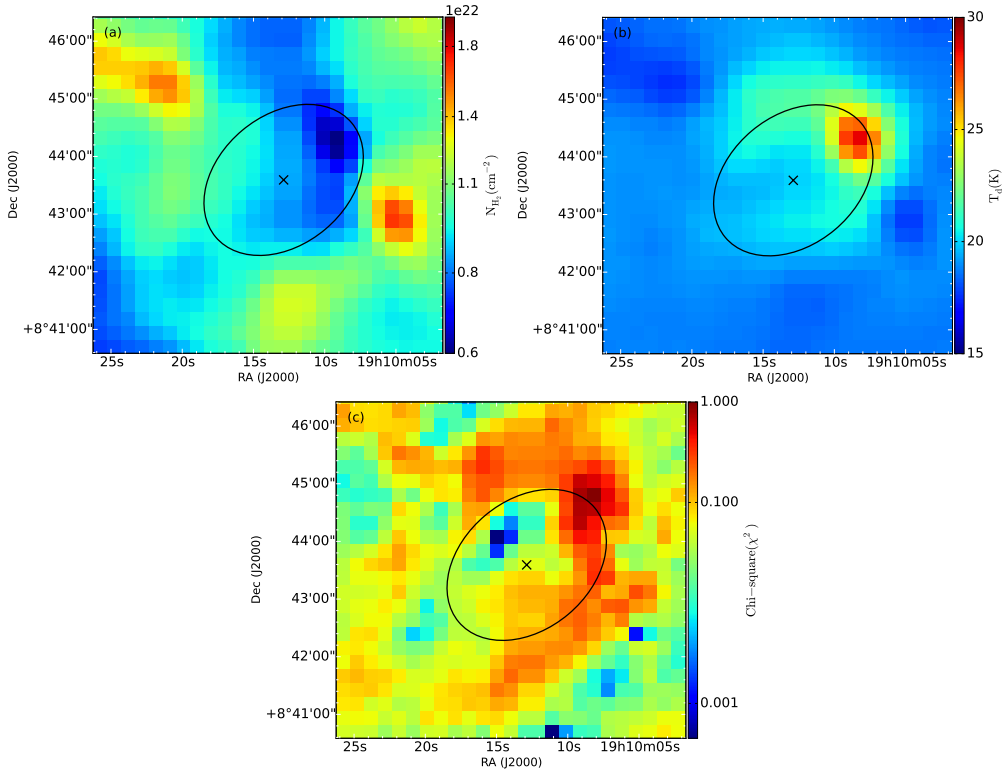

Figure C.9: Same as Figure 6.18, but for bubble N84.

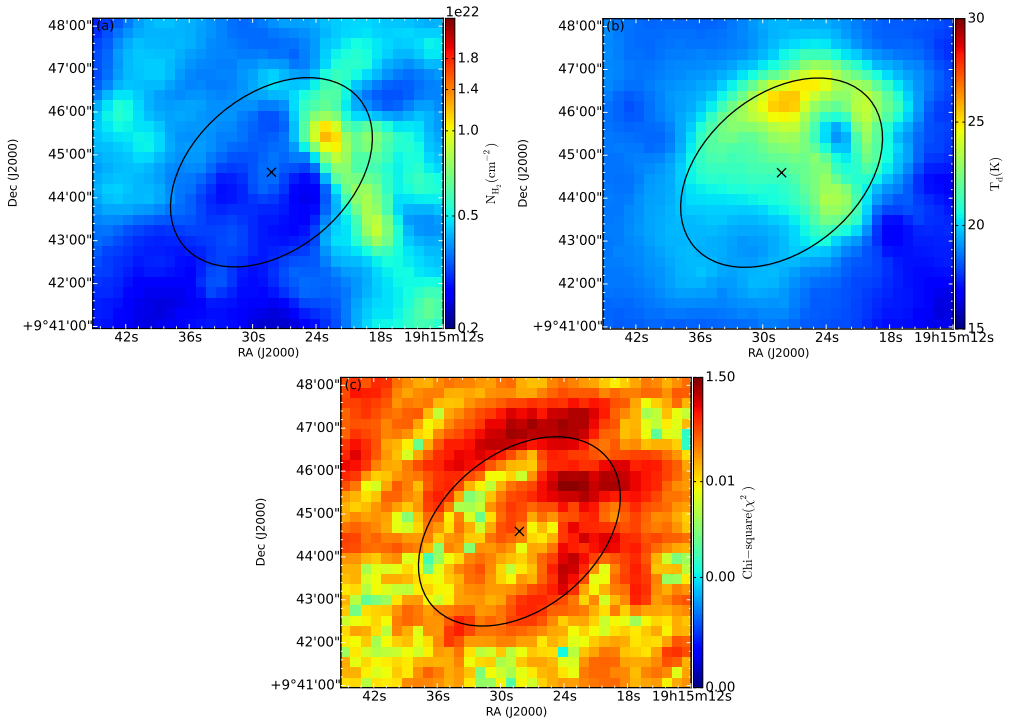

Figure C.10: Same as Figure 6.18, but for bubble N92.

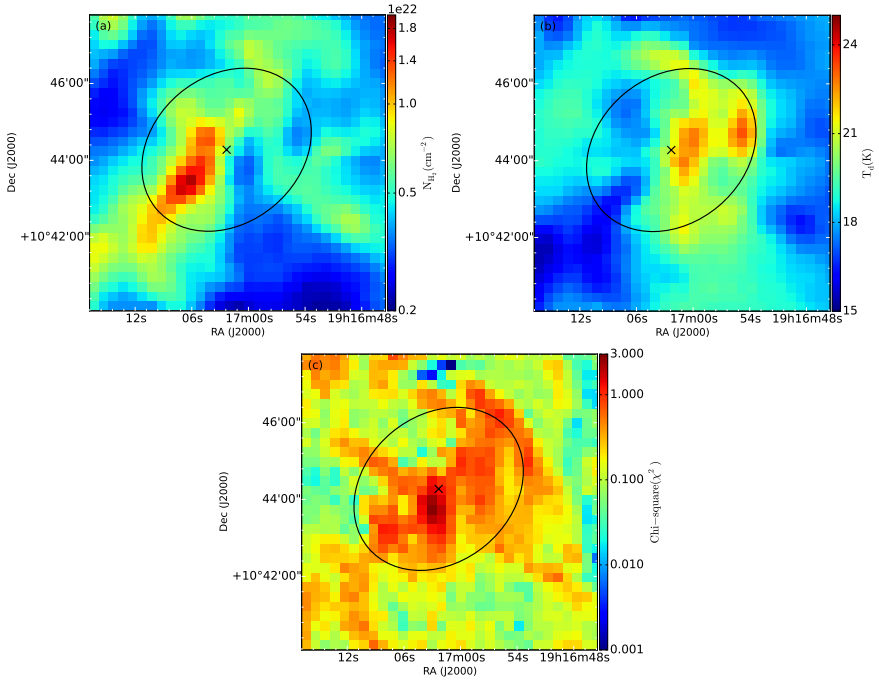

Figure C.11: Same as Figure 6.18, but for bubble N95.

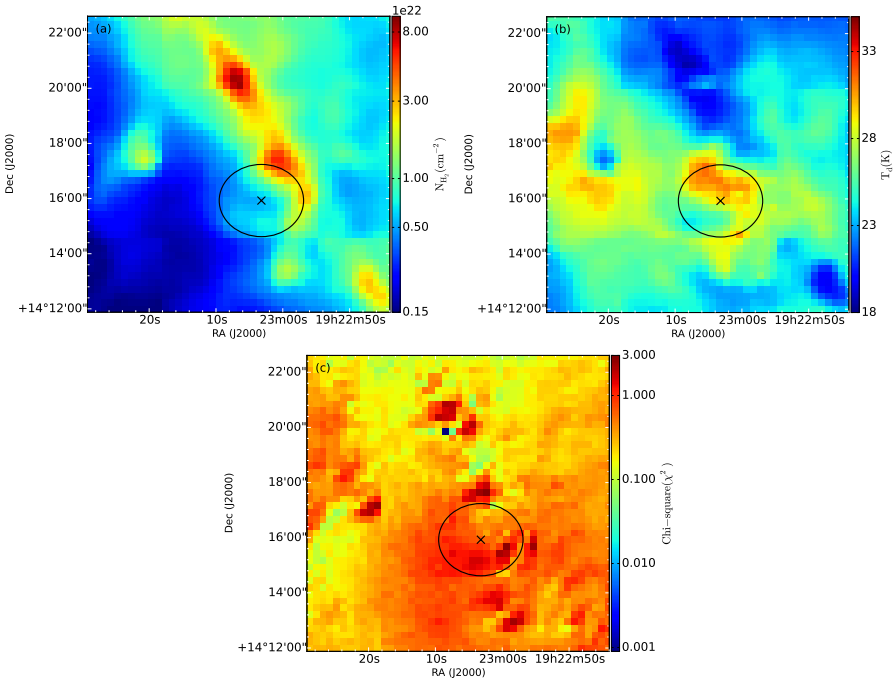

Figure C.12: Same as Figure 6.18, but for bubble N101.

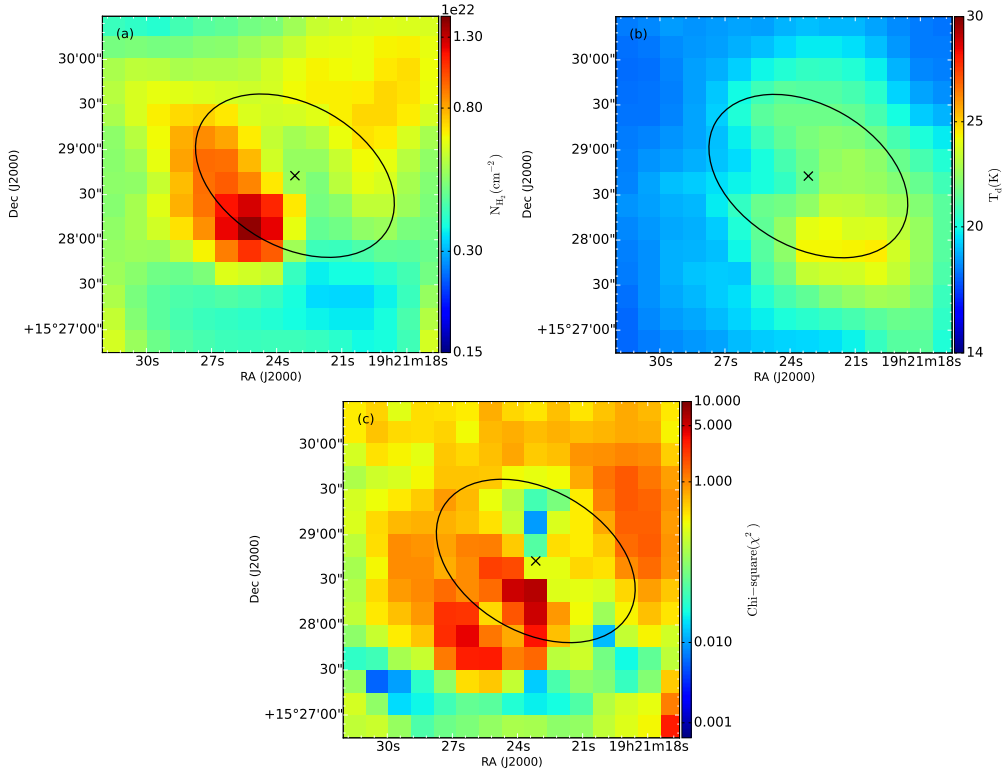

Figure C.13: Same as Figure 6.18, but for bubble N105.

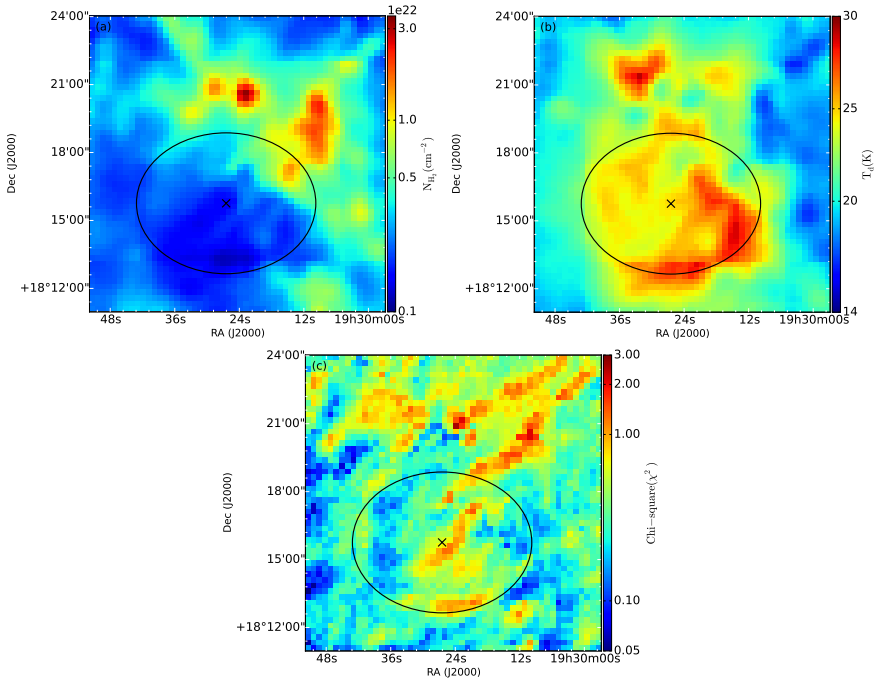

Figure C.14: Same as Figure 6.18, but for bubble N115.

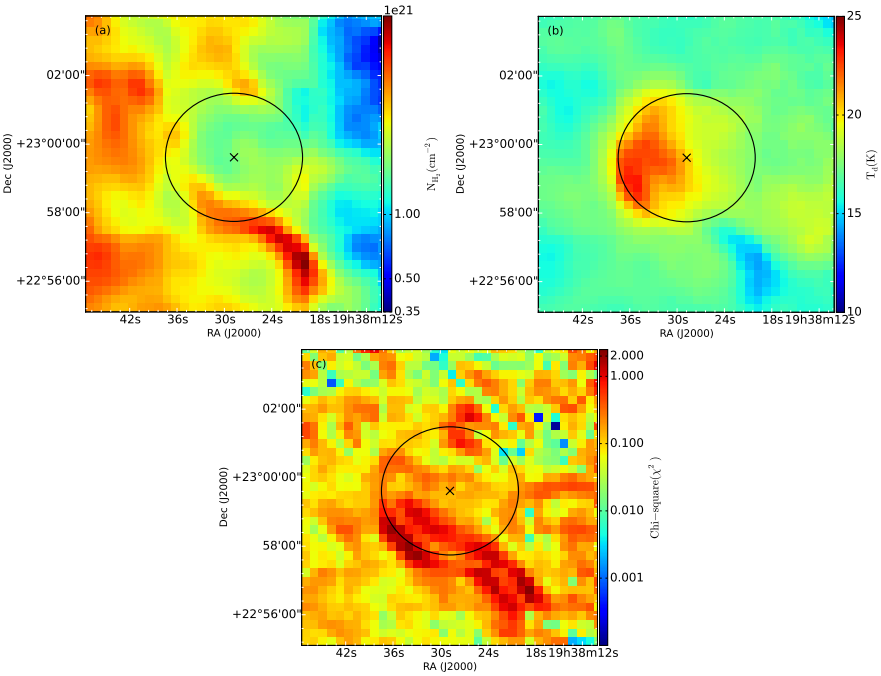

Figure C.15: Same as Figure 6.18, but for bubble N124.

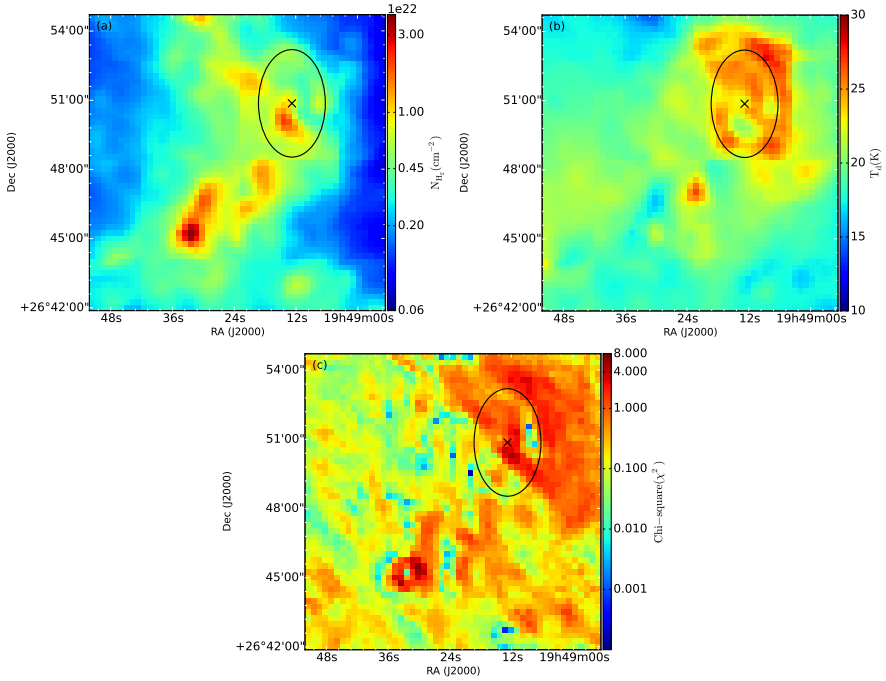

Figure C.16: Same as Figure 6.18, but for bubble N133.

C.2 SED fitting of dust clumps

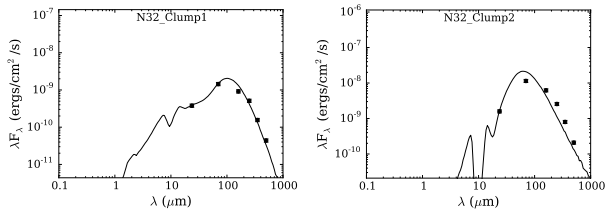

Figure C.17: Same as Figure 6.19, but for clumps associated to bubble N32.

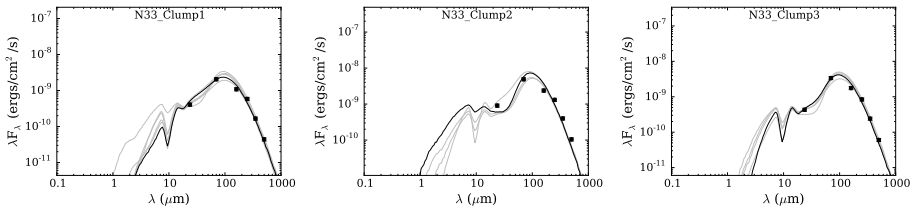

Figure C.18: Same as Figure 6.19, but for clumps associated to bubble N33.

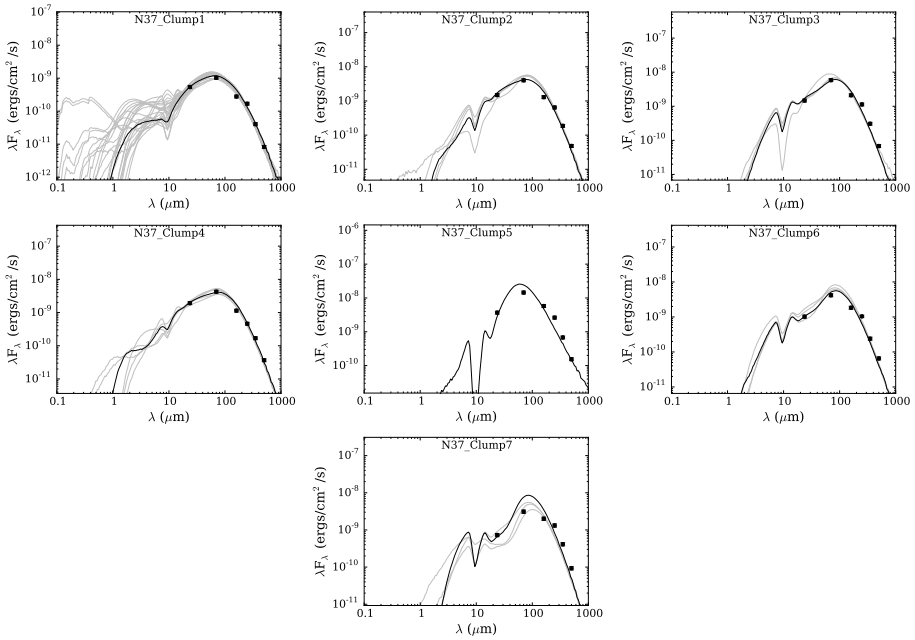

Figure C.19: Same as Figure 6.19, but for clumps associated to bubble N37.

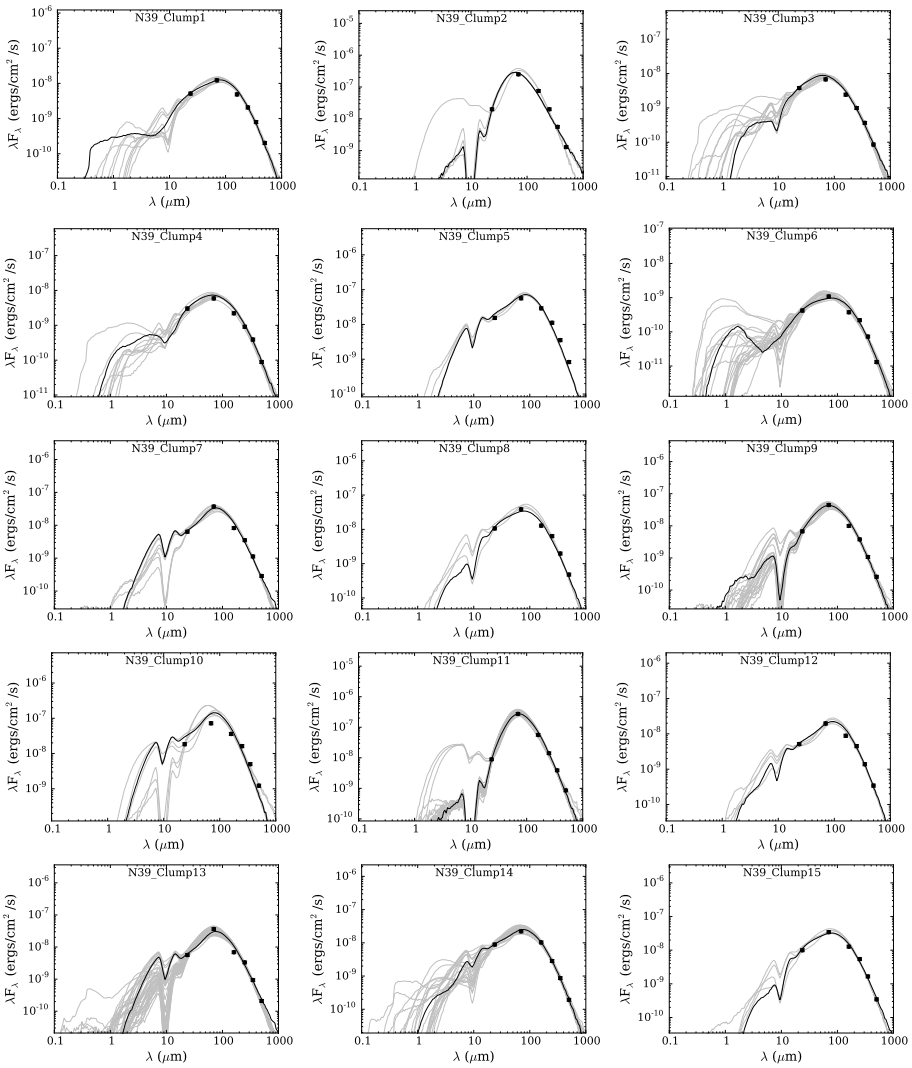

Figure C.20: Same as Figure 6.19, but for clumps associated to bubble N39.

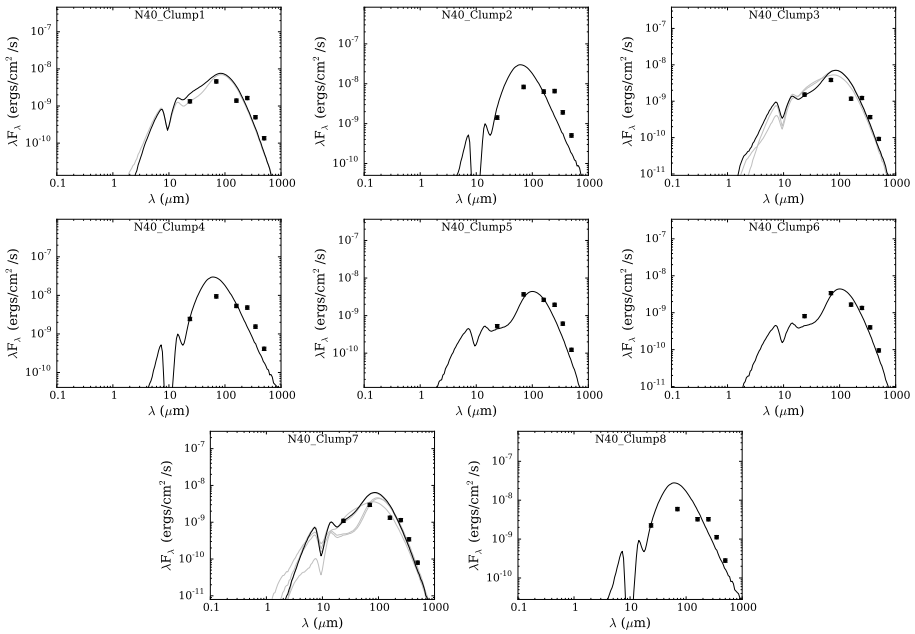

Figure C.21: Same as Figure 6.19, but for clumps associated to bubble N40.

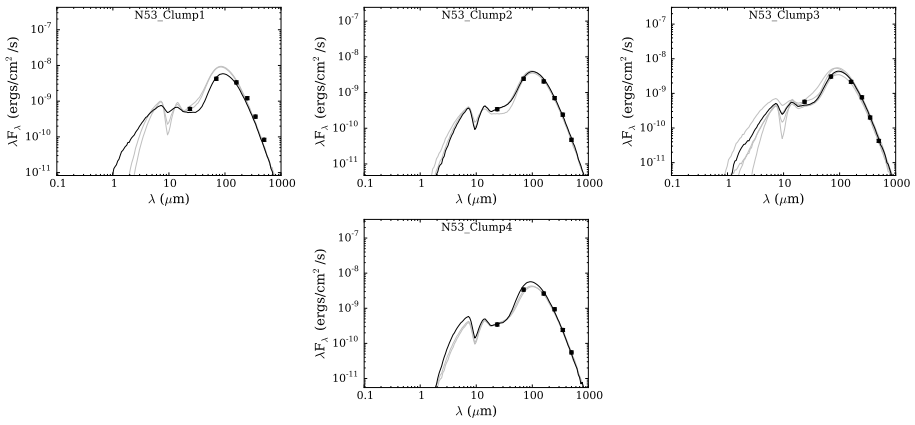

Figure C.22: Same as Figure 6.19, but for clumps associated to bubble N53.

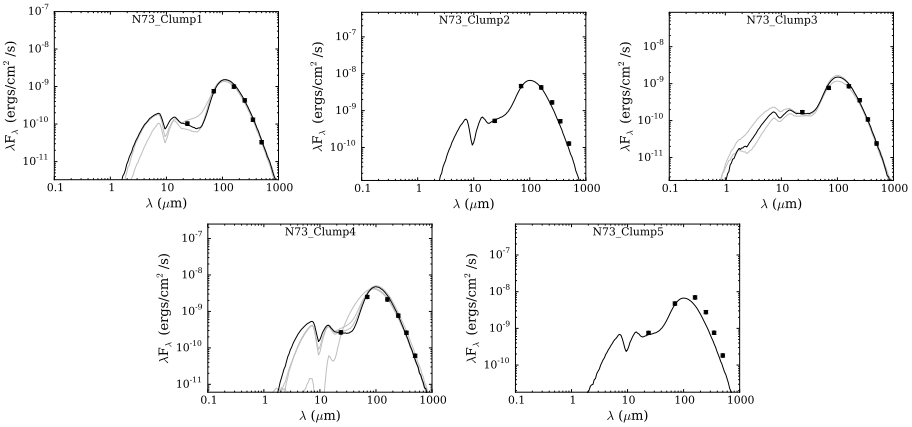

Figure C.23: Same as Figure 6.19, but for clumps associated to bubble N73.

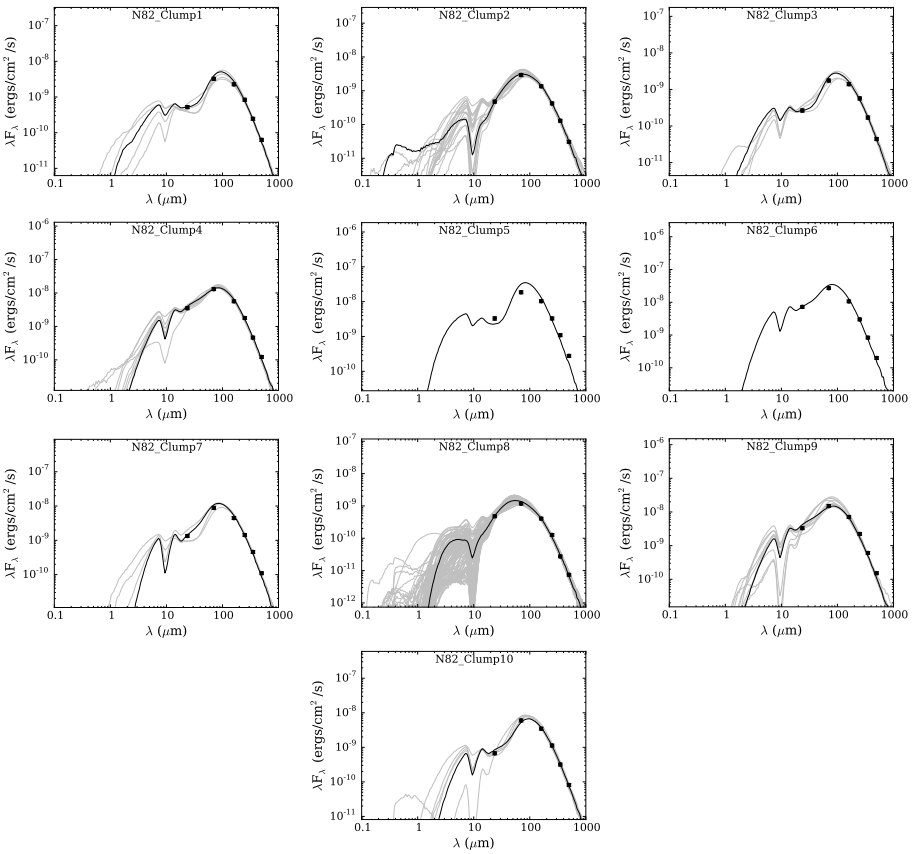

Figure C.24: Same as Figure 6.19, but for clumps associated to bubble N82.

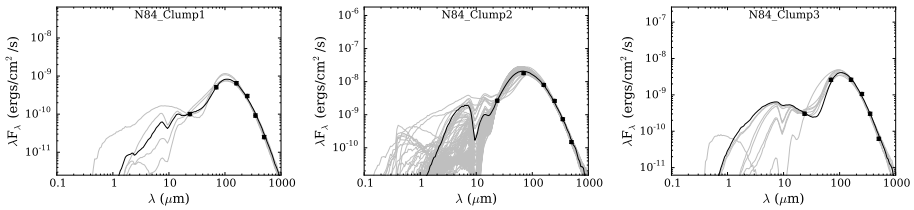

Figure C.25: Same as Figure 6.19, but for clumps associated to bubble N84.

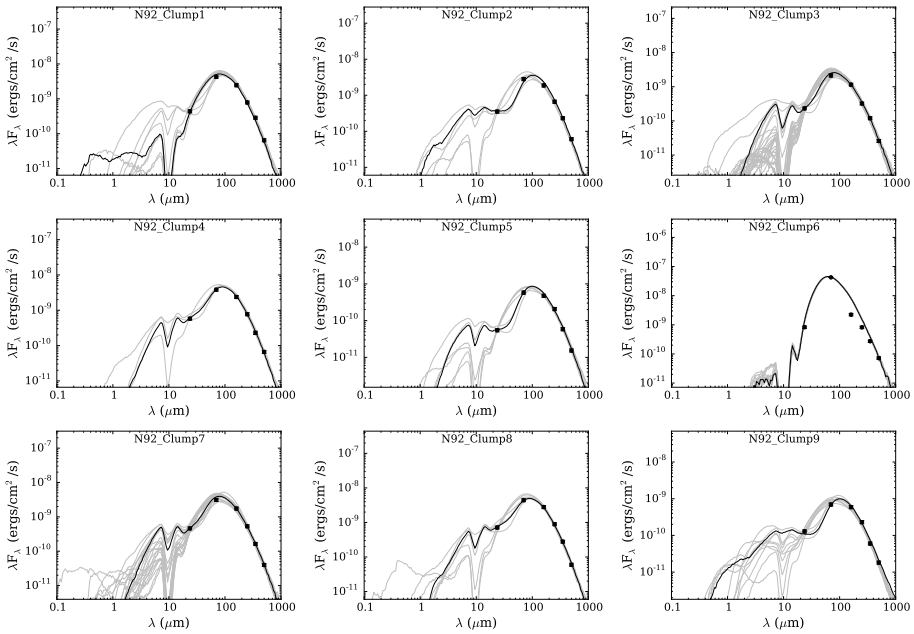

Figure C.26: Same as Figure 6.19, but for clumps associated to bubble N92.

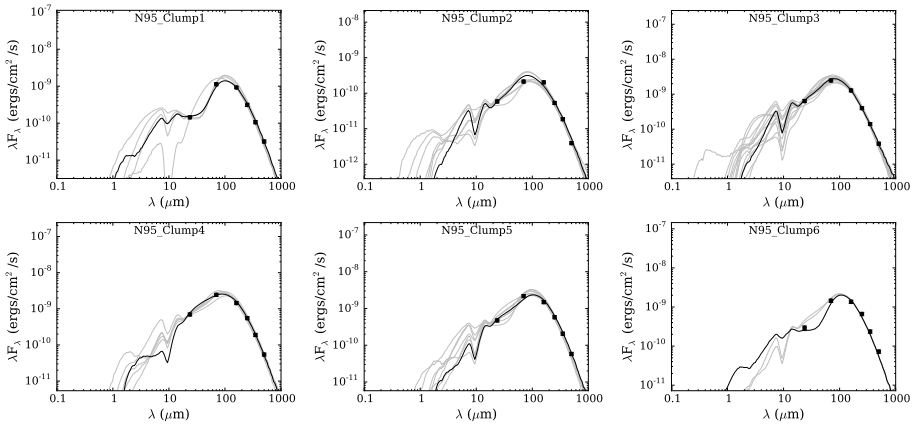

Figure C.27: Same as Figure 6.19, but for clumps associated to bubble N95.

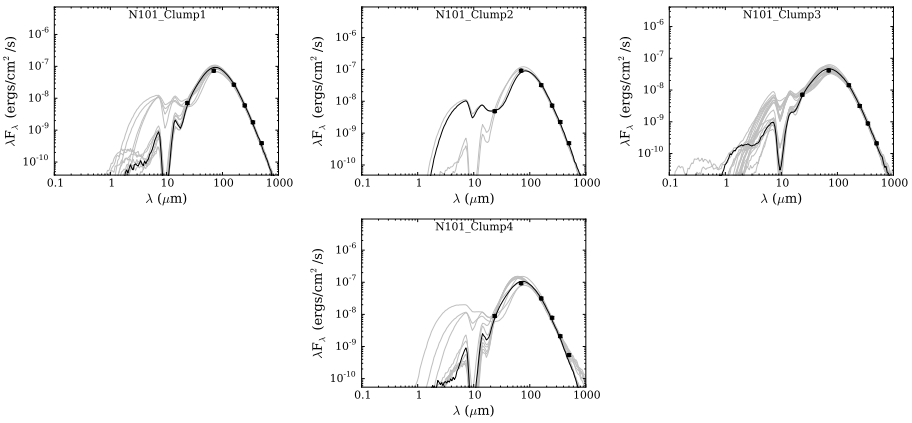

Figure C.28: Same as Figure 6.19, but for clumps associated to bubble N101.

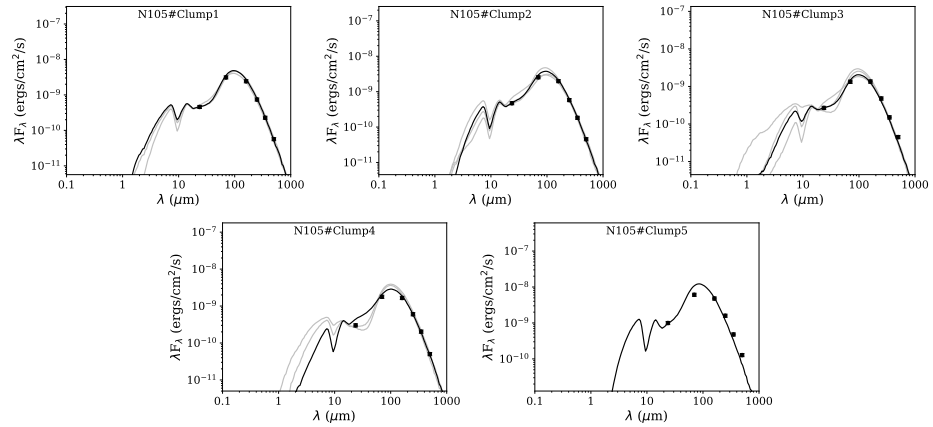

Figure C.29: Same as Figure 6.19, but for clumps associated to bubble N105.

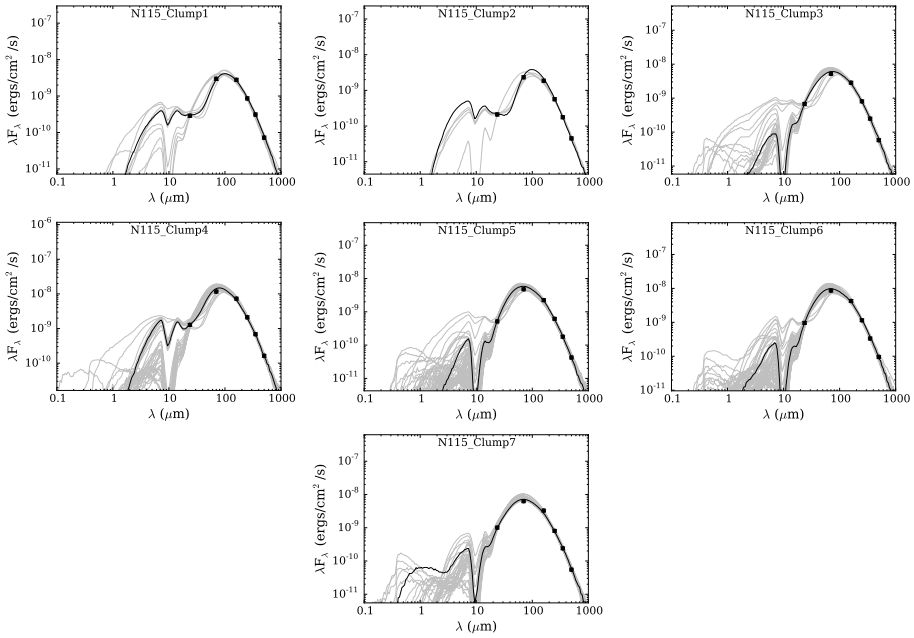

Figure C.30: Same as Figure 6.19, but for clumps associated to bubble N115.

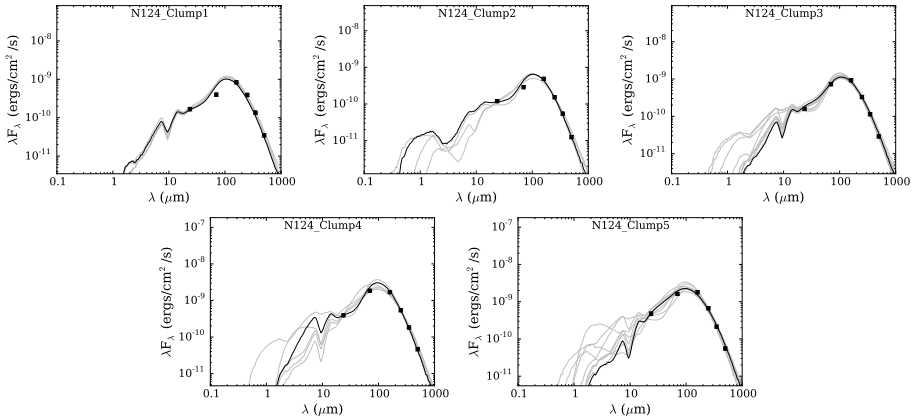

Figure C.31: Same as Figure 6.19, but for clumps associated to bubble N124.

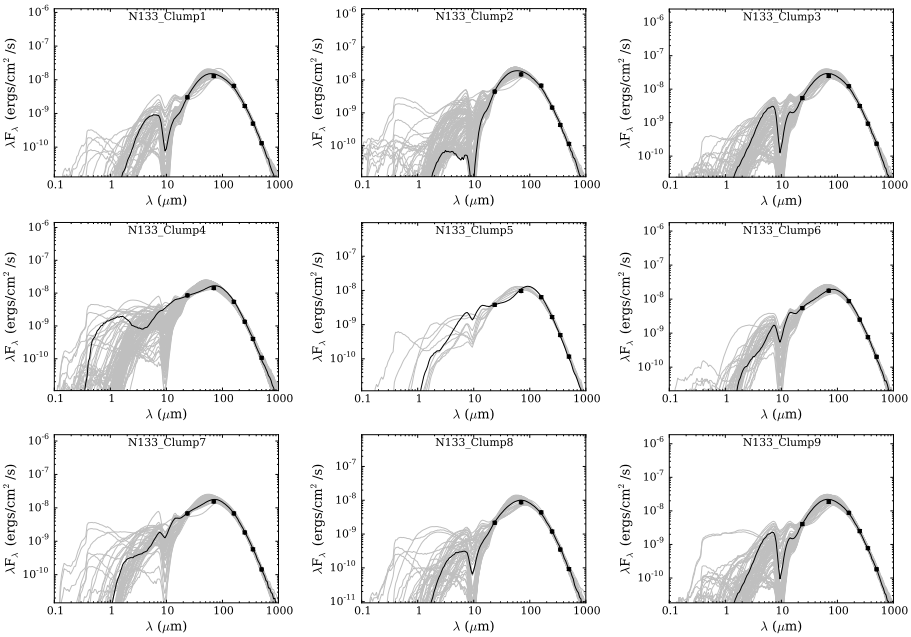

Figure C.32: Same as Figure 6.19, but for clumps associated to bubble N133.

Publications based on the Thesis

1. **High-mass star formation toward southern infrared bubble S10**,
   Swagat Ranjan Das, Anandmayee Tej, Sarita Vig , Swarna K. Ghosh, AJ , 2016, 152, 152

2. **Infrared dust bubble CS51 and its interaction with the surrounding interstellar medium**,
   Swagat Ranjan Das, Anandmayee Tej, Sarita Vig, Hong-Li Liu, Tie Liu, Swarna K. Ghosh, Ishwara Chandra C.H., MNRAS , 2017, 472, 475

3. **Radio and infrared study of southern HII regions G346.056−0.021 and G346.077−0.056**,
   Swagat Ranjan Das, Anandmayee. Tej, Sarita Vig, Tie Liu, Swarna K. Ghosh, Ishwara Chandra C.H, A&A , 2018, 612, A36.

4. **Statistical study of cold dust emission in a sample of IR bubbles**,
   Swagat Ranjan Das, Anandmayee. Tej et al. (under preparation)

Other publications

1. **Radio and infrared study of the star forming region IRAS 20286+4105**
   Varsha R, **Swagat Ranjan Das**, Anandmayee Tej, Sarita Vig , Swarna K. Ghosh, Devendra K. Ojha, MNRAS , 2017, 465, 4753